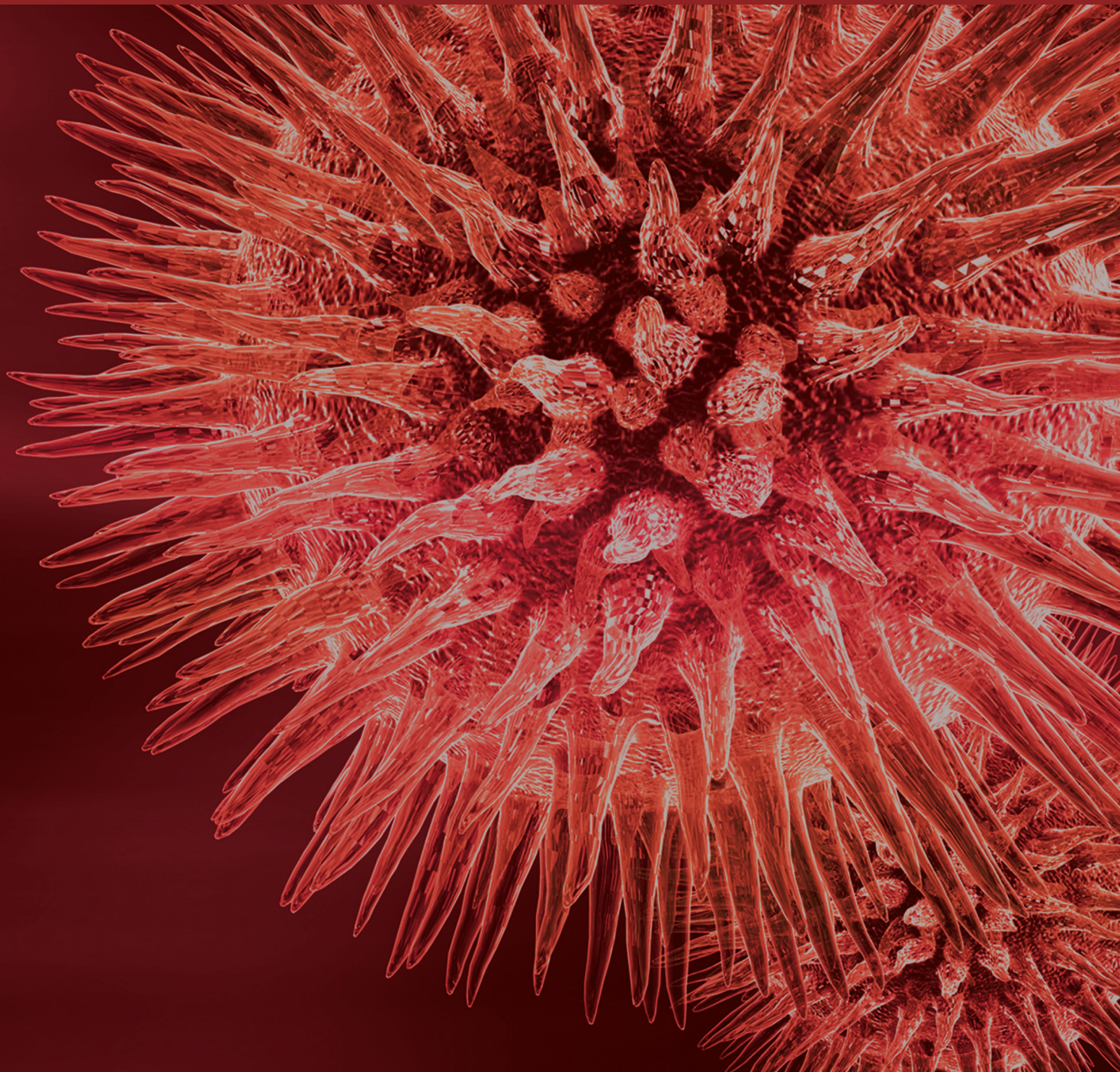


Neural Computation for Rehabilitation

Guest Editors: Xiaoling Hu, Yiwen Wang, Ting Zhao, and Aysegul Gunduz





Neural Computation for Rehabilitation

Neural Computation for Rehabilitation

Guest Editors: Xiaoling Hu, Yiwen Wang, Ting Zhao,
and Aysegul Gunduz



Copyright © 2014 Hindawi Publishing Corporation. All rights reserved.

This is a special issue published in " BioMed Research International." All articles are open access articles distributed under the Creative Commons Attribution License, which permits unrestricted use, distribution, and reproduction in any medium, provided the original work is properly cited.

Contents

Neural Computation for Rehabilitation, Xiaoling Hu, Yiwen Wang, Ting Zhao, and Aysegul Gunduz
Volume 2014, Article ID 603985, 2 pages

Neural Coding for Effective Rehabilitation, Xiaoling Hu, Yiwen Wang, Ting Zhao, and Aysegul Gunduz
Volume 2014, Article ID 286505, 17 pages

A Blood Pressure Monitoring Method for Stroke Management, Heather Ting Ma
Volume 2014, Article ID 571623, 7 pages

DWI-Based Neural Fingerprinting Technology: A Preliminary Study on Stroke Analysis, Chenfei Ye,
Heather Ting Ma, Jun Wu, Pengfei Yang, Xuhui Chen, Zhengyi Yang, and Jingbo Ma
Volume 2014, Article ID 725052, 9 pages

**Circuit Models and Experimental Noise Measurements of Micropipette Amplifiers for Extracellular
Neural Recordings from Live Animals**, Chang Hao Chen, Sio Hang Pun, Peng Un Mak, Mang I Vai,
Achim Klug, and Tim C. Lei
Volume 2014, Article ID 135026, 14 pages

**Movement Type Prediction before Its Onset Using Signals from Prefrontal Area: An
Electrocorticography Study**, Seokyun Ryun, June Sic Kim, Sang Hun Lee, Sehyoon Jeong, Sung-Phil Kim,
and Chun Kee Chung
Volume 2014, Article ID 783203, 9 pages

Robust Deep Network with Maximum Correntropy Criterion for Seizure Detection, Yu Qi,
Yueming Wang, Jianmin Zhang, Junming Zhu, and Xiaoxiang Zheng
Volume 2014, Article ID 703816, 10 pages

**A Study on Decoding Models for the Reconstruction of Hand Trajectories from the Human
Magnetoencephalography**, Hong Gi Yeom, Wonjun Hong, Da-Yoon Kang, Chun Kee Chung, June Sic Kim,
and Sung-Phil Kim
Volume 2014, Article ID 176857, 8 pages

**Gradually Increased Training Intensity Benefits Rehabilitation Outcome after Stroke by BDNF
Upregulation and Stress Suppression**, Jing Sun, Zheng Ke, Shea Ping Yip, Xiao-ling Hu, Xiao-xiang Zheng,
and Kai-yu Tong
Volume 2014, Article ID 925762, 8 pages

Muscle-Based Pharmacokinetic Modeling of Marrow Perfusion for Osteoporotic Bone in Females,
Heather Ting Ma, James F. Griffith, and Ping-Chung Leung
Volume 2014, Article ID 620925, 7 pages

**Neural Decoding Using a Parallel Sequential Monte Carlo Method on Point Processes with Ensemble
Effect**, Kai Xu, Yiwen Wang, Fang Wang, Yuxi Liao, Qiaosheng Zhang, Hongbao Li, and Xiaoxiang Zheng
Volume 2014, Article ID 685492, 11 pages

Nonlinear EEG Decoding Based on a Particle Filter Model, Jinhua Zhang, Jiongjian Wei, Baozeng Wang,
Jun Hong, and Jing Wang
Volume 2014, Article ID 159486, 13 pages

Change of Muscle Architecture following Body Weight Support Treadmill Training for Persons after Subacute Stroke: Evidence from Ultrasonography, Peng Liu, Yanjun Wang, Huijing Hu, Yurong Mao, Dongfeng Huang, and Le Li
Volume 2014, Article ID 270676, 11 pages

Optogenetic Activation of the Excitatory Neurons Expressing CaMKII α in the Ventral Tegmental Area Upregulates the Locomotor Activity of Free Behaving Rats, Songchao Guo, Sicong Chen, Qiaosheng Zhang, Yueming Wang, Kedi Xu, and Xiaoxiang Zheng
Volume 2014, Article ID 687469, 11 pages

Editorial

Neural Computation for Rehabilitation

Xiaoling Hu,¹ Yiwen Wang,² Ting Zhao,³ and Aysegul Gunduz⁴

¹Interdisciplinary Division of Biomedical Engineering, The Hong Kong Polytechnic University, Hung Hom, Kowloon, Hong Kong

²Qiushi Academy for Advanced Studies, Zhejiang University, Zhejiang 310027, China

³Howard Hughes Medical Institute, Janelia Farm Research Campus, Ashburn, VA 20147, USA

⁴J. Crayton Pruitt Family Department of Biomedical Engineering, University of Florida, Gainesville, FL 32611, USA

Correspondence should be addressed to Xiaoling Hu; xiaoling.hu@polyu.edu.hk

Received 29 September 2014; Accepted 29 September 2014; Published 28 December 2014

Copyright © 2014 Xiaoling Hu et al. This is an open access article distributed under the Creative Commons Attribution License, which permits unrestricted use, distribution, and reproduction in any medium, provided the original work is properly cited.

With the rapid growth of ageing population, rehabilitation for neurological disorders such as Alzheimer's, Parkinson's, and stroke is one of the grand challenges faced for the coming years. Knowledge and new technologies are needed for effective rehabilitation to release the increasing demands for long-term medical treatments and healthcare, as well as help the patients regain or maintain independency in their daily lives. Successful rehabilitation depends on the understanding of the pathological mechanisms, effective methods in the treatment, and accurate evaluation of the recovery progress. Advances in neural computation provide solutions to brain modeling, quantitative neural information processing, and neural imaging. New findings in these areas also inspire novel techniques for diagnosis, rehabilitation treatments, and development of novel training devices. Considering the aforementioned trends, neural computation in the area of rehabilitation is a natural choice for the theme of this special issue. In this issue you will find thirteen high-quality, peer-reviewed articles that will provide researchers in diverse backgrounds such as engineering, neuroscience, rehabilitation, and computational sciences with the current state-of-the-art knowledge of this emerging interdisciplinary research area.

The review paper “*Neural coding for effective rehabilitation*” by the special issue editors X. Hu et al. covers a wide range of the latest breakthroughs in neural coding, neural network imaging, and neural informatics techniques with potential applications for more effective rehabilitation, as well as the advancements using electroencephalographic (EEG) and electrocorticographic (ECoG) signals in human patients

for clinical applications and in intelligent robotic systems designed for interactive rehabilitation.

Rehabilitation usually is a long-term process. Its clinical success heavily depends on the accurate diagnosis and follow-up evaluations. Furthermore, for effective rehabilitation a better understanding of the relationships between physical exercise therapies and the motor outcome is essential. This special issue presents two imaging studies for enhancing diagnosis of stroke subtypes and evaluation of rehabilitation outcomes. The paper “*DWI-based neural fingerprinting technology: a preliminary study on stroke analysis*” by C. Ye et al. proposes a new methodology to identify subtypes of ischemic stroke using diffusion weighted imaging to facilitate the efficient clinical diagnosis. P. Liu et al. introduce a cost-effective ultrasonic method for poststroke muscular evaluation and monitoring the outcomes of rehabilitation training in their paper entitled “*Change of muscle architecture following body weight support treadmill training for persons after subacute stroke: evidence from ultrasonography*”.

The paper “*Gradually increased training intensity benefits rehabilitation outcome after stroke by BDNF upregulation and stress suppression*” by J. Sun et al. illustrates the effects of rehabilitation, namely, fixed training regiments versus increased training intensity on the cerebral neuroplasticity. Studying the effects of rehabilitation on the process of neuroplasticity coupled with motor outcome is extremely important for the design of therapies that are likely to expedite recovery. To this end, brain-machine interfaces (BMIs) have been a promising tool, which enables users to learn to modulate their neural

activity through real-time feedback. In this issue, we highlight several articles that focus on the design of BMIs that could have significant applications for rehabilitation. The paper “*Circuit models and experimental noise measurements of micropipette amplifiers for extracellular neural recordings from live animals*” by C. H. Chen et al. presents a study on noise modeling for novel hardware designs utilizing micropipettes for extracellular recordings for BMI applications. “*Neural decoding using a parallel sequential Monte Carlo method on point processes with ensemble effect*” by K. Xu et al. introduces a new sequential Monte Carlo estimation on point processes that can accurately predict movement from neural activity in real time on GPU, providing up to 10 times faster decoding speeds compared to serial implementations. S. Ryun et al. show that it is possible to predict and delineate hand grasping from elbow flexion using ECoG signals prior to movement execution in humans. The novelty of this work is that signals utilized for the prediction were delimited to the prefrontal cortex with no input from sensorimotor areas. The next two papers focused on noninvasive recording methodologies. In “*A study on decoding models for the reconstruction of hand trajectories from the human magnetoencephalography*,” H. G. Yeom et al. present a Kalman filter approach to continuously reconstruct hand trajectories using MEG. The paper “*Nonlinear EEG decoding based on a particle filter model*” by J. Zhang et al. describes a novel nonlinear particle filter model that achieves decoding accuracies comparable to those in the literature and requires smaller training datasets. Y. Qi et al. present a BMI study for clinical applications in epilepsy in the paper “*Robust deep network with maximum correntropy criterion for seizure detection*.”

There are three papers that provide novel methodologies demonstrating promising potential applications for stroke therapy and monitoring. In “*Optogenetic activation of the excitatory neurons expressing CaMKIIα in the ventral tegmental area upregulates the locomotor activity of free behaving rats*” S. Guo et al. successfully and selectively upregulated the locomotor activity of free behaving rats. The authors will further study if they can have similar results in stroke models. The paper “*A blood pressure monitoring method for stroke management*” by H. T. Ma introduces cuffless blood pressure monitors, which can be used for monitoring stroke survivors, since blood pressure is an important risk factor for stroke prognosis. H. T. Ma et al. also present a “*Muscle-based pharmacokinetic modeling of marrow perfusion for osteoporotic bone in females*,” which is a novel muscle-based pharmacokinetic modeling approach to monitor marrow perfusion.

We hope that this special issue will help to promote the further development of neural computation methodologies for rehabilitation. Improved understanding between neural plasticity and rehabilitation, as well as improved methodologies for the diagnosis of disorders and the evaluation of progress in behavior and physiology, may lead to better performance outcomes in neurorehabilitation. Such methods can also reduce the cost, duration, and overall impact of neurological disease. In addition to reducing suffering and improving quality of life, neurorehabilitation when combined with novel neural computation methods has the potential to

advance our knowledge about the mechanisms of the nervous system.

Acknowledgments

We would like to express our deepest gratitude to many reviewers, whose professional comments guaranteed the high quality of the selected papers. In addition, we also would like to express our appreciation to the editorial board members for their help and support throughout the preparation of this special issue.

Xiaoling Hu
Yiwen Wang
Ting Zhao
Aysegul Gunduz

Review Article

Neural Coding for Effective Rehabilitation

Xiaoling Hu,¹ Yiwen Wang,² Ting Zhao,³ and Aysegul Gunduz⁴

¹ Interdisciplinary Division of Biomedical Engineering, The Hong Kong Polytechnic University, Hung Hom, Kowloon, Hong Kong

² Qiushi Academy for Advanced Studies, Zhejiang University, Zhejiang 310027, China

³ Howard Hughes Medical Institute, Janelia Farm Research Campus, Ashburn, VA 20147, USA

⁴ J. Crayton Pruitt Family Department of Biomedical Engineering, University of Florida, Gainesville, FL 32611, USA

Correspondence should be addressed to Xiaoling Hu; xiaoling.hu@polyu.edu.hk

Received 11 April 2014; Revised 23 July 2014; Accepted 10 August 2014; Published 2 September 2014

Academic Editor: Tianming Liu

Copyright © 2014 Xiaoling Hu et al. This is an open access article distributed under the Creative Commons Attribution License, which permits unrestricted use, distribution, and reproduction in any medium, provided the original work is properly cited.

Successful neurological rehabilitation depends on accurate diagnosis, effective treatment, and quantitative evaluation. Neural coding, a technology for interpretation of functional and structural information of the nervous system, has contributed to the advancements in neuroimaging, brain-machine interface (BMI), and design of training devices for rehabilitation purposes. In this review, we summarized the latest breakthroughs in neuroimaging from microscale to macroscale levels with potential diagnostic applications for rehabilitation. We also reviewed the achievements in electrocorticography (ECoG) coding with both animal models and human beings for BMI design, electromyography (EMG) interpretation for interaction with external robotic systems, and robot-assisted quantitative evaluation on the progress of rehabilitation programs. Future rehabilitation would be more home-based, automatic, and self-served by patients. Further investigations and breakthroughs are mainly needed in aspects of improving the computational efficiency in neuroimaging and multichannel ECoG by selection of localized neuroinformatics, validation of the effectiveness in BMI guided rehabilitation programs, and simplification of the system operation in training devices.

1. Introduction

Neurological rehabilitation usually is a long-term process for patients suffering from trauma or disorders of the nervous system. With the growth of the ageing population across the world, the number of patients with degenerative (e.g., Parkinson disease, amyotrophic lateral sclerosis (ALS)) and vascular disorders (e.g., stroke) has increased substantially. In fact, stroke, a cerebrovascular accident, has been identified as the leading cause of adult disability [1, 2]. Providing long-term and effective rehabilitation service has been a grand challenge in many countries and has created pressure to current medical care systems [3]. Neural coding, a technology for interpretation of functional and structural information of the nervous system, has contributed a lot to the advancements in neurological rehabilitation.

Successful neurological rehabilitation firstly depends on the accurate diagnosis of the underlying pathology, its anatomical foci, and the effects on functional networks and structural connections. The advancements in volumetric neuroimaging technology now allow us to visualize neural

networks in detail from macroscale to microscale levels. For instance, functional magnetic resonance imaging (fMRI) is now commonly used clinically for diagnosis on the cerebral network reorganization after stroke, that is, the macroscale imaging, and with the application of high-resolution optical microscopy, the structure and the dynamic connection among a group of neurons could be revealed, that is, microscale imaging [4]. Neural imaging provides not only the diagnostic information, but also the mechanism or theoretical support for designing optimal rehabilitation therapy as an evaluation tool.

Effective treatment is the second important component in the rehabilitation. The traditional physical and occupational therapies are mainly conducted by human therapists, who can interact with a patient and support him/her to complete the desired training tasks. However, with the shortage of the rehabilitation professionals and the growing population of the patients, assistive rehabilitation devices (e.g., rehabilitation robots) are in great demand. The design of rehabilitation devices that can interact with the patients is based on the identification of voluntary motor intention of

a user. Brain-machine interface (BMI), sometimes termed as brain-computer interface (BCI), is a technique that has been explored to decode such voluntary motor intention from brain signals, for example, electroencephalography (EEG) and electrocorticography (ECoG), which are the neural potentials detected from the scalp and the brain, respectively [5, 6]. ECoG, also known as intracranial EEG (iEEG), refers to neural recordings from the cortical surface through a surgical incision to the skull. The detection of ECoG is invasive with the electrode array directly attached to the brain; however, ECoG signals have much higher spatial and temporal resolution than the scalp EEG. BMIs with ECoG detection have been mainly investigated in animal models, for example, monkeys, for possible interaction with external systems, such as a computer game, or even a prosthetic robot [7, 8]. The animal BMI studies paved the road to the application of ECoG BMI to human beings for rehabilitation purposes. BMI technique is important in designing rehabilitation devices for severely paralyzed patients, whose limb motions are hardly to be detected. Besides the neural signals detected from the brain, muscular electricity, that is, electromyography (EMG), also has been used to explore the neural instructions to the muscles. In comparison with neural or neuronal signals, EMG has focalized resolution on individual muscles and relatively higher amplitudes detected noninvasively. Therefore, EMG is also a favorable biosignal in controlling rehabilitation devices for patients with residual muscle functions [9, 10].

The third important component in neural rehabilitation is the quantitative evaluation during and after physical training. Rehabilitative treatment is a long-term intervention that usually lasts for years, during which the development of diseases or the progress of recovery needs to be monitored for the adaptation of treatment programs. However, most of the assessment tools used clinically are subjective based on the observation of practitioners, such as the Fugl-Meyer Assessment [11] for evaluation of upper limb motor function and the Modified Ashworth Scores for assessing muscular spasticity [12]. Due to the lack of manpower in rehabilitation industry, even the subjective evaluations are sparse in most of clinical services currently. New methods are needed for quantitative and long-term assessment on the rehabilitation progress and the posttraining follow-ups. Taking advantage of the neural coding technique, it is possible that training devices also can act as evaluation systems. In this review, we summarized the latest breakthroughs in neural coding with the potential application for more effective rehabilitation on neural network imaging and neural informatics in the cortical areas of monkey during dynamic limb motions; we also reviewed the achievements in neural coding by electrocorticographic interpretation in human beings for clinical applications and intelligent robotic system designed for interactive rehabilitation.

2. Volumetric Neural Imaging

In the past few decades, one of the most exciting achievements in neural coding studies is volumetric functional

imaging, which has enabled monitoring brain-wide neural activities at precise locations. In this section, we reviewed the recent advancements of the macroscale fMRI and the microscale/mesoscale optical microscopy, the two major classes of volumetric imaging techniques that have been used or have potential applications for rehabilitation. We also highlighted the application of volumetric imaging on neural network reconstruction, which is expected to have fundamental impact on rehabilitation.

2.1. Macroscale Imaging-Functional MRI. MRI opens a new window for observing the brain noninvasively. By measuring wave energy emitted from hydrogen atoms excited by a magnetic field, MRI can produce 3D images of anatomical structures or physiological status of a brain. In particular, fMRI, which measures the BOLD (blood-oxygen-level dependent) effect related to neural activities, provides a unique opportunity of recording activities of the whole human brain at a relatively high resolution. We can study neural encoding and decoding with fMRI, which presents individual voxels as the basic coding unit.

Encoding of fMRI predicts voxel-wise activities given certain stimuli. Kay et al. developed a visual encoding model with four components, including the set of stimuli, the features of stimuli, ROI in the brain, and the algorithm of model estimation [13]. This strategy can be adapted for encoding motion, where the first two components become the set of movements and the features of movements. Decoding of fMRI signal has been extensively studied. It maps voxel dynamics to external stimuli [14], motor behaviors [15], or even high-level cognitive states [16]. While general linear models have been successfully used to build mapping models, there are significant efforts underway for applying modern machine learning techniques [17], such as kernel methods [18], random forests [19], and manifold learning [20] for the same purpose.

Another exciting development in fMRI decoding is real-time fMRI (rtfMRI) [21], which takes advantage of online processing of fMRI images. Set up with decoding models trained offline, rtfMRI returns decoding results as interpretable feedback to the human subject within a short delay after acquisition. The process is fast enough for the subject to modulate the brain activity in the sense of real time. Powerful parallel processing frameworks, which are becoming more and more affordable nowadays, can further improve the decoding speed and potentially clear any bottlenecks in computational modules [22]. This creates an opportunity for building high degree-of-freedom noninvasive brain-machine interfaces using fMRI.

2.2. Microscale/Mesoscale Imaging-Optical Microscopy. At the microscopic/mesoscale level, the most common functional imaging technique is calcium imaging, which mainly uses small fluorescence dyes (e.g., fura-2), or genetically encoded fluorescence proteins (e.g., GCaMP), to measure the concentration fluctuation of free calcium ions in response to electrical signals. Calcium imaging can be used to measure a large population of neurons *in vivo*. Assisted by genetic

TABLE 1: Comparison of functional brain imaging methods.

	Temporal resolution	Spatial resolution	Advantage	Limitation
fMRI [144]	≥ 0.5 s	≥ 1 mm	Noninvasive whole brain imaging	Indirect measurement
Optical microscopy [23]	~ 0.2 s	$\sim 0.2 \mu\text{m}$	Single cell resolution	Unsuitable for human subject
Scalp EEG [145]	~ 1 ms	≥ 2 cm (128 channels)	Noninvasive whole brain recording	Low spatial resolution; signals are easily contaminated by noises (e.g., EMG, motion artifacts, etc.)
ECoG [95–99, 146]	~ 5 ms	~ 10 mm	Long-term and continuous recording	Invasive recording by attaching the electrode array on the surface of the brain

engineering, it can measure specific types of neurons or neurons at specific locations. Recent breakthroughs demonstrated the real power of calcium imaging for studying the whole brain at the single cell level: Schrödel et al. recorded $\sim 70\%$ of head neurons of *C. elegans* using wide-field temporal focusing [23] and Ahrens et al. recorded more than 80% of all neurons of the larval zebrafish brain using light-sheet microscopy [4].

Studying neural coding with microscope imaging, however, is a relatively new research area, which has few original methods designed for special properties of calcium imaging data. Therefore, this presents a new opportunity and challenge to computer scientists and engineers to develop innovative computational algorithms and tools. One major challenge would be the big data problem, because scanning the whole brain at the microscopic scale will produce terabytes or even petabytes of data. Decomposing the data into tractable components and mapping them onto a low-dimensional feature space are a key to revealing unknown brain dynamics.

Although its direct clinical application is yet to be clear, microscopic imaging can revolutionize rehabilitation by providing the mechanism or theoretical support for designing optimal rehabilitation therapy. This will rely on animal studies, which are more accessible resources for understanding the human brain than the human brain itself. The relatively small scale of animal brains offers practical opportunities for understanding a complete nervous system at the single cell level. Due to the fundamental similarities among the motor systems of all animal species, we can build disease models on animals to study problems associated with rehabilitation. For example, Li et al. has developed a *C. elegans* model of ALS to evaluate the role of autophagy in the disease [24]. For the vertebrate species, there are mice models for studying motor axon regeneration and muscle reinnervation [25] and zebrafish models for studying brain disorders [26]. Another obvious advantage of setting experiments with animal models is the possibility of using a rich set of genetic tools for targeting specific neurons and manipulating neuron functions [27]. The recent development of optogenetics especially has allowed us to control neural activities more precisely than ever before. Combining optogenetics with calcium imaging will definitely provide a powerful tool for observing neural

activities when activating or inhibiting a specific set of neurons [28].

2.3. Neural Network Reconstruction. The human brain is a highly dynamic network generating coordinated activities of billions of connected neurons. In this sense, neural rehabilitation is basically the recovery of impaired neural networks. Therefore, the advancement of rehabilitation techniques relies on how well we understand neural coding in the neural network, which in turn requires reconstructing functional network or connectome from real data.

Electrophysiological recordings have been used to reconstruct functional neural networks at different scales [29–31], but they have fundamental limitations in resolution or coverage (Table 1). For example, EEG/ECoG can only provide networks with a low spatial resolution due to their recording sites outside of the brain. On the other hand, while extracellular electrophysiological recordings of neuron activities have the single cell resolution, they are limited to a small subset of neurons with obscure identities.

To reconstruct a functional network with better resolution-scale trade-off, we must take advantage of volumetric functional imaging. A common practice for mapping the functional connectivity of human brains is to compute region correlations of the spontaneous fluctuation of the BOLD effect in resting-state fMRI imaging [32]. Various statistical correlation analysis approaches, such as clustering [33], independent component analysis [34], and Bayesian network [35], have been successfully applied. These approaches should also be applicable to microscopic functional imaging, which is currently at the stage of delivering whole brain data at single cell resolution.

We can also reconstruct neural networks anatomically and then infer the functional connectivity. This can be done by diffusion tensor imaging at the macroscopic scale [36], serial two-photon tomography at the mesoscale [37], and fluorescence microscopy [38] or electron microscopy [39] at the microscopic scale. Although structural neural networks do not provide functional connections directly, they have rich clues about how information processing is implemented in the brain. For example, structural analysis of a circuit in the *Drosophila* optical lobe has, for the first time, shown that

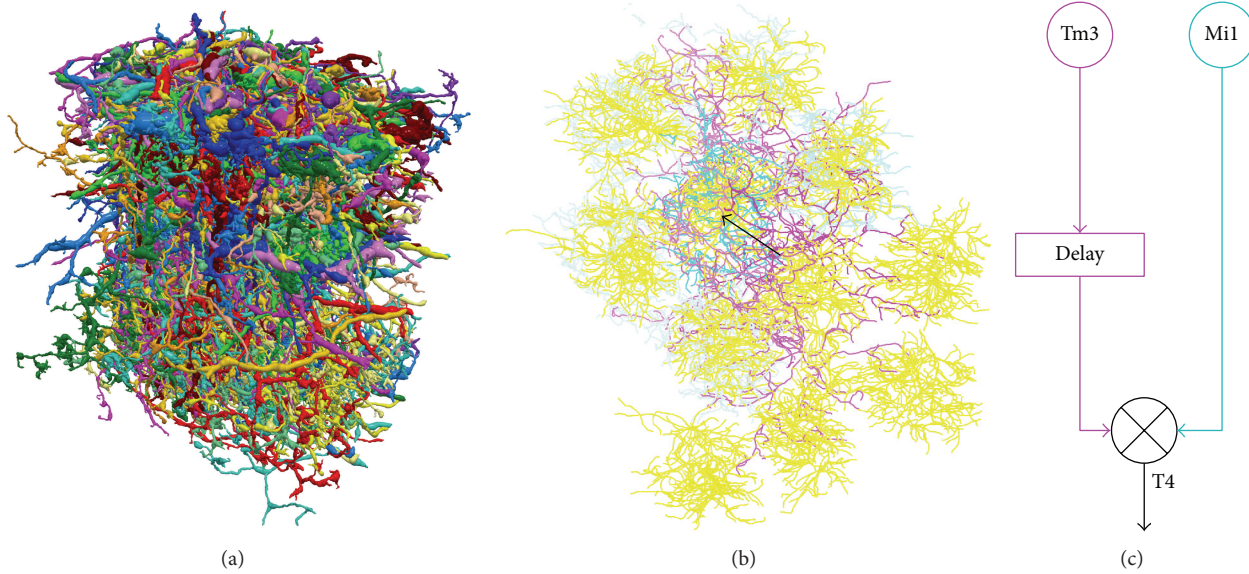


FIGURE 1: The motion detection circuit suggested by a connectome reconstructed from the *Drosophila* brain [39]. (a) Visualization of 379 neurons in the connectome, which is a part of the optical lobe; (b) the offset (black arrow) of the receptive fields computed from the circuit, which involves L1 (yellow), Tm3 (magenta), Mi1 (cyan), and T4 neurons, suggests a potential implementation of (c) the Hassenstein-Reichardt model.

the brain computes the offsets of receptive fields to detect motion (Figure 1) [39]. How to integrate structural and functional neural networks would be a very interesting research topic, which holds promise for revealing fundamental rules of neural computation.

Undoubtedly, a better understanding of the structural and functional properties of the brain network will lead to more accurate simulations of the brain activities and behavior outputs. Recently, Eliasmith et al. reported a large-scale human brain model called “Spaun,” which can drive a physically modeled arm to draw pictures by following visual stimuli [40]. It is possible to use a similar framework to simulate motor behaviors given specific neuron degeneration or impaired conditions. These models can be further combined with realistic muscle-based locomotion models, such as those used in computer graphics [41], to assist in diagnosis or treatment planning.

3. Neural Coding in Brian Machine Interface (BMI)

Brain-machine interfaces exploit the spatial and temporal structure of neural activity of the brain to directly control a prosthetic device. This emerging field has been mainly inspired by the requirements of restoring interactions between the environment and the individuals with severe sensorimotor deficits through BMI-controlled systems. For example, a tetraplegic patient can feed herself with chocolate using a BMI-controlled robot arm [42].

3.1. BMI with Animal Models. Since the first experimental demonstration using the primary motor cortical signals of

a rat to control a lever press [43], nonhuman primates have been utilized as ideal subjects for BMI studies [42–54] due to the similar functional brain structure as human beings [55], which enables the implantation of multiple electrode arrays in different motor cortical regions, and the better capability to perform complicated tasks than other animal models. Starting with a standard center-out movement task in primates, in which monkey’s neural activities were found to be tuning to the directional movement [56], the ensemble of the neural firings could be used to predict more complicated arm movement in a 2D computer cursor control or 3D reaching and grasping, as well as the gripping force [47, 51, 57–59]. In 2008, Schwartz’s group realized a real-time cortical control of a prosthetic robot arm for self-feeding without the real movement of the monkey’s arm [53], which is an important step close to the later clinic BMI applications on human [42, 45].

In a typical motor BMI framework, neuronal activity (local field potentials, single-unit activity, and multiunit activities) is synchronously collected from microelectrode arrays implanted into multiple cortical areas (primary motor cortex (M1), premotor cortex (PMA), supplementary motor cortex (SMA), primary somatosensory motor cortex (S1), posterior parietal area (PP), etc.) while the subjects are performing movement tasks. Several signal-decoding approaches have been applied to extract the functional relationship between the neural recordings and the subjects’ kinematics. The decoder implements a model to predict movements and control a prosthetic robot arm or computer. The first issue in BMI decoding is the choice of the motor parameters, such as position, velocity, acceleration, gripping force, and even EMG signals, which are probably more promising for the patient to accept as the brain-muscular

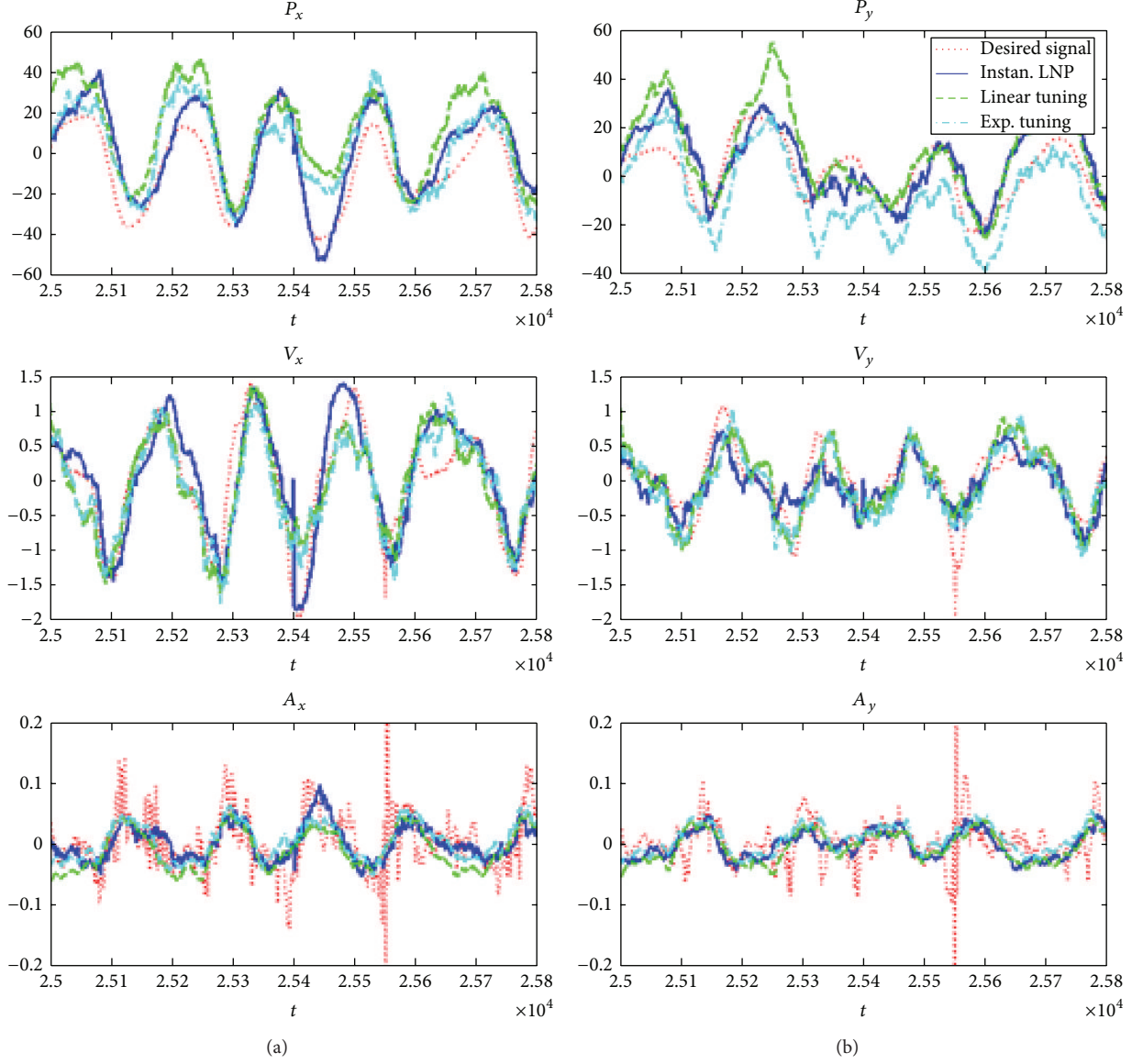


FIGURE 2: The reconstructed kinematics for a 2D reaching task by different tuning models from 185 neurons for 1000 testing samples (10 ms for each time instance) [67]. The left and right panels depict the reconstructed kinematics for the x -axis and the y -axis, respectively. The three rows of plots from top to bottom display the reconstructed position, the velocity, and the acceleration, respectively. In each subplot, the dotted red line indicates the desired signal, the solid blue line indicates the estimation using the proposed instantaneous LNP model, the dashed green line indicates the estimation using linear tuning, and the dot-dashed cyan line indicates the estimation using exponential tuning.

interfaces other than the stiff robot [46]. The second issue is to find a decoding algorithm to translate the cortical activities accurately. Many decoding methodologies use binned spike trains to predict movement based on linear or nonlinear optimal filters [50, 51, 54, 58, 60], but lack of further interpretation of the neurological dynamic tuning properties. Another method that derives the movement states probabilistically from the neural tuning model is to use a Bayesian formulation [61, 62]. It shares the parallel that the brain makes decisions based on prior knowledge [63]. As the binning on the spike does not exploit spike timing structure and may exclude rich neural dynamics in the modeling, the adaptive point process filtering methods have been developed to directly derive the kinematics from the spike trains [64, 65] with the modeling

of the neural tuning properties to the instantaneous time instance and the connectivity among the neural ensemble [66, 67]. For example, Wang's work developed a novel, online, and encoding model that uses the instantaneous kinematic variables (position, velocity, and acceleration in 2D or 3D space) to estimate the mean value of an inhomogeneous Poisson model [67]. Figure 2 shows an implementation of an instantaneous tuning model in sequential Monte Carlo point process estimation based on spike timing, which provided statistically better kinematic reconstructions than the linear and exponential spike-tuning models in monkey.

Aiming at the computational efficiency for the portable BMI devices, researchers also developed techniques to ascertain the neurons that relate the most to the movement

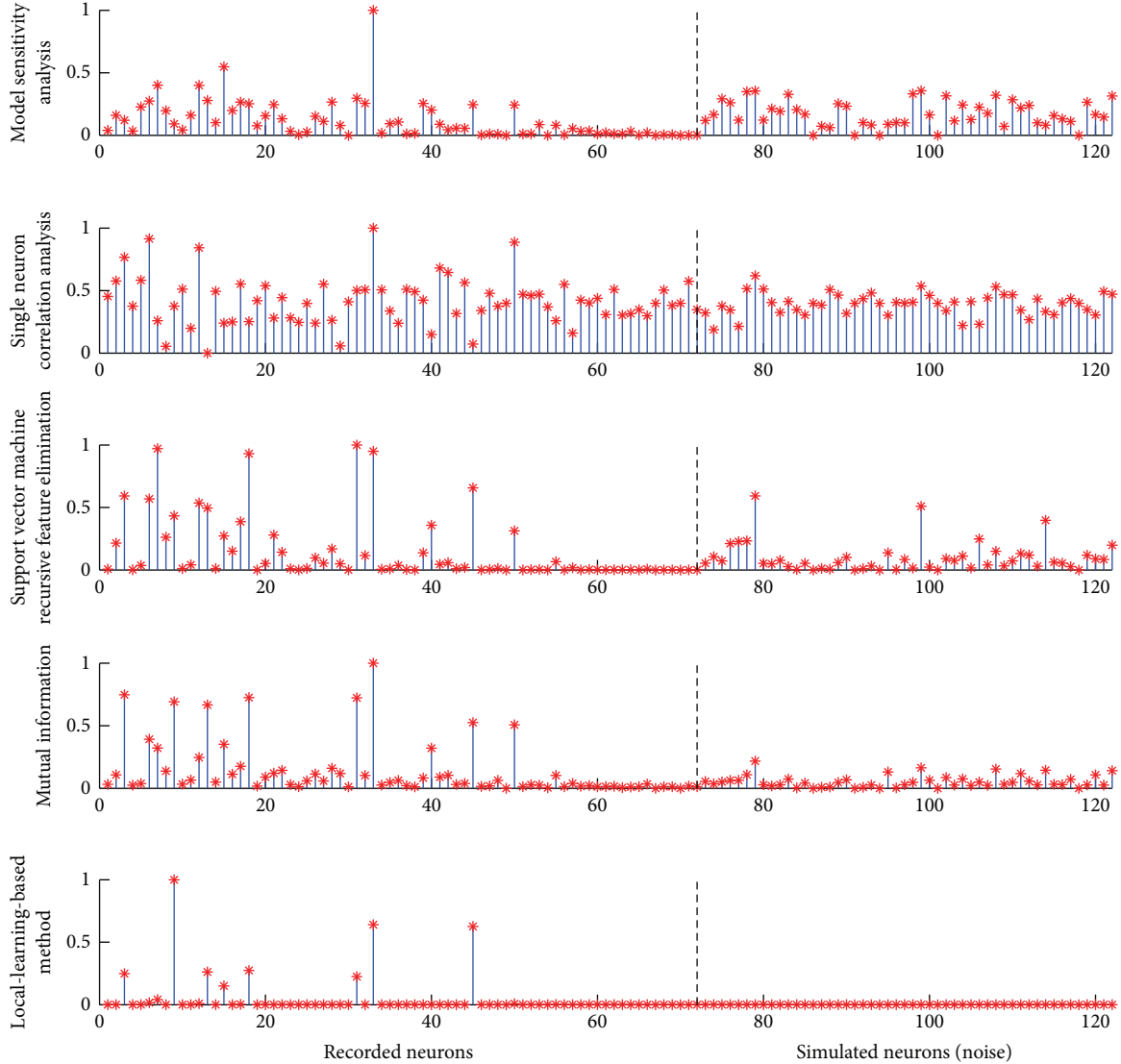


FIGURE 3: Distributions of the neuronal weights calculated by different methods, including single neuron correlation analysis, model sensitivity analysis, support vector machine recursive feature elimination, mutual information, and local-learning-based method. Neurons on the left side of the vertical dash line show real recordings. Neurons on the right are simulated and generated independently from the task. The five approaches show the different abilities of eliminating noisy neurons. The weights of the simulated neurons, learning from our proposed method, are all close to 0, while many of them are assigned with relatively large values by other methods [70].

task and gain better understanding of the individual neuron firing behavior [58, 68–70]. In Xu’s work, a local-learning-based method was proposed to perform neuron selection for the gesture prediction in a monkey’s reaching and grasping task [70]. The algorithm effectively ascertained the neuronal importance without assuming any coding model and provides a high performance with different decoding models. The method showed better robustness of identifying the important neurons with noisy signals presented, as shown in Figure 3. The ascertainment of the important neurons helped to inspect neural patterns visually associated with the movement task (Figure 4).

One important issue for clinical BMI application is to incorporate prosthesis devices into body representation and

make it feel like the subject’s own limb [71]. Introducing the sensory feedback including visual, auditory, and tactile cues, BMI therefore becomes a close loop system [72]. Although visual or auditory information is fed back to the subject in previous BMI designs [50, 51, 58], researchers investigated the possibility to embed peripheral tactile and proprioceptive signals into the prosthesis operation. O’Doherty et al. [48] implemented intracortical microstimulation techniques directly on the cortical area (S1) of the monkey in a BMI task, in which the monkey could distinguish 3 different targets due to the simulated sense of “touch” in the brain. However, arguments still remain whether the true sense of “touch” is reproduced or the monkey just learns the link between the targets and the electrical “tingling.” Other than intracortical

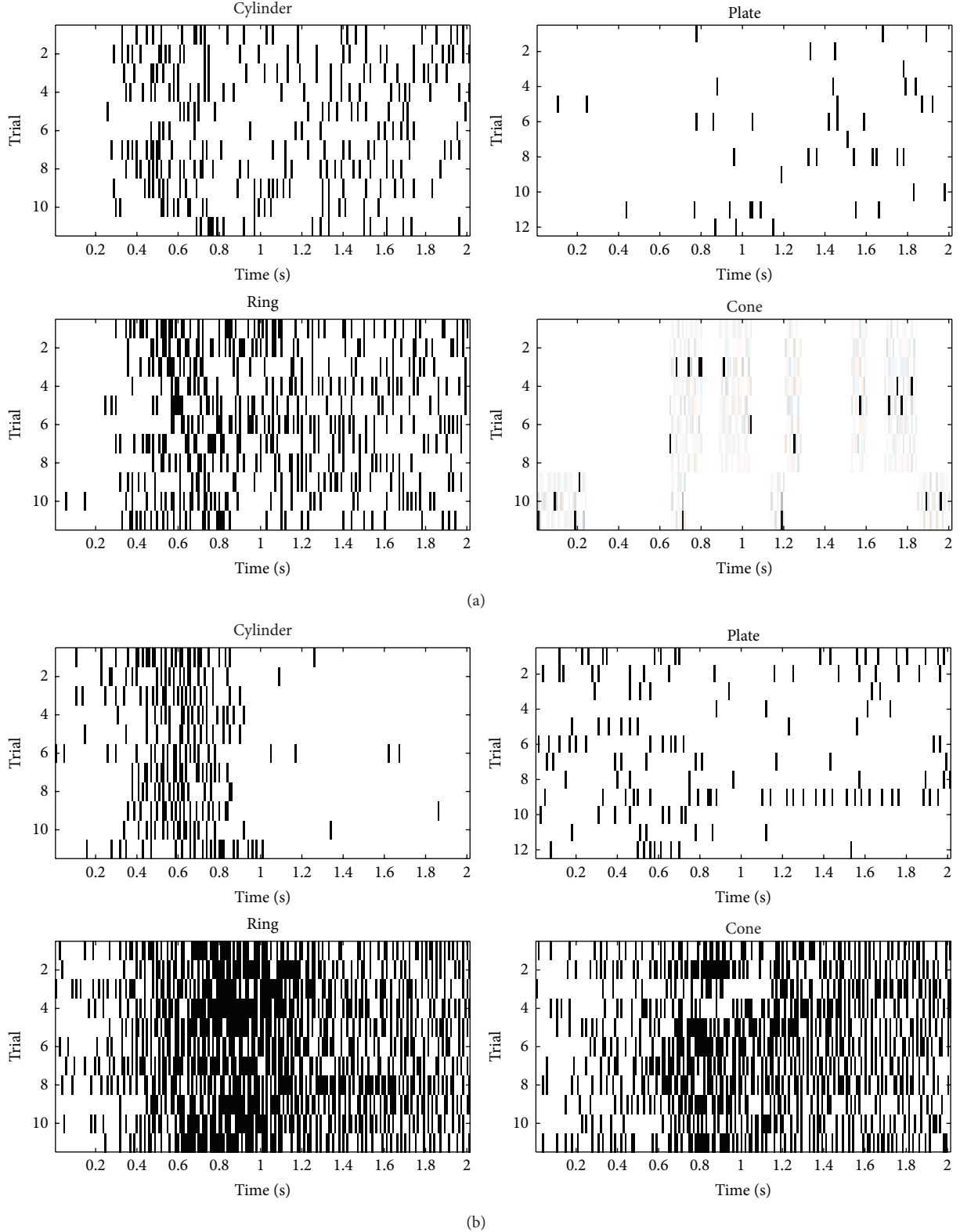


FIGURE 4: Temporal activities of the top two neurons corresponding to different grasping targets. The light was on at time 0; the object was grasped around time 1 s and was held until time 2 s. (a) The first neuron. (b) The second neuron. In each block, the grasping target in the upper left plot is a cylinder. The target in the upper right plot is a plate. The target in the bottom left plot is a ring. The target in the bottom right plot is a cone. Neuron 1 fires more frequently when the target objects were the cylinder and the ring, while much less for the plate and the cone. The activity of neuron 2 clearly distinguished the group of cylinder and plate and the group of ring and cone. Furthermore, neuron 2 ceased to fire around time 1 s, which separated the reaching period and the grasping period [70].

microstimulation, optogenetic techniques become promising to active certain types of cells as stimulation to generate the peripheral tactile and proprioceptive feedback due to better temporal and spatial precision, easier manipulability, and less side effects [73]. Although study shows that mice could be guided to run in a circle by such techniques [74], there are few reports on monkey to appear difference in the behavior level using optogenetics as stimulation [75].

In the closed-loop BMI application, the subject needs to learn how to operate a BMI system using biofeedback. The neuroplasticity, induced by biofeedback, could help the subject adjust brain activity to better adapt to the system control over time [51, 76]. On the other hand, the adaptive decoders need to follow the nonstationary neural activities in order to improve the performance of BMI systems [77, 78]. The coadaptive BMI has later been presented as a novel architecture that goes beyond translational neural interface by merging with above two factors [51, 76, 79, 80]. Allowing brain and the intelligent decoder to adapt to each other during learning according to the task accomplishment, coadaptive BMI becomes attractive for the brain-controlled prosthesis in future clinical applications without requiring the real movements of the patients, for example, with tetraplegia.

3.2. Neural Coding for Human BMI. Similar to the coding methods used in animal models, the brain electrical signals used in BMI systems for human beings are mainly ECoG and scalp EEG. Scalp EEG (referred as EEG later) can be noninvasively detected from the skin surface according to the 10–20 system for positioning the electrodes, with the commonly adopted numbers of 32 and 64 channels for the whole brain recording, or according to 10–5 system for high-density EEG with 128 channels [81]. In comparison with another biosignal captured from the skin surface, EMG ($50\mu\text{V}$ – 10 mV), the amplitude of EEG (10 – $20\mu\text{V}$) is much smaller and easily contaminated by head and neck muscle contractions, as well as artifacts, for example, eye blinks. EEG signals have been proposed for identifying neural instructions. For example, it has been widely known that the motion planning is associated with a decrease in EEG energy in the mu rhythm (8–12 Hz) over sensorimotor cortex, that is, event-related desynchronization (ERD), and after the execution of a motion there will be a rebound in the EEG power around 20 Hz, that is, event-related synchronization (ERS) [82]. EEG-based BMI systems have been successfully applied on external device control by people with severe motor disorders, such as spinal cord injury (SCI) and muscular dystrophies [83, 84]. However, most of them showed little effect on motor recovery for stroke rehabilitation as pointed out in the reviews of Belda-Lois et al. and Mattia et al. [85, 86]. One of the major reasons is that, different from subjects with an intact brain (e.g., SCI), individual stroke survivors have varied brain lesion sites and sizes, which increases the difficulty of recognizing the correct motion patterns for each. The second reason could be that stroke patients are suffered from involuntary muscle hypertonia more often than SCI patients [87], and it would introduce extra noises to

the EEG signals recorded. The third reason might be associated with the method of whole brain EEG recording. Once the learning capability of a BMI algorithm is powerful and easy to converge to a classified pattern with redundant EEG channel information (or even with repeatable patterns of noise, like EMG), the effort from the other side of neuroplasticity in the brain will be weakened. The reported pattern recognition rates of BMI with EEG for stroke varied greatly (e.g., from 60% to 90% [88]), and usually are lower than those for SCI. Therefore, more effective and accurate neural indicators from the brain are needed for human BMI design, especially in stroke rehabilitation.

Different from the skin surface electrodes of EEG, electrode grids that acquire ECoG can be placed subdurally (i.e., below the dura mater) or epidurally (i.e., on top of the dura) directly on the surface of the brain (i.e., subdural recordings) or on top of the dura (i.e., epidural recordings). Hence, ECoG signals are mesoscale activity of ensembles of neurons, which lie in the continuum between microscale single-unit action potential firings recorded intracortically and to macroscale EEG from the surface of the scalp. In fact, the rapidly growing interest in ECoG is mostly due to its improved signal characteristics relative to the artifact prone EEG. Compared with EEG, ECoG has finer spatial resolution (mesoscale (millimeters) versus macroscale (centimeters)) [89–91], broader spectral range (0–500 Hz versus 0–40 Hz) [92], higher amplitude (i.e., 50 – $100\mu\text{V}$ versus 10 – $20\mu\text{V}$) [93], and less vulnerability to movement artifacts [5, 93, 94]. Moreover, ECoG electrode grids, which are typically platinum electrodes 4 mm (2.3 mm exposed) in diameter and are configured in either a grid (e.g., 8×8 electrodes) or strip (e.g., 4 or 6 electrodes) configuration with an interelectrode distance of usually 10 mm, are far more likely to yield long-term functional stability [95–99] than intracortical electrodes, which induce complex histological responses that may impair neuronal recordings [100–102]. In fact, recent studies in primates demonstrated that the signal-to-noise ratio of ECoG signals is stable over several months [103]. Moreover these studies showed that cortical representations of three dimensional arm and joint movements that can be identified [7] and cortical control of three dimensional cursors were achieved [104] and maintained over several months.

However, since the placement of ECoG grid electrodes requires an invasive procedure (craniotomy and in most cases an incision to the dura), most ECoG-based human studies have recruited patients that were implanted as part of brain surgery to excise epileptic focus or mass lesion. Hence, most of the earlier ECoG-based studies often studied behaviors that were relevant to clinical evaluation of these patient populations, such as functional mapping of motor function. These early efforts culminated in the first comprehensive characterization of ECoG responses to visuomotor tasks in the late 1990s [105]. This has led to the appreciation of task-related modulations in high gamma (70–200 Hz) activity. The spatiotemporal patterns of these modulations are consistent sensorimotor function and its functional anatomy [106]. In recent years, however, ECoG has proved to be a vibrant recording technique for studying higher order functions

[6, 107] and for brain-computer interfaces [108, 109] bringing together clinicians, neuroscientists, and engineers in the process. Moreover, epidural studies in animals [104, 110] corroborate the viability of epidural signals as a practical and less invasive signal modality, which can significantly reduce the risks of inflammations and complications.

The first use of ECoG as a practical and robust platform for translational applications beyond epileptology in human beings was demonstrated by Wang et al. [111] with an individual with tetraplegia caused by C4 level spinal cord injury. ECoG signals were recorded over the left sensorimotor cortex using a 32-contact high-density grid. The participant achieved robust volitional control of 3D cursor movement and a robotic arm. The participant was able to modulate his sensorimotor cortex with distinctive cortical activity patterns for different segments of the upper limb. The grid remained implanted for 28 days and did not cause any adverse effects. Another study by Hirata et al. showed control of a robotic arm in patients with moderate motor dysfunction due to stroke [112]. However, the effects of this training on rehabilitation in ipsilesional brain areas have not been recorded.

ECoG as a signal modality has also lent itself to uncovering potential signal features that could be exploited for hemispheric stroke. In recent years, there has been increased interest in how ipsilateral motor and motor-related areas activate in same-sided movements in both healthy and stroke-affected subjects [113–115]. These findings have motivated further explorations of whether ipsilateral activity in unaffected hemispheres could be used in neuroprosthetic applications for stroke-induced hemiparesis. Wisneski et al. [116] utilized ECoG recordings to comprehensively define ipsilateral physiology in motor-intact patients undergoing invasive monitoring. Electrocorticographic signals were recorded while the subjects engaged in ipsilateral and contralateral hand motor tasks. Ipsilateral hand movements were associated with low-frequency modulations (around 37.5 Hz) in premotor cortex ~160 ms before than activity related to contralateral hand movements. The authors therefore hypothesized that ipsilateral cortical activity is involved in motor planning (rather than execution). More recent studies [8, 117] have demonstrated that the ipsilateral cortical signals could be used to decode the direction of the joystick movement. Overall, these studies suggest that in motor-intact human subjects, ipsilateral activity during hand and arm movement is distinguishable from contralateral activity, is involved in planning rather than execution, and can be used as a viable control signal in BMIs [116]. Moreover, the fact that the premotor cortex control signal is in the low-frequency ranges highly suggests that ipsilateral (and contralesional) EEG signals could be used with patients with stroke for BMI control and possibly rehabilitation. In fact, functional imaging has demonstrated increased activity in the premotor cortices of motor-impaired stroke in unaffected hemispheres [118, 119]. This heightened activity could be a result of upregulation of motor planning due to the inability of executing the planned movement [116]. In a recent study Bundy et al. tested whether this heightened activity could be detected with an EEG-based BMI and converted into the desired action [88]. They recorded EEG signals from four chronic

hemispheric stroke patients as they attempted real and imagined hand tasks using either their affected or unaffected hand. Low-frequency ipsilateral motor signals in the unaffected hemisphere, distinguishable from contralateral signals, were identified and subsequently used for a simple online BMI control task. They demonstrated that EEG signals from the unaffected hemisphere, associated with imagined movements of the affected hand, enabled stroke patients to control a cursor in one dimension. There is significant potential for this approach to be used as a novel tool for rehabilitation by slowly disengaging the unaffected hemisphere and engaging the affected hemisphere during BMI control.

4. Intelligent Rehabilitation Robots Based on EMG Coding

Intelligent rehabilitation robots usually refer to the systems that can interact with the voluntary motor intentions of a user. Besides the BMI technology introduced above, EMG-controlled robotic system is another choice for rehabilitation, mainly due to the easy-access of the signal from the skin surface of a muscle. In this part, an overview of the rehabilitation strategies in recent robots was introduced first, and it was followed with a review on some latest representative EMG-controlled rehabilitation robots and their clinical applications.

4.1. Rehabilitation Strategies in Robots. The aims of the treatment in neural rehabilitation are mainly to rebuild the lost sensorimotor functions due to nervous system injuries, such as stroke, and to minimize the related paretic symptoms. The recovery in the rehabilitation is a motor relearning process; that is, the lost functions can be regained and maximized by intensive and repeated voluntary practices [120, 121], and this concept has been applied in the traditional rehabilitation for decades.

Treatments in the rehabilitation are arduous processes. Training programs are usually time-consuming and labor-intensive for both the therapist and the patient in one-to-one manual interaction. In these situations, rehabilitation robots have acted as the assistance to therapists, providing safe and intensive physical training with repeated motions [122–128]. The most commonly reported motion types provided by developed rehabilitation robots are (1) continuous passive motion (CPM), (2) active-assisted movements, and (3) challenge-based movement. In treatments with continuous passive motion, the movements of the patient's limb(s) in the paretic side are guided by the robot system as the patient stays in a relaxed condition. This type of intervention was found to be effective in temporarily reducing muscular hypertonia and maintaining the flexibility of joints for stroke and spinal cord injury [129]; however, it contributed little to a permanent motor recovery in the central nervous system after stroke [129, 130]. In active-assisted robotic treatment (or interactive robotic treatment), the rehabilitation robot provides external assisting forces when the patient can not complete a desired movement independently [123, 131, 132]. In this type of physical training, the robot first needs to identify the motor

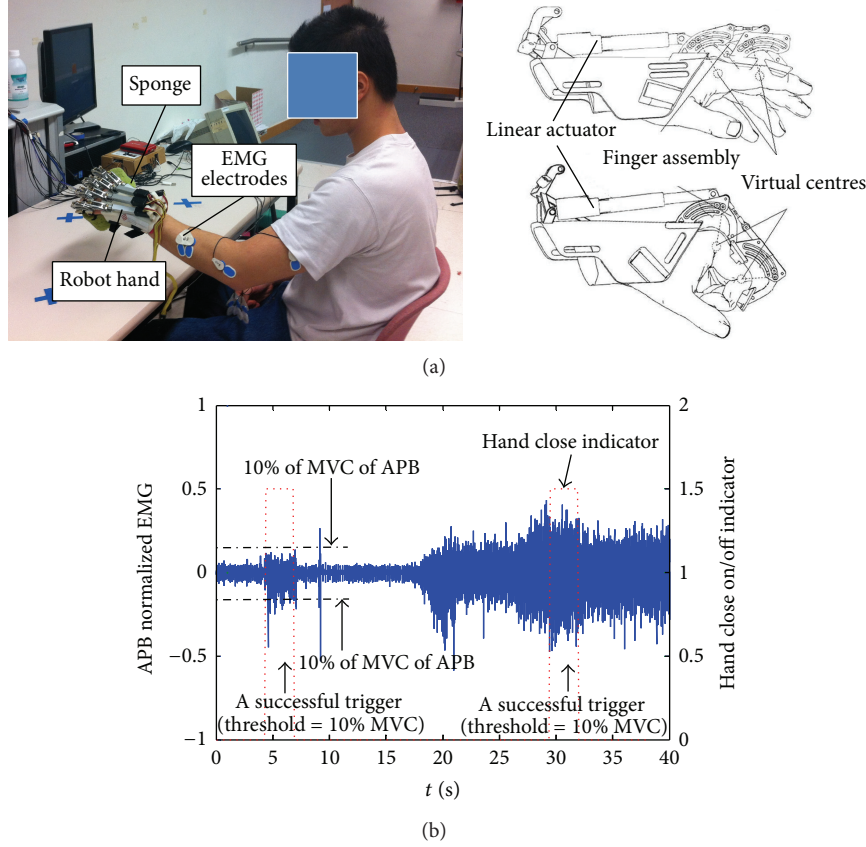


FIGURE 5: (a) The EMG-triggered robot hand for upper limb training and (b) the representative EMG-triggered cycles for hand close of the robot [10].

intention from the patient and then provides the interactive assistance to the paralyzed limb. This type of training has been found to be more effective in motor improvement than CPM in stroke rehabilitation [129]. Robotic treatment with challenge-based movement can assign training tasks with varied difficulty levels [124, 133, 134], which is effective in promotion of voluntary efforts from the patient according to the recovery progress. Active-assisted and challenge-based robotic training can be combined in one treatment to achieve a maximized motor recovery, and the key to a successful rehabilitation is the accurate interpretation of the voluntary motor intention of a user.

4.2. EMG-Controlled Rehabilitation Robots. EMG is the electricity generated in muscles under the control of the nervous systems. When an action potential transmitted from a motor neuron axon to the muscle fibers, a motor unit action potential is evoked. In comparison with the amplitude of neuronal signals, EMG's amplitude is much higher (usually in millivolt) even when detecting from the skin surface [9]. Therefore, EMG is a favorable biosignal to represent a user's voluntary motor intention in robotic design. For interpretation of EMG in the real-time control of robots, there are basically two methods, triggered mode and continuous mode. In the triggered mode, EMG was used to initiate the movement of the robot, and after that, the robot

would work in a CPM mode [10, 123, 132]. A preset threshold for detection of the onset of EMG can be used to trigger the motion of the robot, for example, the EMG-triggered hand robot for upper limb training after stroke introduced in the study of Hu et al., as shown in Figure 5(a) [10]. The robot hand could help a stroke patient perform the hand close/open motions triggered by the residual EMG detected from the abductor pollicis brevis (APB) in the paretic side for controlling the hand close and the extensor digitorum (ED) for the hand open. Figure 5(b) shows the representative triggering cycles in the robot hand for hand close with the EMG from the APB muscle, where the triggering threshold was set at 10% of the EMG amplitude when conducting the maximal voluntary contraction (MVC) [10]. Once the real-time EMG amplitude was above the threshold and kept for 3 seconds, the robot hand would perform hand close motion with a constant angular velocity of $22^\circ/\text{s}$ with the virtual center of the metacarpophalangeal (MCP) joints and $26^\circ/\text{s}$ at that of proximal interphalangeal (PIP) joints. By using this EMG-triggered robot hand, a pilot clinical trial of upper limb training on ten subjects with chronic stroke was conducted, and each of the subjects received 20 training sessions with an intensity of 3–5 sessions/week. After the training, it was found that the robot hand assisted rehabilitation could significantly improve the finger functions and the muscle coordination in the whole upper limb [10].

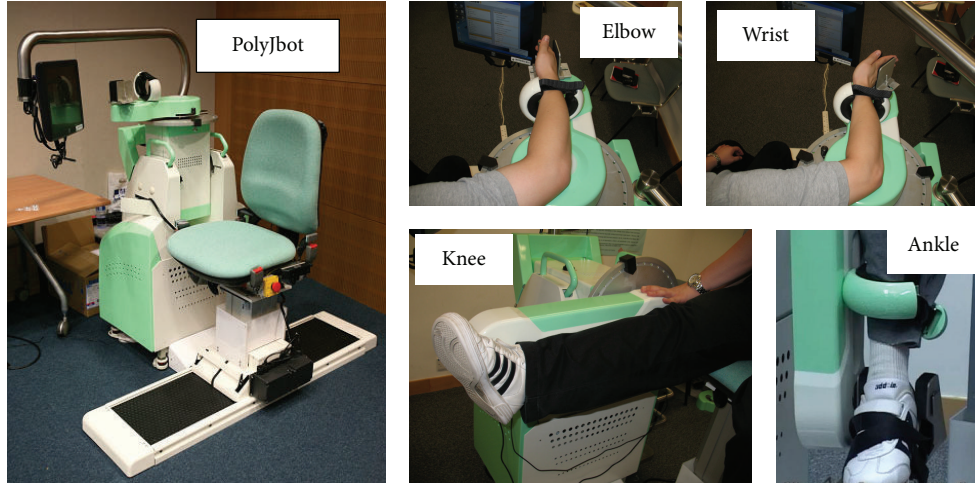


FIGURE 6: The continuous EMG-driven robot (PolyJbot) for joint training at the elbow, the wrist, the knee, and the ankle [130, 135, 136].

In a continuous EMG-driven robot system, the behaviors of the robot are controlled by the continuous variation of EMG, which requires the user to generate desired EMG patterns to instruct the movement of the robot [135], for example, the continuous EMG-driven robotic system (PolyJbot) developed for multijoint training by Tong's group shown in Figure 6 [130, 136, 137]. The robot can provide treatments on the elbow, the wrist, the knee, and the ankle with a continuous EMG-controlled algorithm. During the training, a subject needs to conduct joint extension and flexion by tracing a target cursor on the screen, and the robot will provide assistive torque to the joint, which is proportional to the EMG amplitude of a target muscle, for example, extensor carpi radialis (ECR) in wrist extension. In the algorithm design, the more muscle effort generated, the more assistive torque obtained with an attempt to maximize the voluntary effort during the training. In comparison with the training effects by robot-assisted CPM mode, the continuous EMG-driven mode could achieve more significant improvements in the release of muscle spasticity (i.e., hypertonia) and improvement of muscle coordination in the wrist joint, as well as in the shoulder/elbow part [130, 137]. Furthermore, the motor outcomes gained after the continuous EMG-driven robot-assisted training could be maintained for 3 months [130].

EMG not only can be applied as the controlling signal in rehabilitation robots, but also has been applied on quantitative evaluation of the rehabilitation effects complementary to the subjective clinical assessment tools used in routine practice. For example, the coordination among muscles could be measured by EMG phasic change in muscle pairs [10, 130, 136–138]. The extent of the cocontraction phase was quantitatively evaluated by a cocontraction index (CI) between the EMG trials of two muscles. The CI values could be used to monitor the recovery progress in muscle coordination during the robot-assisted rehabilitation. Figure 7 shows an example of the calculated CIs of the muscles in the upper limb during PolyJbot assisted poststroke wrist training in different sessions [137]. A decrease in the CI values usually was related

to a release of muscle spasticity and more independent contraction of the muscle pair, that is, better coordination.

5. Future Prospects and Conclusions

Modern neural rehabilitation heavily relies on the advances of neural computational techniques in diagnosis, treatment, and evaluation, which promise the future rehabilitation to be more automatic, economical, and convenient. Instead of receiving the treatments in hospitals or medical centers, future rehabilitation will be mainly home-based and subject-customized training with telecommunication for evaluation and follow-up to meet the fast growing market of home health care services [139]. To achieve this, further investigations are needed in neural coding techniques mainly in the following aspects.

- (1) Reduction of the calculation cost: high accuracy usually is sacrificed with the cost of calculation efficiency. Smart computational methods are needed to locate the areas of interest in neural imaging and highly relevant channels in BMI systems for individual subjects, with necessary accuracy for a real-time system. Currently, multichannel EEG systems are used for both invasive and noninvasive BMI systems, which are associated with large amounts of data to be explored. Effective channel selection methods with prioritized channel information should be useful to lower down the calculation cost, as some pioneers reported in the literature [140, 141]. More efforts are needed for the investigation of the long-term rehabilitation programs associated with the variation of neural plasticity in individuals, like persons after stroke who have varied brain lesions.
- (2) Comparative study between scalp EEG and ECoG: ECoG has higher resolution and signal quality than scalp EEG. However, the invasiveness of ECoG as a recording modality limits its usage. Modeling and

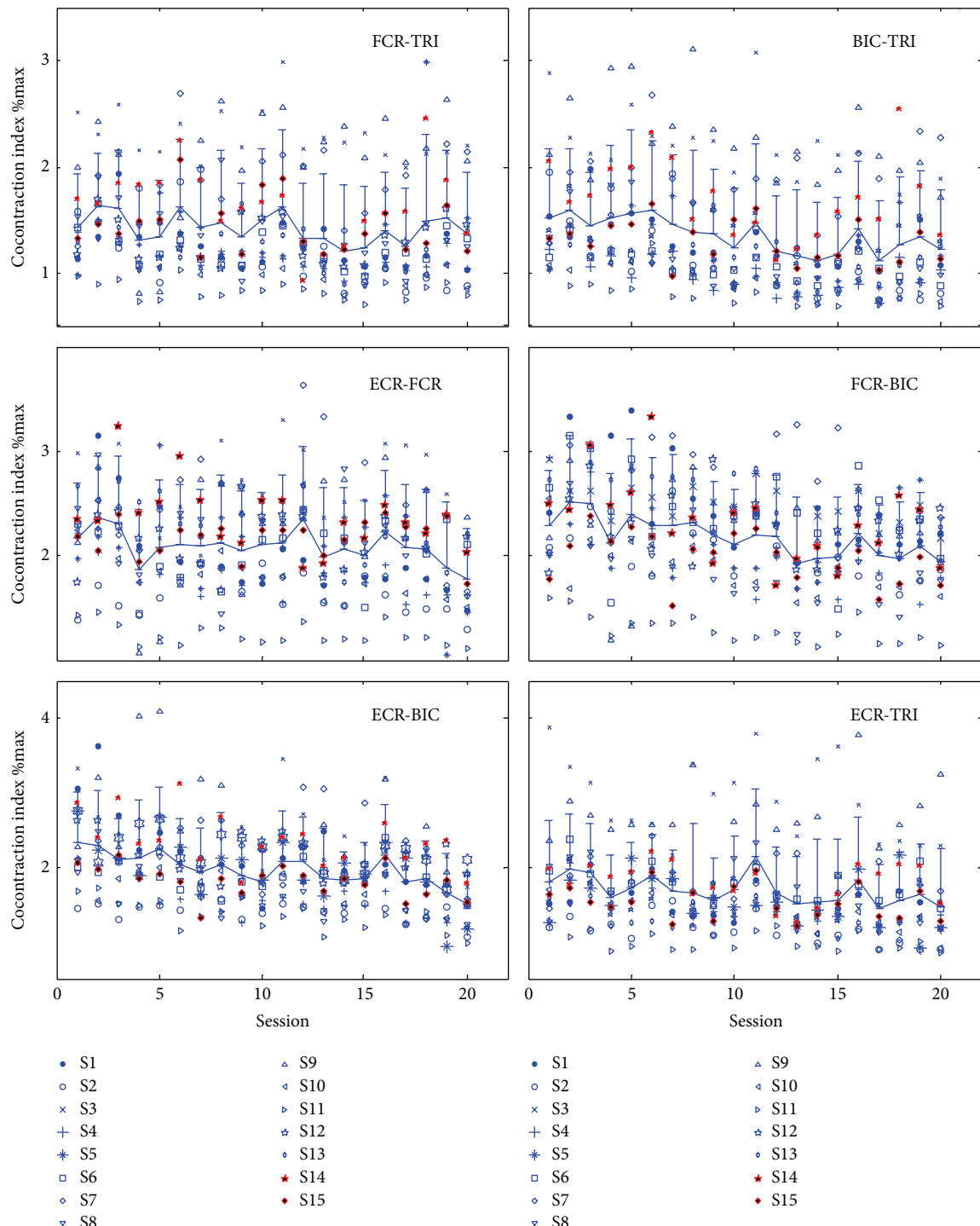


FIGURE 7: The cocontraction indexes between different muscle pairs during the continuous EMG-driven robot-assisted wrist training on 15 subjects with chronic stroke (S1-S15) [136]. FCR, flexor carpi radialis; ECR, extensor carpi radialis; BIC, biceps brachii; TRI, triceps brachii. The cocontraction index has a range from 0 to 1 and represents the extent of cocontraction phase of a pair of muscles, in comparison with the maximum value of 1. If both muscles contract at their maximum level at the same time, then the value will be 1; while if there is no cocontraction of the two muscles, the value will be zero [136].

- source localization/projection studies could be helpful to investigate the relationships between ECoG and scalp EEG, which may lead to noninvasive EEG with needed resolution close to ECoG. For example, attempts have been made to compare the EEG and ECoG in persons with epilepsy [142]. However, more intensive investigations on the projection between EEG and ECoG are needed in other pathological and clinical applications in the future.
- (3) Rehabilitation effectiveness of BMI systems: although BMI-training systems have been proposed for patients with neural disorders, for example, stroke, the rehabilitation effects are still questioned [143]. Stroke patients could use the system with a high recognition rates. However, this may not directly lead to an improvement in the paralyzed limb functions [85, 86]. It is worthwhile to investigate whether redundant EEG channel information in the BMI system made the recognition task too easy to benefit the motor recovery.
- (4) Easy and reliable bioparameters in system control and evaluation of recovery: it is necessary to utilize objective and quantitative evaluation methods for monitoring recovery progress in rehabilitation. However, the operations of most of current robots are not easy for patients to use them at home without supervision. Training systems should be much simplified, especially on the detection of key bioparameters for system control and evaluation in the home-based devices.

Conflict of Interests

No commercial party having a direct financial interest in the results of the research supporting this paper has or will confer a benefit upon the authors or upon any organization with which the authors are associated.

Acknowledgments

The authors acknowledge the financial supports: ITF grant (ITS/033/12) from the Innovation and Technology Commission of the Hong Kong Special Administrative Region; Natural Science Foundation of China (no. 61473261); Zhejiang provincial Natural Science Foundation of China (no. LY14F030015).

References

- [1] X. Wu, B. Zhu, L. Fu et al., "Prevalence, incidence, and mortality of stroke in the Chinese island populations: a systematic review," *PLoS ONE*, vol. 8, no. 11, Article ID e78629, 2013.
- [2] *Heart Disease and Stroke Statistics*, American Heart Association, 2011, http://www.stroke.org/site/DocServer/STROKE-101_Fact_Sheet.pdf?docID=4541.
- [3] *Rehabilitation Service Industry Reports of 2013*, First Research, Christchurch, New Zealand; Census Bureau U.S., Washington, DC, USA, 2013.
- [4] M. B. Ahrens, J. M. Li, M. B. Orger et al., "Brain-wide neuronal dynamics during motor adaptation in zebrafish," *Nature*, vol. 485, no. 7399, pp. 471–477, 2012.
- [5] W. J. Freeman, M. D. Holmes, B. C. Burke, and S. Vanhatalo, "Spatial spectra of scalp EEG and EMG from awake humans," *Clinical Neurophysiology*, vol. 114, no. 6, pp. 1053–1068, 2003.
- [6] A. Gunduz, P. Brunner, A. Daitch et al., "Decoding covert spatial attention using electrocorticographic (ECoG) signals in humans," *NeuroImage*, vol. 60, no. 4, pp. 2285–2293, 2012.
- [7] Z. C. Chao, Y. Nagasaki, and N. Fujii, "Long-term asynchronous decoding of arm motion using electrocorticographic signals in monkey," *Frontiers in Neuroengineering*, vol. 3, article 3, 2010.
- [8] K. Ganguly, L. Secundo, G. Ranade et al., "Cortical representation of ipsilateral arm movements in monkey and man," *Journal of Neuroscience*, vol. 29, no. 41, pp. 12948–12956, 2009.
- [9] K. Nishihara and T. Isho, "Location of electrodes in surface EMG," in *EMG Methods for Evaluating Muscle and Nerve Function*, M. Schwartz, Ed., InTech, 2012.
- [10] X. L. Hu, K. Y. Tong, X. J. Wei, W. Rong, E. A. Susanto, and S. K. Ho, "The effects of post-stroke upper-limb training with an electromyography (EMG)-driven hand robot," *Journal of Electromyography & Kinesiology*, vol. 23, no. 5, pp. 1065–1074, 2013.
- [11] A. R. Fugl-Meyer, L. Jaasko, I. Leyman, S. Olsson, and S. Steglind, "The post stroke hemiplegic patient I: a method for evaluation of physical performance," *Scandinavian Journal of Rehabilitation Medicine*, vol. 7, no. 1, pp. 13–31, 1975.
- [12] B. Ashworth, "Preliminary trials of carisoprodol in multiple sclerosis," *The Practitioner*, vol. 192, pp. 540–542, 1964.
- [13] K. N. Kay, T. Naselaris, R. J. Prenger, and J. L. Gallant, "Identifying natural images from human brain activity," *Nature*, vol. 452, no. 7185, pp. 352–355, 2008.
- [14] T. Naselaris, R. J. Prenger, K. N. Kay, M. Oliver, and J. L. Gallant, "Bayesian reconstruction of natural images from human brain activity," *Neuron*, vol. 63, no. 6, pp. 902–915, 2009.
- [15] J. P. Gallivan, D. A. McLean, K. F. Valyear, and J. C. Culham, "Decoding the neural mechanisms of human tool use," *eLife*, vol. 2, Article ID e00425, 2013.
- [16] T. M. Mitchell, S. V. Shinkareva, A. Carlson et al., "Predicting human brain activity associated with the meanings of nouns," *Science*, vol. 320, no. 5880, pp. 1191–1195, 2008.
- [17] F. Pereira, T. Mitchell, and M. Botvinick, "Machine learning classifiers and fMRI: a tutorial overview," *NeuroImage*, vol. 45, no. 1, pp. S199–S209, 2009.
- [18] C. Chu, Y. Ni, G. Tan, C. J. Saunders, and J. Ashburner, "Kernel regression for fMRI pattern prediction," *NeuroImage*, vol. 56, no. 2, pp. 662–673, 2011.
- [19] R. Genuer, V. Michel, E. Eger, and B. Thirion, "Random Forests based feature selection for decoding fMRI data," in *Proceedings of the 19th International Symposium on Computational Statistics (COMPSTAT '10)*, pp. 1–8, 2010.
- [20] X. Shen and F. G. Meyer, "Low-dimensional embedding of fMRI datasets," *NeuroImage*, vol. 41, no. 3, pp. 886–902, 2008.
- [21] S. M. LaConte, "Decoding fMRI brain states in real-time," *NeuroImage*, vol. 56, no. 2, pp. 440–454, 2011.
- [22] D. Scheinost, M. Hampson, M. Qiu, J. Bhawnani, R. T. Constable, and X. Papademetris, "A graphics processing unit accelerated motion correction algorithm and modular system for real-time fMRI," *Neuroinformatics*, vol. 11, no. 3, pp. 291–300, 2013.

- [23] T. Schrödel, R. Prevedel, K. Aumayr, M. Zimmer, and A. Vaziri, "Brain-wide 3D imaging of neuronal activity in *Caenorhabditis elegans* with sculpted light," *Nature Methods*, vol. 10, pp. 1013–1020, 2013.
- [24] J. Li, K.-X. Huang, and W.-D. Le, "Establishing a novel *C. elegans* model to investigate the role of autophagy in amyotrophic lateral sclerosis," *Acta Pharmacologica Sinica*, vol. 34, no. 5, pp. 644–650, 2013.
- [25] H. Kang and J. W. Lichtman, "Motor axon regeneration and muscle reinnervation in young adult and aged animals," *The Journal of Neuroscience*, vol. 33, no. 50, pp. 19480–19491, 2013.
- [26] D. Sheng, D. Qu, K. H. H. Kwok et al., "Deletion of the WD40 domain of LRRK2 in zebrafish causes parkinsonism-like loss of neurons and locomotive defect," *PLoS Genetics*, vol. 6, no. 4, 2010.
- [27] L. Luo, E. M. Callaway, and K. Svoboda, "Genetic dissection of neural circuits," *Neuron*, vol. 57, no. 5, pp. 634–660, 2008.
- [28] J. J. Mancuso, J. Kim, S. Lee, S. Tsuda, N. B. H. Chow, and G. J. Augustine, "Optogenetic probing of functional brain circuitry," *Experimental Physiology*, vol. 96, no. 1, pp. 26–33, 2010.
- [29] L. Lin, R. Osan, S. Shoham, W. Jin, W. Zuo, and J. Z. Tsien, "Identification of network-level coding units for real-time representation of episodic experiences in the hippocampus," *Proceedings of the National Academy of Sciences of the United States of America*, vol. 102, no. 17, pp. 6125–6130, 2005.
- [30] L. Lin, G. Chen, K. Xie, K. A. Zaia, S. Zhang, and J. Z. Tsien, "Large-scale neural ensemble recording in the brains of freely behaving mice," *Journal of Neuroscience Methods*, vol. 155, no. 1, pp. 28–38, 2006.
- [31] A. Joudaki, N. Salehi, M. Jalili, and M. G. Knyazeva, "EEG-based functional brain networks: does the network size matter?" *PLoS ONE*, vol. 7, no. 4, Article ID e35673, 2012.
- [32] M. D. Greicius, K. Supekar, V. Menon, and R. F. Dougherty, "Resting-state functional connectivity reflects structural connectivity in the default mode network," *Cerebral Cortex*, vol. 19, no. 1, pp. 72–78, 2009.
- [33] A. Venkataraman, K. R. A. van Dijk, R. L. Buckner, and P. Golland, "Exploring functional connectivity in fMRI via clustering," in *Proceedings of the IEEE International Conference on Acoustics, Speech, and Signal Processing (ICASSP 2009)*, pp. 441–444, April 2009.
- [34] M. E. Thomason, M. T. Dassanayake, S. Shen et al., "Cross-hemispheric functional connectivity in the human fetal brain," *Science Translational Medicine*, vol. 5, no. 173, Article ID 173ra24, 2013.
- [35] J. Sun, X. Hu, X. Huang et al., "Inferring consistent functional interaction patterns from natural stimulus fMRI data," *NeuroImage*, vol. 61, no. 4, pp. 987–999, 2012.
- [36] A. W. Toga, K. A. Clark, P. M. Thompson, D. W. Shattuck, and J. D. van Horn, "Mapping the human connectome," *Neurosurgery*, vol. 71, no. 1, pp. 1–5, 2012.
- [37] S. W. Oh, J. A. Harris, L. Ng et al., "A mesoscale connectome of the mouse brain," *Nature*, vol. 508, pp. 207–214, 2014.
- [38] J. Kim, T. Zhao, R. S. Petralia et al., "mGRASP enables mapping mammalian synaptic connectivity with light microscopy," *Nature Methods*, vol. 9, no. 1, pp. 96–102, 2012.
- [39] S.-Y. Takemura, A. Bharioke, Z. Lu et al., "A visual motion detection circuit suggested by *Drosophila* connectomics," *Nature*, vol. 500, no. 7461, pp. 175–181, 2013.
- [40] C. Eliasmith, T. C. Stewart, X. Choo et al., "A large-scale model of the functioning brain," *Science*, vol. 338, no. 6111, pp. 1202–1205, 2012.
- [41] T. Geijtenbeek, M. van de Panne, and F. van der Stappen, "Flexible muscle-based locomotion for bipedal creatures," in *ACM Transactions on Graphics*, 2013.
- [42] J. L. Collinger, B. Wodlinger, J. E. Downey et al., "High-performance neuroprosthetic control by an individual with tetraplegia," *The Lancet*, vol. 381, no. 9866, pp. 557–564, 2013.
- [43] J. K. Chapin, K. A. Moxon, R. S. Markowitz, and M. A. L. Nicolelis, "Real-time control of a robot arm using simultaneously recorded neurons in the motor cortex," *Nature Neuroscience*, vol. 2, no. 7, pp. 664–670, 1999.
- [44] C. Ethier, E. R. Oby, M. J. Bauman, and L. E. Miller, "Restoration of grasp following paralysis through brain-controlled stimulation of muscles," *Nature*, vol. 485, no. 7398, pp. 368–371, 2012.
- [45] L. R. Hochberg, D. Bacher, B. Jarosiewicz et al., "Reach and grasp by people with tetraplegia using a neurally controlled robotic arm," *Nature*, vol. 485, no. 7398, pp. 372–375, 2012.
- [46] C. T. Moritz, S. I. Perlmutter, and E. E. Fetz, "Direct control of paralysed muscles by cortical neurons," *Nature*, vol. 456, no. 7222, pp. 639–642, 2008.
- [47] S. Musallam, B. D. Corneil, B. Greger, H. Scherberger, and R. A. Andersen, "Cognitive control signals for neural prosthetics," *Science*, vol. 305, no. 5681, pp. 258–262, 2004.
- [48] J. E. O'Doherty, M. A. Lebedev, P. J. Ifit et al., "Active tactile exploration using a brain-machine-brain interface," *Nature*, vol. 479, no. 7372, pp. 228–231, 2011.
- [49] G. Santhanam, S. I. Ryu, B. M. Yu, A. Afshar, and K. V. Shenoy, "A high-performance brain-computer interface," *Nature*, vol. 442, no. 7099, pp. 195–198, 2006.
- [50] M. D. Serruya, N. G. Hatsopoulos, L. Paninski, M. R. Fellows, and J. P. Donoghue, "Instant neural control of a movement signal," *Nature*, vol. 416, no. 6877, pp. 141–142, 2002.
- [51] D. M. Taylor, S. I. H. Tillery, and A. B. Schwartz, "Direct cortical control of 3D neuroprosthetic devices," *Science*, vol. 296, no. 5574, pp. 1829–1832, 2002.
- [52] C. E. Vargas-Irwin, G. Shakhnarovich, P. Yadollahpour, J. M. K. Mislow, M. J. Black, and J. P. Donoghue, "Decoding complete reach and grasp actions from local primary motor cortex populations," *The Journal of Neuroscience*, vol. 30, no. 29, pp. 9659–9669, 2010.
- [53] M. Velliste, S. Perel, M. C. Spalding, A. S. Whitford, and A. B. Schwartz, "Cortical control of a prosthetic arm for self-feeding," *Nature*, vol. 453, no. 7198, pp. 1098–1101, 2008.
- [54] J. Wessberg, C. R. Stambaugh, J. D. Kralik et al., "Real-time prediction of hand trajectory by ensembles of cortical neurons in primates," *Nature*, vol. 408, no. 6810, pp. 361–365, 2000.
- [55] G. A. Orban, D. van Essen, and W. Vanduffel, "Comparative mapping of higher visual areas in monkeys and humans," *Trends in Cognitive Sciences*, vol. 8, no. 7, pp. 315–324, 2004.
- [56] A. P. Georgopoulos, J. F. Kalaska, and R. Caminiti, "On the relations between the direction of two-dimensional arm movements and cell discharge in primate motor cortex," *The Journal of Neuroscience*, vol. 2, no. 11, pp. 1527–1537, 1982.
- [57] A. K. Bansal, W. Truccolo, C. E. Vargas-Irwin, and J. P. Donoghue, "Decoding 3D reach and grasp from hybrid signals in motor and premotor cortices: spikes, multiunit activity, and local field potentials," *Journal of Neurophysiology*, vol. 107, no. 5, pp. 1337–1355, 2012.
- [58] J. M. Carmen, M. A. Lebedev, R. E. Crist et al., "Learning to control a brain-machine interface for reaching and grasping by primates," *PLoS Biology*, vol. 1, no. 2, article E42, 2003.

- [59] M. A. Lebedev, J. M. Carmena, J. E. O'Doherty et al., "Cortical ensemble adaptation to represent velocity of an artificial actuator controlled by a brain-machine interface," *The Journal of Neuroscience*, vol. 25, no. 19, pp. 4681–4693, 2005.
- [60] S.-P. Kim, J. C. Sanchez, D. Erdogmus et al., "Divide-and-conquer approach for brain machine interfaces: nonlinear mixture of competitive linear models," *Neural Networks*, vol. 16, no. 5–6, pp. 865–871, 2003.
- [61] A. E. Brockwell, A. L. Rojas, and R. E. Kass, "Recursive Bayesian decoding of motor cortical signals by particle filtering," *Journal of Neurophysiology*, vol. 91, no. 4, pp. 1899–1907, 2004.
- [62] W. Wu, Y. Gao, E. Bienenstock, J. P. Donoghue, and M. J. Black, "Bayesian population decoding of motor cortical activity using a Kalman filter," *Neural Computation*, vol. 18, no. 1, pp. 80–118, 2006.
- [63] K. Doya, S. Ishii, A. Pouget, and R. Rao, *Bayesian Brain: Probabilistic Approaches to Neural Coding*, MIT Press, 2007.
- [64] A. Ergun, R. Barbieri, U. T. Eden, M. A. Wilson, and E. N. Brown, "Construction of point process adaptive filter algorithms for neural systems using sequential Monte Carlo methods," *IEEE Transactions on Biomedical Engineering*, vol. 54, pp. 419–428, 2007.
- [65] Y. Wang, A. R. C. Paiva, J. C. Príncipe, and J. C. Sanchez, "Sequential Monte Carlo point-process estimation of kinematics from neural spiking activity for brain-machine interfaces," *Neural Computation*, vol. 21, no. 10, pp. 2894–2930, 2009.
- [66] W. Truccolo, U. T. Eden, M. R. Fellows, J. P. Donoghue, and E. N. Brown, "A point process framework for relating neural spiking activity to spiking history, neural ensemble, and extrinsic covariate effects," *Journal of Neurophysiology*, vol. 93, no. 2, pp. 1074–1089, 2005.
- [67] Y. Wang and J. C. Príncipe, "Instantaneous estimation of motor cortical neural encoding for online brain-machine interfaces," *Journal of Neural Engineering*, vol. 7, no. 5, Article ID 056010, 2010.
- [68] J. C. Sanchez, J. M. Carmena, M. A. Lebedev, M. A. L. Nicolelis, J. G. Harris, and J. C. Príncipe, "Ascertaining the importance of neurons to develop better brain-machine interfaces," *IEEE Transactions on Biomedical Engineering*, vol. 51, no. 6, pp. 943–953, 2004.
- [69] Y. Wang, J. C. Príncipe, and J. C. Sanchez, "Ascertaining neuron importance by information theoretical analysis in motor Brain-Machine Interfaces," *Neural Networks*, vol. 22, no. 5–6, pp. 781–790, 2009.
- [70] K. Xu, Y. Wang, Y. Wang et al., "Local-learning-based neuron selection for grasping gesture prediction in motor brain machine interfaces," *Journal of Neural Engineering*, vol. 10, no. 2, Article ID 026008, 2013.
- [71] M. A. Lebedev and M. A. L. Nicolelis, "Brain-machine interfaces: past, present and future," *Trends in Neurosciences*, vol. 29, no. 9, pp. 536–546, 2006.
- [72] F. A. Mussa-Ivaldi, S. T. Alford, M. Chiappalone et al., "New perspectives on the dialogue between brains and machines," *Frontiers in Neuroscience*, vol. 4, no. 1, pp. 44–52, 2010.
- [73] O. Yizhar, L. E. Fenn, T. J. Davidson, M. Mogri, and K. Deisseroth, "Optogenetics in neural systems," *Neuron*, vol. 71, no. 1, pp. 9–34, 2011.
- [74] A. M. Aravanis, L.-P. Wang, F. Zhang et al., "An optical neural interface: *in vivo* control of rodent motor cortex with integrated fiberoptic and optogenetic technology," *Journal of Neural Engineering*, vol. 4, no. 3, pp. S143–S156, 2007.
- [75] X. Han, B. Y. Chow, H. Zhou et al., "A high-light sensitivity optical neural silencer: development and application to optogenetic control of non-human primate cortex," *Frontiers in Systems Neuroscience*, vol. 13, article 18, 2011.
- [76] G. J. Gage, K. A. Ludwig, K. J. Otto, E. L. Ionides, and D. R. Kipke, "Naïve coadaptive cortical control," *Journal of Neural Engineering*, vol. 2, no. 2, pp. 52–63, 2005.
- [77] Z. Li, J. E. O'Doherty, M. A. Lebedev, and M. A. Nicolelis, "Adaptive decoding for brain-machine interfaces through Bayesian parameter updates," *Neural Computation*, vol. 23, no. 12, pp. 3162–3204, 2011.
- [78] W. Wu and N. G. Hatsopoulos, "Real-time decoding of nonstationary neural activity in motor cortex," *IEEE Transactions on Neural Systems and Rehabilitation Engineering*, vol. 16, no. 3, pp. 213–222, 2008.
- [79] J. DiGiovanna, B. Mahmoudi, J. Fortes, J. C. Príncipe, and J. C. Sanchez, "Coadaptive brain-machine interface via reinforcement learning," *IEEE Transactions on Biomedical Engineering*, vol. 56, no. 1, pp. 54–64, 2009.
- [80] B. Mahmoudi and J. C. Sanchez, "A symbiotic brain-machine interface through value-based decision making," *PLoS ONE*, vol. 6, no. 3, Article ID e14760, 2011.
- [81] V. Jurcak, D. Tsuzki, and I. Dan, "10/20, 10/10, and 10/5 systems revisited: their validity as relative head-surface-based positioning systems," *NeuroImage*, vol. 34, no. 4, pp. 1600–1611, 2007.
- [82] S. R. Soekadar, M. Witkowski, J. Mellinger, A. Ramos, N. Birbaumer, and L. G. Cohen, "ERD-based online brain-machine interfaces (BMI) in the context of neurorehabilitation: optimizing BMI learning and performance," *IEEE Transactions on Neural Systems and Rehabilitation Engineering*, vol. 19, no. 5, pp. 542–549, 2011.
- [83] N. Birbaumer and L. G. Cohen, "Brain-computer interfaces: communication and restoration of movement in paralysis," *The Journal of Physiology*, vol. 579, no. 3, pp. 621–636, 2007.
- [84] J. R. Wolpaw, "Brain-computer interfaces as new brain output pathways," *Journal of Physiology*, vol. 579, no. 3, pp. 613–619, 2007.
- [85] J.-M. Belda-Lois, S. Mena-del Horro, I. Bermejo-Bosch et al., "Rehabilitation of gait after stroke: a review towards a top-down approach," *Journal of NeuroEngineering and Rehabilitation*, vol. 8, no. 1, article 66, 2011.
- [86] D. Mattia, F. Pichiorri, M. Molinari, and R. Rupp, "Brain computer interface for hand motor function restoration and rehabilitation," in *Towards Practical Brain-Computer Interfaces*, B. Allison, Ed., Springer, Berlin, Germany, 2012.
- [87] A. Thibaut, C. Chatelle, E. Ziegler, M.-A. Bruno, S. Laureys, and O. Gosseries, "Spasticity after stroke: physiology, assessment and treatment," *Brain Injury*, vol. 27, no. 10, pp. 1093–1105, 2013.
- [88] D. T. Bundy, M. Wronkiewicz, M. Sharma, D. W. Moran, M. Corbetta, and E. C. Leuthardt, "Using ipsilateral motor signals in the unaffected cerebral hemisphere as a signal platform for brain-computer interfaces in hemiplegic stroke survivors," *Journal of Neural Engineering*, vol. 9, no. 3, Article ID 036011, 2012.
- [89] W. J. Freeman, L. J. Rogers, M. D. Holmes, and D. L. Silbergeld, "Spatial spectral analysis of human electrocorticograms including the alpha and gamma bands," *Journal of Neuroscience Methods*, vol. 95, no. 2, pp. 111–121, 2000.
- [90] E. C. Leuthardt, Z. Freudenberg, D. Bundy, and J. Roland, "Microscale recording from human motor cortex: implications

- for minimally invasive electrocorticographic brain-computer interfaces,” *Neurosurgical Focus*, vol. 27, no. 1, article E10, 2009.
- [91] M. W. Slutzky, L. R. Jordan, T. Krieg, M. Chen, D. J. Mogul, and L. E. Miller, “Optimal spacing of surface electrode arrays for brain-machine interface applications,” *Journal of Neural Engineering*, vol. 7, no. 2, Article ID 026004, 2010.
- [92] R. J. Staba, C. L. Wilson, A. Bragin, and I. Fried, “Quantitative analysis of high-frequency oscillations (80–500 Hz) recorded in human epileptic hippocampus and entorhinal cortex,” *Journal of Neurophysiology*, vol. 88, no. 4, pp. 1743–1752, 2002.
- [93] A. T. Valderrama, R. Oostenveld, M. J. Vansteensel, G. M. Huiskamp, and N. F. Ramsey, “Gain of the human dura in vivo and its effects on invasive brain signal feature detection,” *Journal of Neuroscience Methods*, vol. 187, no. 2, pp. 270–279, 2010.
- [94] T. Ball, E. Demandt, I. Mutschler et al., “Movement related activity in the high gamma range of the human EEG,” *NeuroImage*, vol. 41, no. 2, pp. 302–310, 2008.
- [95] L. A. Bullara, W. F. Agnew, T. G. H. Yuen, S. Jacques, and R. H. Pudenz, “Evaluation of electrode array material for neural prostheses,” *Neurosurgery*, vol. 5, no. 6, pp. 681–686, 1979.
- [96] G. E. Loeb, A. E. Walker, S. Uematsu, and B. W. Konigsmark, “Histological reaction to various conductive and dielectric films chronically implanted in the subdural space,” *Journal of Biomedical Materials Research*, vol. 11, no. 2, pp. 195–210, 1977.
- [97] E. Margalit, J. D. Weiland, R. E. Clatterbuck et al., “Visual and electrical evoked response recorded from subdural electrodes implanted above the visual cortex in normal dogs under two methods of anesthesia,” *Journal of Neuroscience Methods*, vol. 123, no. 2, pp. 129–137, 2003.
- [98] W. H. Pilcher and W. G. Rusyniak, “Complications of epilepsy surgery,” *Neurosurgery Clinics of North America*, vol. 4, no. 2, pp. 311–325, 1993.
- [99] T. G. H. Yuen, W. F. Agnew, and L. A. Bullara, “Tissue response to potential neuroprosthetic materials implanted subdurally,” *Biomaterials*, vol. 8, no. 2, pp. 138–141, 1987.
- [100] W. Shain, L. Spataro, J. Dilgen et al., “Controlling cellular reactive responses around neural prosthetic devices using peripheral and local intervention strategies,” *IEEE Transactions on Neural Systems and Rehabilitation Engineering*, vol. 11, no. 2, pp. 186–188, 2003.
- [101] J. Thelin, H. Jörntell, E. Psouni et al., “Implant size and fixation mode strongly influence tissue reactions in the CNS,” *PLoS ONE*, vol. 6, no. 1, Article ID e16267, 2011.
- [102] J. C. Williams, J. A. Hippensteel, J. Dilgen, W. Shain, and D. R. Kipke, “Complex impedance spectroscopy for monitoring tissue responses to inserted neural implants,” *Journal of Neural Engineering*, vol. 4, no. 4, pp. 410–423, 2007.
- [103] G. Schalk, “Can electrocorticography (ECoG) support robust and powerful brain-computer interfaces?” *Frontiers in Neuroengineering*, vol. 3, article 9, 2010.
- [104] A. G. Rouse, J. J. Williams, J. J. Wheeler, and D. W. Moran, “Cortical adaptation to a chronic micro- electrocorticographic brain computer interface,” *The Journal of Neuroscience*, vol. 33, no. 4, pp. 1326–1330, 2013.
- [105] N. E. Crone, D. L. Miglioretti, B. Gordon, and R. P. Lesser, “Functional mapping of human sensorimotor cortex with electrocorticographic spectral analysis: II. Event-related synchronization in the gamma band,” *Brain*, vol. 121, no. 12, pp. 2301–2315, 1998.
- [106] K. J. Miller, E. C. Leuthardt, G. Schalk et al., “Spectral changes in cortical surface potentials during motor movement,” *The Journal of Neuroscience*, vol. 27, no. 9, pp. 2424–2432, 2007.
- [107] N. Mesgarani and E. F. Chang, “Selective cortical representation of attended speaker in multi-talker speech perception,” *Nature*, vol. 484, no. 7397, pp. 233–236, 2012.
- [108] E. C. Leuthardt, C. Gaona, M. Sharma et al., “Using the electrocorticographic speech network to control a brain-computer interface in humans,” *Journal of Neural Engineering*, vol. 8, no. 3, Article ID 036004, 2011.
- [109] E. C. Leuthardt, G. Schalk, J. R. Wolpaw, J. G. Ojemann, and D. W. Moran, “A brain-computer interface using electrocorticographic signals in humans,” *Journal of Neural Engineering*, vol. 1, no. 2, pp. 63–71, 2004.
- [110] R. D. Flint, E. W. Lindberg, M. O. Krucoff, J. M. Rosenow, and M. W. Slutzky, “Decoding human grasp kinematics and dynamics using epidural and subdural cortical signals,” in *Society for Neuroscience*, Washington, DC, USA, 2011.
- [111] W. Wang, J. L. Collinger, A. D. Degenhart et al., “An electrocorticographic brain interface in an individual with tetraplegia,” *PLoS ONE*, vol. 8, no. 2, Article ID e55344, 2013.
- [112] M. Hirata, T. Yanagisawa, K. Matsushita et al., “Brain-machine interface using brain surface electrodes: real-time robotic control and a fully implantable wireless system,” in *Technological Advancements in Biomedicine for Healthcare Applications*, J. Wu, Ed., Okayama University, Okayama, Japan, 2012.
- [113] H. Shibasaki and M. Kato, “Movement associated cortical potentials with unilateral and bilateral simultaneous hand movement,” *Journal of Neurology*, vol. 208, no. 3, pp. 191–199, 1975.
- [114] I. M. Tarkka and M. Hallett, “Cortical topography of pre-motor and motor potentials preceding self-paced, voluntary movement of dominant and non-dominant hands,” *Electroencephalography and Clinical Neurophysiology*, vol. 75, no. 2, pp. 36–43, 1990.
- [115] A. Urbano, C. Babiloni, P. Onorati et al., “Responses of human primary sensorimotor and supplementary motor areas to internally triggered unilateral and simultaneous bilateral one-digit movements: a high-resolution EEG study,” *European Journal of Neuroscience*, vol. 10, no. 2, pp. 765–770, 1998.
- [116] K. J. Wisneski, N. Anderson, G. Schalk, M. Smyth, D. Moran, and E. C. Leuthardt, “Unique cortical physiology associated with ipsilateral hand movements and neuroprosthetic implications,” *Stroke*, vol. 39, no. 12, pp. 3351–3359, 2008.
- [117] M. Sharma, C. Gaona, J. Roland, N. Anderson, Z. Freudenberg, and E. C. Leuthardt, “Ipsilateral directional encoding of joystick movements in human cortex,” in *Proceedings of the Annual International Conference of the IEEE Engineering in Medicine and Biology Society (EMBS '09)*, 2009.
- [118] R. J. Seitz, P. Höflich, F. Binkofski, L. Tellmann, H. Herzog, and H.-J. Freund, “Role of the premotor cortex in recovery from middle cerebral artery infarction,” *Archives of Neurology*, vol. 55, no. 8, pp. 1081–1088, 1998.
- [119] C. Weiller, F. Chollet, K. J. Friston, R. J. S. Wise, and R. S. J. Frackowiak, “Functional reorganization of the brain in recovery from striatocapsular infarction in man,” *Annals of Neurology*, vol. 31, no. 5, pp. 463–472, 1992.
- [120] C. Bütefisch, H. Hummelsheim, P. Denzler, and K.-H. Mauritz, “Repetitive training of isolated movements improves the outcome of motor rehabilitation of the centrally paretic hand,” *Journal of the Neurological Sciences*, vol. 130, no. 1, pp. 59–68, 1995.
- [121] J. Farmer, X. Zhao, H. van Praag, K. Wodtke, F. H. Gage, and B. R. Christie, “Effects of voluntary exercise on synaptic plasticity

- and gene expression in the dentate gyrus of adult male sprague-dawley rats in vivo," *Neuroscience*, vol. 124, no. 1, pp. 71–79, 2004.
- [122] R. Colombo, F. Pisano, S. Micera et al., "Robotic techniques for upper limb evaluation and rehabilitation of stroke patients," *IEEE Transactions on Neural Systems and Rehabilitation Engineering*, vol. 13, no. 3, pp. 311–324, 2005.
- [123] L. Dipietro, M. Ferraro, J. J. Palazzolo, H. I. Krebs, B. T. Volpe, and N. Hogan, "Customized interactive robotic treatment for stroke: EMG-triggered therapy," *IEEE Transactions on Neural Systems and Rehabilitation Engineering*, vol. 13, no. 3, pp. 325–334, 2005.
- [124] S. E. Fasoli, H. I. Krebs, J. Stein, W. R. Frontera, and N. Hogan, "Effects of robotic therapy on motor impairment and recovery in chronic stroke," *Archives of Physical Medicine and Rehabilitation*, vol. 84, no. 4, pp. 477–482, 2003.
- [125] E. Swinnen, J. P. Baeyens, K. Knaepen et al., "Walking with robot assistance: the influence of body weight support on the trunk and pelvis kinematics," *Disability and Rehabilitation: Assistive Technology*, 2014.
- [126] S. Masiero, P. Poli, G. Rosati et al., "The value of robotic systems in stroke rehabilitation," *Expert Review of Medical Devices*, vol. 11, pp. 187–198, 2014.
- [127] H. I. Krebs and B. T. Volpe, "Rehabilitation robotics," in *Handbook of Clinical Neurology*, vol. 110 of *Neurological Rehabilitation*, chapter 23, pp. 283–294, Elsevier, 2013.
- [128] H. I. Krebs, N. Hogan, M. L. Aisen, and B. T. Volpe, "Robot-aided neurorehabilitation," *IEEE Transactions on Rehabilitation Engineering*, vol. 6, no. 1, pp. 75–87, 1998.
- [129] B. T. Volpe, M. Ferraro, D. Lynch et al., "Robotics and other devices in the treatment of patients recovering from stroke," *Current Atherosclerosis Reports*, vol. 6, no. 4, pp. 314–319, 2004.
- [130] X. L. Hu, K.-Y. Tong, R. Song, X. J. Zheng, and W. W. F. Leung, "A comparison between electromyography-driven robot and passive motion device on wrist rehabilitation for chronic stroke," *Neurorehabilitation and Neural Repair*, vol. 23, no. 8, pp. 837–846, 2009.
- [131] F. Abdollahi, E. D. Case Lazarro, M. Listenberger et al., "Error augmentation enhancing arm recovery in individuals with chronic stroke: a randomized crossover design," *Neurorehabilitation and Neural Repair*, vol. 28, pp. 120–128, 2014.
- [132] H. Kawamoto, S. Taal, H. Niniss et al., "Voluntary motion support control of Robot Suit HAL triggered by bioelectrical signal for hemiplegia," in *Proceedings of the 32nd Annual International Conference of the IEEE Engineering in Medicine and Biology Society (EMBC '10)*, pp. 462–466, Buenos Aires, Argentina, September 2010.
- [133] R. Colombo, I. Sterpi, A. Mazzone, C. Delconte, and F. Pisano, "Taking a lesson from patients' recovery strategies to optimize training during robot-aided rehabilitation," *IEEE Transactions on Neural Systems and Rehabilitation Engineering*, vol. 20, no. 3, pp. 276–285, 2012.
- [134] A. Panarese, R. Colombo, I. Sterpi, F. Pisano, and S. Micera, "Tracking motor improvement at the subtask level during robot-aided neurorehabilitation of stroke patients," *Neurorehabilitation and Neural Repair*, vol. 26, no. 7, pp. 822–833, 2012.
- [135] R. Song, K.-Y. Tong, X. Hu, and L. Li, "Assistive control system using continuous myoelectric signal in robot-aided arm training for patients after stroke," *IEEE Transactions on Neural Systems and Rehabilitation Engineering*, vol. 16, no. 4, pp. 371–379, 2008.
- [136] X. L. Hu, R. Song, K. Y. Tong, S. F. Tsang, P. O. Leung, and L. Li, "Variation of muscle coactivation patterns in chronic stroke during robot-assisted elbow training," *Archives of Physical Medicine and Rehabilitation*, vol. 88, no. 8, pp. 1022–1029, 2007.
- [137] X. L. Hu, K. Y. Tong, R. Song et al., "Quantitative evaluation of motor functional recovery process in chronic stroke patients during robot-assisted wrist training," *Journal of Electromyography & Kinesiology*, vol. 19, no. 4, pp. 639–650, 2009.
- [138] X. L. Hu, K. Y. Tong, R. Li, J. J. Xue, S. K. Ho, and P. N. Chen, "Combined functional electrical stimulation (FES) and robotic system driven by user intention for post-stroke wrist rehabilitation," in *Biomechantronics in Medicine and Health Care*, K. Y. Tong, Ed., Pan Stanford Publishing, Singapore, 2011.
- [139] "Home health care services—industry report," NAICS, vol. 621610, 2012.
- [140] A. Gonzalez, I. Nambu, H. Hokari, and Y. Wada, "EEG channel selection using particle swarm optimization for the classification of auditory event-related potentials," *The Scientific World Journal*, vol. 2014, Article ID 350270, 11 pages, 2014.
- [141] W.-K. Tam, K.-Y. Tong, F. Meng, and S. Gao, "A minimal set of electrodes for motor imagery BCI to control an assistive device in chronic stroke subjects: a multi-session study," *IEEE Transactions on Neural Systems and Rehabilitation Engineering*, vol. 19, no. 6, pp. 617–627, 2011.
- [142] B. Lanfer, C. Röer, M. Scherg, S. Rampp, C. Kellinghaus, and C. Wolters, "Influence of a silastic ECoG grid on EEG/ECoG based source analysis," *Brain Topography*, vol. 26, no. 2, pp. 212–228, 2013.
- [143] A. Zimmermann-Schlatter, C. Schuster, M. A. Puhan, E. Siekierka, and J. Steurer, "Efficacy of motor imagery in post-stroke rehabilitation: a systematic review," *Journal of NeuroEngineering and Rehabilitation*, vol. 5, article 8, 2008.
- [144] R. S. Menon and S.-G. Kim, "Spatial and temporal limits in cognitive neuroimaging with fMRI," *Trends in Cognitive Sciences*, vol. 3, no. 6, pp. 207–216, 1999.
- [145] T. C. Ferree, M. T. Clay, and D. M. Tucker, "The spatial resolution of scalp EEG," *Neurocomputing*, vol. 38–40, pp. 1209–1216, 2001.
- [146] E. Asano, C. Juhász, A. Shah et al., "Origin and propagation of epileptic spasms delineated on electrocorticography," *Epilepsia*, vol. 46, no. 7, pp. 1086–1097, 2005.

Research Article

A Blood Pressure Monitoring Method for Stroke Management

Heather Ting Ma

Department of Electronic and Information Engineering, Harbin Institute of Technology Shenzhen Graduate School, Shenzhen 518055, China

Correspondence should be addressed to Heather Ting Ma; heather.tma@gmail.com

Received 27 February 2014; Revised 28 May 2014; Accepted 2 July 2014; Published 17 August 2014

Academic Editor: Xiaoling Hu

Copyright © 2014 Heather Ting Ma. This is an open access article distributed under the Creative Commons Attribution License, which permits unrestricted use, distribution, and reproduction in any medium, provided the original work is properly cited.

Blood pressure is one important risk factor for stroke prognosis. Therefore, continuous monitoring of blood pressure is crucial for preventing and predicting stroke. However, current blood pressure devices are mainly air-cuff based, which only can provide measurements intermittently. This study proposed a new blood pressure estimation method based on the pulse transit time to realize continuous monitoring. The proposed method integrated a linear model with a compensation algorithm. A calibration method was further developed to guarantee that the model was personalized for individuals. Variation and variability of pulse transit time were introduced to construct the compensation algorithm in the model. The proposed method was validated by the data collected from 30 healthy subjects, aged from 23 to 25 years old. By comparing the estimated value to the measurement from an oscillometry, the result showed that the mean error of the estimated blood pressure was -0.2 ± 2.4 mmHg and 0.5 ± 3.9 mmHg for systolic and diastolic blood pressure, respectively. In addition, the estimation performance of the proposed model is better than the linear model, especially for the diastolic blood pressure. The results indicate that the proposed method has promising potential to realize continuous blood pressure measurement.

1. Introduction

It has been reported that ambulatory blood pressure values were linearly related to stroke risk, which has stronger predictive power than screening blood pressure [1]. The predictive value of home blood pressure measurement increased progressively with the number of measurements within 24 hours [2]. Studies also showed that hypertension would increase the risk of stroke [3], especially for those subjects who had stroke history [4]. It was found that a 10 mmHg greater reduction in systolic blood pressure (SBP) would be associated with a 31% reduction in stroke risk within a follow-up duration of average 4.5 years for the elderly [5, 6]. Therefore, continuous blood pressure monitoring is crucial for both predicting stroke and hypertension management [7, 8]. 24-hour ambulatory blood pressure monitoring has been increasingly used in clinic for hypertension management [9–11]. Current blood pressure devices (by oscillometry or sphygmomanometry) are mainly based on air-cuff, which only can measure blood pressure intermittently and may not be suitable for long term blood pressure monitoring. Therefore, cuffless blood pressure monitoring method would be valuable in stroke prevention and management.

Pulse transit time (PTT) has been reported to be correlated with blood pressure, especially for the SBP [12–17], and has been proposed as a potential surrogate of blood pressure [18–20]. Pulse transit time can be measured between the characteristic points of the electrocardiography (ECG) and photoplethysmography (PPG) at peripheral sites [17, 21]. Since ECG and PPG measurements can be implemented by wearable devices, PTT provides a very practical solution for continuous blood pressure monitoring. A lot of studies have focused on the blood pressure estimation by using PTT [22–26] and different applications have been proposed based on the blood pressure estimation methods [27–29]. Linear model [17] was mostly adopted to describe the relationship between blood pressure and PTT. But the linear model cannot provide accurate estimation because PTT was found highly correlated with SBP rather than diastolic blood pressure (DBP) [30]. An accurate model describing the relationship between PTT and blood pressure is crucial for the PTT-based blood pressure estimation. Sophisticated models were further proposed to enhance the accuracy of PTT-based blood pressure estimation. Some studies investigated the relationship between PTT and blood pressure under static and exercise status [26, 31, 32]. Considering the relationship

between PTT and blood pressure could vary from person to person, calibration was proposed by some researchers to design personalized estimation model [33, 34]. Some studies took advantage of the hydrostatic pressure change in the calibration [18, 35, 36]. Nevertheless, the major challenge for PTT-based blood pressure measurement is to derive a personalized estimation model.

Apart from the estimation accuracy, implementation of the estimation model in a device for clinical or healthcare use is the ultimate goal. The linear mapping between PTT and blood pressure has not been proved to provide the best blood pressure estimation. However, it is still the best applicable for coarse blood pressure trend indications [37]. Therefore, in present study, we proposed a new method for PTT-based blood pressure estimation by integrating a compensation part in the linear model, which was further combined with a new calibration approach.

2. Methodology

A previous study pointed out that PTT variability had high coherence with heart rate variability and blood pressure variability [38], both of which reflect neural regulation of cardiovascular system. Douniama et al. [37] also suggested introducing variability information in PTT-based blood pressure estimation to reflect the frequency-dependent arterial vessel compliance and the autonomic nervous system on vascular tone. Therefore, in current study, the variation in PTT and PTT variability are regarded carrying important information of blood pressure regulation and are integrated into the traditional linear model as a compensation part. Further, a posture-based calibration method was adopted by using the hydrostatic pressure change to personalize the estimation model for individuals.

2.1. Subjects and Devices. This study involved 31 healthy subjects (aged from 23 to 25 years) without known cardiovascular abnormalities. The subjects were recruited in a university campus with submitting a written consent with full understanding of the experiment procedure. Each subject was asked to refrain from coffee and alcohol at least 2 hours and instructed about the procedures before conducting the experiment. Then the experiment was carried out in a temperature-controlled room ($24 \pm 2^\circ\text{C}$) for all the subjects.

For the data collection, standard lead I ECG and reflective PPG signals were recorded simultaneously by a self-designed device at a sampling rate of 250 Hz for each channel and digitized by a 12-bit A/D converter. The ECG signal was collected from the index fingertip of left hand and the index and middle fingertips of right hand, while the PPG signal was collected from the index fingertip of right hand at the same time. Standard blood pressure was measured by an oscillometry (OMRON HEM-7012, Japan) at subjects' left upper arms.

2.2. Experimental Protocol. The experiment procedure was arranged into four sessions, namely, pretest, calibration sitting, calibration standing, and estimation test. In pretest

TABLE 1: Procedure of routine data collection.

Tasks	Duration	Remarks
Keep the testing posture	2 mins	
ECG and PPG recording	3 mins	
Blood pressure measurement		
Rest	5 mins	
Blood pressure measurement		
Rest	5 mins	
Blood pressure measurement		Optional

TABLE 2: Outline of the experiment.

Pretest	10-minute rest Preparation	
Calibration-sitting	ECG and PPG recording Blood pressure measurement	
Calibration-standing	2-minute posture holding ECG and PPG recording Blood pressure measurement	
Estimation-test (sitting)	2-minute posture holding ECG and PPG recording Blood pressure measurement	

session, each subject was required to sit down and relax for 10 minutes to stabilize his/her blood pressure. During this time, the participant got prepared for the experiment, such as wearing the sensors. The rest of the three sessions followed a routine data collection procedure, which is shown in Table 1. Considering the blood pressure fluctuation would influence the calibration accuracy, the difference between the blood pressure measurements by the oscillometry in each session was checked. Specifically, for each routine data collection, if the difference between the first two blood pressure measurements was less than 5 mmHg, the first measurement was adopted as the blood pressure value for this dataset. If the difference ranged between 5 and 10 mmHg, another measurement would be carried out after 5-minute rest and the average of the three measurements would be taken as the blood pressure value for this dataset. If the difference exceeded 10 mmHg, the experiment would be ceased and another appointment would be made with the participant. The measurements by oscillometry in the same session were carried out under a peaceful situation so that the blood pressure was supposed to be stable. When the blood pressure measurements under the same conditions exceeded 10 mmHg, some unstable factor was supposed to happen during the measurement. The unstable factor could be a wrong operation of the experiment, motion artifact, or unstable physiological status, which would also influence the estimation results. Therefore, the data collected under such situation were discarded.

The experiment outline is summarized in Table 2. Between any two successive sessions, there was a rest with at least 5 minutes. Specifically, data collected in the middle two sessions were used for calibration and that in the last session was used for blood pressure estimation. In the two calibration

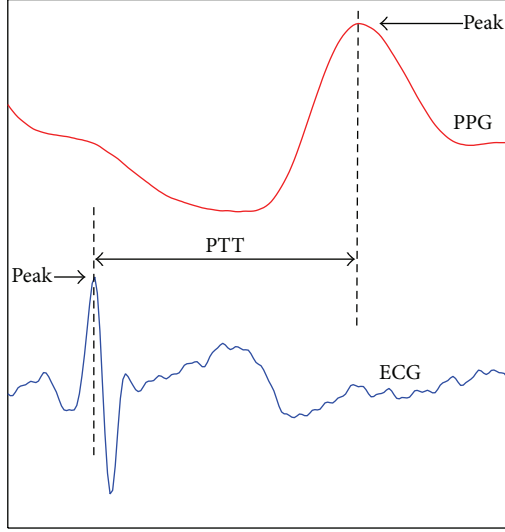


FIGURE 1: Pulse transit time is defined as the time interval between the R-peak of ECG and the peak of PPG within the same cardiac cycle.

sessions, the subject sat and stood upright during the data collection, respectively.

2.3. Parameter Extraction. Ninety-three datasets were finally recorded for the 31 subjects and processed offline. The raw data were first filtered by a sliding window with window length of 10 milliseconds. The beat-to-beat PTT was defined as the time interval between the R-wave of ECG and the peak of the PPG pulse within the same cardiac cycle (see in Figure 1). The fluctuation of the recorded signals was checked, where the signal with large fluctuation was considered as invalid because it might indicate an unstable physiology conditions during the recording. By such criteria, one subject's data were removed. Finally, 90 datasets from 30 subjects were included in the blood pressure estimation analysis.

2.4. Estimation Model. In previous study, it has been confirmed that the variation in PTT can reflect the blood pressure changes [17] based on which linear model was proposed for blood pressure estimation. However, no factor of blood pressure regulation mechanism has been included in the traditional linear model. Neural control is one important BP regulation mechanism. Studies have shown that vital cardiovascular parameters' variability can reflect the neural regulation [39–41]. Further, a previous study showed that the variability in blood pressure and PTT has high coherence [38]. Considering the feasibility of the model implementation, we chose to formulate the model based on the traditional linear algorithm and integrate with the variation and variability of PTT as the indication of neural control. Finally, a blood pressure estimation model was formulated as shown in the following equation:

$$BP = \frac{a}{PTT} + b + c * VPTT + d * (PTTV - PTT_0), \quad (1)$$

where BP refers to blood pressure value; a , b , c , and d are coefficient constants; PTT is the pulse transit time value for estimation; PTTV is the PTT variability during the signal recording, which is defined as (2); PTT_0 is PTT at the *Calibration-sitting* session; and VPTT is the PTT variation at the measurement time, which is formulated as (3):

$$PTTV = \sqrt{\frac{\sum_{i=1}^N (\Delta PTT_i - \text{mean}(\Delta PTT))^2}{N - 1}} \quad (2)$$

$$VPTT = \frac{PTT - PTT_0}{PTT_0}, \quad (3)$$

where ΔPTT is the difference between any two successive PTTs; N is the number of PTT used for variability calculation. In present study, N was set to 5. Due to the signal fluctuation, PTT value in (1) was set as the average of the 5 measurements. In other words, (1) can provide blood pressure estimation for each beat based on past 5 measurements.

2.5. Calibration. Considering that the relationship between blood pressure and PTT varies from subject to subject, individual calibration is necessary for blood pressure estimation. Specifically, the coefficient constants in (1) should be calibrated for the individual blood pressure estimation. First, all coefficient constants were derived by data regression by using all collected data from the subjects. Then coefficient constants a and b were further calibrated for each individual by calibration.

Blood pressure would vary due to hydrostatic effect, which provides an effective solution for the calibration [35, 42]. Different body postures, such as sitting and standing, will result in different blood pressure situation. Therefore, in current study, the scenario of personalized model calibration is to use the recorded PTT and blood pressure values at *Calibration-sitting* and *Calibration-standing* sessions to derive the value of a and b in (1). Thereafter, blood pressure estimation was carried out on the dataset measured in *Estimation-test* session.

3. Results

In order to evaluate the accuracy of the proposed method, the estimated blood pressure values were compared with the paired blood pressure measurements from the oscillometry. Further, we also compared the blood pressure value estimated from the proposed method with that by linear model, as shown in the following equation:

$$BP = \frac{a}{PTT} + b, \quad (4)$$

where a and b are coefficient constants and also calibrated by the datasets from *Calibration-sitting* and *Calibration-standing* sessions. For model implementation, in order to be comparable with the proposed method, PTT value in (4) was also set as the average of the 5 measurements. As a result, the estimations from both the proposed method and the traditional linear model were based on 5 measurements of PTTs.

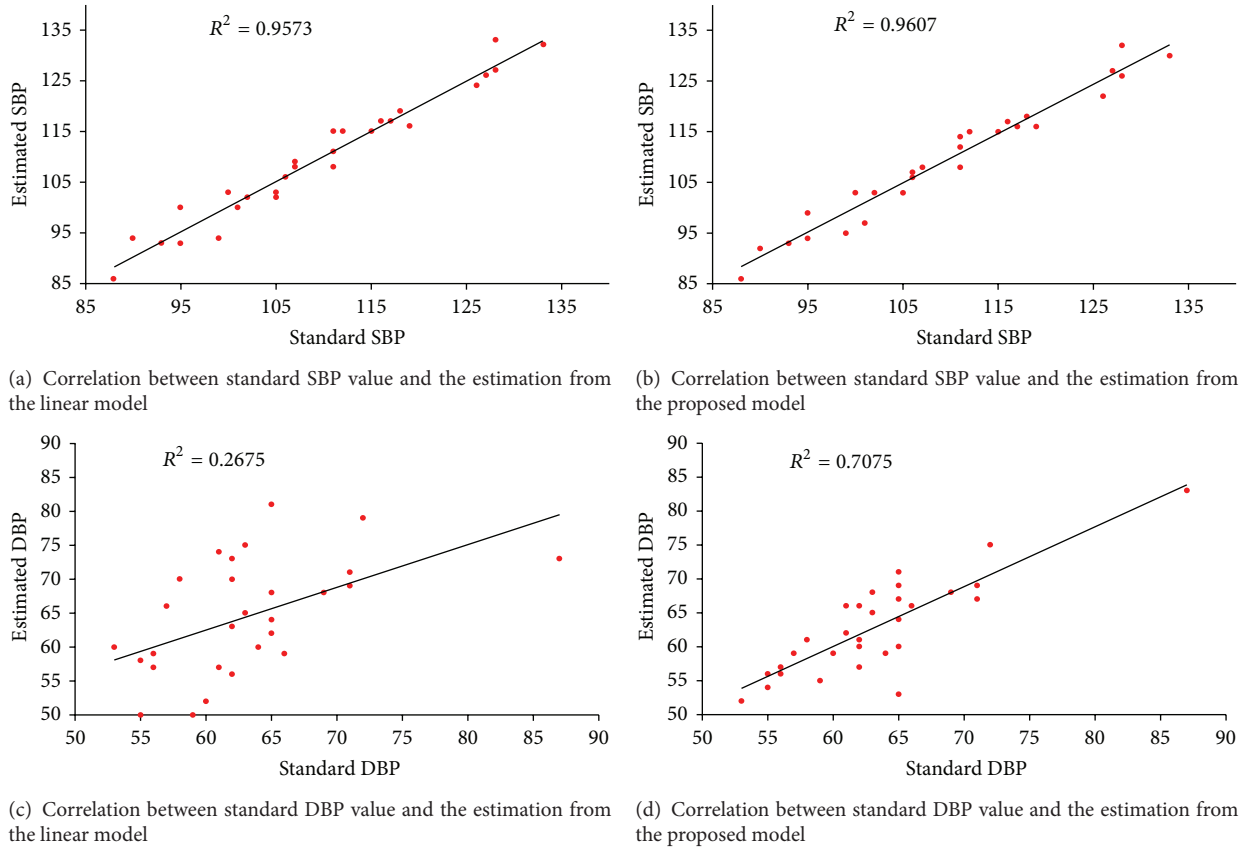


FIGURE 2: Correlation between the estimated blood pressure and the standard blood pressure for both linear model and the proposed model.

The correlation between any paired variables was analyzed by the correlation coefficient R^2 . The error between paired variables was evaluated by the Bland Altman plot. The linear regression was determined using the least squares method. The results were presented in the form of mean \pm standard deviation (SD).

The blood pressure measured by the oscillometry was regarded as the standard value. Correlation between estimated blood pressure values from the two estimation models and the standard value was first analyzed, as shown in Figure 2. It appears that both estimation models could provide an acceptable estimation on SBP as the correlation coefficient R^2 around 0.96 ($P < 0.001$) for the estimation results derived from two models. However, for the DBP, the proposed model showed a better performance with R^2 of 0.71 ($P < 0.001$), while it is 0.27 ($P < 0.01$) for the linear model estimation results. The correlation analysis indicates that the proposed method provides better estimation performance on blood pressure especially for the DBP.

The mean estimation error of the proposed model was -0.2 ± 2.4 mmHg and -0.5 ± 3.9 mmHg, while it was 0.1 ± 2.5 mmHg and 1.3 ± 7.4 mmHg from the linear model, for the SBP and DBP, respectively. The result again showed that the proposed method had a better performance on the DBP estimation. This is evident in the Bland Altman plot shown in Figures 3 and 4.

4. Discussions

As an important risk factor, blood pressure has prognostic value for stroke. Continuous blood pressure measurement will assist for the preventing and predicting of stroke. The PTT-based blood pressure estimation provides the most practical solution for the continuous measurement since the required signal (ECG and PPG) can be obtained by wearable devices. The purpose of this study was to develop a PTT-based blood pressure estimation method with personalized model and easy implementation. The underlying mechanism blood pressure estimation is that pulse wave velocity, which is the inverse of PTT, is directly determined by the elasticity of vessel wall that is associated with blood pressure level [43]. Wong et al. [44] carried out a longitudinal study to show that PTT-based blood pressure estimation had a good performance within half year but the estimation accuracy went worse for longer time. Payne et al. [30] proved that pulse wave velocity was deeply related to SBP but the estimation of DBP was still barely satisfactory. Factors that contribute to blood pressure regulation were suggested to be included in the PTT-based blood pressure estimation model [18, 45]. Baek et al. [46] tried to take heart rate and arterial stiffness into account for the blood pressure estimation model, which improved the estimation accuracy. However, the multifactor model is too complex for application.

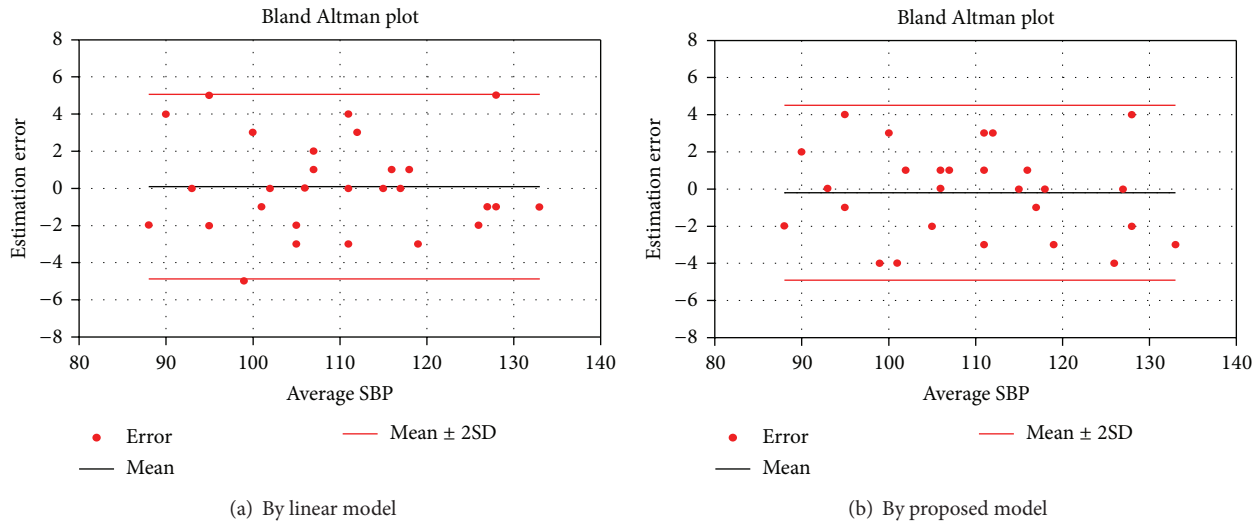


FIGURE 3: Bland Altman plot of estimation error of systolic blood pressure.

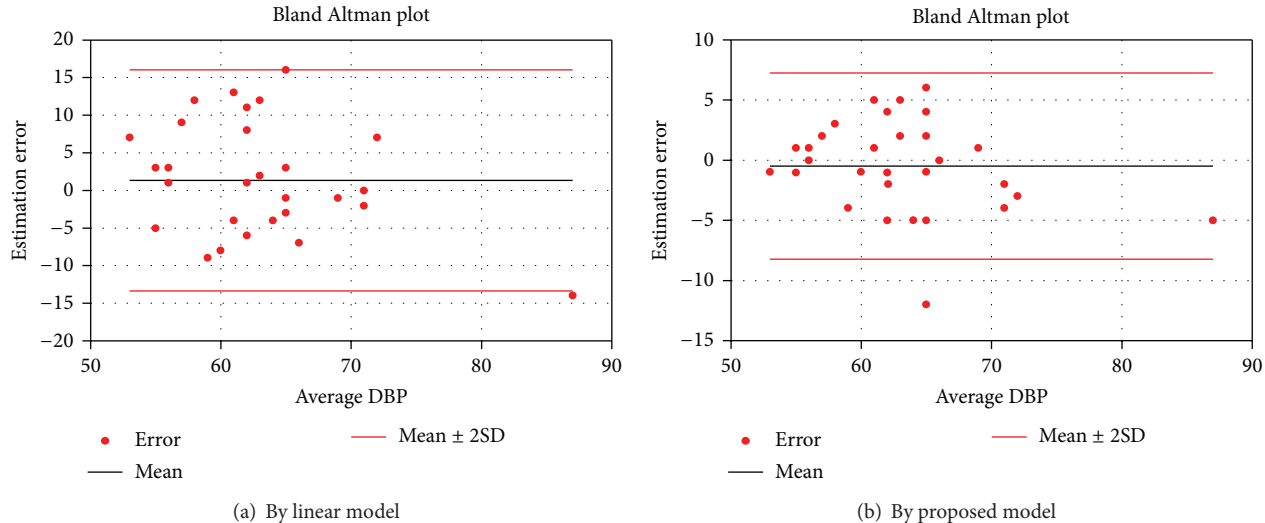


FIGURE 4: Bland Altman plot of estimation error of diastolic blood pressure.

Considering all above factors, we proposed a PTT-based blood pressure estimation method including a new model with compensation and calibration procedure. Hydrostatic effect has been approved to be influencing blood pressure level and included in current method in calibration to derive personalized coefficients in the estimation model for each individual [35, 47]. Sitting and standing postures were adopted as the calibration procedure in current study. The results showed that estimation from linear model with calibration already can provide a good performance for SBP estimation, indicating that personalized model is important for blood pressure estimation. However, the estimation of the DBP by the linear model with calibration was still poor, which was consistent with previous reports [30].

It is well known that the variability in heart rate and blood pressure carries important neural control information for the cardiovascular system [39–41]. One previous study showed

that the variability in PTT had high coherence with that in blood pressure, indicating that some regulating factors affect both signals, simultaneously. Therefore, in current study, the variation in PTT was included as one compensation part to reflect the blood pressure change, while the variability in PTT was adopted as the other compensation part to indicate the neural control. The results made it evident that the model with the compensation provided a better estimation, especially for the DBP. It is possibly because the regulation mechanism of DBP has been included in the estimation model by employing the compensation. As a whole, the model with compensation can provide a better blood pressure estimation. Variability in PTT has potential to improve the blood pressure estimation.

The proposed model has shown promising potential for continuously monitoring blood pressure. As the risk of stroke is much dependent on the blood pressure level [5–7], such a

method would help blood pressure control and enhance the hypertension management, especially for stroke patients. It will be much helpful if such a method can be introduced in the stroke rehabilitation to achieve a better blood pressure control. Patients must benefit from the hypertension management for preventing stroke or predicting stroke.

Although the current study shows promising results, there is one limitation. This study only tested the proposed method on healthy young subjects. It is well known that in hypertension patients, the blood pressure regulation is different from the healthy. Such method needs to be validated further on people with different conditions, such as patients with stroke and hypertension.

Conflict of Interests

The author declares that there is no conflict of interests regarding the publication of this paper.

Acknowledgments

This study is supported by the High-End Talent Oversea Returnees Foundation of Shenzhen (KQC201109020052A), Basic Research Foundation (Outstanding Young Investigator Track) of Shenzhen (JC201005260124A), and the National Natural Science Foundation of China (81000647).

References

- [1] T. Ohkubo, A. Hozawa, K. Nagai et al., "Prediction of stroke by ambulatory blood pressure monitoring versus screening blood pressure measurements in a general population: the Ohasama study," *Journal of Hypertension*, vol. 18, no. 7, pp. 847–854, 2000.
- [2] T. Ohkubo, K. Asayama, and Y. Imai, "The value of self-measured home blood pressure in predicting stroke," *Expert Review of Neurotherapeutics*, vol. 6, no. 2, pp. 163–173, 2006.
- [3] J. Leonardi-Bee, P. M. W. Bath, S. J. Phillips, and P. A. G. Sandercock, "Blood pressure and clinical outcomes in the International Stroke Trial," *Stroke*, vol. 33, no. 5, pp. 1315–1320, 2002.
- [4] C. M. M. Lawes, D. A. Bennett, V. L. Feigin, and A. Rodgers, "Blood pressure and stroke an overview of published reviews," *Stroke*, vol. 35, no. 3, pp. 776–785, 2004.
- [5] W. B. Kannel, "Blood pressure as a cardiovascular risk factor: prevention and treatment," *The Journal of the American Medical Association*, vol. 275, no. 20, pp. 1571–1576, 1996.
- [6] T. G. Pickering and W. B. White, "ASH position paper: home and ambulatory blood pressure monitoring. When and how to use self (home) and ambulatory blood pressure monitoring," *Journal of Clinical Hypertension*, vol. 10, no. 11, pp. 850–855, 2008.
- [7] T. G. Pickering, J. E. Hall, L. J. Appel et al., "Subcommittee of professional and public education of the American heart association council on high blood pressure research. Recommendations for blood pressure measurement in humans and experimental animals: part 1: blood pressure measurement in humans: a statement for professionals from the subcommittee of professional and public education of the American heart association council on high blood pressure research," *Hypertension*, vol. 45, no. 1, pp. 142–161, 2005.
- [8] K. R. Dobbin, "Noninvasive blood pressure monitoring," *Critical Care Nurse*, vol. 22, no. 2, pp. 123–124, 2002.
- [9] B. P. McGrath, "Ambulatory blood pressure monitoring," *Medical Journal of Australia*, vol. 176, no. 12, pp. 588–592, 2002.
- [10] K. Shimada, Y. Imai, K. Kario et al., "Guidelines for the clinical use of 24 hour ambulatory blood pressure monitoring (ABPM) (JCS 2010)—digest version," *Circulation Journal*, vol. 76, no. 2, pp. 508–519, 2010.
- [11] J. Handler, "The importance of accurate blood pressure measurement," *The Permanente Journal*, vol. 13, no. 3, p. 51, 2009.
- [12] E. R. NYE, "The effect of blood pressure alteration on the pulse wave velocity," *British Heart Journal*, vol. 26, no. 2, pp. 261–265, 1964.
- [13] B. Gribbin, A. Steptoe, and P. Sleight, "Pulse wave velocity as a measure of blood pressure change," *Psychophysiology*, vol. 13, no. 1, pp. 86–90, 1976.
- [14] A. Steptoe, H. Smulyan, and B. Gribbin, "Pulse wave velocity and blood pressure change: calibration and applications," *Psychophysiology*, vol. 13, no. 5, pp. 488–493, 1976.
- [15] N. Lutter, H.-G. Engl, F. Fischer, and R. D. Bauer, "Noninvasive continuous blood pressure control by pulse wave velocity," *Zeitschrift fur Kardiologie*, vol. 85, no. 3, pp. 124–126, 1996.
- [16] R. A. Allen, J. A. Schneider, D. M. Davidson, M. A. Winchester, and C. B. Taylor, "The covariation of blood pressure and pulse transit time in hypertensive patients," *Psychophysiology*, vol. 18, no. 3, pp. 301–306, 1981.
- [17] M. Landowne, "A method using induced waves to study pressure propagation in human arteries," *Circulation Research*, vol. 5, no. 6, pp. 594–601, 1957.
- [18] C. C. Y. Poon and Y. T. Zhang, "Cuff-less and noninvasive measurements of arterial blood pressure by pulse transit time," in *Proceedings of the 27th Annual International Conference of the Engineering in Medicine and Biology Society (IEEE-EMBS '05)*, pp. 5877–5880, September 2005.
- [19] Y. Chen, C. Wen, G. Tao, M. Bi, and G. Li, "Continuous and noninvasive blood pressure measurement: a novel modeling methodology of the relationship between blood pressure and pulse wave velocity," *Annals of Biomedical Engineering*, vol. 37, no. 11, pp. 2222–2233, 2009.
- [20] Y. Chen, C. Wen, G. Tao, and M. Bi, "Continuous and non-invasive measurement of systolic and diastolic blood pressure by one mathematical model with the same model parameters and two separate pulse wave velocities," *Annals of Biomedical Engineering*, vol. 40, no. 4, pp. 871–882, 2012.
- [21] H. C. Bazett and N. B. Dreyer, "Measurements of pulse wave velocity," *American Journal of Physiology—Legacy Content*, vol. 63, no. 1, pp. 94–116, 1922.
- [22] J. D. Lane, L. Greenstadt, D. Shapiro, E. Rubenstein, and D. James, "Pulse transit time and blood pressure: an intensive analysis," *Psychophysiology*, vol. 20, no. 1, pp. 45–49, 1983.
- [23] M. E. Safar, B. I. Levy, and H. Struijker-Boudier, "Current perspectives on arterial stiffness and pulse pressure in hypertension and cardiovascular diseases," *Circulation*, vol. 107, no. 22, pp. 2864–2869, 2003.
- [24] S. Ahmad, S. Chen, K. Soueidan et al., "Electrocardiogram-assisted blood pressure estimation," *IEEE Transactions on Biomedical Engineering*, vol. 59, no. 3, pp. 608–618, 2012.
- [25] R. Ochiai, J. Takeda, H. Hosaka, Y. Sugo, R. Tanaka, and T. Soma, "The relationship between modified pulse wave transit time and cardiovascular changes in isoflurane anesthetized dogs," *Journal of Clinical Monitoring and Computing*, vol. 15, no. 7–8, pp. 493–501, 1999.

- [26] D. Barschdorff and M. Erig, "Continuous blood pressure determination during exercise ECG recording," *Biomedizinische Technik*, vol. 43, no. 3, pp. 34–39, 1998.
- [27] D. J. Pitson and J. R. Stradling, "Value of beat-to-beat blood pressure changes, detected by pulse transit time, in the management of the obstructive sleep apnoea/hypopnoea syndrome," *European Respiratory Journal*, vol. 12, no. 3, pp. 685–692, 1998.
- [28] C. F. Wippermann, D. Schranz, and R. G. Huth, "Evaluation of the pulse wave arrival time as a marker for blood pressure changes in critically ill infants and children," *Journal of Clinical Monitoring*, vol. 11, no. 5, pp. 324–328, 1995.
- [29] T. Kawasaki, S. Sasayama, S. I. Yagi, T. Asakawa, and T. Hirai, "Non-invasive assessment of the age related changes in stiffness of major branches of the human arteries," *Cardiovascular Research*, vol. 21, no. 9, pp. 678–687, 1987.
- [30] R. A. Payne, C. N. Symeonides, D. J. Webb, and S. R. J. Maxwell, "Pulse transit time measured from the ECG: an unreliable marker of beat-to-beat blood pressure," *Journal of Applied Physiology*, vol. 100, no. 1, pp. 136–141, 2006.
- [31] G. V. Marie, C. R. Lo, J. van Jones, and D. W. Johnston, "The relationship between arterial blood pressure and pulse transit time during dynamic and static exercise," *Psychophysiology*, vol. 21, no. 5, pp. 521–527, 1984.
- [32] C. M. McEniry, S. Wallace, I. S. Mackenzie et al., "Relationship between arterial pressure and pulse wave velocity using photoplethysmography during the post-exercise recovery period," *Acta Universitatis Latviensis: Biology*, vol. 753, pp. 59–68, 2009.
- [33] W. Chen, T. Kobayashi, S. Ichikawa, Y. Takeuchi, and T. Togawa, "Continuous estimation of systolic blood pressure using the pulse arrival time and intermittent calibration," *Medical & Biological Engineering & Computing*, vol. 38, no. 5, pp. 569–574, 2000.
- [34] Y. L. Zheng, C. C. Y. Poon, and Y. T. Zhang, "Investigation of temporal relationship between cardiovascular variables for cuffless blood pressure estimation," in *Proceedings of the IEEE-EMBS International Conference on Biomedical and Health Informatics (BHI '12)*, pp. 644–646, Hong Kong, China, January 2012.
- [35] C. C. Y. Poon and Y. T. Zhang, "Using the changes in hydrostatic pressure and pulse transit time to measure arterial blood pressure," in *Prceeding of the 29th Annual International Conference of IEEE-EMBS, Engineering in Medicine and Biology Society (EMBC '07)*, pp. 2336–2337, Lyon, France, August 2007.
- [36] Y. Liu, C. C. Y. Poon, and Y.-T. Zhang, "A hydrostatic calibration method for the design of wearable PAT-based blood pressure monitoring devices," in *Proceedings of the 30th Annual International Conference of the IEEE Engineering in Medicine and Biology Society (EMBS '08)*, pp. 1308–1310, Vancouver, Canada, August 2008.
- [37] C. Douniama, C. U. Sauter, and R. Couronne, "Blood pressure tracking capabilities of pulse transit times in different arterial segments: a clinical evaluation," *Computers in Cardiology*, pp. 201–204, 2009.
- [38] T. Ma and Y. T. Zhang, "A correlation study on the variabilities in pulse transit time, blood pressure, and heart rate recorded simultaneously from healthy subjects," in *Proceedings of the 27th Annual International Conference of the Engineering in Medicine and Biology Society (IEEE-EMBS '05)*, September 2005.
- [39] S. L. Dawson, B. N. Manktelow, T. G. Robinson, R. B. Panerai, and J. F. Potter, "Which parameters of beat-to-beat blood pressure and variability best predict early outcome after acute ischemic stroke?" *Stroke*, vol. 31, no. 2, pp. 463–468, 2000.
- [40] P. Van De Borne, N. Montano, K. Narkiewicz et al., "Importance of ventilation in modulating interaction between sympathetic drive and cardiovascular variability," *The American Journal of Physiology*, vol. 280, no. 2, pp. H722–H729, 2001.
- [41] M. Pagani, "Circadian heart rate and blood pressure variability considered for research and patient care," *International Journal of Cardiology*, vol. 87, no. 1, pp. 29–30, 2003.
- [42] X. M. Guo, L. S. Chen, M. Chen, and C. L. Peng, "Design of real-time ECG monitoring system based on smart-phone," *Application Research of Computers*, vol. 6, pp. 2181–2191, 2010.
- [43] T. W. Hansen, J. A. Staessen, C. Torp-Pedersen et al., "Prognostic value of aortic pulse wave velocity as index of arterial stiffness in the general population," *Circulation*, vol. 113, no. 5, pp. 664–670, 2006.
- [44] M. Y. Wong, C. C. Poon, and Y. Zhang, "An evaluation of the cuffless blood pressure estimation based on pulse transit time technique: a half year study on normotensive subjects," *Cardiovascular Engineering*, vol. 9, no. 1, pp. 32–38, 2009.
- [45] A. P. Avolio, M. Butlin, and A. Walsh, "Arterial blood pressure measurement and pulse wave analysis—their role in enhancing cardiovascular assessment," *Physiological Measurement*, vol. 31, no. 1, pp. R1–R47, 2010.
- [46] H. J. Baek, K. K. Kim, J. S. Kim, B. Lee, and K. S. Park, "Enhancing the estimation of blood pressure using pulse arrival time and two confounding factors," *Physiological Measurement*, vol. 31, no. 2, pp. 145–157, 2010.
- [47] P. Shaltis, A. Reisner, and H. Asada, "A hydrostatic pressure approach to cuffless blood pressure monitoring," in *Proceeding of the 26th Annual International Conference of the IEEE Engineering in Medicine and Biology Societ (EMBC '04)*, pp. 2173–2176, September 2004.

Research Article

DWI-Based Neural Fingerprinting Technology: A Preliminary Study on Stroke Analysis

Chenfei Ye,¹ Heather Ting Ma,¹ Jun Wu,² Pengfei Yang,¹ Xuhui Chen,² Zhengyi Yang,³ and Jingbo Ma¹

¹ Department of Electronic and Information Engineering, Harbin Institute of Technology Shenzhen Graduate School, HIT Campus, University Town, Room 205C, C Building, Xili, Nanshan, Shenzhen 518055, China

² Department of Neurology, Peking University Shenzhen Hospital, Shenzhen 18036, China

³ School of Information Technology and Electrical Engineering, The University of Queensland, St. Lucia, QLD 4072, Australia

Correspondence should be addressed to Heather Ting Ma; heather.tma@gmail.com

Received 28 March 2014; Revised 4 June 2014; Accepted 6 June 2014; Published 12 August 2014

Academic Editor: Ting Zhao

Copyright © 2014 Chenfei Ye et al. This is an open access article distributed under the Creative Commons Attribution License, which permits unrestricted use, distribution, and reproduction in any medium, provided the original work is properly cited.

Stroke is a common neural disorder in neurology clinics. Magnetic resonance imaging (MRI) has become an important tool to assess the neural physiological changes under stroke, such as diffusion weighted imaging (DWI) and diffusion tensor imaging (DTI). Quantitative analysis of MRI images would help medical doctors to localize the stroke area in the diagnosis in terms of structural information and physiological characterization. However, current quantitative approaches can only provide localization of the disorder rather than measure physiological variation of subtypes of ischemic stroke. In the current study, we hypothesize that each kind of neural disorder would have its unique physiological characteristics, which could be reflected by DWI images on different gradients. Based on this hypothesis, a DWI-based neural fingerprinting technology was proposed to classify subtypes of ischemic stroke. The neural fingerprint was constructed by the signal intensity of the region of interest (ROI) on the DWI images under different gradients. The fingerprint derived from the manually drawn ROI could classify the subtypes with accuracy 100%. However, the classification accuracy was worse when using semiautomatic and automatic method in ROI segmentation. The preliminary results showed promising potential of DWI-based neural fingerprinting technology in stroke subtype classification. Further studies will be carried out for enhancing the fingerprinting accuracy and its application in other clinical practices.

1. Introduction

Magnetic resonance imaging (MRI) has been widely employed in research as well as in clinical practice. For instance, diffusion weighted imaging (DWI) and diffusion tensor imaging (DTI) technologies provide remarkable detailed information of nervous system and have become the important examinations for neural diseases diagnosis in neurology department of hospital. Specifically, DTI measures the water diffusion situation in neural fibre so that it is frequently used to investigate the abnormal diffusion in the brain. Based on DWI principles, DTI can provide the contrast of the diffusion anisotropy that was further developed to trace the fibre tracts [1]. Both DWI and DTI technologies produce special contrast of nervous system in terms of diffusion ability, fibre integrity, fibre bundle

directions, and so forth. In order to take advantage of these neuroimaging approaches, quantitative analysis is crucial for the image interpretation, which is also important for clinical applications. Quantitative measures, such as mean diffusivity (MD) and fractional anisotropy (FA), were proposed to measure the cellular diffusion state and the anisotropy of fibre tract in white matter [2] based on DTI. An increasing number of quantitative methods were introduced to DTI data analysis, such as voxel-based analysis (VBA) [3] and tract-based spatial statistics (TBSS) [4, 5]. These methods can automatically localize the lesion in the brain by comparing patients' images with a normal control group [6]. However, the existing quantitative analysis methods of DTI are sensitive to the lesion location but not the physiological changes in nature. For instance, a lesion in the brain can be localized by VBA according to the FA value changes while the inherent

physical meaning for such changes cannot be reflected by this analysis. According to the imaging principles, images of DTI and DWI can not only provide structural information but also contain physiological meanings [7]. Further development on the quantitative analysis will facilitate interpretation of DWI data that is much helpful in both neuroscience research and clinical practice.

Stroke is a common neural disease especially for the elderly and the people with hypertension [8]. In clinical applications, DWI has shown accurate identification of ischemic tissue and the ability to discriminate between dead and salvageable ischemic brain [9–11]. Acute ischemic lesions in DWI can be detected with greater sensitivity than conventional MRI, such as T1 and T2 weighted imaging [12–15]. Besides, defining different stroke states by MRI images is important to follow up patients' response to a therapy. It is reported that decreased apparent diffusion coefficient (ADC) values indicate good sensitivity and specificity in an infarct less than 10 days old [16]. Appearances on DWI images following stroke also vary in different states [17]. However, the performance of acute infarct detection or stroke state determination is unsatisfactory by simply identifying hyperintensity or hypointensity on DWI images by thresholding [18]. Current quantitative measures, such as ADC and FA [19], are employed to provide different contrasts of lesion to identify the infarction area and location. Better utility of DWI and DTI data would make it possible to identify subtypes of stroke, which will enhance the diagnosis of physiological variation of the patients and thus affect further clinical management. A quantitative measure, which contains comprehensive features of the nerve, should be developed to exploit the rich information in DWI images for detecting subtypes of ischemic stroke.

In this study, we proposed a method called DWI-based neural fingerprinting to characterize the neural physiological changes that can be used for subtype classification of ischemic stroke. The “fingerprinting” concept was borrowed from magnetic resonance fingerprinting (MRF) [20] technique, permitting the accelerating acquisition of multiple magnetic resonance parameters, while in current proposal the “fingerprint” refers to a feature vector constructed from the DWI images with different diffusion gradients that contains comprehensive neural information. As anisotropy measurement shows sensitivity to degrees of fibre damage in disease affecting white matter [21–23], we hypothesize that specific diffusivity change within ischemic stroke could be considered as a fingerprint reflecting unique neural property. Therefore, pathological changes within the infarction of patients after stroke would be associated with the fingerprint extracted from the DWI data with different gradients. By applying clustering algorithms on the fingerprints, the subjects can possibly be classified into normal controls, patients with acute stroke, and patients with stroke sequela.

2. Methodology

2.1. Data Acquisition and Image Preprocessing. The present study adopted retrospective clinical data from the Neurology

Department of Peking University Shenzhen Hospital. Clinical data from 19 subjects (13 men and 6 women, 49 ± 19 years old) were collected, where MRI examinations with the same protocol were conducted on the subjects. The 19 subjects were diagnosed as eight healthy people (4 men and 4 women, 31 ± 4 years old), eight with acute stroke lesions (6 men and 2 women, 64 ± 15 years old), and three with stroke sequela (3 men, 58 ± 8 years old). For the 11 patients with acute stroke and stroke sequela, 11, 10, and 9 lesions were located in the internal capsule, the striatocapsular, and the motor cortex, respectively. Extensive information about participants' health status has been obtained through symptomatic evaluation. The diagnosis reports were issued by two neurologists in the Peking University Shenzhen Hospital. All the participants underwent MR imaging with 1.5 T Siemens Sigma System (Siemens Medical Systems). The typical MRI protocol consisted of turbo spin echo (TSE) sequence to generate T2 weighted images (TE = 89 ms; TR = 4000 ms; flip angle = 150° ; acquisition matrix = 768×624 ; FOV = 230×187 mm 2) and single-shot echo-planar spin-echo (EPSE) sequence to obtain DWI images (TE = 88 ms; TR = 2700 ms; flip angle = 90° ; acquisition matrix = 128×128 ; FOV = 250×250 mm 2 ; in-plane resolution 1×1 mm 2 ; b = 1000 s/mm 2 ; 20 diffusion weighted gradient directions and 1 without diffusion weighting). Nineteen axial sections in 6.5 mm slice gap with 5 mm thickness were obtained.

The 20 DWI images in Digital Imaging and Communications in Medicine (DICOM) format of each subject were imported into the SPM8 software (Wellcome Trust Centre, UCL) for preprocessing [24], involving spatial normalization to the standard MNI space [25, 26] and Gaussian smoothing (FWHM of 3 mm) [27].

2.2. ROI Segmentation and Fingerprint Construction. Obtaining diffusion weighted signals of the infarct is much dependent on the accurate localization of infarct area. Three methods were used in the present study, named manual, semiautomatic, and automatic ROI segmentation. The manual ROI was segmented by clinicians, which was also supposed to be the reference for the semiautomatic method.

First, the manual ROI was defined by clinicians. For stroke patients, two experienced neurologists blinded to clinical symptoms drew target ROI of stroke lesion independently on T2 weighted images while taking the T1 and ADC images as reference. To evaluate the drawing agreement of different operators, the error of ROI's areas and center coordinates regarding each participant were evaluated by Bland-Altman plots and correlation coefficients. The interrater reliability of ROI is shown in Figures 1 and 2. All evaluation measures show good agreement between the two operators (correlation coefficients > 0.95) to guarantee robust and accurate ROI segmentation. Then, the intersection parts of ROIs were mapped to the corresponding DWI images to produce the final infarct location through multimodal registration, as shown in Figure 3. For normal subjects, one arbitrary cerebral hemisphere was selected as target ROI to be investigated as there was no infarct in their brain. The manual ROI was supposed to provide the most accurate segmentation on

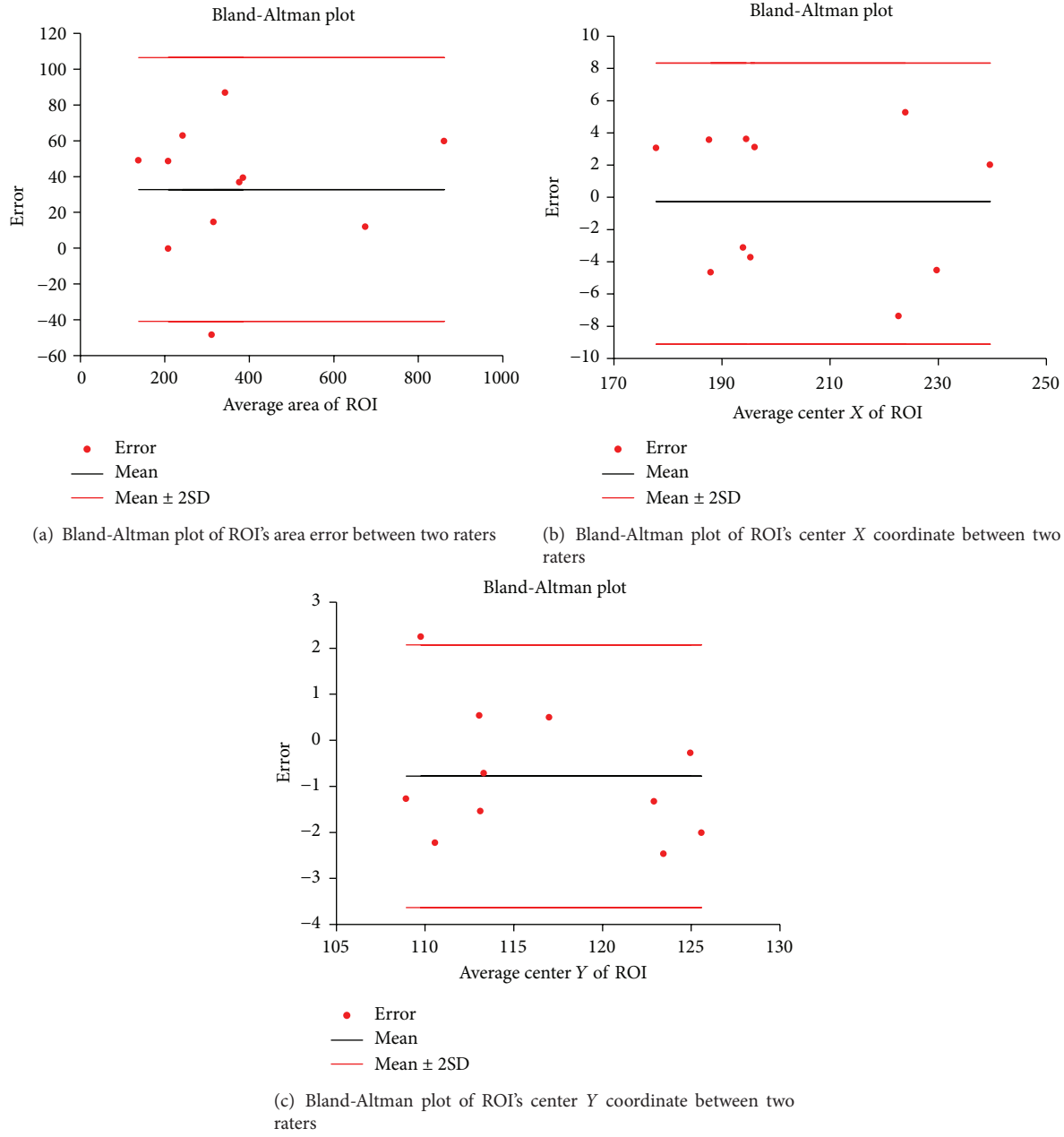


FIGURE 1: Bland-Altman plot of ROI between two raters.

the stroke lesion due to the professional knowledge of the operators.

A semiautomatic method for ROI location was proposed based on morphological segmentation. Firstly, DWI images of each participant were registered to a normal brain template. Then, we averaged 20 slices of registered DWI images into one image for each subject. Three stroke subjects were arbitrarily selected from normal subjects, patients with acute stroke, and patients with stroke sequela, respectively. The ROIs were drawn accordingly to provide necessary references to differentiate normal brain tissue and stroke lesions. Image signal intensity was compared voxelwise between the ROI and the mirror area on the opposite hemisphere for each

subject. The histogram of the signal intensity difference was mapped to derive the optimal thresholds to differentiate the lesion from the normal brain tissue. Figure 4 shows the probability density function based on the histogram, where two optimized thresholds were determined as the criteria for lesion identification. Then, the two thresholds were used for lesion ROI segmentation on other patients' DWI images.

In order to segment the lesion ROI automatically, we also proposed a TBSS based method. We hypothesized that the stroke lesion in the brain would contain water diffusibility changes that vary the fractional anisotropy of the pixel. Then, through TBSS approach, pixels with significant FA change were detected and used to compose the lesion ROI. This

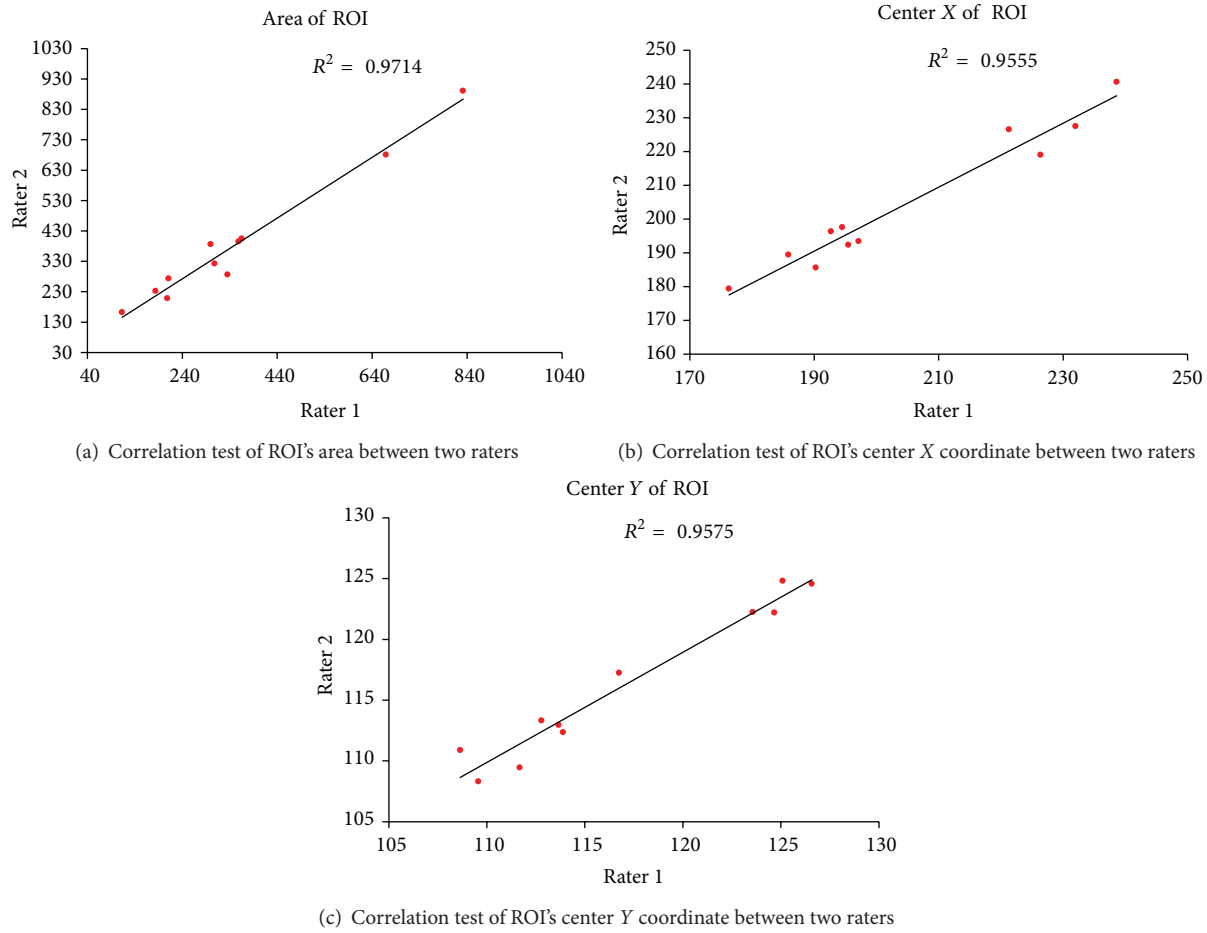


FIGURE 2: Correlation test of ROI between two raters.

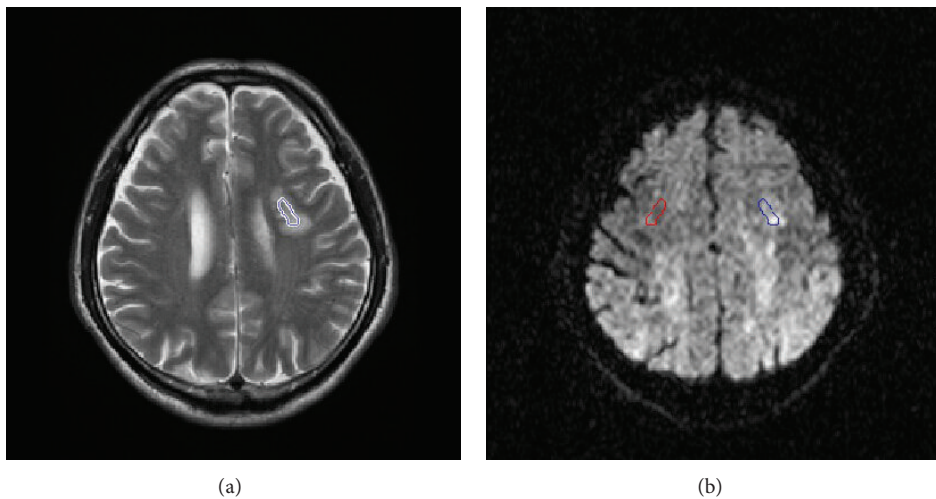


FIGURE 3: Manual drawings of ROIs of stroke lesion on DWI images. The stroke lesion was observed in the brain DWI image. (a) T2 weighted image facilitated infarct location on the corresponding DWI images. (b) Stroke lesion was localized in DWI image (blue circle) by image registration with T2 image, while the contralateral region generated automatically in red.

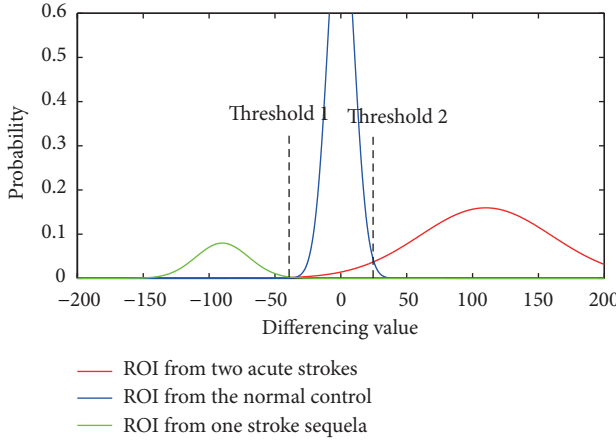


FIGURE 4: The probability density curve of voxelwise differencing value. Blue curve represents the normal control; red curve represents the acute stroke group; green curve represents the stroke sequela group. Two thresholds are determined to discriminate the different distributions.

method was implemented using FMRIB Software Library (FSL 4.1.9; <http://www.fmrib.ox.ac.uk/fsl>) [28]. First of all, a brain template in the software was identified as a common registration target. We aligned all subjects' FA images to this target by nonlinear registration. Then, a skeletonised mean FA image was created by a nonmaximum suppression perpendicular to the local tract structure. Each subject's FA image (aligned) was projected onto the skeleton by filling the skeleton with FA values from the nearest relevant tract center. Finally, based on the voxelwise statistics across the stroke patients and the normal controls, the target ROI was defined as the voxels with significant difference (uncorrected $P < 0.005$), as illustrated in Figure 5.

After segmenting the target ROIs with the above three methods, neural fingerprints can be constructed from them, respectively, to reduce intersubject variations in DWI intensity, the mirror ROI (the contralateral region) corresponding to the target ROI was used as a reference. An example of mirror ROI from the manual segmentation is shown by the red circle generated automatically in Figure 3. The design of diffusion gradients is also critical for the construction of neural fingerprints. Considering that the arrangement of diffusion gradients in the three-dimensional space did not affect classification of neural fingerprints only if applying a constant order, we applied 20 diffusion gradients distributed randomly in a constant order in every subject's DWI data. The neural fingerprint for each ROI segmentation method is defined as a vector of 20 elements. Each element is a ratio between the mean image intensities within the target ROI and the mirror ROI calculated with each diffusion gradient. An example of neural fingerprint from manual ROI in DWI images is shown in Figure 6.

2.3. Clustering. To validate the DWI-based neural fingerprinting method, unsupervised learning was employed to cluster the nineteen subjects. Fingerprints used are the

ratio values calculated from manual, semiautomatic, and automatic ROIs, respectively. As the clustering metrics, two types of distance were employed [29]. The Euclidean distance was calculated as follows:

$$D_E = \sqrt{(\mathbf{x}_s - \mathbf{x}_t)(\mathbf{x}_s - \mathbf{x}_t)'}, \quad (1)$$

where \mathbf{x}_s and \mathbf{x}_t are feature vectors of two subjects (the principal components of average image signal intensity sequences). The Cosine distance was calculated as follows:

$$D_C = 1 - \frac{\mathbf{x}_s \mathbf{x}_t'}{\sqrt{(\mathbf{x}_s \mathbf{x}_s') (\mathbf{x}_t \mathbf{x}_t')}}. \quad (2)$$

The K-means algorithm [30, 31] was performed for finger-print clustering. By setting the number of clusters k , each observation was assigned by minimizing the least within-cluster sum of squares (WCSS) until the assignments no longer change. WCSS was defined as follows:

$$\arg \min_{\mathbf{s}} \sum_{i=1}^k \sum_{x_j \in S_i} \|x_j - \mu_i\|^2, \quad (3)$$

where x_j belongs to observation (x_1, x_2, \dots, x_n) , $\mathbf{S} = (S_1, S_2, \dots, S_k)$ is k clusters, and μ_i is the mean of points in S_i . We compared 6 sets of clustering results obtained using the combinations of the three ROI methods and the two distance metrics (Euclidean and Cosine distance), respectively.

To evaluate the clustering results, F score, a common metric to estimate how close the clustering is to the predetermined benchmark classes, was calculated as follows [32]:

$$F = \sum_{j=1}^s \frac{|P_j|}{\sum_{i=1}^s |P_i|} \cdot \max_{1 \leq i \leq m} \frac{2 \cdot P(P_j, C_i) \cdot R(P_j, C_i)}{P(P_j, C_i) + R(P_j, C_i)}, \quad (4)$$

where P is the preclassified sample clusters and s is its corresponding number of clusters. C is the sample clusters and m is its corresponding number of clusters. Precision $P(P_j, C_i)$ is the correct results divided by the number of all returned results, and recall $R(P_j, C_i)$ is the number of correct results divided by the results that should have been returned [33]. The F score can be interpreted as a weighted average of the precision and recall, where F score reaches its best score at 1 and worst score at 0.

3. Results

Based on the fingerprint, the clustering results are shown in Table 1. The clinical diagnosis in the first column is taken as the standard reference, where “1” represents the normal control, “2” represents the group with acute stroke lesions, and “3” represents the group with stroke sequela. For the manual ROI method, it can be observed that clustering result approached 100% accuracy with Euclidean distance. In other words, the fingerprint based on the manual ROI with Euclidean distance gives the best clustering performance compared to others. However, the accuracy is relatively poor when applying Cosine distance (accuracy = 68%, 95% CI:

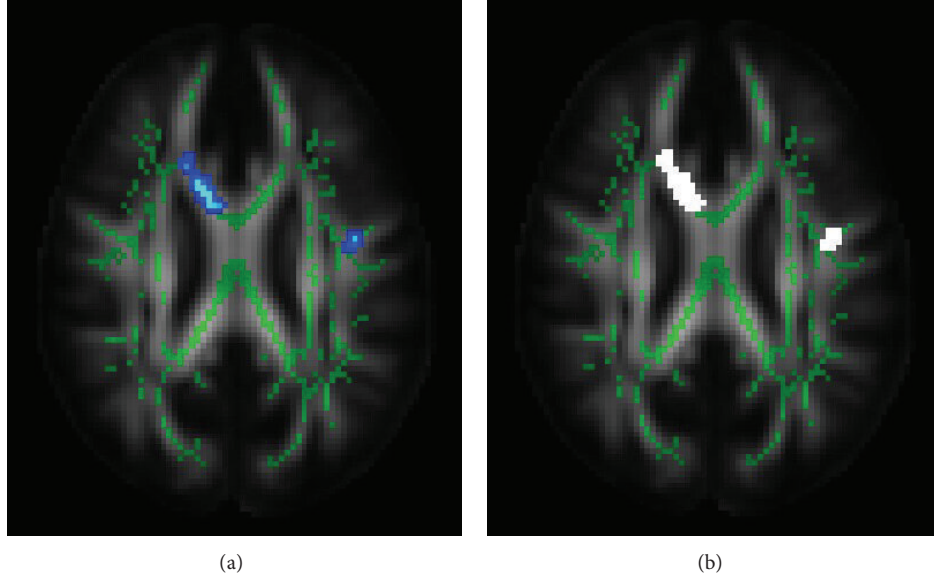


FIGURE 5: Automatic ROI generation on FA map by TBSS. (a) Blue regions indicate significantly decreased FA ($P < 0.005$) in patients with stroke relative to normal controls. (b) White regions indicate the corresponding lesion ROIs. Green regions represented the mean FA skeleton.

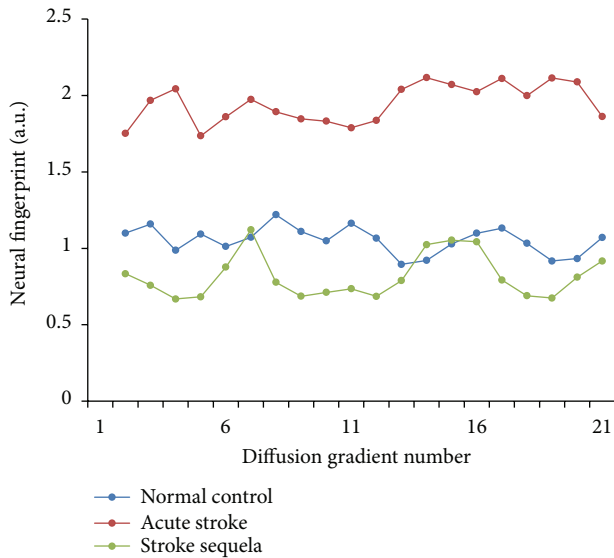


FIGURE 6: An example of neural fingerprints from manual ROI in DWI images. These neural fingerprints are averaged from manual ROI method. Blue curve represents the normal control; red curve represents the acute stroke group; green curve represents the stroke sequela group.

48%–89%). For the semiautomatic segmentation method, two subjects with acute stroke (Subjects 13 and 15) were falsely included into the normal group with Cosine distance, and the corresponding accuracy remained at high level (accuracy = 89%, 95% CI: 76%–97%). It indicates that the semiautomatic method is only sensitive to stroke sequela. With Euclidean distance, the accuracy for semiautomatic method is 74% (95% CI: 54%–93%). For automatic TBSS method, mismatch occurs much more frequently in all of the three groups, as the

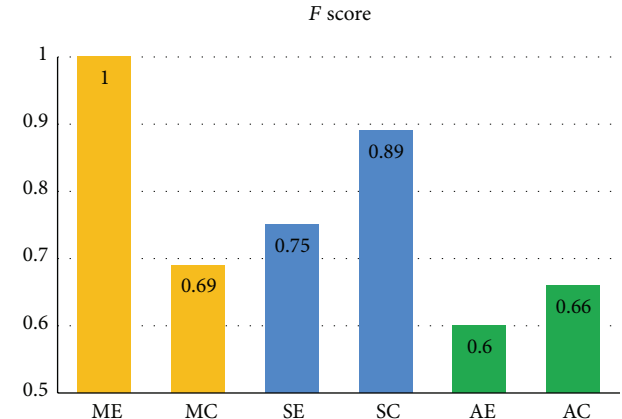


FIGURE 7: F scores using two distance metrics combined with manual, semiautomatic, and automatic ROIs. ME: Euclidean distance using manual ROI; MC: Cosine distance using manual ROI; SE: Euclidean distance using semiautomatic ROI; SC: Cosine distance using semiautomatic ROI; AE: Euclidean distance using automatic ROI; AC: Cosine distance using automatic ROI.

accuracy with Euclidean and Cosine distance is 58% (95% CI: 36%–80%) and 63% (95% CI: 41%–85%), respectively.

The comparison between F scores provides an overall clustering evaluation for each method, as shown in Figure 7. F score of the manual ROI method with Euclidean distance shows accurate clustering performance ($F = 1$). The difference of F scores between two distances for manual method is relatively larger than that in other methods. For the semiautomatic segmentation method, the F scores are higher (i.e., 0.75 and 0.89) than those in automatic TBSS method (i.e., 0.6 and 0.66) with both distances. In other words,

TABLE 1: Clustering result and evaluation.

Clinical reference	Manual ROI		Semiautomatic ROI		Automatic ROI	
	Euclidean distance	Cosine distance	Euclidean distance	Cosine distance	Euclidean distance	Cosine distance
Subject 1	1	1	1	1	1	1
Subject 2	1	1	1	1	1	1
Subject 3	1	1	1	1	1	1
Subject 4	1	1	1	1	1	3
Subject 5	1	1	1	1	1	1
Subject 6	1	1	1	1	1	1
Subject 7	1	1	1	1	3	1
Subject 8	1	1	1	1	3	1
Subject 9	2	2	1	3	1	3
Subject 10	2	2	2	3	2	3
Subject 11	2	2	1	2	2	2
Subject 12	3	3	3	1	3	3
Subject 13	2	2	1	2	1	3
Subject 14	2	2	1	2	2	2
Subject 15	2	2	2	2	1	2
Subject 16	3	3	3	1	3	2
Subject 17	2	2	1	3	2	1
Subject 18	2	2	1	2	2	3
Subject 19	3	3	3	1	3	1
F value		1	0.69	0.75	0.89	0.6
						0.66

Clinical reference classification and DWI-based neural fingerprinting clustering results are shown. For the clinical reference, 1 represents the normal control; 2 represents the group with acute stroke lesion; and 3 represents the group with stroke sequela. For manual, semiautomatic, and automatic ROI methods, different numbers are different clustering labels.

the clustering of semiautomatic method provided a better classification result than that of automatic TBSS method.

4. Discussions

With the development of neuroimaging technology, the detection and analysis of ischemic stroke relying on MRI have achieved high reliability and availability. T1, T2, DWI, DTI, and ADC maps are commonly used in clinics to detect stroke lesions based on hyperintensity or hypointensity on the images. Medical doctors usually check several types of MRI images to determine the subtypes of the ischemic stroke lesion. The DWI-based neural fingerprinting method presented here is a new quantitative approach, which takes advantage of diffusion weighted data to construct a feature vector representing the unique neurophysiological information of the brain tissue. We further applied the fingerprint to determine the subtypes of ischemic stroke which can be only based on the DWI images on different diffusion gradients. The fingerprint produced in this study can quantitatively measure pathological change of neural tissue, which reflects the specific states of stroke lesions, as shown in Figure 6. The preliminary results basically validated the hypothesis that neural physiological change in ischemic stroke can be reflected by the diffusion signal variation on different gradients. Further, the fingerprint proposed in current study can be

used for subtype determination for ischemic stroke. Based on neural fingerprint technology, it is possible to further develop a tool to assist medical doctors in the diagnosis of stroke disease.

For the fingerprint generation, lesion ROI segmentation is a key step for the final clustering results. It appeared that the manual ROI method yielded the best clustering result among the three segmentation methods. As shown in Table 1, a perfect match between clustering results and clinical reference occurs when manual ROI with Euclidean distance was used (F score = 1). It indicates that different phases of ischemic stroke could be distinguished accurately when lesions have been perfectly localized and distance has been properly defined. It also implies that DTI protocol is suitable to generate fingerprints for ischemic stroke. The precise mechanism leading to diffusion changes of ischemic stroke is still not for certain. Wallerian degeneration in the nervous system was found in animal model [34], which involved the breakdown of the myelin sheath and disintegration of axonal microfilaments [35]. Although disruption of myelin and axons around acute infarct lesions might be expected to increase the water diffusivity, an accumulation of cellular debris from the breakdown of axons may hinder water molecule motion [36], which is more likely to occur in late stage of stroke. Another explanation could be the redistribution of extracellular water into the intracellular

compartment, which leads to the shrinkage of extracellular space overtime [37]. These scientific findings may explain why the fingerprint constructed by the DTI images can distinguish the subtypes of the ischemic stroke.

The semiautomatic and automatic ROI segmentation methods were proposed to develop automatic neural fingerprint construction method. The *F* scores for both methods are lower than those obtained in manual ROI with Euclidean distance. It is probably due to the inaccuracy in the ROI localization of stroke lesions. For the semiautomatic method, the thresholds were determined only by three subjects' data, which may not reflect the comprehensive features of the lesion. More samples in the training set are necessary to improve a priori knowledge of the lesion feature. As for the automatic method, the inherent hypothesis, FA value varied significantly for stroke, may not be perfect for the ischemic stroke lesion. In addition, FA images without diffusion tensor orientation information could contribute to false location of significantly abnormal areas. Another limitation may come from the TBSS itself. Usually TBSS method is based on the group comparison, not for single brain lesion detection. The weighting of one specific lesion from a single patient is weakened by the group statistical analysis. The semiautomatic segmentation method overcomes the constraints of TBSS; thus, it has a better discrimination as shown in the clustering result. But the subjects with acute stroke and the normal control fail to be classified perfectly, probably because that threshold 1 with mixed area under curve is more difficult to determine than threshold 2 (Figure 4). The clustering result also implies that appropriate distance metrics should be used to achieve sufficient discriminative power of DWI-based neural fingerprinting. The investigation of optimal distance metric is one of the future works.

The current study is the first effort trying to construct a fingerprint representing neurophysiological information and we implemented the technology on ischemic stroke classification. As an ongoing research, a system should be finally built up to achieve the true fingerprinting function, that is, identification. The identity here refers to the neural specific physiology, which can be represented by a unique fingerprint. In the current study, we chose to use the DWI images on different diffusion gradients to construct the fingerprint. Other MRI protocols are also possible for fingerprint construction once the protocol can provide unique pattern of specified neural physiology. Huge efforts should be carried out to construct a fingerprint bank, which covers massive amounts of neural fingerprints with matched information (age, gender, pathology, etc.). Then, the neural fingerprinting technology can be finally realized by providing neural fingerprint identification or verification through comparing an arbitrary neural fingerprint that comes from a patient to the fingerprint bank. Many applications can be rooted from the neural fingerprinting technology, such as autodiagnosis and risk evaluation for some diseases. Despite the specific brain disease detection, the quantification of general neural property distributed in the whole nervous system relies on the integrated fingerprint bank. Building up the whole system would involve the professional knowledge and efforts from

the medical doctors, biologists, engineers, MRI physicists, and so forth.

In conclusion, this preliminary study demonstrated that the proposed DWI-based neural fingerprinting method had the potential to classify brain abnormalities, such as acute stroke and stroke sequela, due to its ability to exploit comprehensive information contained in DWI data. Further development on such technology could assist clinical practice in the future.

Conflict of Interests

The authors declare that there is no conflict of interests regarding the publication of this paper.

Acknowledgments

This study is supported by the High-End Talent Overseas Returnees Foundation of Shenzhen (KQC201109020052A), the National Natural Science Foundation of China (8100-0647), and the Basic Research Foundation (Outstanding Young Investigator Track) of Shenzhen (JC201005260124A).

References

- [1] P. J. Basser, J. Mattiello, and D. LeBihan, "MR diffusion tensor spectroscopy and imaging," *Biophysical Journal*, vol. 66, no. 1, pp. 259–267, 1994.
- [2] M. Symms, H. R. Jäger, K. Schmierer, and T. A. Yousry, "A review of structural magnetic resonance neuroimaging," *Journal of Neurology, Neurosurgery & Psychiatry*, vol. 75, no. 9, pp. 1235–1244, 2004.
- [3] J. Ashburner and K. J. Friston, "Voxel-based morphometry—the methods," *NeuroImage*, vol. 11, no. 6 I, pp. 805–821, 2000.
- [4] S. M. Smith, M. Jenkinson, H. Johansen-Berg et al., "Tract-based spatial statistics: voxelwise analysis of multi-subject diffusion data," *NeuroImage*, vol. 31, no. 4, pp. 1487–1505, 2006.
- [5] M. Afzali, H. Soltanian-Zadeh, and K. V. Elisevich, "Tract based spatial statistical analysis and voxel based morphometry of diffusion indices in temporal lobe epilepsy," *Computers in Biology and Medicine*, vol. 41, no. 12, pp. 1082–1091, 2011.
- [6] S. Mori, K. Oishi, H. Jiang et al., "Stereotaxic white matter atlas based on diffusion tensor imaging in an ICBM template," *NeuroImage*, vol. 40, no. 2, pp. 570–582, 2008.
- [7] P. J. Basser, "Inferring microstructural features and the physiological state of tissues from diffusion-weighted images," *NMR in Biomedicine*, vol. 8, no. 7–8, pp. 333–344, 1995.
- [8] W. Rosamond, K. Flegal, K. Furie et al., "Heart disease and stroke statistics—2008 update: a report from the American Heart Association Statistics Committee and Stroke Statistics Subcommittee," *Circulation*, vol. 117, no. 4, e25, 2008.
- [9] J. W. Prichard and R. I. Grossman, "New reasons for early use of MRI in stroke," *Neurology*, vol. 52, no. 9, pp. 1733–1736, 1999.
- [10] W. Hacke and S. Warach, "Diffusion-weighted MRI as an evolving standard of care in acute stroke," *Neurology*, vol. 54, no. 8, pp. 1548–1549, 2000.
- [11] P. C. Sundgren, Q. Dong, D. Gómez-Hassan, S. K. Mukherji, P. Maly, and R. Welsh, "Diffusion tensor imaging of the brain: review of clinical applications," *Neuroradiology*, vol. 46, no. 5, pp. 339–350, 2004.

- [12] M. G. Lansberg, G. W. Albers, C. Beaulieu, and M. P. Marks, "Comparison of diffusion-weighted MRI and CT in acute stroke," *Neurology*, vol. 54, no. 8, pp. 1557–1561, 2000.
- [13] P. A. Barber, D. G. Darby, P. M. Desmond et al., "Identification of major ischemic change: diffusion-weighted imaging versus computed tomography," *Stroke*, vol. 30, no. 10, pp. 2059–2065, 1999.
- [14] R. G. González, P. W. Schaefer, F. S. Buonanno et al., "Diffusion-weighted MR imaging: diagnostic accuracy in patients imaged within 6 hours of stroke symptom onset," *Radiology*, vol. 210, no. 1, pp. 155–162, 1999.
- [15] M. Fisher and G. W. Albers, "Applications of diffusion-perfusion magnetic resonance imaging in acute ischemic stroke," *Neurology*, vol. 52, no. 9, pp. 1750–1756, 1999.
- [16] M. G. Lansberg, V. N. Thijs, M. W. O'Brien et al., "Evolution of apparent diffusion coefficient, diffusion-weighted, and T2-weighted signal intensity of acute stroke," *American Journal of Neuroradiology*, vol. 22, no. 4, pp. 637–644, 2001.
- [17] P. M. Desmond, A. C. Lovell, A. A. Rawlinson et al., "The value of apparent diffusion coefficient maps in early cerebral ischemia," *The American Journal of Neuroradiology*, vol. 22, no. 7, pp. 1260–1267, 2001.
- [18] M. E. Mullins, P. W. Schaefer, A. G. Sorensen et al., "CT and conventional and diffusion-weighted MR imaging in acute stroke: study in 691 patients at presentation to the emergency department," *Radiology*, vol. 224, no. 2, pp. 353–360, 2002.
- [19] T. E. Conturo, "Differences between gray matter and white matter water diffusion in stroke: diffusion-tensor MR imaging in 12 patients," *Brain*, vol. 215, no. 1, pp. 211–220, 2000.
- [20] D. Ma, V. Gulani, N. Seiberlich et al., "Magnetic resonance fingerprinting," *Nature*, vol. 495, no. 7440, pp. 187–192, 2013.
- [21] D. J. Werring, D. Brassat, A. G. Droogan et al., "The pathogenesis of lesions and normal-appearing white matter changes in multiple sclerosis. A serial diffusion MRI study," *Brain*, vol. 123, no. 8, pp. 1667–1676, 2000.
- [22] D. J. Werring, C. A. Clark, G. J. Barker, A. J. Thompson, and D. H. Miller, "Diffusion tensor imaging of lesions and normal-appearing white matter in multiple sclerosis," *Neurology*, vol. 52, no. 8, pp. 1626–1632, 1999.
- [23] J. S. Thornton, R. J. Ordidge, J. Penrice et al., "Anisotropic water diffusion in white and gray matter of the neonatal piglet brain before and after transient hypoxia-ischaemia," *Magnetic Resonance Imaging*, vol. 15, no. 4, pp. 433–440, 1997.
- [24] N. Tzourio-Mazoyer, B. Landeau, D. Papathanassiou et al., "Automated anatomical labeling of activations in SPM using a macroscopic anatomical parcellation of the MNI MRI single-subject brain," *NeuroImage*, vol. 15, no. 1, pp. 273–289, 2002.
- [25] T. White, A. T. K. Kendi, S. Lehéricy et al., "Disruption of hippocampal connectivity in children and adolescents with schizophrenia—a voxel-based diffusion tensor imaging study," *Schizophrenia Research*, vol. 90, no. 1–3, pp. 302–307, 2007.
- [26] R. N. Giuliani, D. V. Calhoun, and D. G. Pearlson, "Voxel-based morphometry versus region of interest: a comparison of two methods for analyzing gray matter differences in schizophrenia," *Schizophrenia Research*, vol. 74, no. 2, pp. 135–147, 2005.
- [27] H. Jiang, P. van Zijl, J. Kim et al., "DtStudio: resource program for diffusion tensor computation and fiber bundle tracking," *Computer Methods and Programs in Biomedicine*, vol. 81, no. 2, pp. 106–116, 2006.
- [28] M. Anjari, L. Srinivasan, J. M. Allsop et al., "Diffusion tensor imaging with tract-based spatial statistics reveals local white matter abnormalities in preterm infants," *NeuroImage*, vol. 35, no. 3, pp. 1021–1027, 2007.
- [29] T. Korenius, J. Laurikkala, and M. Juhola, "On principal component analysis, cosine and Euclidean measures in information retrieval," *Information Sciences*, vol. 177, no. 22, pp. 4893–4905, 2007.
- [30] J. Hartigan A and A. Wong M, "Algorithm AS 136: a k-means clustering algorithm," *Applied Statistics*, vol. 28, no. 1, pp. 100–108, 1979.
- [31] L. H. Juang and M. N. Wu, "MRI brain lesion image detection based on color-converted K-means clustering segmentation," *Measurement*, vol. 43, no. 7, pp. 941–949, 2010.
- [32] C. Goutte and E. Gaussier, "A probabilistic interpretation of precision, recall and F-score, with implication for evaluation," in *Advances in Information Retrieval*, pp. 345–359, Springer, Berlin, Germany, 2005.
- [33] D. M. W. Powers, "Evaluation, from precision, recall and F-measure to ROC, informedness, markedness and correlation," *Journal of Machine Learning Technologies*, vol. 2, no. 1, pp. 37–63, 2011.
- [34] D. J. Werring, A. T. Toosy, C. A. Clark et al., "Diffusion tensor imaging can detect and quantify corticospinal tract degeneration after stroke," *Journal of Neurology, Neurosurgery & Psychiatry*, vol. 69, no. 2, pp. 269–272, 2000.
- [35] C. Beaulieu, M. D. Does, R. E. Snyder, and P. S. Allen, "Changes in water diffusion due to Wallerian degeneration in peripheral nerve," *Magnetic Resonance in Medicine*, vol. 36, no. 4, pp. 627–631, 1996.
- [36] S. Love, D. Louis, and W. Ellison D, *Greenfield's Neuropathology 2-Volume Set*, CRC Press, 2008.
- [37] K. Liu, F. Li, T. Tatlisumak et al., "Regional variations in the apparent diffusion coefficient and the intracellular distribution of water in rat brain during acute focal ischemia," *Stroke*, vol. 32, no. 8, pp. 1897–1905, 2001.

Research Article

Circuit Models and Experimental Noise Measurements of Micropipette Amplifiers for Extracellular Neural Recordings from Live Animals

**Chang Hao Chen,^{1,2} Sio Hang Pun,¹ Peng Un Mak,²
Mang I Vai,^{1,2} Achim Klug,³ and Tim C. Lei⁴**

¹ State Key Laboratory of Analog and Mixed-Signal VLSI, University of Macau, Taipa 999078, Macau

² Department of Electrical and Computer Engineering, Faculty of Science and Technology, University of Macau, Taipa 999078, Macau

³ Department of Physiology and Biophysics, University of Colorado School of Medicine, Aurora, CO 80045, USA

⁴ Department of Electrical Engineering, University of Colorado Denver, Denver, CO 80217-3364, USA

Correspondence should be addressed to Sio Hang Pun; lodge@mail.eee.umac.mo

Received 27 March 2014; Revised 5 June 2014; Accepted 6 June 2014; Published 16 July 2014

Academic Editor: Xiaoling Hu

Copyright © 2014 Chang Hao Chen et al. This is an open access article distributed under the Creative Commons Attribution License, which permits unrestricted use, distribution, and reproduction in any medium, provided the original work is properly cited.

Glass micropipettes are widely used to record neural activity from single neurons or clusters of neurons extracellularly in live animals. However, to date, there has been no comprehensive study of noise in extracellular recordings with glass micropipettes. The purpose of this work was to assess various noise sources that affect extracellular recordings and to create model systems in which novel micropipette neural amplifier designs can be tested. An equivalent circuit of the glass micropipette and the noise model of this circuit, which accurately describe the various noise sources involved in extracellular recordings, have been developed. Measurement schemes using dead brain tissue as well as extracellular recordings from neurons in the inferior colliculus, an auditory brain nucleus of an anesthetized gerbil, were used to characterize noise performance and amplification efficacy of the proposed micropipette neural amplifier. According to our model, the major noise sources which influence the signal to noise ratio are the intrinsic noise of the neural amplifier and the thermal noise from distributed pipette resistance. These two types of noise were calculated and measured and were shown to be the dominating sources of background noise for *in vivo* experiments.

1. Introduction

Neurons in the brain communicate via action potentials, which are small and fast changes in the voltage of the cell membrane [1]. During periods of inactivity, the cell membrane of a neuron is typically hyperpolarized to about -60 mV (cell's interior environment negative). During periods of activity, the membrane potential depolarizes and subsequently repolarizes over a period of about one to several milliseconds [1]. Action potential is the unit of information processing in neurons, and as a result many neuroscience research projects involve recordings of action potentials or action potential sequences from single neurons or neural networks. One way to record action potentials is to use high-impedance extracellular electrodes that are advanced into

brain tissue and placed directly next to a single neuron, allowing for the extracellular recording of action potentials through the electrode [2–6]. The signal is sent to an amplifier, digitized, and subsequently evaluated [7]. For extracellular recording, the action potential voltage can be as low as just a few microvolts, making it challenging to record it reliably against various sources of noise. Alternatively, an investigator may attempt to impale the neuron of interest with the electrode or to establish an electrical connection to the neuron's interior via a patch clamp. While these techniques result in larger signals which are easier to measure, intracellular or patch-clamp techniques are very challenging in live animals, making extracellular recordings the technique of choice for many investigators.

Voltage spikes acquired in extracellular recording are typically between $50\text{ }\mu\text{V}$ to $500\text{ }\mu\text{V}$ peak-to peak, with rise times of 0.2 ms or more and pulse durations of 1 ms or more [8]. Amplification is required before these small signals can be analyzed. In addition, several intrinsic and extrinsic noise sources are present during the recordings, affecting the signal-to-noise ratio of the measured voltages. Thus, it is not only important to use low-noise recording amplifiers, but also an understanding of these noise sources is required such that a strategy to eliminate or to minimize them can be developed. Several studies [8–18] have been published describing designs of low noise neural acquisition amplifiers, and a variety of commercially available amplifiers currently exist in the market and are used by neuroscientists. However, most of these studies only discuss how to reduce the intrinsic noise of the amplifier. Discussions of various biological noise sources as well as the electrode noise are largely lacking. For example, the role of the electrode's input impedance, which is one of the important parameters for extracellular recordings, has not received much attention in many designs [10–12, 14–18]. Choosing electrodes with suitable impedances makes the amplifier design appropriate for recording local field potential, which results from the activity of small neural networks, or appropriate for recording activity from a single neuron extracellularly.

For *in vivo* recordings from neurons, both Yang et al. [19] and Lopez et al. [20] have proposed noise models to study the multiple noise sources that need to be considered for the recording. However, these models are largely based on the use of metal electrodes, such as tungsten, platinum, or titanium nitride electrodes, not glass micropipettes. Metal electrodes generally have better noise performance than glass micropipette electrodes [13, 19, 20]. For example, Millar and Barnett [13] reported that there is $65\text{ }\mu\text{V}$ peak-to-peak thermal noise generated from a $1\text{ M}\Omega$ glass micropipette over a recording frequency range between 100 Hz to 8 kHz , while a tungsten electrode in the same condition usually shows a noise level of $\sim 20\text{--}50\text{ }\mu\text{V}$ peak-to-peak. The reason that noise generated from a metal electrode is less than that of a glass micropipette is because the impedance of a metal electrode is largely capacitive [21], resulting in a smaller real component (resistance) to generate thermal noise. While these types of metal electrodes are widely used, they have some disadvantages. For example, metal electrodes cannot easily be combined with microiontophoretic drug testing [22–45]. Also, glass pipettes are typically produced by the investigator with programmable electrode pullers that allow for the adjustment of many different parameters, resulting in virtually endless possibilities in adjusting the shape of the electrode tip [4, 46]. Finally, only glass pipettes can be filled with dyes, viral constructs, tracers, and other materials that can be ejected during the experiment for various purposes [47, 48]. One example is that we have developed a piggyback multibarrel glass pipette system to measure neural signals and to simultaneously inject chemical agents to manipulate neural responses [23]. It is therefore not surprising that both glass and metal electrodes are widely used.

A number of noise models have been proposed for various forms of neural recording [8–16, 18–20, 49]. Yet there

is still a lack of a comprehensive noise model to describe extracellular neural recording using glass micropipettes as the recording electrode. For example, most of the studies [10–12, 14–18] only described intrinsic noise generated by the amplifiers themselves. Chae et al. [9], Budai [8] and Millar and Barnett [13] discussed the additional noise of power-line interference but noise of biological origins and noise generated from electrodes were not included in their models. Yang et al. [19] and Lopez et al. [20] included both biological and electrode noise but their models are for metal electrodes only. When using glass micropipettes as recording electrodes, other noise sources, such as dielectric noise generated from the distributed capacitance of the glass pipette wall [49, 50], have to be considered. Reference [49] modeled the glass micropipette which has a membrane-to-glass seal to describe the situation of intracellular recording inside the cell membrane of a neuron. In extracellular recording single cells selectively are determined by the position of the micropipette tip relative to the cell membrane. Additional noise will arise from nearby cells and from the cerebrospinal fluids. Therefore, a comprehensive mathematical model to describe all noise generated during extracellular recording using glass microelectrodes is necessary and is proposed in this paper.

The purpose of this study is to propose an equivalent circuit model and a noise model for *in vivo* extracellular neural recording using glass micropipettes and to test models using a two-stage amplifier design. Experiments using dead brain tissue from a gerbil and also directly measuring neural activities triggered by external auditory stimulations from the brain of an anesthetized gerbil were performed to further verify our models. According to our simulation and experimental results, the major noise sources which influence the signal-to-noise ratio (SNR) are the intrinsic noise of neural amplifier and the thermal noise from distributed pipette resistance.

2. Methods

The purpose of this study was to assess the various noise sources that affect extracellular recordings and to create model systems in which novel amplifier designs could be tested. In the first part of this manuscript, we develop an equivalent mathematical model that accurately describes the various noise sources involved in extracellular recordings with glass micropipettes. In the second part, we describe several measurement schemes to measure noise performance and the amplification efficacy of the proposed micropipette neural amplifier.

2.1. Circuit Modeling for Micropipette Neural Amplifier

2.1.1. Equivalent Circuit Model of a Micropipette for Extracellular Neural Recording. Figure 1(a) is the equivalent circuit model of a glass micropipette connected to the front-end of a neural signal amplifier for *in vivo* extracellular neural recording in a live rodent. This model is based on previous studies which examine the various physical phenomena attributed to noise generated in extracellular recording [8, 13, 19, 20, 49–56]. Our goal is to provide a unified yet simple mathematical

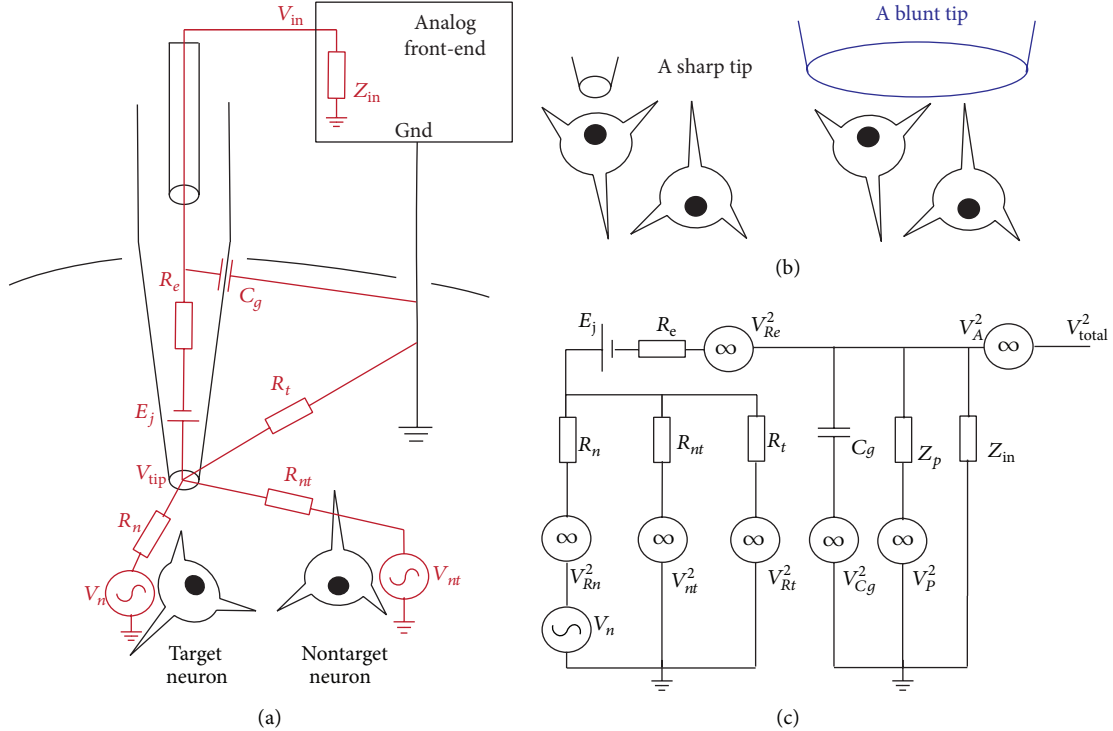


FIGURE 1: (a) Equivalent circuit model of a micropipette used for *in vivo* extracellular neural recordings of conscious animals. V_n : neural voltage of target neuron; V_{nt} : neural voltage of non-target neurons; R_n : equivalent resistance between target neuron and the micropipette tip; R_{nt} : equivalent resistance between nontarget neurons and the micropipette tip; R_t : equivalent resistance between the micropipette tip and the ground; V_{tip} : micropipette tip voltage; E_j : liquid junction potential and half-cell potential; R_e : distributed resistance of the electrolyte; C_g : equivalent capacitance of the glass pipette wall; Z_{in} : overall input impedance of the amplifier; V_{in} : input voltage of the amplifier. (b) Illustrations of using a sharp micropipette and a blunt micropipette. (c) Equivalent noise model of a glass micropipette connected to a neural amplifier. (V_{Rn}^2 : thermal noise generated from equivalent resistor between target neuron and the micropipette tip; V_{Rt}^2 : thermal noise generated from equivalent resistor between the micropipette tip and the ground; V_{Cg}^2 : dielectric noise of the micropipette wall; V_p^2 : environmental noise; V_{Re}^2 : thermal noise generated by the distributed resistance of the electrolyte; V_A^2 : intrinsic noise of the neural amplifier; Z_p : equivalent impedance between the amplifier and the power line. V_{total}^2 : total noise of the micropipette neural amplifier).

model to help understand the important noise factors for neural recordings. For these types of *in vivo* recordings, the micropipette tip is typically positioned outside of but very close to the cell membrane. As shown in our equivalent circuit model, V_n and V_{nt} represent the extracellular neural voltages generated by a target neuron which one would like to record and other nontarget neurons surrounding the target neuron, respectively. R_n and R_{nt} are the equivalent resistance which span between the respective neurons (target and nontarget) and the glass micropipette tip. The resistance of R_n and the resistance of R_{nt} are proportional to both the electrical resistivity of the cerebrospinal fluid and the distance between the membrane of the respective cells and the micropipette tip. In addition, the resistive values of R_n and R_{nt} largely depend on the physical locations of the neurons against the micropipette tip. If the opening of the micropipette tip is directly above the target neuron, the majority of the ionic current induced at the neuron membrane can be captured by the micropipette tip; hence, the resistance R_n is significantly reduced. On the other hand for the surrounding nontarget neurons, the ionic currents generated by these neurons will

have difficult time getting inside the micropipette and instead will be dispersed in the cerebrospinal fluid and eventually captured by the ground, resulting in a significant increase of the R_{nt} resistance to the micropipette tip. For this reason, R_{nt} is assumed to be significantly larger than R_n ($R_{nt} \gg R_n$). R_t is an equivalent resistor representing the electrical resistance between the ground and the micropipette tip. R_t is also proportional to both the cerebrospinal fluid resistivity and the distance between the micropipette tip and the ground.

V_{tip} is the voltage at the opening of the micropipette tip and can be estimated based on the neural voltages and the equivalent resistances of cerebrospinal fluid,

$$\begin{aligned}
 V_{tip} &= V_n \frac{R_{nt} \parallel R_t}{R_n + R_{nt} \parallel R_t} + V_{nt} \frac{R_n \parallel R_t}{R_{nt} + R_n \parallel R_t} \\
 &= V_n \frac{1}{R_n / (R_{nt} \parallel R_t) + 1} \\
 &\quad + V_{nt} \frac{1}{R_{nt} / (R_n \parallel R_t) + 1}.
 \end{aligned} \tag{1}$$

One method of understanding how neurons of a specific brain area process information involves measurements of neural voltages generated from single neurons. To do this, the pipette tip is placed very close to the target neuron, resulting in the resistive value of R_n significantly smaller than those of R_{nt} and R_t . Thus, $R_n/(R_{nt} \parallel R_t) \approx 0$ and $R_{nt}/(R_n \parallel R_t) \gg 1$, and (1) reduces to

$$V_{\text{tip}} \approx V_n. \quad (2)$$

If a blunt micropipette tip is used for *in vivo* extracellular recording, several neurons can be simultaneously located under the tip of the micropipette ($R_n \approx R_{nt}$), as shown in Figure 1(b). In this case, V_{tip} will pick up voltages from multiple neurons, which is not desirable for understanding specific neural function.

The inside of the micropipette can be further modeled. A liquid junction potential is formed inside the pipette due to the ionic concentration difference between the electrolyte in the glass micropipette and the cerebrospinal fluid. In addition, a half-cell potential is also present due to the electrode-electrolyte interface. These two potentials can be modeled together by a voltage source (E_j) in our equivalent circuit model. R_e is the distributed resistance of the electrolyte filled inside the micropipette. C_g is the equivalent capacitor between the electrolyte and the electrical ground located in the cerebrospinal fluid separated by the glass wall of the micropipette. Finally, Z_{in} and V_{in} are the input impedance and the input voltage of the analog amplifier, respectively. Therefore, V_{in} can be modeled based on the equivalent circuit model of the micropipette as follows:

$$V_{\text{in}} \approx (V_{\text{tip}} + E_j) \frac{Z_{Cg} \parallel Z_{\text{in}}}{R_e + Z_{Cg} \parallel Z_{\text{in}}}, \quad (3)$$

where $Z_{Cg} = 1/j2\pi f C_g$ and f is the working frequency. For a high quality glass micropipette, C_g is typically less than 0.1 pF [49, 50] and the input impedance of the analog front-end Z_{in} is typically two orders of magnitude larger than Z_{Cg} . Using a sharp micropipette to record single cell activity ($V_{\text{tip}} \approx V_n$), (3) is further simplified to

$$V_{\text{in}} \approx (V_n + E_j) \frac{Z_{\text{in}}}{R_e + Z_{\text{in}}}. \quad (4)$$

Equation (4) gives us two important circuit design guidelines for *in vivo* extracellular neural recording. In order to optimally measure the neural voltage generated by a single neuron ($V_{\text{in}} \approx V_n$), first the DC offset E_j should be rejected; otherwise, it will be amplified together with the neural voltage and may saturate the subsequent stages of amplification. Second, the input impedance of the analog front-end (Z_{in}) should be significantly larger than the resistance of the electrolyte (R_e) to avoid signal reduction at the input front-end.

2.1.2. Noise Analysis of the Micropipette Neural Amplifier. Figure 1(c) shows the electronic noise model [19, 20, 49, 51, 53, 57–60] for our equivalent circuit model for *in vivo*

micropipette recordings. V_{Rn}^2 is the thermal noise generated from the equivalent resistance between the target neuron and the micropipette tip. Thermal noise can be estimated based on the well-known Johnson-Nyquist thermal noise relation [51, 54, 61]

$$V_R^2 = 4k_B T R, \quad (5)$$

where k_B is the Boltzmann's constant, T is the temperature in Kelvin, and R is the equivalent resistance. For single cell recording where the tip is very close to the target neuron, V_{Rn}^2 can be simply neglected due to the small resistance. V_{nt}^2 is the noise generated from other nontarget neurons. As explained above, voltages from nontarget neurons registered at the micropipette tip are small when a sharp tip is used. However, the voltages generated from nontarget neurons can still contribute to the background noise [19, 52, 55, 62–64] superimposed on the target neural signal. This background noise can be determined by using

$$V_{nt}(t) = \sum_i \sum_k V_{nt,i}(t - t_{i,k}); \quad (6)$$

$V_{nt}(t)$ is the algebraic sum (background noise) of all nontarget neural voltages. $V_{nt,i}(t - t_{i,k})$ is the neural voltage at the micropipette tip of a neuron i firing a sequence of neural action potentials at various time instants $t_{i,k}$. This overall background noise $V_{nt}(t)$ contributes a $1/f^x$ noise spectrum ($x \approx 0.5$ to 1.5) in the frequency domain [19, 52, 55]. Because of the $1/f^x$ nature of this background noise which dominates in the low frequencies [19, 52, 55, 58, 63], it can be rejected using a high-pass filter after the unity-gain first stage amplification. V_{Rt}^2 is the thermal noise generated by the equivalent resistance between the ground and the micropipette tip. This thermal noise can also be neglected due to the small tip opening in consideration.

There are also noise sources inside the micropipette. V_{Re}^2 is the thermal noise generated from distributed resistance of the electrolyte and can be estimated using (5). This thermal noise can be minimized by reducing the distributed resistance by increasing the ion concentration of the electrolyte inside the micropipette. V_{Cg}^2 represents the dielectric noise generated from the distributed pipette capacitance of the glass pipette wall. This noise can be described using the following equation [49, 50]:

$$V_{Cg}^2(f) = 4kTDC_g(2\pi f), \quad (7)$$

where D is the dissipation factor of the glass material. Equation (7) shows that the noise generated from the pipette wall dominates in higher frequencies. For the frequencies of interest in neural recording, this noise can be minimized using high quality glass pipette having a $D < 0.0001$.

There are also noise sources from the environment. V_P^2 represents all noise generated from the environment, in particular the 50/60 Hz power line noise. Z_p is the equivalent impedance between the amplifier input and power line. For this reason, the amplifier front-end should be carefully designed to eliminate any electronic ground loops [8, 13] to

avoid coupling environmental noise to the amplifier. Thus, in our model the impedance of Z_p is assumed to be larger than Z_{in} ($Z_p \gg Z_{in}$). Finally, V_A^2 is the intrinsic noise from the amplifier, which is inherited due to the imperfection of circuit elements in the neural amplifier. Careful design of the low-noise amplifier front-end and subsequent amplifier stages is crucial to obtain optimal neural signal.

Using the aforementioned model, assuming these noise sources are independent, the overall input referred noise of the micropipette neural recording amplifier for conscious rodents can be summarized as

$$\begin{aligned} V_{\text{total}}^2 = & V_A^2 + V_P^2 \left| \frac{Z_{in} \parallel R_e \parallel Z_{Cg}}{Z_p + Z_{in} \parallel R_e \parallel Z_{Cg}} \right|^2 \\ & + V_{Cg}^2 \left| \frac{Z_{in} \parallel R_e \parallel Z_p}{Z_{Cg} + Z_{in} \parallel R_e \parallel Z_p} \right|^2 \\ & + \left[E_j^2 + V_{Re}^2 + V_{Rn}^2 \left(\frac{R_t \parallel R_{nt}}{R_n + R_t \parallel R_{nt}} \right)^2 \right. \\ & \left. + V_{nt}^2 \left(\frac{R_t \parallel R_n}{R_{nt} + R_t \parallel R_n} \right)^2 + V_{Rt}^2 \left(\frac{R_{nt} \parallel R_n}{R_t + R_{nt} \parallel R_n} \right)^2 \right] \\ & \times \left| \frac{Z_{in} \parallel Z_{Cg} \parallel Z_p}{R_e + Z_{in} \parallel Z_{Cg} \parallel Z_p} \right|^2. \end{aligned} \quad (8)$$

To simplify the above equation in order to obtain a high SNR, several considerations are necessary to prepare the micropipettes and to design the neural amplifier. First, the amplifier should be well-designed to avoid any environmental interference, such that $Z_p \gg Z_{in}$. Second, the glass micropipette should be made out of good quality glass such that the distributed capacitance C_g is small enough to make Z_{Cg} much larger than Z_{in} . Third, the half-cell potential and the liquid junction potential (E_j) should be rejected by using a high-pass filter after the analog front-end. It is reported that the liquid junction potential has a voltage of several millivolts to several hundred millivolts, depending on the concentration and chemical composition of the electrolytes [56, 65]. If these DC voltage offsets are not rejected, the amplifier gain may be saturated resulting in difficulty measuring the neural voltages. Finally, a fine-tip glass micropipette should be used and placed close to the target neuron. Equation (8) then reduces to

$$V_{\text{total}}^2 \approx V_A^2 + V_{Re}^2 \left| \frac{Z_{in}}{R_e + Z_{in}} \right|^2. \quad (9)$$

From (4), the neural voltage of the target neuron $V_{n,in}$ presented at the analog front-end is approximately

$$V_{n,in} \approx V_n \frac{Z_{in}}{R_e + Z_{in}}. \quad (10)$$

Thus, the overall input referred SNR in the bandwidth of $(f_1 - f_2)$ can be estimated by

SNR

$$= \frac{|V_n|}{\sqrt{\left(1/|Z_{in}/(R_e + Z_{in})|^2 \right) \int_{f_2}^{f_1} |V_A|^2 df + |V_{Re}|^2 (f_1 - f_2)}}. \quad (11)$$

Equation (11) indicates that the overall input referred noise is mainly contributed by the intrinsic noise of the amplifier and the thermal noise arising from the distributed resistance of the electrolyte contained in the glass micropipette. Therefore, it is important to carefully design the amplifier to achieve low intrinsic noise, as well as adjusting the electrolyte concentration to reduce the overall noise for recording.

2.2. Overall Gain and Input Impedance Equations. A typical extracellular action potential is on the order of 50–500 μVpp with a frequency bandwidth of 100 Hz to 5 kHz [8]. To record such a small voltage, a low-noise high-quality analog amplifier is required. As mentioned in the previous section, the amplifier should have relatively low intrinsic noise compared to the extracellular neural voltages. Meanwhile, a high-pass filter should be introduced to reject the DC offset induced by the liquid junction at the micropipette tip and the half-cell potential at the metal-electrolyte interface. In addition, according to (11), the input impedance of the analog front-end should be designed to be as large as possible so that the overall SNR can be improved.

Figure 2(a) shows the circuit diagram of our neural amplifier used in the measurements reported in this paper. The amplifier is designed to record extracellular neural activities of conscious rodents based on the analysis discussed in the previous section. Our neural amplifier implementation is a two-stage design to achieve a unity gain ($A_1 = 1$) for the first stage and a gain of 200 ($A_2 = 200$) for the second stage. The overall voltage gain (A_0) of our amplifier can be mathematically expressed as

$$\begin{aligned} A_0(f) = & A_1(f) \cdot A_2(f) \\ = & \left[\frac{R_1 \parallel Z_{in,A}}{R_1 \parallel Z_{in,A} + (1/j2\pi f C_1)} \right] \\ & \cdot \left[\frac{R_2 \parallel Z_{in,A}}{R_2 \parallel Z_{in,A} + (1/j2\pi f C_2)} \times \left(1 + \frac{R_6}{R_5} \right) \right], \end{aligned} \quad (12)$$

where $Z_{in,A}$ is the input impedance of operational amplifiers used in the circuit (same operational amplifier used for both stages) and f is the working frequency. In addition, according to Figure 2(a), the input impedance of the neural amplifier is

$$Z_{in} \approx \frac{1}{j2\pi f C_1} + R_1 \parallel Z_{in,A}. \quad (13)$$

With the electronic components used for the amplifier, (12) and (13) can further be simplified. Two low-noise CMOS

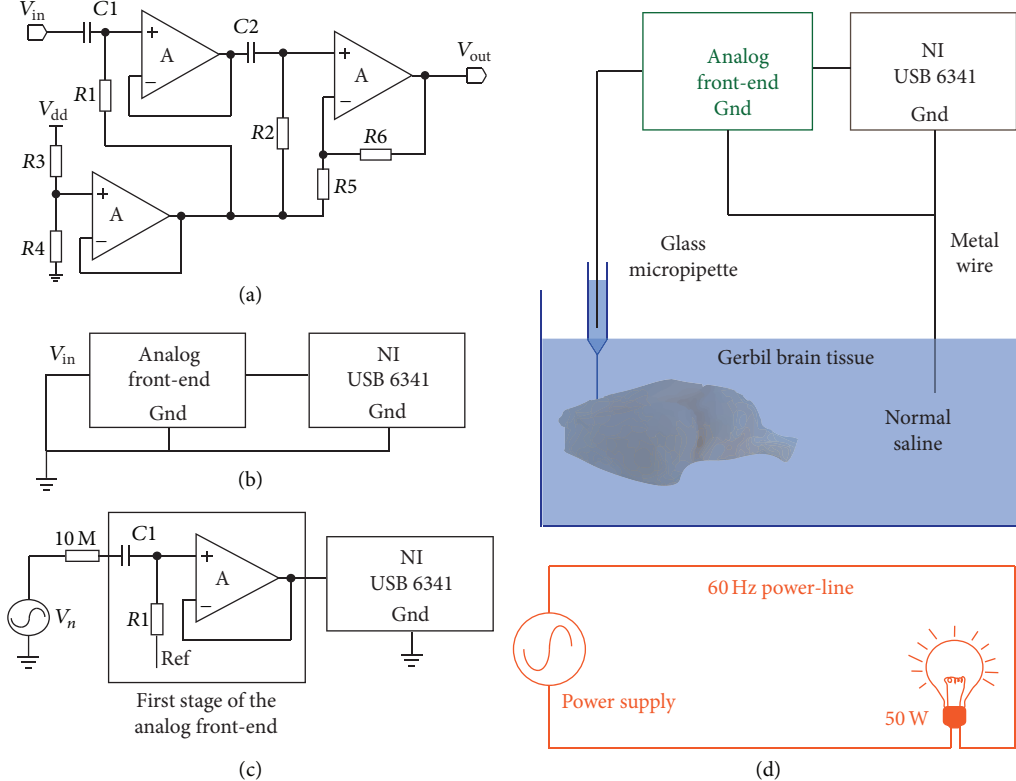


FIGURE 2: (a) Circuit diagram of the micropipette neural amplifier designed for *in vivo* single-cell extracellular neural recordings of conscious rodents using a sharp-tipped glass micropipette. ($C_1 = 1.5 \text{ nF}$, $C_2 = 0.1 \mu\text{F}$, $R_1 = 1 \text{ G}\Omega$, $R_2 = 20 \text{ K}\Omega$, $R_3 = 27 \text{ K}\Omega$, $R_4 = 10 \text{ K}\Omega$, $R_5 = 1 \text{ K}\Omega$, and $R_6 = 200 \text{ K}\Omega$) (b) Schematic diagram illustrating the experimental setup used to measure the intrinsic input-referred noise of the neural amplifier. (c) Schematic diagram of measuring the input capacitance of the neural amplifier. (d) Experimental setup to characterize the overall noise of the neural amplifier with the glass micropipette (light off) and the environmental noise (light on) generated by a 60 Hz power-line attached to a light bulb using dead gerbil brain tissue submerged in normal saline.

amplifiers (LMP7702, Texas Instruments, Dallas, Texas, USA) [66–71] were used to build both the first and second stages of the neural amplifier. This particular operational amplifier has excellent low-noise characteristics. Its input referred noise reduces from its highest point of $120 \text{ nV}/\sqrt{\text{Hz}}$ at 1 Hz to $9 \text{ nV}/\sqrt{\text{Hz}}$ at 1 KHz and maintains this low noise level for frequencies above 1 KHz. The LMP7702 also has small input capacitance $C_{\text{in}} \approx 25 \text{ pF}$, which is two orders of magnitude smaller than $C_1 = 1.5 \text{ nF}$. Thus, $A_1 \approx 1$ and the imaginary part of $Z_{\text{in},A}$ becomes the dominant term in (13). Therefore, for the frequency range (100 Hz to 5 kHz) of interest in extracellular neural recording, (12) and (13) are simplified to

$$A_0(f) \approx 1 \cdot \left[\frac{R_2}{R_2 + (1/j2\pi f C_2)} \left(1 + \frac{R_6}{R_5} \right) \right], \quad (14)$$

$$Z_{\text{in}} \approx \frac{1}{j2\pi f C_{\text{in}}}. \quad (15)$$

There are several points worth mentioning in the design. The RC high-pass filter (C_1 and R_1) is used to reject the DC offset induced by the liquid junction potential and half-cell potential in the glass micropipette with a 3-db cut-off frequency at 0.1 Hz. Another RC high-pass filter (C_2 and R_2) sandwiched between the first unity-gain stage and the second gain stage is

designed to reject other low frequency interference from the environment with a 3-db cut-off frequency at 80 Hz. A 1 V offset was added as a reference to the amplifier output voltage in order to capture both the positive and negative sides of the extracellular action potentials.

2.3. Intrinsic Noise and Input Capacitance Measurements. To measure the intrinsic noise of our neural amplifier, the input of the amplifier is directly shorted to the input ground as depicted by Figure 2(b). A data acquisition system (NI USB-6341, National Instruments, Austin, Texas, USA) was used to record the output voltage at a sampling rate of 50 kS/s. A Fourier transform is performed on the measured output voltage and subjects the voltage spectrum to a 100 to 5000 Hz digital filter to reject unwanted noise outside the signal bandwidth. The data processing and analysis were performed using Origin (OriginLab, Northampton, USA) data processing software. The intrinsic amplifier noise was also simulated by Multisim software (Austin, Texas, USA).

In addition, the input impedance of the amplifier is also measured because it greatly influences the SNR as described by (11) and (15). According to (15), the input impedance of the amplifier can be approximated by C_{in} within the frequency range of measurements. The input capacitance of

the amplifier consists of the intrinsic input capacitance of the operational amplifier and the parasitic capacitance of the printed circuit board. In order to measure the total input capacitance of the amplifier, the frequency response of the amplifier is measured as depicted by Figure 2(c). A high quality D/A converter (RP 2.1, Tucker-Davis Technology, Alachua, USA) was used to generate a sinusoidal voltage with a 1V peak-to-peak amplitude for frequencies from 1Hz to 2000 Hz. The sinusoidal voltage was connected in series to a $10\text{ M}\Omega$ resistor and the input stage of the neural amplifier. Since the first-stage operational amplifier has a unit gain with a 2.5 MHz bandwidth, the 3 dB cutoff in the frequency spectrum is solely due to the RC low-pass filter formed by the $10\text{ M}\Omega$ resistor and the overall input capacitance. Therefore, the overall input capacitance can be calculated using the time constant relationship for this measured 3-dB bandwidth (f_c):

$$C_{in} = \frac{1}{2\pi (10\text{ M}\Omega) f_c}. \quad (16)$$

2.4. Micropipette and Environmental Noise Estimation Using Dead Brain Tissue. To estimate the noise of the amplifier together with the micropipette electrode and the influence of environmental (power-line) interference, dead brain tissue was used for easy accessibility. The setup for measuring the noise of these conditions is shown in Figure 2(d). A 70-day-old wild type Mongolian gerbil (*Meriones unguiculatus*) was sacrificed. All experimental procedures involving animals were approved by the University of Colorado's institutional animal care and use committee (IACUC, protocol number B-88412(05)1C). Once deep anesthesia was confirmed, the gerbil's head was removed and put into 0.9% normal saline, and the brain was excised. Subsequently, the brain was washed in 0.9% normal saline to remove the blood from the surface, put into a 25 mL glass beaker filled with saline, and maintained at 37 degrees Celsius. A single barrel glass micropipette (GC150F-10 borosilicate glass, Harvard Apparatus, Edenbridge, United Kingdom) was pulled to a $1\text{-}2\mu\text{m}$ tip diameter using a DMZ-Universal puller (Zeitz Instruments, Martinsried, Germany). The glass pipette was filled with 27% saturated sodium chloride solution using a carbon fiber needle (Microfil MF 28G67-5, World Precision Instrument, Sarasota, USA) such that the complete electrode had a total impedance of $5\text{ M}\Omega$ to $15\text{ M}\Omega$. Subsequently, the filled micropipette was inspected with a microscope to make sure the tip was not broken, and no air bubbles were left in the tip of the micropipette. Then the pipette was positioned in an electrode holder attached to a piezo-electric drive (Inchworm controller 8200, EXFO Burleigh Products, Victor, NY), and a silver-silver chloride wire was inserted into the solution in the pipette. The input of the neural amplifier was connected to the other end of the wire. Meanwhile, a copper wire having a 1 mm diameter was immersed into normal saline as a ground for the neural amplifier. Then the pipette was slowly advanced into the brain tissue and the output of the neural amplifier both in an electrically quiet (light off) and an electrically noisy environment (light on) was measured. The electrical noise was introduced through a 50 W halogen light bulb placed 10 cm away from the brain. The output voltage of

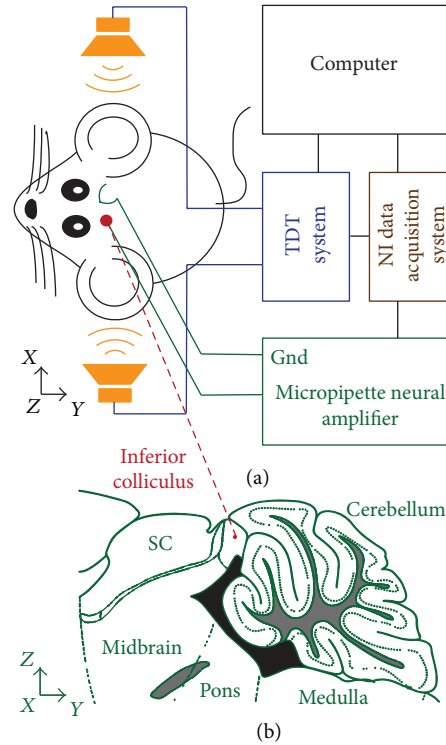


FIGURE 3: (a) Experimental setup of measuring neural voltage responses in the inferior colliculus (IC) induced by auditory stimulation in the ears of an anesthetized gerbil. The auditory stimulation is triggered by a high-quality signal generator. A sharp-tipped micropipette is inserted into the brain of the gerbil held by a piezo drive to reach to the IC for recording. The neural voltage is amplified by the micropipette neural amplifier. The output voltage of the amplifier is subsequently digitized by an analog-to-digital converter and recorded by the computer for further analysis. (b) Illustrated diagram of a gerbil's brain showing the relative position of the IC.

the micropipette neural amplifier was recorded by the NI USB-6341 data acquisition system for further data analysis.

2.5. In Vivo Recordings from the Brain of an Anesthetized Rodent. In this section, animal testing was applied to test the efficacy of the micropipette neural amplifier in *in vivo* neural recording as depicted by Figure 3. All experimental procedures using animals were approved under University of Colorado IACUC protocol number B-88412(05)1C. During these experiments, a glass micropipette was advanced into an auditory area, the inferior colliculus (IC) of a Mongolian gerbil. We recorded action potentials from neurons in the IC in response to sound stimulation of the animal's ears.

2.5.1. Animal Preparation (See [72]). Before surgery, a 68-day-old gerbil was anesthetized by initial intraperitoneal injection (0.5 mL/100 g body weight) of a mixture of Ketamine (20%) and Xylazine (2%), both diluted in physiological saline. During surgery and the recording session, a supplemental dose of 0.25 mL/100 g body weight of the same mixture was administered subcutaneously every 30 minutes.

Constant body temperature was maintained using a thermostatically controlled heating pad.

Skin and tissue overlying the top part of the skull were removed and a small silver hook was attached to the subcutaneous tissue near the head as the ground of the amplifier. Custom-made earphone holders were attached to the head, allowing for the safe insertion of earphones into the ear canal. The animal was then transferred to a sound-attenuated chamber and mounted in a custom made stereotaxic instrument. The animal's position in the stereotaxic apparatus was standardized with reference to stereotaxic landmarks on the skull. For electrode penetrations of the IC, a small hole of approximately 1 mm^2 was cut into the skull lateral to the lambdoid suture. Micromanipulators were used to position the recording electrode according to the landmarks on the skull surface and a reference point. The meninges overlaying the cortex were removed and normal saline was applied to the opening to prevent dehydration of the brain. After successful recordings were taken, the animal was sacrificed by injection of an overdose of ketamine and xylazine.

2.5.2. Setup for Neural Recording Triggered by Sound Stimulation of Inferior Colliculus Neurons. When the animal was positioned in the stereotaxic instrument, a single barrel glass micropipette as described above was positioned above the opening in the skull and advanced perpendicular to the skull surface using a piezo drive which could be remotely controlled from outside the sound-attenuated chamber. A real-time processor with a high-quality analog I/O (RP 2.1, Tucker-Davis Technology, Alachua, FL, USA) was used to generate modulated sinusoidal wave signals to drive the two headphones. The modulation of the sinusoidal wave was programmed with a RPvdsEx program (Tucker-Davis Technology, Alachua, FL, USA), which was used to control the real-time processor. The sinusoidal wave was modulated to have a 20 ms rise time, a 20 ms fall time, and a 50 ms/550 ms ON/OFF period. Two programmable attenuators (PA 5, TDT) were used to attenuate the sinusoidal wave before it was applied to two speaker drivers (ED1, TDT) to drive the headphones. The micropipette neural amplifier was applied to amplify the neural action potential signals. The NI USB-6341 data acquisition system was used to record the output signal of the micropipette neural amplifier.

3. Results

3.1. Characterization of the Neural Amplifier

3.1.1. Intrinsic Noise of the Neural Amplifier. Here we report the measurement results obtained by using the techniques described in the method section. Figure 4(a) shows the time trace of the measured input referred noise of the micropipette neural amplifier for a time period of 200 ms. The measured noise voltage is $11.95\text{ }\mu\text{Vpp}$ in peak-to-peak voltage or $1.81\text{ }\mu\text{V}_{\text{rms}}$ in root-mean-square voltage [73–75]. Figure 4(b) shows the corresponding simulated (red) and measured noise densities of the intrinsic amplifier. Within the frequency range of interest for neural recording (100 to 5000 Hz), the amplifier noise is simulated to be $9.50\text{ }\mu\text{Vpp}$ or $1.44\text{ }\mu\text{V}_{\text{rms}}$

using Multisim. The measured noise density is higher than the simulated results and we attributed this discrepancy to imperfections and manufacturing deviations when making the printed circuit board and electronic components. Based on our circuit simulation, the amplifier suffers from flicker noise which linearly decays from 100 Hz to 500 Hz. At 100 Hz, the noise density is highest of $32\text{ nV}/\sqrt{\text{Hz}}$ with our simulated result. The noise density reduces to $20\text{ nV}/\sqrt{\text{Hz}}$ above 500 Hz where thermal noise dominates.

3.1.2. Input Capacitance Measurement and SNR Estimation. The input capacitance of the micropipette neural amplifier is measured in accordance with the methodologies described in the previous section. As shown in (11), the input capacitance of the amplifier is very important in determining the signal-to-noise ratio of the amplifier. The frequency response of the amplifier is measured (data not shown) and the 3-dB cut-off frequency of the amplifier was determined to be 751 Hz. Thus, the input capacitance is estimated to be $C_{\text{in}} = 21.23\text{ pF}$ using (16). The measured input impedance conforms to our analysis stated in (13) and is dominated by the input capacitance of the CMOS amplifier LMP7702 (25 pF as stated in the datasheet). Thus, if a glass micropipette with $5\text{ M}\Omega$ impedance is used, the SNR of a $500\text{ }\mu\text{Vpp}$ 1 KHz sinusoidal signal is calculated to be 8.74 according to (11).

3.2. Noise Characterization of the Neural Amplifier with Micropipette Using Dead Brain Tissue

3.2.1. Noise of the Amplifier with Glass Micropipette. Noise measurement to characterize the performance of the amplifier can be performed using dead brain tissue extracted from a gerbil. In order to measure the background noise generated by the amplifier and the glass micropipette, we insert the micropipette directly into the dead brain tissue submerged in a saline solution to maintain tissue freshness. Figure 4(c) shows the measured input referred noise of the micropipette amplifier over a course of 200 ms. Figure 4(d) shows the corresponding noise densities for the simulated (red) and measured results. To avoid any environmental interference impairing our result, the brain tissue and the amplifier were enclosed by a Faraday cage. The input referred noise was measured at $78.54\text{ }\mu\text{Vpp}$, or $11.9\text{ }\mu\text{V}_{\text{rms}}$. For the glass micropipette with a $5\text{ M}\Omega$ impedance, the 3-db cut-off frequency is ~ 1.5 KHz. Thus, the thermal noise generated by the glass micropipette is calculated to be $73.59\text{ }\mu\text{Vpp}$ or $11.15\text{ }\mu\text{V}_{\text{rms}}$ and the overall input referred noise is $74.18\text{ }\mu\text{Vpp}$ or $11.24\text{ }\mu\text{V}_{\text{rms}}$ using (9), which is in agreement with the measurements.

3.2.2. Environmental (Power-Line) Noise. Environmental (power-line) noise can also be estimated using dead brain tissue. Figure 4(e) shows the noise acquired when a power line placed near our measurement setup powering a 50 W halogen light-bulb. Power-line noise overwhelms the intrinsic noise of the amplifier and the micropipette, and the overall input referred noise was measured to be $\sim 1.75\text{ mVpp}$. Compared to a typical neural spike of $50\text{ }\mu\text{Vpp}$ to $500\text{ }\mu\text{Vpp}$,

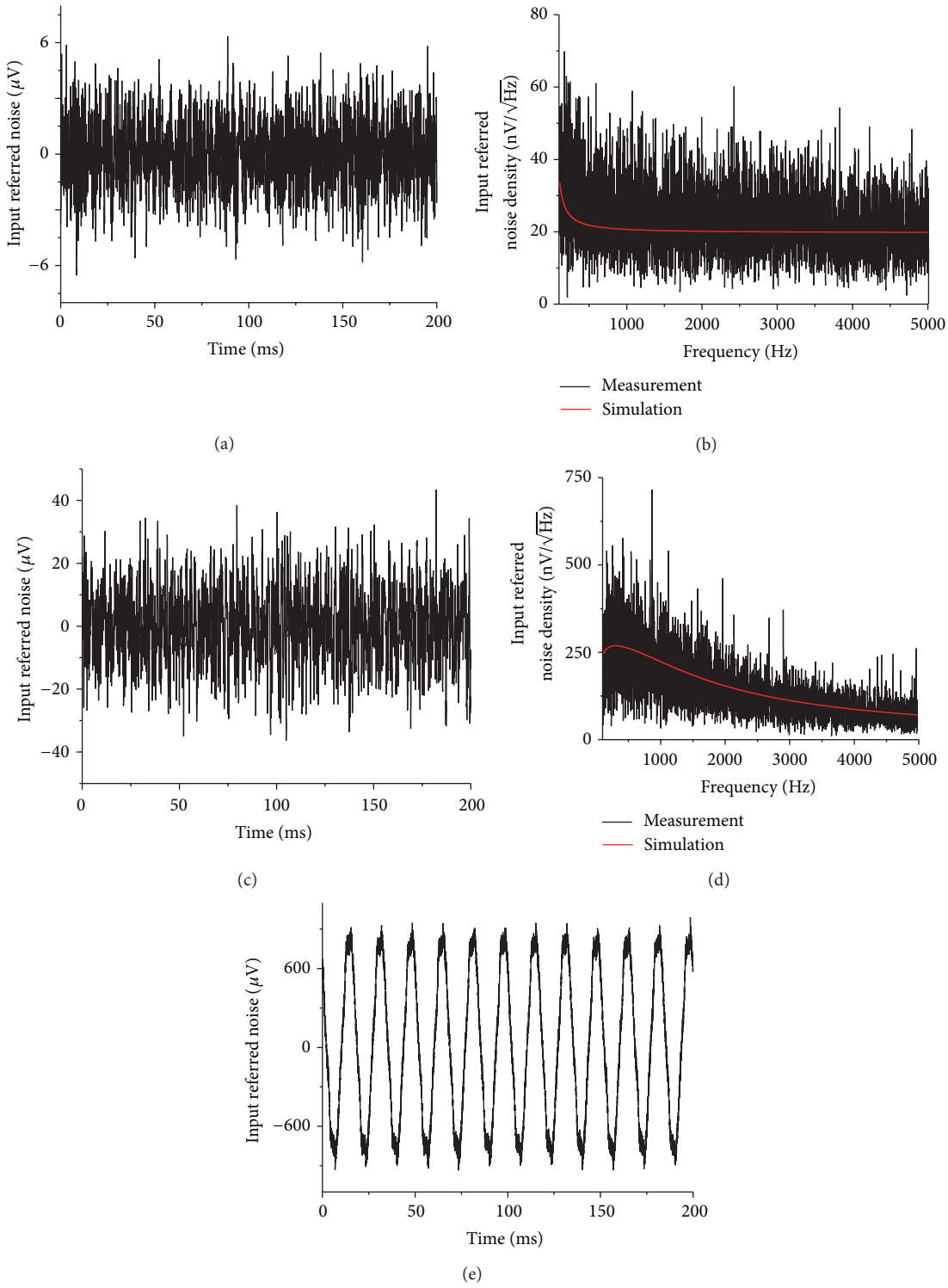


FIGURE 4: (a) The measured intrinsic input referred noise of the neural amplifier. (b) Circuit simulation and measurement results of the intrinsic input referred spectral noise density of the neural amplifier calculated from the data in (a). (c) Input referred noise of the neural amplifier with the glass micropipette electrode measured in dead gerbil brain tissue with an electrical quiet environment (light off) (d) Circuit simulation and measurement results of the input referred spectral noise density calculated from the data measured in (c). (e) Input referred noise measured in dead gerbil brain tissue in an electrical noisy environment (light on).

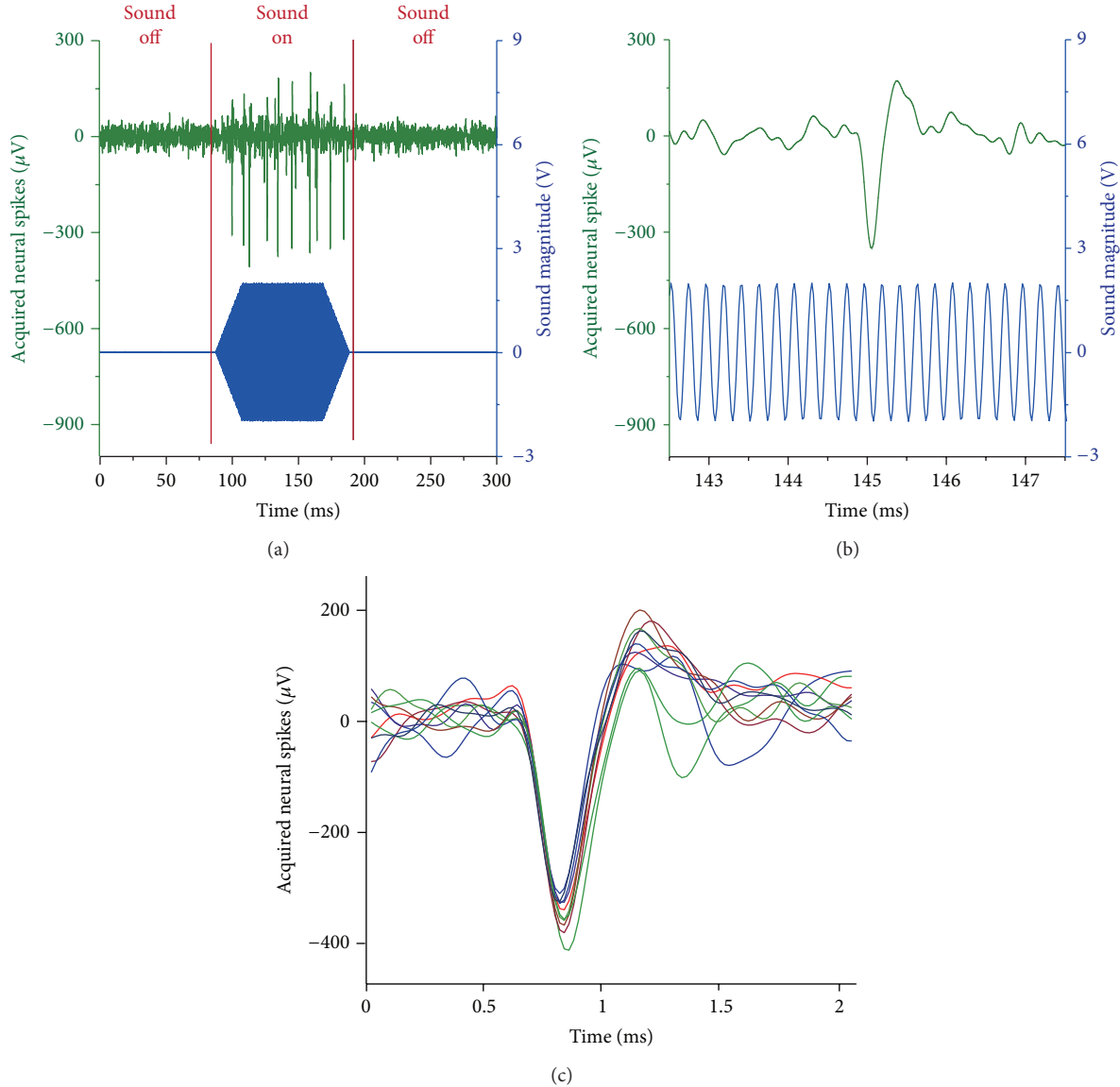


FIGURE 5: (a) Extracellular neural voltage spiking (green) acquired by the micropipette neural amplifier in the inferior colliculus (IC) of an anesthetized gerbil. The ears of the gerbil are attached to audio speakers and sound frequency sweeps are periodically played to the anesthetized gerbil. The recorded neural voltage spiking was recorded simultaneously with the sound frequency sweeps during the experiment. The magnitude of the sound sweep (blue) is plotted together with the neural voltage spiking (green) in the same graph to show that the neural spiking is only observed with the auditory stimulated. (b) The neural voltage (green) and the sound magnitude (green) of (a) are magnified in time for a period of 5 ms to show better details of both signals. (c) Individual neural voltages of (a) are plotted on top of one another. All individual neural signals have a similar temporal shape which indicates that the signals all originated from a single neuron.

the power-line noise is extremely strong. For this reason, a Faraday cage and other environmental noise elimination strategies are necessary for *in vivo* extracellular neural recording of conscious animals.

3.3. In Vivo Measurements of Neural Responses to Sound Stimulation from an Anesthetized Gerbil. The IC is an auditory neural target and neural voltages are generated when triggered by sound. Figure 5(a) shows neural spiking recorded by the micropipette neural amplifier when the anesthetized gerbil was triggered externally by a sound sweep. Figure 5(b)

shows the magnified neural spike and the corresponding sound magnitude over a 5 ms time period for better resolution of the signals.

The occurrence of the neural spikes strongly correlates with the sound excitation and the neural spikes only appeared when external sound sweep was active. The neural signal likely originated from a single neuron in the IC, since it disappeared when the micropipette was retracted by several μ m. The signal was restored when the micropipette was moved back to its original location. Figure 5(c) overlays the neural spikes of Figure 5(b) on top of each other to demonstrate

TABLE 1: Comparison of noise levels of theoretical predictions and experimentally measured results. Values in parenthesis indicate the percentage increase in the experimental results over the simulated results.

	Theoretical predication (μV_{rms})	Measurements in a dead gerbil brain (μV_{rms})	<i>In vivo</i> measurements with an anesthetized gerbil (μV_{rms})
Intrinsic amplifier noise (V_A)	1.44	1.81 (26%)	1.81 (26%)
Micropipette thermal noise (V_{Re})	11.15	—	—
Overall noise (V_{total})	11.24	11.90 (6%)	15.15 (35%)

that all the measured action potentials have similar temporal shapes, indicating that all the measured neural responses are indeed originating from a single neuron [76]. These results demonstrate the efficacy of the micropipette amplifier for recording extracellular neural signals originating from a single neuron for *in vivo* experiments. The average voltage of the background noise was measured at around $100 \mu\text{V}_{\text{pp}}$ or $15.15 \mu\text{V}_{\text{rms}}$ (averaged over the first 50 ms of the measurement when no sound was played). This background level is close to the measured noise level with dead gerbil brain ($78.54 \mu\text{V}_{\text{pp}}$, or $11.9 \mu\text{V}_{\text{rms}}$). The neural spikes have an average maximum voltage of $\sim 500 \mu\text{V}_{\text{pp}}$. Thus, the SNR of the micropipette neural amplifier is estimated to be larger than 5.

We tabulated the noise performance of the micropipette amplifier in Table 1. The simulated results of the intrinsic amplifier noise (V_A), the micropipette thermal noise (V_{Re}), and the overall amplifier noise (V_{total}) were compared to the empirical results of the intrinsic amplifier noise (V_A) and the overall noise (V_{total}) measured in a dead gerbil brain and in the brain of an anesthetized gerbil. (The micropipette thermal noise cannot be directly measured empirically since other noise sources, such as environmental noise, cannot be completely excluded in the laboratory.) The comparison shows that the noise characteristics of our micropipette amplifiers are closely matched to the theoretical predictions. The measured overall noise (V_{total}) only differs from the theoretical prediction by 6% and 35% when measured in a dead gerbil brain and in an anesthetized gerbil.

4. Discussion

In this paper, we have developed an equivalent circuit and a noise analysis model for extracellular neural recordings using a low-noise amplifier with a glass micropipette. The models were developed to help understand and to quantify the various noise sources contributing to the overall noise of the recording. Experimental measurements were also proposed to verify the accuracy of our models. In addition, we have designed and constructed a low-noise two-stage amplifier based on the mathematical models. The intrinsic noise of the amplifier and environmental (power-line) interference were measured using a dead gerbil brain. In addition, we also performed *in vivo* neural recordings from the brain of an anesthetized gerbil to confirm that the amplifier has adequate SNR for extracellular *in vivo* neural recordings. The recorded neural spiking at the IC, which is an auditory nucleus in the brain, correlates with the sound stimulation in the animal's ear.

The main finding of our study is that two chief noise sources degrade the neural voltage signal in the recordings, namely, the intrinsic noise (V_A^2) of the amplifier and the thermal noise of the glass pipette ($4kTR_e$), as shown in (11). Since intrinsic noise is one of the major noise contributors, it is important for circuit designers to develop noise-reduction strategies in the design of amplifiers with low noise characteristics. Many research groups have been working vigorously on improving amplifier designs, and the input referred noise of most neural amplifiers described in literature is already better than $5 \mu\text{V}_{\text{rms}}$ [8–18, 77]. Some designs achieve an overall noise as low as $1\text{--}2 \mu\text{V}_{\text{rms}}$ [8, 11, 77]. Besides intrinsic amplifier noise, our noise analysis also indicates that the thermal noise generated by the electrolyte inside the micropipette is another significant noise contributor to the overall measurement noise. Millar and Barnett [13] reported a noise figure of $13 \mu\text{V}_{\text{rms}}$ over a bandwidth of 100 Hz to 8 kHz for a $1 \text{ M}\Omega$ glass micropipette. Budai [8] also reports a $5.6 \mu\text{V}_{\text{rms}}$ thermal noise with a bandwidth of 5 kHz for $0.4 \text{ M}\Omega$ electrode. Therefore, it is important to develop strategies in future designs to lower the resistance of the glass pipette to further reduce thermal noise.

In this paper, we used excised gerbil brain tissue to characterize environmental interference with neural recordings. Our measurements conclude that interference from power lines is significant and can easily exceed neural signals from extracellular recordings. Therefore, it is necessary to enclose the entire neural recording setup with a Faraday cage as a shield from these noise sources. Faraday cages, however, are bulky and also add another layer of difficulty to neuroscience experiments, in particular for *in vivo* neural recordings from conscious behaving animals where the experimental setup requires a large area. Therefore, it is imperative to develop noise-cancelation strategies on the amplifier circuit itself to eliminate the need for Faraday cages for noise shielding.

We have also successfully recorded neural responses triggered by external auditory stimulation. Our recorded spike trains from neurons in the IC are in step with the delivery of the sound frequency sweep. In modern neuroscience research, the ability to measure neural signals from a single cell and to correlate the recordings with behavioral responses, such as sound sweeps, is important in the study of brain functionality, such as studies of sensory processing, memory and decision making, as well as understanding the pathophysiology of neural disorders, such as Parkinson's diseases. Therefore, engineering designs that allow an investigator to advance the electrode accurately into a specific brain nucleus

and the ability to control neural activity *in vivo* in conscious animals are critical for many future neuroscience studies.

Another important development is the use of optogenetic proteins to excite or inhibit action potentials using optical stimulation in the brain [78]. Optogenetics is a new frontier in neuroscience research and uses light-gated ion-channels that allow stimulation and inhibition of a specific cell-type of a brain nucleus using biochemical techniques and optical methods [79, 80]. Optical stimulation can be delivered to a brain nucleus via optical fibers or implanted LEDs. It is therefore imperative to develop electrical systems that allows simultaneously stimulating and/or inhibiting neural responses and records neural voltages at the same or another remote neural target in the brain. Some optogenetic applications, however, require the use of high-current LED drivers which can generate a strong electrical interference to the sensitive recording amplifiers. Optical interference from these high-power optical sources to the recording amplifier has been reported [80]. Therefore, we plan to include the strong electrical interference generated by these high-current LED drivers in our noise models to guide our future designs of electronic systems for neural manipulation.

5. Conclusion

In this paper, we proposed a comprehensive mathematical model to predict the overall noise of a neural amplifier using a glass micropipette as the recording electrode in extracellular neural recording. Our model shows that both thermal noise generated inside the glass micropipette and the intrinsic amplifier noise are major contributors to the overall noise of the amplifier. We compared the results calculated from our proposed noise model to experimental measurements obtained from a dead gerbil brain, as well as *in vivo* measurements from an anesthetized gerbil. We experimentally measured noise spectral densities and the measurements were well matched to our theoretical predictions, validating the accuracy of our proposed model. Moreover, neural response originating from a single neuron measured in the IC was observed to be temporally correlated with auditory stimulation with a conscious gerbil.

Conflict of Interests

The authors declare that there is no conflict of interests regarding the publishing of this paper.

Acknowledgments

This work was supported by The Science and Technology Development Fund of Macau (FDCT) under Grants 024/2009/A1, 087/2012/A3, and 047/2013/A2; The Research Committee of the University of Macau under Grants RG072/09-10S/MPU/FST, MYRG076(Y1-L2)-FST12-MPU, MYRG2014-00010-AMSV, MYRG079(Y1-L2)-FST12-VMI, MYRG103(Y1-L3)-FST13-VMI, and MRG014/MPU/2014/FST; the National Institutes of Health (NIH) NIDDK grant 1K25DK095232-01A1; and NIH/NIDCD Grant R01 DC011582. The authors would like to thank Dr. Anna Dondzillo and Dr. Otto

Albrecht for providing technical guidance for the *in vivo* neural measurements from anesthetized rodents and Mr. Gregory Glazner for proofreading the paper. Dr. Peng Un Mak also thanks the Department of Physiology and Biophysics during his stay at the University of Colorado in 2013.

References

- [1] A. Hodgkin and A. Huxley, "Resting and action potentials in single nerve fibres," *The Journal of Physiology*, vol. 104, pp. 176–195, 1945.
- [2] L. A. Geddes, *Electrodes and the Measurement of Bioelectric Events*, Wiley-Interscience, 1972.
- [3] R. F. Thompson, *Methods in Physiological Psychology: Bioelectric Recording Techniques*, vol. 1 of *Cellular Processes and Brain Potentials*, Academic Press, 1973.
- [4] D. J. Simons and P. W. Land, "A reliable technique for marking the location of extracellular recording sites using glass micropipettes," *Neuroscience Letters*, vol. 81, no. 1-2, pp. 100–104, 1987.
- [5] R. H. Browner and D. B. Webster, "Projections of the trapezoid body and the superior olfactory complex of the kangaroo rat (*Dipodomys merriami*)," *Brain, Behavior and Evolution*, vol. 11, no. 5–6, pp. 322–354, 1975.
- [6] D. Caird and R. Klinke, "Processing of binaural stimuli by cat superior olfactory complex neurons," *Experimental Brain Research*, vol. 52, no. 3, pp. 385–399, 1983.
- [7] B. Renshaw, A. Forbes, and B. Morison, "Activity of isocortex and hippocampus: electrical studies with micro-electrodes," *Journal of Neurophysiology*, vol. 3, pp. 74–105, 1940.
- [8] D. Budai, "Ultralow-noise headstage and main amplifiers for extracellular spike recording," *Acta Biologica Szegediensis*, vol. 48, no. 1–4, pp. 13–17, 2004.
- [9] M. S. Chae, Z. Yang, M. R. Yuce, L. Hoang, and W. Liu, "A 128-channel 6 mW wireless neural recording IC with spike feature extraction and UWB transmitter," *IEEE Transactions on Neural Systems and Rehabilitation Engineering*, vol. 17, no. 4, pp. 312–321, 2009.
- [10] D. Fan, D. Rich, T. Holtzman et al., "A wireless multi-channel recording system for freely behaving mice and rats," *PLoS ONE*, vol. 6, no. 7, Article ID e22033, 2011.
- [11] R. R. Harrison and C. Charles, "A low-power low-noise CMOS amplifier for neural recording applications," *IEEE Journal of Solid-State Circuits*, vol. 38, no. 6, pp. 958–965, 2003.
- [12] R. R. Harrison, P. T. Watkins, R. J. Kier et al., "A low-power integrated circuit for a wireless 100-electrode neural recording system," *IEEE Journal of Solid-State Circuits*, vol. 42, no. 1, pp. 123–133, 2007.
- [13] J. Millar and T. G. Barnett, "A low-noise optically isolated preamplifier for use with extracellular microelectrodes," *Journal of Neuroscience Methods*, vol. 51, no. 2, pp. 119–122, 1994.
- [14] R. Olsson, M. N. Gulari, and K. D. Wise, "A fully-integrated bandpass amplifier for extracellular neural recording," in *Proceedings of the 1st International IEEE EMBS Conference on Neural Engineering*, pp. 165–168, IEEE, March 2003.
- [15] S. Park, D. A. Borton, M. Kang, A. V. Nurmikko, and Y.-K. Song, "An implantable neural sensing microsystem with fiber-optic data transmission and power delivery," *Sensors*, vol. 13, no. 5, pp. 6014–6031, 2013.
- [16] G. E. Perlin and K. D. Wise, "An ultra compact integrated front end for wireless neural recording Microsystems," *Journal*

- of Microelectromechanical Systems*, vol. 19, no. 6, pp. 1409–1421, 2010.
- [17] M. Yin and M. Ghovanloo, “A low-noise preamplifier with adjustable gain and bandwidth for biopotential recording applications,” in *Proceedings of the IEEE International Symposium on Circuits and Systems (ISCAS ’07)*, pp. 321–324, May 2007.
- [18] M. Yin, S. B. Lee, and M. Ghovanloo, “In vivo testing of a low noise 32-channel wireless neural recording system,” in *Proceedings of the Annual International Conference of the IEEE Engineering in Medicine and Biology Society (EMBC ’09)*, pp. 1608–1611, IEEE, 2009.
- [19] Z. Yang, Q. Zhao, E. Keefer, and W. Liu, “Noise characterization, modeling, and reduction for in vivo neural recording,” in *Proceedings of the 23rd Annual Conference on Neural Information Processing Systems (NIPS ’09)*, pp. 2160–2168, December 2009.
- [20] C. M. Lopez, M. Welkenhuysen, S. Musa et al., “Towards a noise prediction model for in vivo neural recording,” in *Proceedings of the Annual International Conference of the IEEE Engineering in Medicine and Biology Society (EMBC ’12)*, pp. 759–762, San Diego, Calif, USA, August-September 2012.
- [21] D. A. Robinson, “The electrical properties of metal microelectrodes,” *Proceedings of the IEEE*, vol. 56, pp. 1065–1071, 1968.
- [22] E. E. Bauer, A. Klug, and G. D. Pollak, “Features of contralaterally evoked inhibition in the inferior colliculus,” *Hearing Research*, vol. 141, no. 1-2, pp. 80–96, 2000.
- [23] A. Dondzillo, J. L. Thornton, D. J. Tollin, and A. Klug, “Manufacturing and using piggy-back multibarrel electrodes for in vivo pharmacological manipulations of neural responses,” *Journal of Visualized Experiments*, vol. 71, Article ID e4358, 2013.
- [24] D. C. Havey and D. M. Caspary, “A simple technique for constructing “piggy-back” multibarrel microelectrodes,” *Electroencephalography and Clinical Neurophysiology*, vol. 48, no. 2, pp. 249–251, 1980.
- [25] D. R. Curtis, “A method for assembly of “parallel” micropipettes,” *Electroencephalography and Clinical Neurophysiology*, vol. 24, no. 6, pp. 587–589, 1968.
- [26] B. Carette, “A new method of manufacturing multi barreled micropipettes with projecting recording barrel,” *Electroencephalography and Clinical Neurophysiology*, vol. 44, no. 2, pp. 248–250, 1978.
- [27] A. J. M. Verberne, N. C. Owens, and G. P. Jackman, “A simple and reliable method for construction of parallel multibarrel microelectrodes,” *Brain Research Bulletin*, vol. 36, no. 1, pp. 107–108, 1995.
- [28] A. P. Oliver, “A simple rapid method for preparing parallel micropipette electrodes,” *Electroencephalography and Clinical Neurophysiology*, vol. 31, no. 3, pp. 284–286, 1971.
- [29] J. P. Oswald, A. Klug, and T. J. Park, “Interaural intensity difference processing in auditory midbrain neurons: effects of a transient early inhibitory input,” *Journal of Neuroscience*, vol. 19, no. 3, pp. 1149–1163, 1999.
- [30] T. J. Park and G. D. Pollak, “GABA shapes a topographic organization of response latency in the mustache bat’s inferior colliculus,” *Journal of Neuroscience*, vol. 13, no. 12, pp. 5172–5187, 1993.
- [31] D. C. Peterson, K. Nataraj, and J. Wenstrup, “Glycinergic inhibition creates a form of auditory spectral integration in nuclei of the lateral lemniscus,” *Journal of Neurophysiology*, vol. 102, no. 2, pp. 1004–1016, 2009.
- [32] J. Wenstrup and S. A. Leroy, “Spectral integration in the inferior colliculus: role of glycinergic inhibition in response facilitation,” *The Journal of Neuroscience*, vol. 21, no. 3, p. RCI24, 2001.
- [33] C. L. Faingold, G. Gehlbach, and D. M. Caspary, “On the role of GABA as an inhibitory neurotransmitter in inferior colliculus neurons: Iontophoretic studies,” *Brain Research*, vol. 500, no. 1-2, pp. 302–312, 1989.
- [34] C. L. Faingold, W. E. Hoffmann, and D. M. Caspary, “Effects of excitant amino acids on acoustic responses of inferior colliculus neurons,” *Hearing Research*, vol. 40, no. 1-2, pp. 127–136, 1989.
- [35] L. M. Hurley and G. D. Pollak, “Serotonin shifts first-spike latencies of inferior colliculus neurons,” *Journal of Neuroscience*, vol. 25, no. 34, pp. 7876–7886, 2005.
- [36] L. M. Hurley and G. D. Pollak, “Serotonin effects on frequency tuning of inferior colliculus neurons,” *Journal of Neurophysiology*, vol. 85, no. 2, pp. 828–842, 2001.
- [37] L. M. Hurley and G. D. Pollak, “Serotonin differentially modulates responses to tones and frequency-modulated sweeps in the inferior colliculus,” *The Journal of Neuroscience*, vol. 19, no. 18, pp. 8071–8082, 1999.
- [38] A. Klug, E. E. Bauer, and G. D. Pollak, “Multiple components of ipsilaterally evoked inhibition in the inferior colliculus,” *Journal of Neurophysiology*, vol. 82, no. 2, pp. 593–610, 1999.
- [39] A. Klug, T. J. Park, and G. D. Pollak, “Glycine and GABA influence binaural processing in the inferior colliculus of the mustache bat,” *Journal of Neurophysiology*, vol. 74, no. 4, pp. 1701–1713, 1995.
- [40] M. J. Moore and D. M. Caspary, “Strychnine blocks binaural inhibition in lateral superior olivary neurons,” *Journal of Neuroscience*, vol. 3, no. 1, pp. 237–242, 1983.
- [41] K. Nataraj and J. J. Wenstrup, “Roles of inhibition in creating complex auditory responses in the inferior colliculus: facilitated combination-sensitive neurons,” *Journal of Neurophysiology*, vol. 93, no. 6, pp. 3294–3312, 2005.
- [42] I. Fukui, R. M. Burger, H. Ohmori, and E. W. Rubel, “GABAergic inhibition sharpens the frequency tuning and enhances phase locking in chicken nucleus magnocellularis neurons,” *The Journal of Neuroscience*, vol. 30, no. 36, pp. 12075–12083, 2010.
- [43] R. M. Burger and G. D. Pollak, “Reversible inactivation of the dorsal nucleus of the lateral lemniscus reveals its role in the processing of multiple sound sources in the inferior colliculus of bats,” *The Journal of Neuroscience*, vol. 21, no. 13, pp. 4830–4843, 2001.
- [44] R. M. Burger and G. D. Pollak, “Analysis of the role of inhibition in shaping responses to sinusoidally amplitude-modulated signals in the inferior colliculus,” *Journal of Neurophysiology*, vol. 80, no. 4, pp. 1686–1701, 1998.
- [45] W. L. Coleman, M. J. Fischl, S. R. Weimann, and R. M. Burger, “GABAergic and glycinergic inhibition modulate monaural auditory response properties in the avian superior olivary nucleus,” *Journal of Neurophysiology*, vol. 105, no. 5, pp. 2405–2420, 2011.
- [46] R. D. Purves, “The mechanics of pulling a glass micropipette,” *Biophysical Journal*, vol. 29, no. 3, pp. 523–529, 1980.
- [47] D. Pinault, “A novel single-cell staining procedure performed in vivo under electrophysiological control: morpho-functional features of juxtagullularly labeled thalamic cells and other central neurons with biocytin or Neurobiotin,” *Journal of Neuroscience Methods*, vol. 65, no. 2, pp. 113–136, 1996.
- [48] A. Arieli and A. Grinvald, “Optical imaging combined with targeted electrical recordings, microstimulation, or tracer injections,” *Journal of Neuroscience Methods*, vol. 116, no. 1, pp. 15–28, 2002.
- [49] R. Sherman-Gold, *The Axon Guide for Electrophysiology & Biophysics: Laboratory Techniques*, Axon Instruments, 1993.

- [50] R. A. Levis and J. L. Rae, "The use of quartz patch pipettes for low noise single channel recording," *Biophysical Journal*, vol. 65, no. 4, pp. 1666–1677, 1993.
- [51] R. J. Baker, *CMOS: Circuit Design, Layout, and Simulation*, Wiley-IEEE Press, 2011.
- [52] J. Davidsen and H. G. Schuster, "Simple model for $1/f\alpha$ noise," *Physical Review E*, vol. 65, no. 2, Article ID 026120, 2002.
- [53] A. Hassibi, R. Navid, R. W. Dutton, and T. H. Lee, "Comprehensive study of noise processes in electrode electrolyte interfaces," *Journal of Applied Physics*, vol. 96, no. 2, pp. 1074–1082, 2004.
- [54] J. B. Johnson, "Thermal agitation of electricity in conductors," *Physical Review*, vol. 32, no. 1, pp. 97–109, 1928.
- [55] J. Martinez, C. Pedreira, M. J. Ison, and R. Quian Quiroga, "Realistic simulation of extracellular recordings," *Journal of Neuroscience Methods*, vol. 184, no. 2, pp. 285–293, 2009.
- [56] E. Neher, "Correction for liquid junction potentials in patch clamp experiments," *Methods in Enzymology*, vol. 207, pp. 123–131, 1992.
- [57] K. Benndorf, *Low-Noise Recording. Single-Channel Recording*, Springer, 1995.
- [58] D. Johnston, S. M.-S. Wu, and R. Gray, *Foundations of Cellular Neurophysiology*, The MIT Press, Cambridge, Mass, USA, 1995.
- [59] M. A. Moffitt and C. C. McIntyre, "Model-based analysis of cortical recording with silicon microelectrodes," *Clinical Neurophysiology*, vol. 116, no. 9, pp. 2240–2250, 2005.
- [60] J. L. Rae and R. A. Levis, "A method for exceptionally low noise single channel recordings," *Pflügers Archiv*, vol. 420, no. 5–6, pp. 618–620, 1992.
- [61] F. Sigworth, "Electronic design of the patch clamp," in *Single-Channel Recording*, pp. 95–127, 2009.
- [62] C. Fall, E. Marland, J. Wagner, and J. Tyson, Eds., *Computational Cell Biology*, Springer, 1st edition, 2002.
- [63] J. Keener and J. Sneyd, *Mathematical Physiology: I: Cellular Physiology*, Springer, 2010.
- [64] A. Manwani, P. N. Steinmetz, and C. Koch, "Channel noise in excitable neuronal membranes," in *Advances in Neural Information Processing Systems 12: Proceedings of the 1999 Conference*, p. 143, MIT Press, 2000.
- [65] B. Sakmann and E. Neher, *Single-Channel Recording*, Plenum Press, New York, NY, USA, 1995.
- [66] Y. M. Chi and G. Cauwenberghs, "Wireless non-contact EEG/ECG electrodes for body sensor networks," in *Proceedings of the International Conference on Body Sensor Networks (BSN '10)*, pp. 297–301, Singapore, June 2010.
- [67] Y. M. Chi, T. P. Jung, and G. Cauwenberghs, "Dry-contact and noncontact biopotential electrodes: methodological review," *IEEE Reviews in Biomedical Engineering*, vol. 3, pp. 106–119, 2010.
- [68] Y. M. Chi, C. Maier, and G. Cauwenberghs, "Ultra-high input impedance, low noise integrated amplifier for noncontact biopotential sensing," *IEEE Journal on Emerging and Selected Topics in Circuits and Systems*, vol. 1, no. 4, pp. 526–535, 2011.
- [69] Y. M. Chi, P. Ng, E. Kang, J. Kang, J. Fang, and G. Cauwenberghs, "Wireless non-contact cardiac and neural monitoring," in *Wireless Health*, pp. 15–23, ACM, New York, NY, USA, 2010.
- [70] Y. M. Chi, Y.-T. Wang, Y. Wang, C. Maier, T.-P. Jung, and G. Cauwenberghs, "Dry and noncontact EEG sensors for mobile brain-computer interfaces," *IEEE Transactions on Neural Systems and Rehabilitation Engineering*, vol. 20, no. 2, pp. 228–235, 2012.
- [71] SNOSAI9H, LMP7701/LMP7702/LMP7704 Precision, CMOS Input, RRIO, Wide Supply Range Amplifiers, 2013, <http://www.ti.com/>.
- [72] J. Hermann, M. Pecka, H. von Gersdorff, B. Grothe, and A. Klug, "Synaptic transmission at the calyx of held under in vivo-like activity levels," *Journal of Neurophysiology*, vol. 98, no. 2, pp. 807–820, 2007.
- [73] K. Blake, "Op amp precision design: random noise," Application Note AN1228, Microchip Technology, 2008.
- [74] M. E. Brinson, S. Jahn, and H. Nabijou, "A tabular source approach to modelling and simulating device and circuit noise in the time domain," *International Journal of Numerical Modelling*, vol. 24, no. 6, pp. 555–567, 2011.
- [75] A. Kay, *Operational Amplifier Noise: Techniques and Tips for Analyzing and Reducing Noise*, Elsevier, 2012.
- [76] I. Siveke, C. Leibold, and B. Grothe, "Spectral composition of concurrent noise affects neuronal sensitivity to interaural time differences of tones in the dorsal nucleus of the lateral lemniscus," *Journal of Neurophysiology*, vol. 98, no. 5, pp. 2705–2715, 2007.
- [77] M. P. B. G. Carlquist, *ISO-80 Instruction Manual*, 2001, <http://www.wpiinc.com>.
- [78] F. Zhang, A. M. Aravanis, A. Adamantidis, L. de Lecea, and K. Deisseroth, "Circuit-breakers: optical technologies for probing neural signals and systems," *Nature Reviews Neuroscience*, vol. 8, pp. 577–581, 2007.
- [79] S. I. Al-Juboori, A. Dondzillo, E. A. Stubblefield, G. Felsen, T. C. Lei, and A. Klug, "Light scattering properties vary across different regions of the adult mouse brain," *PLoS ONE*, vol. 8, no. 7, Article ID e67626, 2013.
- [80] J. A. Cardin, M. Carlén, K. Meletis et al., "Targeted optogenetic stimulation and recording of neurons *in vivo* using cell-type-specific expression of Channelrhodopsin-2," *Nature Protocols*, vol. 5, no. 2, pp. 247–254, 2010.

Research Article

Movement Type Prediction before Its Onset Using Signals from Prefrontal Area: An Electrocorticography Study

Seokyun Ryun,^{1,2} June Sic Kim,^{1,3,4} Sang Hun Lee,^{1,2} Sehyoon Jeong,¹
Sung-Phil Kim,⁵ and Chun Kee Chung^{1,2,3,6}

¹ MEG Center, Department of Neurosurgery, Seoul National University Hospital, Seoul 110-744, Republic of Korea

² Interdisciplinary Program in Neuroscience, Seoul National University College of Natural Sciences, Seoul 151-747, Republic of Korea

³ Department of Neurosurgery, Seoul National University College of Medicine, 103 Daehak-ro, Jongno-gu, Seoul 110-799, Republic of Korea

⁴ Sensory Organ Research Institute, Seoul National University, Seoul 151-742, Republic of Korea

⁵ School of Design and Human Engineering, Ulsan National Institute of Science and Technology, Ulsan 689-798, Republic of Korea

⁶ Department of Brain and Cognitive Sciences, Seoul National University College of Natural Sciences, Seoul 151-747, Republic of Korea

Correspondence should be addressed to June Sic Kim; jskim@meg.re.kr

Received 28 March 2014; Revised 29 May 2014; Accepted 24 June 2014; Published 14 July 2014

Academic Editor: Yiwen Wang

Copyright © 2014 Seokyun Ryun et al. This is an open access article distributed under the Creative Commons Attribution License, which permits unrestricted use, distribution, and reproduction in any medium, provided the original work is properly cited.

Power changes in specific frequency bands are typical brain responses during motor planning or preparation. Many studies have demonstrated that, in addition to the premotor, supplementary motor, and primary sensorimotor areas, the prefrontal area contributes to generating such responses. However, most brain-computer interface (BCI) studies have focused on the primary sensorimotor area and have estimated movements using postonset period brain signals. Our aim was to determine whether the prefrontal area could contribute to the prediction of voluntary movement types before movement onset. In our study, electrocorticography (ECoG) was recorded from six epilepsy patients while performing two self-paced tasks: hand grasping and elbow flexion. The prefrontal area was sufficient to allow classification of different movements through the area's premovement signals (-2.0 s to 0 s) in four subjects. The most pronounced power difference frequency band was the beta band (13–30 Hz). The movement prediction rate during single trial estimation averaged 74% across the six subjects. Our results suggest that premovement signals in the prefrontal area are useful in distinguishing different movement tasks and that the beta band is the most informative for prediction of movement type before movement onset.

1. Introduction

The aim of brain-computer interface (BCI) is to translate brain signals into comprehensible information useful for sending commands to the external world [1]. In particular, BCI technology is important for patients who lack control of their motor faculties; such loss can result from a variety of issues such as spinal cord injuries, amyotrophic lateral sclerosis, and brainstem strokes. A BCI can improve the quality of life for such patients by enabling them to communicate with the outside world by using their brain activities [2].

The term BCI was formulated by Vidal in 1973 [3]. Over the following four decades, numerous studies attempted to improve the accuracy and reaction time performance of BCI

systems [4–6]. Nevertheless, there is still a marked time delay between patient's actions and the BCI's responses. To address this issue, some authors have focused on earlier neural signals during the premovement stage [7–9].

Voluntary movement, which contains movement intention, comes into action through movement selection, planning, and preparation [10]. Two specific brain responses reflect these aspects. First, a slow negative cortical potential occurs 2 s prior to movement onset. This potential is referred to as Bereitschaftspotential (BP) or readiness potential (RP) [11]. Second, power changes in specific frequency bands appear during the same preonset period. These changes are reflected by an amplitude decrease in cortical rhythms that are disclosed in the alpha and beta ranges [12]. Though it

is widely known that the supplementary motor, premotor, and primary sensorimotor areas can be generator sources of those two brain responses, some researchers report that the prefrontal area also contributes to their generation [13–16]. However, most researches regarding the prediction of motor intention or movement type have recorded early neural signals from only the central and parietal areas covering the primary sensorimotor cortex. Those areas are closely related to motor control, but the prefrontal area also contributes to generating BP and power changes in specific frequency bands [7, 8, 17].

Two brain circuits that converge on the primary motor area contribute to human voluntary action [18–20]. One is a pathway from the supplementary motor area, which receives inputs from the basal ganglia and the prefrontal area, to the primary motor area. The other is from the premotor area, which receives inputs from sensory related areas, to the primary motor area. The first circuit, including the prefrontal area, is closely related to self-paced actions as well as the motor planning or preparation. This implies that the prefrontal area may be involved in the prediction of movement types. In practice, the prefrontal area is involved in the intention to move or in the performance of willed action as evinced by several electrophysiological studies utilizing electrocorticography (ECoG), intracerebral electrodes, and neuroimaging studies using functional magnetic resonance imaging (fMRI) [18, 21–23]. On that basis, it is suggested that prefrontal area neural signals occurring during premovement stages should be considered when predicting the type of movement that is going to occur.

In order to investigate whether the prefrontal area generates useful premovement signals, high-spatial resolution and a high signal-to-noise ratio in the cortical activity signal are required because this area is close to the premotor and supplementary motor areas. Electroencephalography- (EEG-) based BCI requires numerous types of postprocessing and multichannel information processing for BCI functioning. A practical alternative, in spite of its invasiveness, is ECoG as it has higher spatial resolution, higher amplitude, greater signal-to-noise ratio, and fewer artifacts than EEG [24, 25]. Moreover, reported in other studies [17], highly accurate movement prediction can be obtained by using only a few electrodes in an ECoG-based BCI. Thus, an ECoG-based BCI approach appears to be a robust way to investigate the contribution of the prefrontal area in movement prediction before its onset time.

In this paper, we focus on the power changes in specific frequency bands to determine whether the prefrontal area generates useful information in movement prediction during the preonset period. Several researchers have indicated that high gamma oscillation in the prefrontal area might be used for predicting movement intention and motor preparation in a BCI system [26–28]. However, few studies have been performed to determine the other properties of prefrontal activity which can be useful in movement prediction. To our knowledge, movement type classification via specific frequency band power changes in the prefrontal signals during the preonset period is sparsely documented.

In this study, by using relatively simple method, we were able to classify two types of single trial ECoG signals that preceded voluntary movements. The signals were recorded from a few electrodes on the motor related and prefrontal areas. Second, we report on our investigation into whether the prefrontal area generates useful premovement signals, and we determined the frequency range that provides the most informative signals for movement prediction. Finally, we evaluate the predictive performance obtained by including prefrontal electrodes.

2. Materials and Methods

2.1. Subjects. Six patients (three females and three males, aged 25–37 years) with intractable epilepsy participated in the study. All patients underwent chronic implantation of subdural electrodes over the prefrontal area (Brodmann areas 8, 9, 10 11, 44, 45, 46, and 47), the premotor and supplementary motor areas (Brodmann area 6), and the primary sensorimotor area (Brodmann areas 1, 2, 3, and 4). The clinical profiles of each subject are presented in Table 1. Each subject underwent magnetic resonance imaging (MRI) and computed tomography (CT) before and after subdural electrode implantations. Experimentation occurred after receiving the subjects' consent forms which were approved by the Institutional Review Board of Seoul National University Hospital (IRB number H-0912-067-304).

2.2. Experimental Protocol and Data Acquisition. We instructed the subjects to perform self-paced hand grasping or elbow flexion with the contralateral hand or elbow side of the implantation hemisphere. Each performed the movements precisely with an interval of more than 5 s in accordance with study directions. We emphasized the importance of movement intention immediately before performing the movements and told patients not to count the number of seconds in an interval. Each session took 5 min with 2 min of rest between each session. Three task sessions were recorded for each patient except for Subject 4 who complained of sickness related to vertigo. Only two sessions were recorded for Subject 4. The number of movements per session and the interval between movements are presented in Table 2.

Each patient had between 48 and 82 subdural electrodes (Ad-tech Medical Instrument, Racine, WI, USA) implanted. The diameter of each electrode was 4 mm with an interelectrode distance of 10 mm. The brain model and implanted electrodes were reconstructed from the individual MRI and CT images by using CURRY software (version 5.0, Compumedics Neuroscan, Charlotte, NC, USA). The ECoG data were recorded by using a 128-channel digital video monitoring system (Telefactor Beehive Horizon with an AURA LTM 64- & 128-channel amplifier system, Natus Neurology, West Warwick, RI, USA) digitized at sampling rates of 200, 400, or 1600 Hz and filtered from 0.1 to 80 Hz for the 200 Hz sampling rate and from 0.1 to 100 Hz for the 400 and 1600 Hz sampling rates. The cheekbone was used as a reference site. Additionally, electromyography

TABLE 1: Clinical profiles.

Subject	Age	Sex	Side of hand motion	Electrodes	
				Location	Number
Subject 1	25	Female	Right	Left hemisphere	72
Subject 2	36	Male	Left	Right hemisphere	52
Subject 3	26	Female	Right	Left hemisphere	48
Subject 4	26	Female	Right	Left hemisphere	82
Subject 5	37	Male	Left	Right hemisphere	58
Subject 6	28	Male	Left	Right hemisphere	58

TABLE 2: Behavior information. The number of movements per session and interval between movements of all subject.

Subject	Hand grasping			Interval (s)	Elbow flexion			Interval (s)
	Session 1	Session 2	Session 3		Session 1	Session 2	Session 3	
Subject 1	49	49	40	6.64 ± 1.12	42	36	40	7.75 ± 1.09
Subject 2	27	28	18	12.65 ± 3.96	25	21	19	13.84 ± 2.99
Subject 3	30	42	36	8.47 ± 1.81	32	37	29	9.41 ± 1.71
Subject 4	39	47	n.a.	7.39 ± 2.04	34	35	n.a.	9.44 ± 1.93
Subject 5	35	44	36	8.75 ± 2.21	28	31	29	11.28 ± 2.55
Subject 6	33	37	32	9.05 ± 2.68	25	28	15	12.68 ± 3.30

n.a.: not applicable.

Interval (s): mean ± SD.

(EMG) was used to detect the onset of motor performance from the opponens pollicis for hand grasping and from the biceps brachii for elbow flexion. Electrooculography (EOG) using electrodes that monitor eye movement was performed concurrently. The whole experiment was video-recorded to monitor motor performance and to obtain precise definition of movement onset.

2.3. Signal Preprocessing. The ECoG data were analyzed by using MATLAB software (Mathworks, Natick, MA, USA). The recorded data were downsampled to 200 Hz for unification of the various sampling rates in the analysis. The ECoG channels showing abnormal signals resulting from pathology or technical problems were excluded from further analysis. Movement onset was the time when the subject was about to move her/his hand or elbow and was determined from the EMG signals. To confirm that the EMG activity is not excited during the premovement onset period, EMG onset to preonset ratios, power ratios between EMG onset periods (0 to 1 s), and EMG preonset periods (-2 to 0 s) were calculated and averaged for all trials. Evaluated ratios were 13.18 ± 5.18 (mean ± SD) dB and 21.79 ± 5.00 dB for hand grasping and elbow flexion, respectively. In addition, no significant transient EMG bursts were detected in all trials during the premovement onset periods.

2.4. Feature Extraction. To extract features from premovement signals, first, epoching was performed with a window of -2 s to 0 s of movement onset (EMG onset) for the first session of each ECoG data type (hand grasping and elbow flexion) for all subjects. Note that we used only the first session for feature extraction. Trials contaminated by technical and epileptic artifacts were excluded from further analyses.

22 of the 1150 trials from all subjects (2%) were discarded. A Hamming window was applied to each epoched window. A fast Fourier transform (FFT) was used to transform single trial ECoG signals in the time domain into the frequency domain for each channel. Subsequently, power spectra were computed and averaged for all trials. Power spectral density is shown in a logarithmic scale. The frequencies of interest in a spectrum were from 1 Hz to 80 Hz. A higher frequency range could not be investigated because of limited sampling frequency. To determine which electrodes showed marked difference between the two movement types, we applied specific criteria, that is, a power difference between movement types of greater than 3 dB at a specific point and with a frequency range of 4 Hz or greater. Throughout these procedures, 13 electrodes were selected from among all electrodes of all subjects (two or three electrodes per subject). To verify that the selected electrodes from among those meeting our criteria were not chosen by chance, a bootstrap method was applied. We used the same ECoG task datasets for all subjects for the random epoch sampling (epoch start times were randomly selected). The same criteria were applied to the random sampled data. This process was repeated for all electrodes, after which the number of selected electrodes was counted. Subsequently, this procedure was iterated 500 times to obtain a distribution. The estimated *P* value associated with the bootstrap procedure was <0.002.

Finally, each subject had two or three electrodes selected by our criteria (subjects 1 and 3–6, 2 electrodes; subject 2, 3 electrodes; total, 13 electrodes). Specific frequency bands showing power differences were simultaneously selected during electrode selection. Single trial ECoG signals recorded from the selected electrodes along with the pronounced power difference frequency bands were filtered by using a

custom band-pass filter. The power value of each filtered signal sample was then averaged. This average was used for feature.

2.5. Classification. To confirm whether the extracted features represent their respective movement type on a trial-by-trial basis, we applied a linear classifier. Specifically, a linear support vector machine (SVM), which provides relatively robust classification performance [29, 30], was used. The optimized hyperplane with a maximum margin was determined from the training dataset by applying the linear SVM. To evaluate classification performance, we used fivefold cross validation [31]. All ECoG features were randomly partitioned into five subsamples. Four of the subsamples were used for training the classifier. The remaining subsample was used for estimating performance. This process was repeated five times. Finally, the averaged correct rate from all processes represented the accuracy level for evaluating classification performance. The prediction rate was then compared with the chance level.

3. Results

The selected electrodes from each subject were marked with three different black shapes on the respective reconstructed brain models (Figure 1(a)). Two electrodes were chosen for each subject except for Subject 2 (three electrodes chosen). The selected electrodes were placed on the primary sensorimotor area (6 electrodes in 4 subjects), premotor and supplementary areas (3 electrodes in 3 subjects), and prefrontal area (4 electrodes in 4 subjects). Notably, electrodes on the prefrontal area of four subjects were selected by applying our criteria. This suggests that the premovement neuronal activity power of the prefrontal area changes depending on the type of movement and can be detected by ECoG. The premovement power spectra for the selected electrodes for Subjects 1 and 2 are shown in Figure 1(b). The gray line indicates the frequency band that exhibits a marked power difference (>3 dB at the specific point with frequency range of ≥ 4 Hz) between the two movement types.

Subject-specific frequency bands are illustrated for all subjects in Figure 2. The results demonstrate that the filtering bands of 10 of the 13 electrodes included the beta band (13–30 Hz) and 6 of the 13 electrodes covered the alpha band (8–13 Hz). However, only 3 and 4 electrodes were used for feature extraction from the delta (<4 Hz) and gamma (30–70 Hz) bands, respectively. Furthermore, most of the selected frequency bands were in the alpha or beta ranges. In other words, the power spectral density (PSD) patterns disclosed in the alpha (8–13 Hz) and beta (13–30 Hz) rhythms were more informative than those in other bands. In particular, the beta band (13–30 Hz) was the most informative band at discriminating between the two movement types when using premovement signals, regardless of the related brain areas.

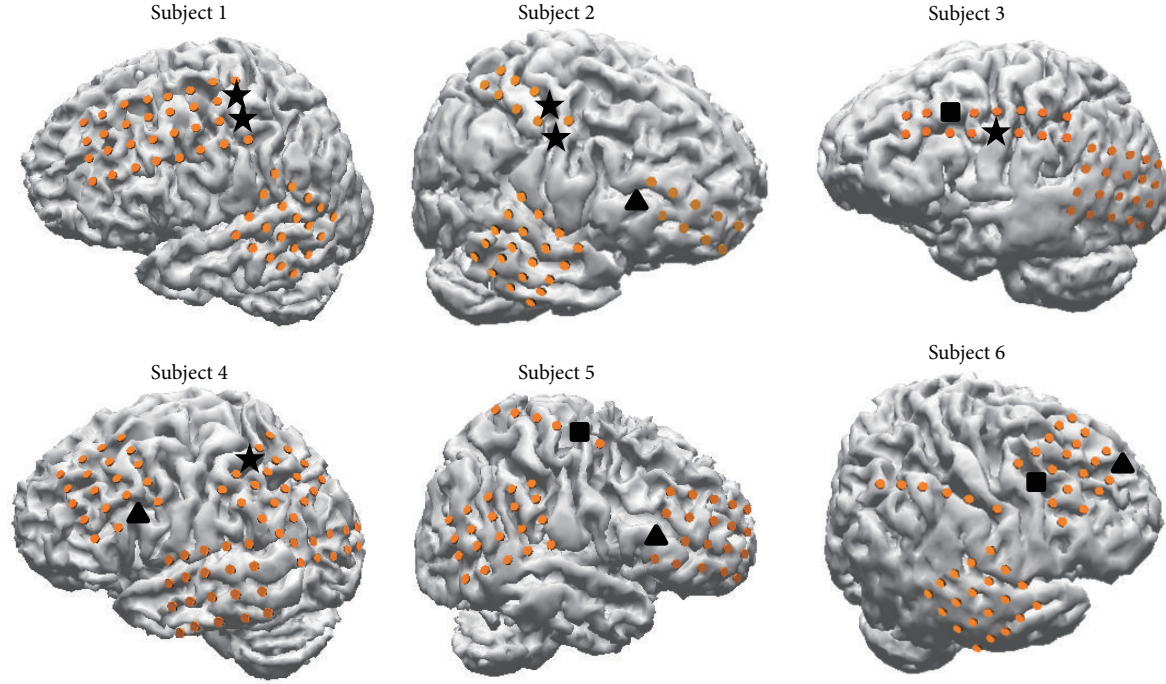
The movement type classification accuracy across the six subjects averaged 74.0%. The average recognition rate achieved in this study ranged from 55.4 to 99.3% (Figure 3). As mentioned in Section 2.4, the subject-specific frequency bands were selected based only on the data from the first

session. Subsequently, the same bands in other sessions were used to determine the reliability of our method. In other words, the subject-specific frequency bands in the first session were optimized. Thus, first session accuracy was generally higher than that in the other sessions (Figure 3). The average accuracy of the first session was 80.3% across the six subjects, well above that expected from chance. The accuracy rates of the other sessions were also significantly higher than expected from chance level. Specifically, the accuracies of the second and third sessions were 70.1% and 69.3%, respectively. These results demonstrate that the selected features provide consistent movement type classification accuracy.

To investigate whether features from the prefrontal area increase the classification accuracy, we compared the motor + prefrontal case (features from the motor related area and prefrontal area) and the motor related area only case. However, this comparison cannot be performed directly because not all subjects had features from both the prefrontal area and motor related area. Therefore, we performed this comparison for the subjects who had features from both the motor related area and prefrontal area. This result is shown in Figure 4. The accuracies of the cases that included the prefrontal and motor related area (case 1) and motor related area only (case 2) were compared in the four subjects. Classification accuracies decreased in 10 of the 11 sessions. The accuracy of case 1 was significantly higher than that of case 2 (paired *t*-test, $P < 0.01$).

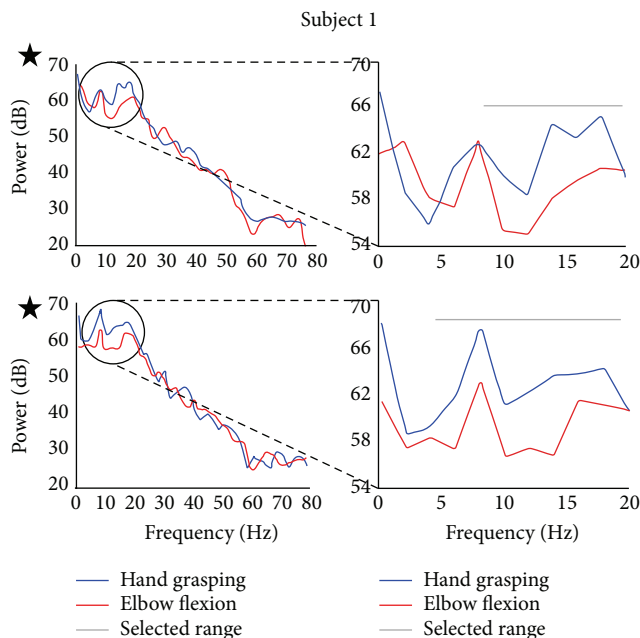
4. Discussion

4.1. Regions of the Brain Involved in Prediction of Motor Planning or Preparation. Research into motor intention has predominantly focused on motor related areas activated by real motor tasks or kinesthetic illusions such as the supplementary motor area, the premotor area, and the primary sensorimotor area [32]. To this list, we added the prefrontal area as an area of interest in our study into the prediction of movement. We observed that the positions of electrodes selected by our criteria were on the primary sensorimotor area ($N = 6$), the premotor and supplementary motor area ($N = 3$), and the prefrontal area ($N = 4$). By using the signals from these areas, significant overall movement type classification accuracy (74%) was obtained. This result indicates that these regions, including the prefrontal area, contribute to prediction of motor planning or preparation. When a human performs a voluntary action, a set of decision processes within that decision determines whether to perform an action, what action to select, and whether action execution proceeds. During the decision processes, the prefrontal area, along with other regions such as the basal ganglia, supplementary motor area, premotor area, and primary sensorimotor area, is involved [18, 23]. In electrophysiological studies with intracerebral electrodes and ECoG, the prefrontal area has been observed to be a source of the slow cortical potential and frequency power shifts in the alpha and beta bands, which physiologically implies the presence of cognitive functions such as motor planning or preparatory states before movement onset [13, 14, 33].

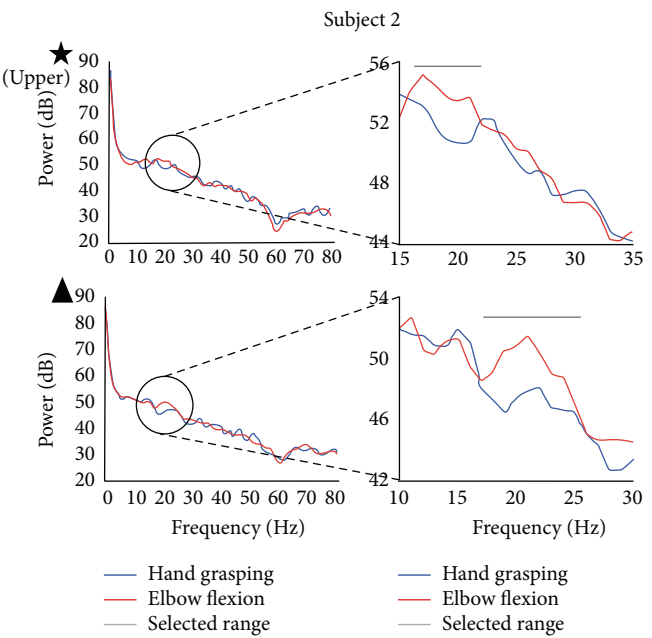


★ Primary sensorimotor area
■ Premotor and supplementary motor area
▲ Prefrontal area

(a)



(A)



(B)

FIGURE 1: Brain models and projected electrode locations for all subjects (a). Some electrodes are not shown because they were located on invisible sites or excluded by epileptic activities. All selected electrodes of each subject are marked with an asterisk, square, and triangle on the reconstructed brain models. These three black shapes represent electrodes within the implanted areas: asterisk (primary sensorimotor area), square (premotor and supplementary motor areas), and triangle (prefrontal area). Results of FFT analysis for selected electrodes of Subject 1 (A) and Subject 2 (B) (b). The FFT results of the prefrontal area (triangle) show a distinct difference between the two movement types in the beta range. The y-axis has a log power scale (dB). The gray horizontal line shows a region of pronounced power differences and indicates a selected frequency band. Blue and red lines represent the hand grasping and elbow flexion movement types, respectively.

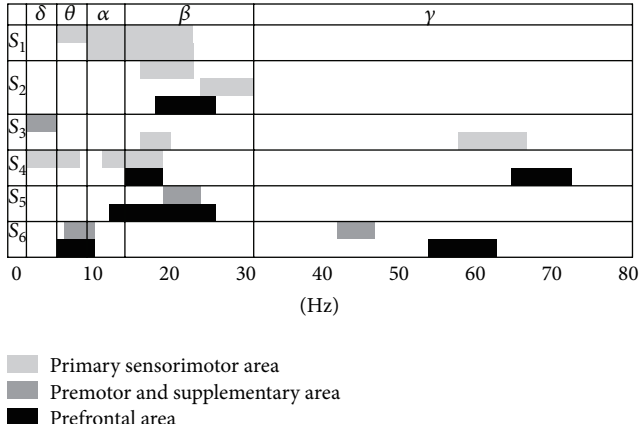


FIGURE 2: Frequency ranges of each subject's selected electrodes located in the primary sensorimotor, premotor and supplementary motor (Brodmann area 6), and prefrontal areas. The frequencies were divided into the delta, theta, alpha, beta, and gamma brain waves. The predominant frequency range was in the beta band (13–30 Hz). S: subject.

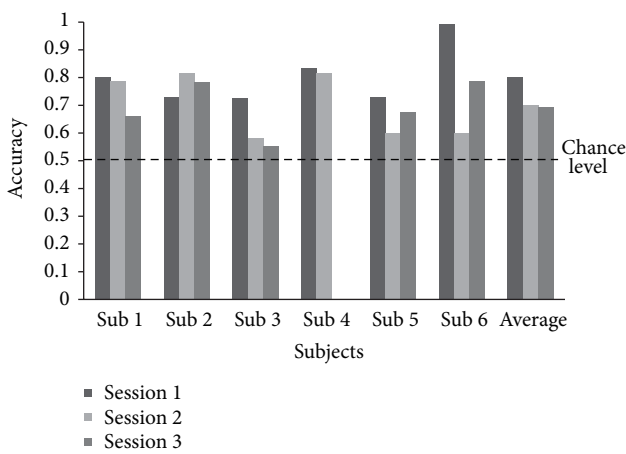


FIGURE 3: The accuracy of movement type classification. Each bar represented the accuracy of each session in each subject and the average accuracy of each session for all six subjects. The dashed line indicates the chance level for the movement classification. The average accuracy of all sessions was 74.0%.

Through our results and by considering these points, we have demonstrated that signals from the prefrontal area can be used to predict the occurrence of motor planning or preparations. In addition, our results carry important implications for paralyzed patients. In particular in patients with paralysis or trauma to the primary sensorimotor cortex, functioning of motor related areas is most likely to be damaged over time, and this damage may result in poor performance of a BCI system utilizing the primary sensorimotor area. Therefore, the usefulness of other regions needs to be investigated. In this respect, our results suggest that the prefrontal area should be considered when using a BCI to predict motor planning or preparation.

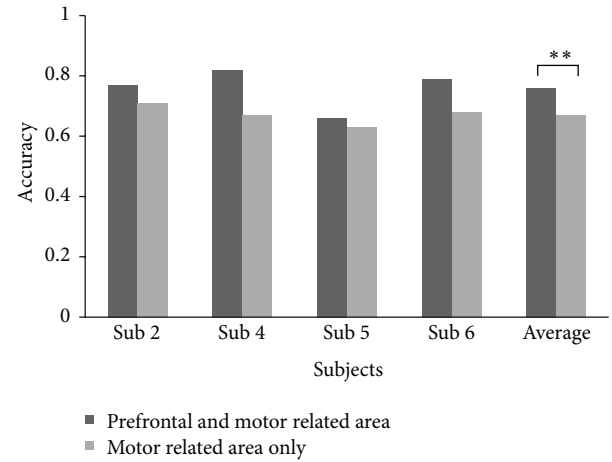


FIGURE 4: Difference in accuracy difference between two cases: a case including the prefrontal and motor related area (black, case 1) and a case including the motor related area only (gray, case 2). Each bar represents the averaged accuracy of each session in each subject and the average accuracy of each session for four subjects. The average accuracies of each case for all four subjects were 76.0 and 67%, respectively. The accuracy of case 1 was significantly higher than that of case 2 (paired *t*-test, *P* < 0.01).

4.2. Importance of Beta Oscillation in Prediction of Motor Planning or Preparation. Human motor control mechanisms are associated with changes in the neuronal oscillations in motor related areas. Accordingly, several electrophysiological studies of motor preparation and execution have focused on oscillatory activity in the human cortex [8, 34, 35]. Specifically, alpha and beta band neuronal oscillatory activities during motor preparation have been quantified as exhibiting decreases or increases in power relative to a baseline period over the prefrontal, premotor and supplementary motor, and primary sensorimotor areas, and this power shift is generally referred to as an event-related desynchronization (ERD) or event-related synchronization (ERS) indicating a state of active cortical processing [14, 33]. As shown in Figure 2, beta waves (13–30 Hz) as signal features were more common than the other waves. This implies that beta band activity is the most informative for predicting movement types. This result partly supports findings in previous studies that have demonstrated that the most specific feature of premovement signals for classifying movement type is in the 8–30 Hz range [7, 8]. Several studies into brain neural oscillation have indicated that beta frequency neural oscillation might encode specific information related to motor activity or preparation [36], and it is modulated by the future task during the intention and preparation periods [37]. In addition, beta band activity can represent the status quo by receiving new information about the state or the motor command [38]. In an animal study, beta band oscillation reflected not only the maintenance of a motor plan, but also the decision outcome [39]. In contrast to beta oscillation, alpha oscillation did not fully represent the selection of the mode of action and it was not modulated by the task, but it did reflect the motor preparation state [37, 40]. To conclude, the beta

frequency oscillation is an important neural activity pattern in classifying movement types.

4.3. Practical Advantages of Our Movement Prediction Approach Using ECoG. In this study, we showed that movement type could be predicted before the subject moves by using only three or fewer ECoG electrodes. This result has profound implications for an ECoG-based BCI system. The capacity to utilize a minimal number of electrodes in an invasive BCI system would reduce the extent of external injuries to users and would lighten their surgical burden. In addition, the feature extraction method described herein is relatively simple and does not require more complex noise reduction and signal classification methods such as those in independent component analysis and principle component analysis.

In our study, once the predictive electrodes and their associated specific frequency bands were selected from our first session data, prediction accuracy was approximately maintained during subsequent sessions. This predictive consistency indicates that an ECoG-based BCI system that utilized our approach would be helpful when implementing a robust, reliable, real-time movement classification system because of its high signal stability. In general, ECoG data obtained from the surface of the cortex has several advantages including better location stability, greater freedom from muscle and movement artifacts, higher signal-to-noise ratio, broader bandwidth, higher amplitude, and higher spatial resolution over EEG recordings [24]. Therefore, we suggest that our ECoG-based approach can provide useful preonset information about movements and is a good prospect for incorporation into a BCI system.

4.4. Prediction of Voluntary Movement Using Premovement Signals for Fast BCI Responses. Based on our successful prediction results, we anticipate that our method of preonset movement prediction may allow faster BCI responses. For successive prediction of a complex voluntary movement, a BCI system should perform four steps: onset prediction, movement type prediction, precise prediction of movement, and offset detection. These steps must be done sequentially. Recently, several researchers demonstrated that the onset and direction of human voluntary movement could be detected by using premovement signals of motor related areas [8, 9]. Considering these works and the results of our study, the initial two BCI steps can be performed before movement onset. In that case, a BCI system could initiate the third step faster, although postonset signals are needed for performing that step. In particular, such a BCI system could provide additional setup time for real-time prediction of complex movement such as three-dimensional trajectory estimation and bimanual movement prediction, which typically require long computation times.

4.5. Other Considerations and Limitations. Although we obtained high classification accuracy by using premovement signals from motor related and prefrontal areas, we did

not directly compare the accuracy levels among the prefrontal, premotor and supplementary motor, and primary sensorimotor areas. Comparing the individual accuracies of each area by adding or subtracting electrodes in other areas is not effective because our classification accuracy was optimized by the extracted features. In this study, the areas for the selected electrodes were mixed, except for those in the primary sensorimotor area (Subject 1). However, we tested all electrodes of a subject to extract features by using criteria that selected specific frequency band that showed a marked power difference. In addition, the criteria did not contain *a priori* information about the location of the electrodes. In other words, the excluded electrodes did not show marked power difference between the two movement types. To compare the accuracy of each area directly, a feature extraction method that functioned without electrode selection would be required. However, such an approach was beyond the scope of this study. Hence, although there are several methodological limitations to our study, our results imply that the prefrontal area should be considered when attempting to predict motor planning or preparation because the neuronal activities in this area were shown to contribute to the classification of two movement types in four of our six subjects.

In this paper, we could not investigate the high gamma neuronal activities because of the limited sampling rates. Several researchers have indicated high gamma power changes in the dorsolateral prefrontal cortex during movement preparation and mental processing [26–28]. According to these findings, broadband high gamma power was altered depending on the movement stages which are determined by the pre- and postmovement time series. Taking into account these findings, high gamma power may be important features in movement type classification. In our study, some prefrontal area features contained gamma power in a relatively high frequency range. Although the selected frequency ranges of these features did not cover a broad range, they might reflect the previous findings. Hence, further investigation is needed to include features from high gamma neuronal activity to improve the classification accuracy.

In this study, the averaged classification accuracy was 74%. This is considered a successful result in movement prediction using the premovement stage signal. However, our classification accuracy could be improved by several ways. First, considering feature interaction might improve our classification accuracy. Although the signals of adjacent ECoG electrodes are less similar than that of the EEG electrodes, large scale neuronal oscillatory activity such as alpha oscillations in the sensorimotor area might increase the signal dependency among adjacent ECoG electrodes. Second, feature extraction taking into account time dependency during the premovement period (-2 to 0 s) might improve our BCI system. Many studies have indicated that there are several neural states during that period [11]. In addition, the electrophysiological brain signal is highly variable over time even in time-locked event-related responses. Therefore, a time-dependent feature extraction method such as short time Fourier transforms during the preonset movement period might improve the classification accuracy of our model.

5. Conclusion

In this paper, we demonstrate that movement type can be predicted by including prefrontal signals before the subject moves. Our results suggest that the prefrontal area can generate meaningful neuronal activity signals that can be used to predict movement before the movement occurs. Our results also suggest that beta band oscillation is the most informative for prediction of movement types before movement onset. Our findings should be of interest to those applying BCI systems in neurological rehabilitation. Our approach to ECoG-based BCI systems that utilizes signals provided by the prefrontal area carries important implications for patients with paralysis or trauma to the primary sensorimotor area.

Conflict of Interests

The authors declare that there is no conflict of interests regarding the publication of this paper.

Acknowledgments

This work was supported by the Global Frontier R&D Program on Human-Centered Interaction for Coexistence funded by the National Research Foundation of Korea Grant funded by the Korean Government (MSIP) (2012M3A6A3055889).

References

- [1] J. R. Wolpaw, N. Birbaumer, D. J. McFarland, G. Pfurtscheller, and T. M. Vaughan, "Brain-computer interfaces for communication and control," *Clinical Neurophysiology*, vol. 113, no. 6, pp. 767–791, 2002.
- [2] J. R. Wolpaw, N. Birbaumer, W. J. Heetderks et al., "Brain-computer interface technology: a review of the first international meeting," *IEEE Transactions on Rehabilitation Engineering*, vol. 8, no. 2, pp. 164–173, 2000.
- [3] J. J. Vidal, "Toward direct brain-computer communication," *Annual Review of Biophysics and Bioengineering*, vol. 2, pp. 157–180, 1973.
- [4] N. J. Hill, T. N. Lal, M. Schröder et al., "Classifying EEG and ECoG signals without subject training for fast BCI implementation: comparison of nonparalyzed and completely paralyzed subjects," *IEEE Transactions on Neural Systems and Rehabilitation Engineering*, vol. 14, no. 2, pp. 183–186, 2006.
- [5] R. Scherer, B. Graimann, J. E. Huggins, S. P. Levine, and G. Pfurtscheller, "Frequency component selection for an ECoG-based brain-computer interface," *Biomedizinische Technik*, vol. 48, no. 1-2, pp. 31–36, 2003.
- [6] T. Yanagisawa, M. Hirata, Y. Saitoh et al., "Neural decoding using gyral and intrasulcal electrocorticograms," *NeuroImage*, vol. 45, no. 4, pp. 1099–1106, 2009.
- [7] V. Morash, O. Bai, S. Furlani, P. Lin, and M. Hallett, "Classifying EEG signals preceding right hand, left hand, tongue, and right foot movements and motor imageries," *Clinical Neurophysiology*, vol. 119, no. 11, pp. 2570–2578, 2008.
- [8] O. Bai, V. Rathi, P. Lin et al., "Prediction of human voluntary movement before it occurs," *Clinical Neurophysiology*, vol. 122, no. 2, pp. 364–372, 2011.
- [9] Z. Wang, A. Gunduz, P. Brunner, A. L. Ritaccio, Q. Ji, and G. Schalk, "Decoding onset and direction of movements using electrocorticographic (ECoG) signals in humans," *Frontiers in Neuroengineering*, vol. 5, article 15, 2012.
- [10] E. Hoshi and J. Tanji, "Distinctions between dorsal and ventral premotor areas: anatomical connectivity and functional properties," *Current Opinion in Neurobiology*, vol. 17, no. 2, pp. 234–242, 2007.
- [11] H. Shibasaki and M. Hallett, "What is the bereitschaftspotential?" *Clinical Neurophysiology*, vol. 117, no. 11, pp. 2341–2356, 2006.
- [12] G. Pfurtscheller and F. H. L. da Silva, "Event-related EEG/MEG synchronization and desynchronization: basic principles," *Clinical Neurophysiology*, vol. 110, no. 11, pp. 1842–1857, 1999.
- [13] M. Jahanshahi, G. Dirnberger, A. Liassis, A. Towell, and S. Boyd, "Does the pre-frontal cortex contribute to movement-related potentials? Recordings from subdural electrodes," *Neurocase*, vol. 7, no. 6, pp. 495–501, 2001.
- [14] D. Sochurková, I. Rektor, P. Jurák, and A. Stančák, "Intracerebral recording of cortical activity related to self-paced voluntary movements: a Bereitschaftspotential and event-related desynchronization/synchronization. SEEG study," *Experimental Brain Research*, vol. 173, no. 4, pp. 637–649, 2006.
- [15] I. Rektor, M. Bareš, P. Kaňovský, and M. Kukleta, "Intracerebral recording of readiness potential induced by a complex motor task," *Movement Disorders*, vol. 16, no. 4, pp. 698–704, 2001.
- [16] S. Ohara, A. Ikeda, M. Matsuhashi et al., "Bereitschaftspotentials recorded from the lateral part of the superior frontal gyrus in humans," *Neuroscience Letters*, vol. 399, no. 1-2, pp. 1–5, 2006.
- [17] E. C. Leuthardt, G. Schalk, J. R. Wolpaw, J. G. Ojemann, and D. W. Moran, "A brain-computer interface using electrocorticographic signals in humans," *Journal of Neural Engineering*, vol. 1, no. 2, pp. 63–71, 2004.
- [18] P. Haggard, "Human volition: towards a neuroscience of will," *Nature Reviews Neuroscience*, vol. 9, no. 12, pp. 934–946, 2008.
- [19] N. Picard and P. L. Strick, "Motor areas of the medial wall: a review of their location and functional activation," *Cerebral Cortex*, vol. 6, no. 3, pp. 342–353, 1996.
- [20] G. Rizzolatti, G. Luppino, and M. Matelli, "The organization of the cortical motor system: new concepts," *Electroencephalography and Clinical Neurophysiology*, vol. 106, no. 4, pp. 283–296, 1998.
- [21] M. D. Hunter, R. D. J. Green, I. D. Wilkinson, and S. A. Spence, "Spatial and temporal dissociation in prefrontal cortex during action execution," *NeuroImage*, vol. 23, no. 3, pp. 1186–1191, 2004.
- [22] M. D'Esposito, D. Ballard, E. Zarahn, and G. K. Aguirre, "The role of prefrontal cortex in sensory memory and motor preparation: an event-related fMRI study," *NeuroImage*, vol. 11, no. 5, pp. 400–408, 2000.
- [23] J. M. Fuster, "Executive frontal functions," *Experimental Brain Research*, vol. 133, no. 1, pp. 66–70, 2000.
- [24] G. Schalk, "Can electrocorticography (ECoG) support robust and powerful brain-computer interfaces?" *Frontiers in Neuroengineering*, vol. 3, p. 9, 2010.
- [25] G. Schalk and E. C. Leuthardt, "Brain-computer interfaces using electrocorticographic signals," *IEEE Reviews in Biomedical Engineering*, vol. 4, pp. 140–154, 2011.

- [26] N. Anderson, "Electrocorticographic Neural Correlates of Arm Movements and Associated Goal Orientation in Humans," *Electronic Theses and Dissertations*, Paper 16, 2009.
- [27] N. F. Ramsey, M. P. van de Heuvel, K. H. Kho, and F. S. S. Leijten, "Towards human BCI applications based on cognitive brain systems: an investigation of neural signals recorded from the dorsolateral prefrontal cortex," *IEEE Transactions on Neural Systems and Rehabilitation Engineering*, vol. 14, no. 2, pp. 214–217, 2006.
- [28] M. J. Vansteensel, D. Hermes, E. J. Aarnoutse et al., "Brain-computer interfacing based on cognitive control," *Annals of Neurology*, vol. 67, no. 6, pp. 809–816, 2010.
- [29] O. Bai, P. Lin, S. Vorbach, J. Li, S. Furlani, and M. Hallett, "Exploration of computational methods for classification of movement intention during human voluntary movement from single trial EEG," *Clinical Neurophysiology*, vol. 118, no. 12, pp. 2637–2655, 2007.
- [30] K. Müller, C. W. Anderson, and G. E. Birch, "Linear and non-linear methods for brain-computer interfaces," *IEEE Transactions on Neural Systems and Rehabilitation Engineering*, vol. 11, no. 2, pp. 165–169, 2003.
- [31] Y. Bengio and Y. Grandvalet, "No unbiased estimator of the variance of K-fold cross-validation," *Journal of Machine Learning Research*, vol. 5, pp. 1089–1105, 2004.
- [32] E. Naito and H. H. Ehrsson, "Kinesthetic illusion of wrist movement activates motor-related areas," *NeuroReport*, vol. 12, no. 17, pp. 3805–3809, 2001.
- [33] I. Rektor, D. Sochůrková, and M. Bočková, "Intracerebral ERD/ERS in voluntary movement and in cognitive visuomotor task," *Progress in Brain Research*, vol. 159, pp. 311–330, 2006.
- [34] O. Bai, Z. Mari, S. Vorbach, and M. Hallett, "Asymmetric spatiotemporal patterns of event-related desynchronization preceding voluntary sequential finger movements: A high-resolution EEG study," *Clinical Neurophysiology*, vol. 116, no. 5, pp. 1213–1221, 2005.
- [35] G. Pfurtscheller and F. H. Lopes da Silva, "Event-related EEG/MEG synchronization and desynchronization: basic principles," *Clinical Neurophysiology*, vol. 110, no. 11, pp. 1842–1857, 1999.
- [36] N. J. Davis, S. P. Tomlinson, and H. M. Morgan, "The role of beta-frequency neural oscillations in motor control," *Journal of Neuroscience*, vol. 32, no. 2, pp. 403–404, 2012.
- [37] S. Bickel, E. C. Dias, M. L. Epstein, and D. C. Javitt, "Expectancy-related modulations of neural oscillations in continuous performance tasks," *NeuroImage*, vol. 62, no. 3, pp. 1867–1876, 2012.
- [38] A. K. Engel and P. Fries, "Beta-band oscillations-signalling the status quo?" *Current Opinion in Neurobiology*, vol. 20, no. 2, pp. 156–165, 2010.
- [39] S. Haegens, V. Nácher, A. Hernández, R. Luna, O. Jensen, and R. Romo, "Beta oscillations in the monkey sensorimotor network reflect somatosensory decision making," *Proceedings of the National Academy of Sciences of the United States of America*, vol. 108, no. 26, pp. 10708–10713, 2011.
- [40] M. P. Deiber, E. Sallard, C. Ludwig, C. Ghezzi, J. Barral, and V. Ibañez, "EEG alpha activity reflects motor preparation rather than the mode of action selection," *Frontiers in Integrative Neuroscience*, vol. 6, article 59, 2012.

Research Article

Robust Deep Network with Maximum Correntropy Criterion for Seizure Detection

Yu Qi,^{1,2} Yueming Wang,^{1,2} Jianmin Zhang,³ Junming Zhu,³ and Xiaoxiang Zheng^{1,4}

¹ QIUSHI Academy for Advanced Studies, Zhejiang University, Hangzhou 310027, China

² Department of Computer Science, Zhejiang University, Hangzhou 310027, China

³ Second Affiliated Hospital of Zhejiang University, College of Medicine, Hangzhou 310000, China

⁴ Department of Biomedical Engineering, Zhejiang University, Hangzhou 310027, China

Correspondence should be addressed to Yueming Wang; ymingwang@zju.edu.cn

Received 27 March 2014; Accepted 4 June 2014; Published 6 July 2014

Academic Editor: Ting Zhao

Copyright © 2014 Yu Qi et al. This is an open access article distributed under the Creative Commons Attribution License, which permits unrestricted use, distribution, and reproduction in any medium, provided the original work is properly cited.

Effective seizure detection from long-term EEG is highly important for seizure diagnosis. Existing methods usually design the feature and classifier individually, while little work has been done for the simultaneous optimization of the two parts. This work proposes a deep network to jointly learn a feature and a classifier so that they could help each other to make the whole system optimal. To deal with the challenge of the impulsive noises and outliers caused by EMG artifacts in EEG signals, we formulate a robust stacked autoencoder (R-SAE) as a part of the network to learn an effective feature. In R-SAE, the maximum correntropy criterion (MCC) is proposed to reduce the effect of noise/outliers. Unlike the mean square error (MSE), the output of the new kernel MCC increases more slowly than that of MSE when the input goes away from the center. Thus, the effect of those noises/outliers positioned far away from the center can be suppressed. The proposed method is evaluated on six patients of 33.6 hours of scalp EEG data. Our method achieves a sensitivity of 100% and a specificity of 99%, which is promising for clinical applications.

1. Introduction

Epilepsy is a common and serious brain disorder, which affects about 50 million people worldwide [1]. Epileptic seizures are characterized by convulsions, loss of consciousness, and muscle spasms resulting from excessive synchronization of neuronal activities in the brain [2]. The abnormal neuronal discharges lead to epileptic patterns such as closely spaced spikes and slow waves in electroencephalogram (EEG). In seizure diagnosis and evaluation, visual inspection of these epileptic patterns from long-term EEG is a routine job for the doctors, which could be highly tedious and time-consuming [3]. Therefore, reliable seizure detection system that identifies seizure events automatically would facilitate seizure diagnosis and has great potential in clinical applications.

There are two key points in automatic seizure detection. One is how to capture the diverse patterns of seizure EEG. For different individuals, the morphologies of seizure patterns could vary considerably. Therefore, effective feature extraction plays a key role in seizure detection and lots of efforts

have been made. In order to characterize the changes in amplitude and energy in epileptic EEG, Saab and Gotman [4] proposed to use three measures, relative average amplitude, relative scale energy, and coefficient of variation of amplitude. Similarly, Majumdar and Vardhan [5] utilized the variance of differentiation of time window to detect significant changes in EEG signals. To identify the sharp waves which typically appear in seizure signals, Yadav et al. [6] introduced a morphology-based detector based on the slopes of the half-waves of signals. To characterize the intrinsic time-frequency components of seizure patterns, Ghosh-Dastidar et al. [7] used principal component analysis and Zandi et al. [8] applied wavelet transform to decompose the EEG signal for feature enhancement. To encode the changes in dynamics of epileptic signal, Jouny and Bergey [9] utilized nonlinear measures of sample entropy and Lempel-Ziv complexity. To describe the topology state of epilepsy, Santaniello et al. [10] transformed the multichannel EEG data into a cross-power matrix, and eigenvalues of the matrix are used for seizure detection. The other key point is how to reduce the effect

of noise. The noises caused by electromyography (EMG) or electrode movements commonly appear in EEG signal and are prone to trigger false alarms. These artifacts could bring impulsive changes with large amplitudes in EEG signal and lead to outlying values in the feature space. Some existing methods simply assumed these noises to be Gaussian [11, 12] and thus would be fragile given large amounts of outliers. Other approaches applied specific false alarm avoidance methods against these noises [4–6].

Although existing methods have shown some strengths in specific EEG datasets, the following problems have not yet been well explored. First, most existing features are designed according to the observation of a few seizure patterns, which seems too empirical to cover a wide range of seizure patterns; thus the features are usually suboptimal. Second, existing methods could be sensitive to the noises in EEG signals. Artifacts caused by EMG or electrode movements probably lead to a EEG signal shape similar to that of seizure states. A simple Gaussian assumption for the noises can be incorrect and the approaches designed based on this can cause high false alarms [11, 12]. Finally, most methods design the feature and classifier individually. Few efforts have been made to study the relationship between them or simultaneously optimize both of the two parts to maximize the abilities of them.

Inspired by the great success of deep network in image retrieval, speech recognition, and computer vision [13–21], this paper proposes a deep model framework to deal with the above issues. The main contributions of our work can be summarized as follows.

- (i) Instead of manually designing a feature, we propose a network called robust stacked autoencoder (R-SAE) to automatically learn a feature to represent seizure patterns. The reconstruction error is first used to learn an initial feature.
- (ii) To reduce the effect of noises on EEG signals, we formulate a maximum correntropy criterion (MCC) to the R-SAE network. Unlike the traditional autoencoder model which uses the mean square error (MSE) as the reconstruction cost, the output of the new kernel MCC increases more slowly than that of MSE when the input goes away from the center. Thus, the effect of those noises/outliers positioned far away from the center can be suppressed.
- (iii) The R-SAE part and classification part are integrated to a new deep network. The objective of the network is the best seizure classification accuracy. Thus, both the initial feature and the classifier could be optimized according to the detection objective so that the whole detection system could be as optimal as possible. Besides, the optimal feature is completely data-driven. Given enough training data, the optimal feature learned by our method is able to represent various seizure patterns.

Our method is evaluated on 33.6 hours of EEG signals from six patients. With the MCC-based R-SAE model, robust features are extracted from noisy EEG signal that the sensitivity and specificity increase by 14% and 1% compared with

TABLE 1: Patient information and selected frequency bands.

Patient	Sex	Chan. #	Sei. #	Hours	Freq. band
Pt01	Female	28	2	5.6	14–30 Hz
Pt02	Female	28	2	5.6	8–13 Hz
Pt03	Female	28	3	5.6	4–7 Hz
Pt04	Male	28	3	5.6	14–30 Hz
Pt05	Male	28	3	5.6	8–13 Hz
Pt06	Male	28	3	5.6	8–13 Hz

the traditional stacked autoencoder (S-SAE). By supervised joint optimization of our deep model, the features are further optimized with better separability in the feature space and the sensitivity and specificity increase by 8% and 15%, respectively. In comparison with other methods, the proposed R-SAE model outperforms the competitors and achieves a high sensitivity of 100% and a specificity of 99%.

The rest of this paper is organized as follows. Section 2 presents the detail of the R-SAE deep model. The experimental results and discussions are shown in Section 3. Finally, we draw the conclusions in Section 4.

2. Materials and Methods

The framework of our method is shown in Figure 1. The multichannel EEG signals are firstly divided into short-time segments, and we calculate the cross-power matrix for each segment to reveal the spatial patterns of the brain. Then, compact features are extracted from the cross-power matrix by a deep network cascaded to a softmax classifier. In our method, the deep network is first pretrained with the R-SAE model to extract useful features, and then the features are further optimized jointly with the classifier to obtain optimal seizure detection system.

2.1. EEG Data. Scalp EEG data of six patients are used in this study. The EEG data were recorded during long-term presurgical epilepsy monitoring using NicoletOne amplifier at Second Affiliated Hospital of Zhejiang University, College of Medicine. A total of 28 channels were acquired at the sample rate of 256 Hz according to 10–20 electrode placement systems. The detail of the EEG data is given in Table 1. For each patient, all the available seizure EEG signals are used, and we randomly choose two 2.8-hour-long EEG segments as the nonseizure data segmentation and data preparation.

2.2. Segmentation and Data Preparation. In the preprocessing stage, the multichannel EEG data are divided into 5-second-long segments with a sliding window. For each patient, a total of 4000 segments of nonseizure data and 1000 segments of seizure data are divided from the EEG signals. There is no overlap between nonseizure segments, while, for seizure segments, the proportion of overlap is configured considering the total length of the seizure signal and number of segments required.

After segmentation, all the segments are disordered and we randomly pick 750 seizure segments and 750 nonseizure

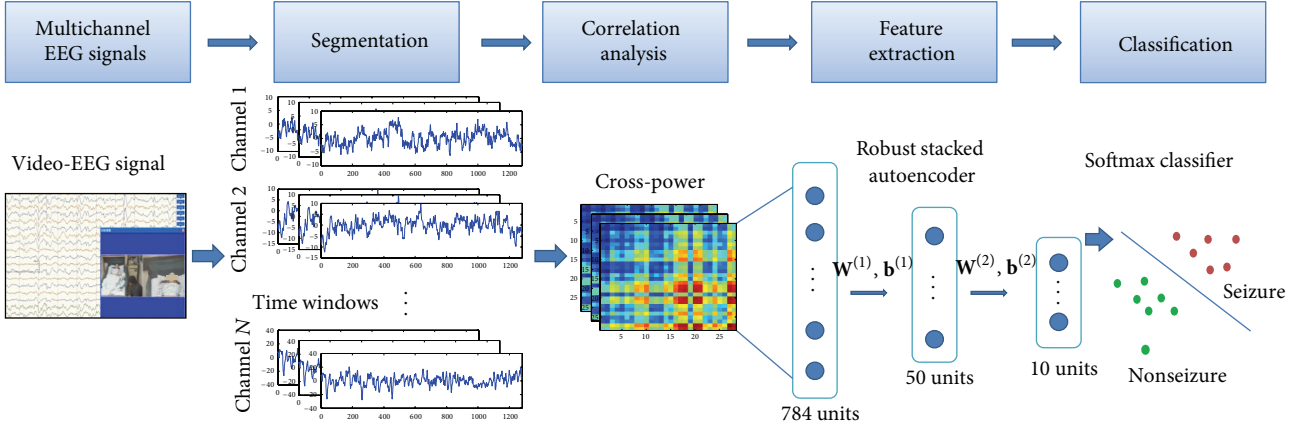


FIGURE 1: Framework of our method.

segments as the training set and the rest 3500 segments are used as the testing set. All the experiments are carried out on the same training and testing set.

2.3. Multichannel Analysis. Studies have shown that the correlation structure of all pairs of EEG channels could reflect the spatiotemporal evolution of electrical ictal activities [22–24]. By characterizing the spatiotemporal patterns, it is possible to identify seizures and analyze seizure dynamics.

In this study, we adopt cross-power matrix [10] to reflect the spatial patterns of the brain. For each time window with N channels, the cross-power matrix \mathbf{A} is $N \times N$. Each element a_{ij} in \mathbf{A} is defined by the cross-power [10] between the two EEG channels i and j in a given frequency band of $[lb, ub]$ as follows:

$$a_{ij} = \int_{lb}^{ub} P_{ij}(\omega) d\omega, \quad (1)$$

where $P_{ij}(\omega)$ is the cross-power spectral density of channels i and j at frequency ω .

2.4. Frequency Band Selection. Considering the diversity of epileptic patterns among patients, we choose the frequency band patient specifically from theta (4–7 Hz), alpha (8–13 Hz), and beta (14–30 Hz) bands. In order to select the frequency band that best reflects the difference between seizure and nonseizure states, we adopt Fisher's discriminant ratio (FDR) [25] as the criterion as follows:

$$C = \frac{(\mu_s - \mu_n)^2}{\sigma_s^2 + \sigma_n^2}, \quad (2)$$

where μ_s and σ_s^2 are means and covariance, respectively, of cross-power matrix of seizure segments and μ_n and σ_n^2 are those of nonseizure segments. For each patient, only the training segments are utilized for frequency band selection, and the frequency band with the highest FDR is used for seizure detection. The frequency band selected for each patient is shown in Table 1.

2.5. Robust Stacked Autoencoder. After multichannel analysis, each time window is represented by a cross-power matrix of $N \times N$, where N denotes the number of EEG channels. We propose to employ robust stacked autoencoders to extract reliable and compact features from the cross-power matrix.

In this section, first, we briefly introduce the basic autoencoder. Then, the robust autoencoder with MCC is presented to improve the feature learning ability under noises. Finally, we stack the robust autoencoders into a deep model for compact feature extraction.

2.5.1. Basic Autoencoder. Here, we begin with the traditional standard stacked autoencoder model (S-SAE). An autoencoder is a three-layer artificial network including an encoder and a decoder. The encoder takes an input vector \mathbf{x} and maps it to a hidden representation \mathbf{x}' through a nonlinear function as follows:

$$\mathbf{x}' = s(\mathbf{W}^{(1)}\mathbf{x} + \mathbf{b}^{(1)}), \quad (3)$$

where $s(\cdot)$ is the sigmoid function. Suppose \mathbf{x} and \mathbf{x}' are d -dimensional and d' -dimensional vectors, respectively; then $\mathbf{W}^{(1)}$ is a $d' \times d$ weight matrix and $\mathbf{b}^{(1)}$ is a d' -dimensional bias vector.

Then, the vector \mathbf{x}' is mapped back to a reconstruction vector \mathbf{y} by the decoder as follows:

$$\mathbf{y} = s(\mathbf{W}^{(2)}\mathbf{x}' + \mathbf{b}^{(2)}), \quad (4)$$

where the output vector is d -dimensional, $\mathbf{W}^{(2)}$ is $d \times d'$, and $\mathbf{b}^{(2)}$ is a d -dimensional bias vector.

The parameter set $\theta = \{\mathbf{W}^{(1)}, \mathbf{b}^{(1)}, \mathbf{W}^{(2)}, \mathbf{b}^{(2)}\}$ is optimized by minimizing the average reconstruction error as follows:

$$\theta = \operatorname{argmin}_{\theta} \frac{1}{n} \sum_{i=1}^n L(\mathbf{x}_i, \mathbf{y}_i), \quad (5)$$

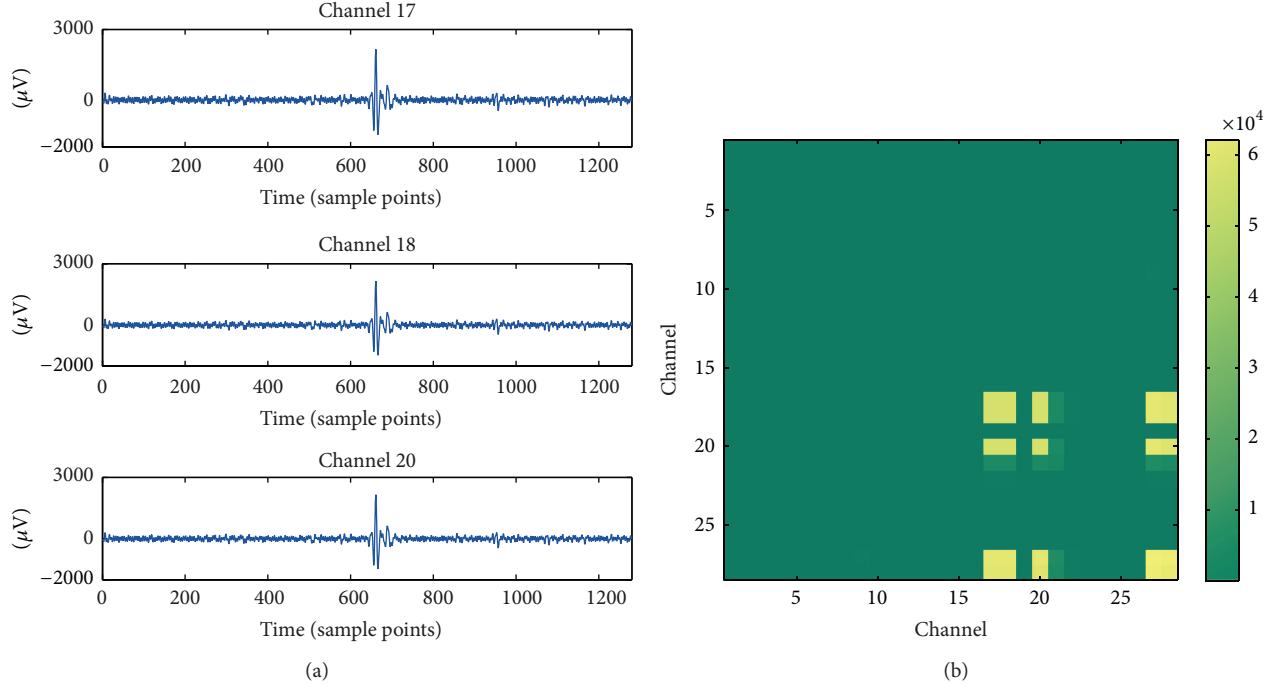


FIGURE 2: An EEG segment with impulsive noises. (a) EMG artifacts cause short-term burst noises in some channels of EEG signal; (b) visualization of the cross-power matrix of the segment with noises. The vertical and horizontal axes denote the channels and each point (i, j) in this figure is the cross-power value of channel i and channel j . The cross-power matrix contains outliers with large values. Because of the noise, the cross-power between channel 17 and channel 18 is far away from the interquartile range value (5.41×10^4 versus 395.3).

where L is the loss function. Mostly, the mean square error (MSE) is used as

$$\begin{aligned} J_{\text{MSE}}(\theta) &= \frac{1}{n} \sum_{i=1}^n L_{\text{MSE}}(\mathbf{x}_i, \mathbf{y}_i) \\ &= \frac{1}{n} \sum_{i=1}^n \left(\frac{1}{2} \|\mathbf{y}_i - \mathbf{x}_i\|^2 \right). \end{aligned} \quad (6)$$

2.5.2. Robust Autoencoder. The traditional autoencoder model based on MSE loss is not suitable for stable feature learning in EEG signals. In EEG, especially in scalp EEG signals, the large amount of noises caused by EMG artifacts or electrode movements could bring abrupt changes in EEG signal and lead to outliers in both time and frequency domain. A typical example is shown in Figure 2. In this time window, the EEG signals are noised by short-term EMG artifacts which lead to abrupt large-amplitude vibrations in some of the channels as shown in Figure 2(a). In the cross-power domain, such artifacts lead to outlying large values as in the light blocks in Figure 2(b). In the example illustrated, the cross-power between channel 17 and channel 18 is 5.41×10^4 , which is far away from the interquartile range value of 395.3. In this situation, the MSE-based cost of the traditional autoencoder model could be dominated by these outliers so that the feature learning ability is weakened.

In order to learn robust features from EEG signals, we replace the loss function of the autoencoder model with correntropy-based criterion to build robust autoencoder.

Maximum Correntropy Criterion. Correntropy is defined as a localized similarity measure [26] and it has shown good outlier suppression ability in studies [27, 28]. For two random variables X and Y , the correntropy is defined as

$$V_\sigma(X, Y) = E[\kappa_\sigma(X - Y)], \quad (7)$$

where $E[\cdot]$ is the mathematical expectation and $\kappa_\sigma(\cdot)$ is the Gaussian kernel with kernel size of σ as follows:

$$\kappa_\sigma(\cdot) = \frac{1}{\sqrt{2\pi}\sigma} \exp\left(-\frac{(\cdot)^2}{2\sigma^2}\right). \quad (8)$$

The correntropy induces a new metric that, as the distance between X and Y gets larger, the equivalent distance evolves from 2-norm to 1-norm and eventually to zero-norm when X and Y are far apart [29]. Compared with second-order statistics such as MSE, correntropy is less sensitive to outliers. Figure 3 compares the second-order cost and correntropy cost. As the input x goes further from the center, the second-order cost increases sharply, so that it is sensitive to outliers. By contrast, the correntropy is only sensitive in a local range and the increase of the cost is extremely slow when the input value goes out of the central area. Therefore, the correntropy measure is particularly effective in outlier suppression.

In practice, the joint probability density function is unknown and usually only a finite set of samples of

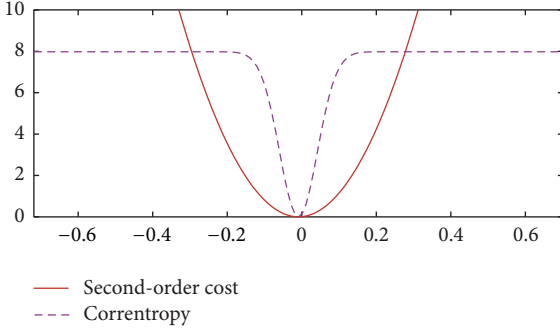


FIGURE 3: Illustration of second-order cost (red solid line) and correntropy cost (purple dashed line).

$\{(x_i, y_i)\}_{i=1}^N$ is available for both X and Y ; then the estimated correntropy can be calculated by

$$\tilde{V}_\sigma(X, Y) = \frac{1}{N} \sum_{i=1}^N \kappa_\sigma(x_i - y_i). \quad (9)$$

The maximum of correntropy error in (9) is called the maximum correntropy criterion (MCC) [29]. Due to the good outlier rejection property of correntropy, MCC is suitable for robust algorithm design.

Robust Autoencoder Based on MCC. In order to improve the antinoise ability of traditional autoencoders, we measure the reconstruction loss between the input vector x and the output vector y by MCC instead of MSE. In the MCC-based robust autoencoder, the cost function J is formulated as

$$\begin{aligned} J_{\text{MCC}}(\theta) &= \frac{1}{n} \sum_{i=1}^n L_{\text{MCC}}(x_i, y_i) \\ &= \frac{1}{n} \sum_{i=1}^n \sum_{j=1}^m \kappa_\sigma(x_i^j - y_i^j), \end{aligned} \quad (10)$$

where n is the number of training samples and m is the length of each training sample. The optimal parameter θ is obtained when $J_{\text{MCC}}(\theta)$ is maximized.

In order to encourage the deep model to capture more implicit patterns, a sparsity-inducing term is adopted. Studies of sparse coding have shown that the sparseness seems to play a key role in learning useful features [30, 31]. Xie et al. [32] combined the virtues of sparse coding and deep networks into a sparse stacked denoising autoencoder to achieve better feature learning and denoising performance. In our model, we regularize the reconstruction loss by a sparsity-inducing term defined as in [32] as follows:

$$J_{\text{sparse}}(\theta) = \beta \sum_{i=1}^{s_2} \text{KL}(\rho \parallel \hat{\rho}_i), \quad (11)$$

where β is the weight adjustment parameter, s_2 is the number of units in the second layer, $\hat{\rho}_i$ is the activation value for the i th hidden layer unit, and ρ is a small number. The sparsity-inducing term constrains that the value of $\hat{\rho}_i$ should be near ρ under Kullback-Leibler divergence.

Also, a weight decay term $J_{\text{weight}}(\theta)$ is added to avoid overfitting. It is defined as follows:

$$J_{\text{weight}}(\theta) = \frac{\lambda}{2} \sum_{l=1}^2 \sum_{i=1}^{s_l} \sum_{j=1}^{s_{l+1}} (w_{ji}^{(l)})^2, \quad (12)$$

where $w_{ji}^{(l)}$ represents an element in $W^{(l)}$, λ is the parameter to adjust the weight of $J_{\text{weight}}(\theta)$, and s_l denotes number of units in layer l . Therefore, the cost function of the proposed robust autoencoder is defined as

$$J_{\text{R-SAE}}(\theta) = -J_{\text{MCC}}(\theta) + J_{\text{weight}}(\theta) + J_{\text{sparse}}(\theta). \quad (13)$$

By minimizing the cost of $J_{\text{R-SAE}}(\theta)$, the parameter set θ could be optimized.

2.5.3. Stacking Robust Autoencoders into Deep Network. In order to learn more effective features for seizure classification, we stack the robust autoencoders into a deep model. Stacking the robust autoencoders works in the same way as stacking the ordinary autoencoders [17] and the output from the highest layer is cascaded to a softmax classifier for seizure detection. Such a model aims at the best seizure classification accuracy, and it is able to simultaneously optimize the feature and classifier.

The training process of the deep network includes two stages: unsupervised pretraining and supervised fine-tuning. In the pretraining stage, the network is trained layer-wisely by the proposed robust autoencoder model to learn useful filters for feature extraction. A well pretrained network yields a good starting point for fine-tuning [33]. In the fine-tuning stage, a softmax classifier is added to the output of the stack, and the parameters of the whole system are tuned to minimize the classification error in a supervised manner. The network is globally tuned through back-propagation and all the parameters of both feature extraction and classification are jointly optimized. After fine-tuning, the deep network is well configured to obtain optimal overall classification performance.

3. Results and Discussion

In this section, experiments are carried out to evaluate the seizure detection performance of our model. The experiments include four parts: (1) we compare the unsupervised feature learning performance of the modified R-SAE model and the standard stacked autoencoder (S-SAE); (2) we compare the features before and after supervised fine-tuning to demonstrate the strength of joint optimization; (3) we compare the seizure detection performance of R-SAE model with other methods; (4) we evaluate the influence of parameters in the R-SAE model on the seizure detection performance.

In our experiments, the seizure detection performance is evaluated with the two commonly used criteria, sensitivity and specificity. Sensitivity is defined as the percentage of true seizure segments detected and specificity is the proportion of nonseizure segments correctly classified.

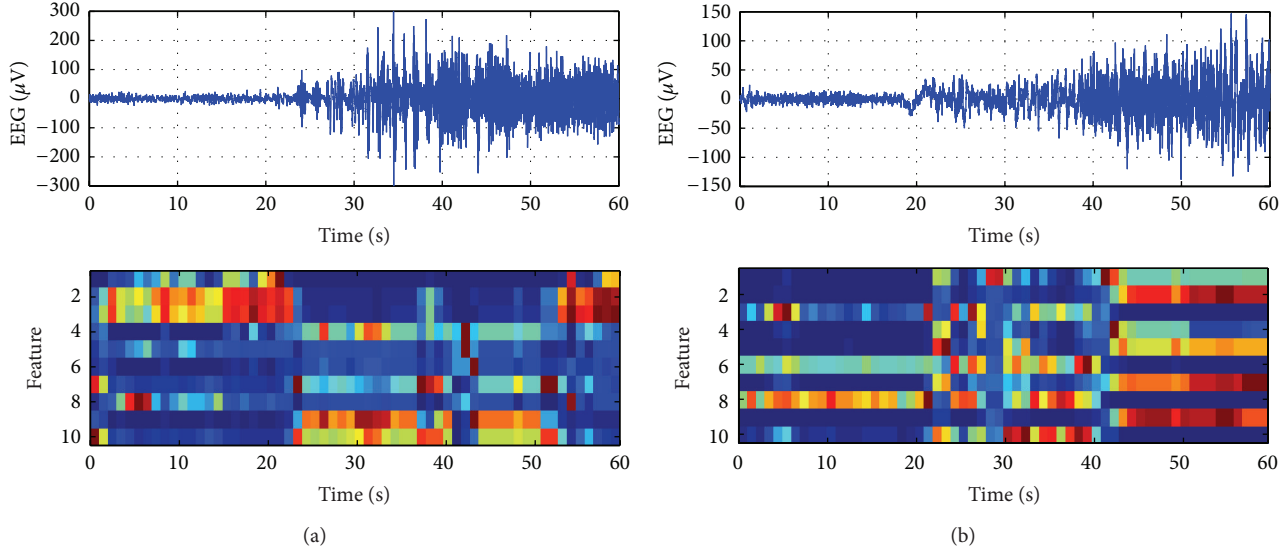


FIGURE 4: Unsupervised feature learning results by R-SAE model for patient pt03 (a) and pt04 (b). For each subfigure, the top is the original EEG signal from one channel and the bottom is the features extracted by the R-SAE model.

3.1. Performance of Feature Learning. In this experiment, we evaluate the unsupervised feature learning ability of the R-SAE model with EEG signals. In our method, we train the R-SAE model to learn compact features from the cross-power matrix. After the layer-wised self-taught training, the deep network is well configured to learn useful features. The feature extraction results of the proposed R-SAE model are illustrated in Figure 4. For both illustrations, the seizure begins at about the 20th second. After seizure onset, the patterns of features extracted by R-SAE model show clear differences from nonseizure ones.

The feature learning performance of R-SAE and S-SAE is compared using EEG signal. In order to evaluate the ability of the features quantitatively, we utilize the classification performance as the criterion. In this experiment, the cost function of the S-SAE model is as follows:

$$J_{\text{S-SAE}}(\theta) = J_{\text{MSE}}(\theta) + J_{\text{weight}}(\theta) + J_{\text{sparse}}(\theta), \quad (14)$$

where the loss function $J_{\text{MSE}}(\theta)$ is formulated with MSE-based loss function as in (6) and $J_{\text{weight}}(\theta)$ and $J_{\text{sparse}}(\theta)$ are formulated the same as R-SAE.

We stack two autoencoders to constitute a three-layer network with 784 input units, 50 hidden units, and 10 output units. The same stacked architectures are applied for both R-SAE and S-SAE. The networks are initialized randomly and trained layer-wisely using back-propagation to minimize the cost functions. The parameters are set as $\lambda = 0.003$, $\beta = 3$, and $\rho = 0.1$ for both methods and $\sigma = 0.05$ for R-SAE.

The seizure detection results of both R-SAE model and S-SAE model are shown in Table 2. In order to eliminate the effects of randomness in network initialization, we present all the results averaged over 10 trials. Results show that the average sensitivity of R-SAE is 97%, which demonstrates 14% improvement compared with S-SAE. With specificity, the average result is 92% for R-SAE which is also higher than that

of S-SAE. Thus, R-SAE outperforms S-SAE in both sensitivity and specificity.

In the analysis of the detection results, we find that S-SAE fails mostly on EEG segments with impulsive noises such as the segment illustrated in Figure 2. Since such abrupt artifacts could appear frequently in EEG signals, the S-SAE model could not be well trained because the MSE-based cost could be dominated by the large outliers. Thus, these EEG segments could not be well represented by the S-SAE model. By contrast, the MCC in the R-SAE model is more robust to large outliers. Therefore, the proposed R-SAE method could handle noises in EEG signal well, and it provides more robust feature extraction performance than S-SAE.

3.2. Performance of Joint Feature Optimization. In this experiment, we test the effects of joint feature optimization. After the MCC-based unsupervised learning, the deep network is well configured to extract useful features from EEG signals. On this basis, the deep model is fine-tuned through back-propagation to jointly optimize both feature and classifier, so that the optimal overall classification performance could be achieved. In this experiment, the parameters of R-SAE are set the same as in Section 3.1 that only the unit number of the output layer is set to 3 for visualization convenience.

The visual comparison of features before and after fine-tuning is illustrated in Figure 5. In Figures 5(a) and 5(b), the red circles denote features of seizure segments while the blue stars are nonseizure ones. It can be seen that, after fine-tuning, the seizure and nonseizure segments are more separable in the feature space. We quantitatively analyze the separability of the features before and after fine-tuning with the FDR criterion as in (2) using the first four patients. As illustrated in Figure 5(c), the fine-tuned features achieve about ten times higher FDR than do the original ones, which strongly indicates that the joint optimization could help to

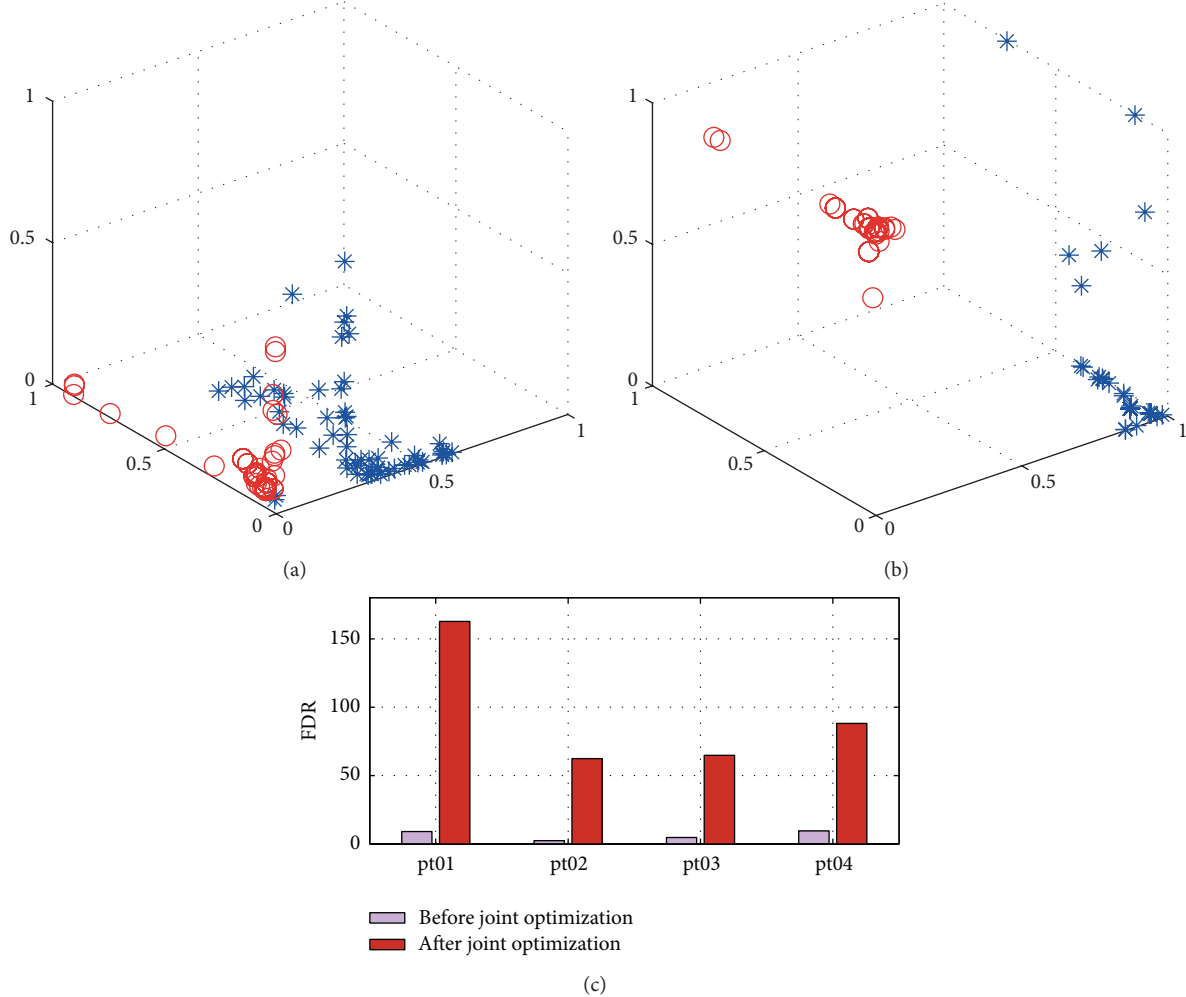


FIGURE 5: Comparison between features before and after joint optimization. (a-b) Visualization of features for seizure and nonseizure segments. The red circles denote features of seizure segments while the blue stars are nonseizure ones. (c) The FDR value of features before and after joint optimization.

TABLE 2: Comparison between R-SAE and S-SAE (before fine-tuning).

Patient	R-SAE		S-SAE	
	Sensitivity	Specificity	Sensitivity	Specificity
Pt01	$0.99 \pm 8.1 \times 10^{-3}$	$0.96 \pm 2.0 \times 10^{-2}$	$0.83 \pm 2.0 \times 10^{-1}$	$0.92 \pm 3.2 \times 10^{-2}$
Pt02	$0.96 \pm 2.0 \times 10^{-2}$	$0.91 \pm 1.7 \times 10^{-2}$	$0.90 \pm 1.0 \times 10^{-1}$	$0.83 \pm 7.6 \times 10^{-2}$
Pt03	$0.96 \pm 1.5 \times 10^{-2}$	$0.93 \pm 2.1 \times 10^{-2}$	$0.82 \pm 2.8 \times 10^{-1}$	$0.93 \pm 3.2 \times 10^{-2}$
Pt04	$0.95 \pm 3.7 \times 10^{-2}$	$0.91 \pm 1.3 \times 10^{-2}$	$0.91 \pm 4.1 \times 10^{-2}$	$0.92 \pm 2.6 \times 10^{-2}$
Pt05	$0.98 \pm 1.7 \times 10^{-2}$	$0.94 \pm 1.5 \times 10^{-2}$	$0.70 \pm 1.3 \times 10^{-1}$	$0.96 \pm 2.4 \times 10^{-2}$
Pt06	$0.97 \pm 2.9 \times 10^{-2}$	$0.84 \pm 5.5 \times 10^{-2}$	$0.82 \pm 1.7 \times 10^{-1}$	$0.90 \pm 1.5 \times 10^{-2}$
Avg.	$0.97 \pm 1.3 \times 10^{-2}$	$0.92 \pm 3.8 \times 10^{-2}$	$0.83 \pm 6.9 \times 10^{-2}$	$0.91 \pm 4.0 \times 10^{-2}$

learn superior features with high separability, so that the seizure detection performance could be improved.

The seizure detection performance of features before and after fine-tuning is presented in Table 3. After joint feature learning, the average sensitivity of six patients increases by 8% and the specificity increases by 15%. Therefore, the joint learning process enhances the separability of features

between the two classes and greatly facilitates seizure detection performance.

3.3. Performance of Seizure Detection. In this experiment, seizure detection performance of the proposed R-SAE model is evaluated and compared with singular value decomposition-(SVD-) based method. The SVD method is the most popular

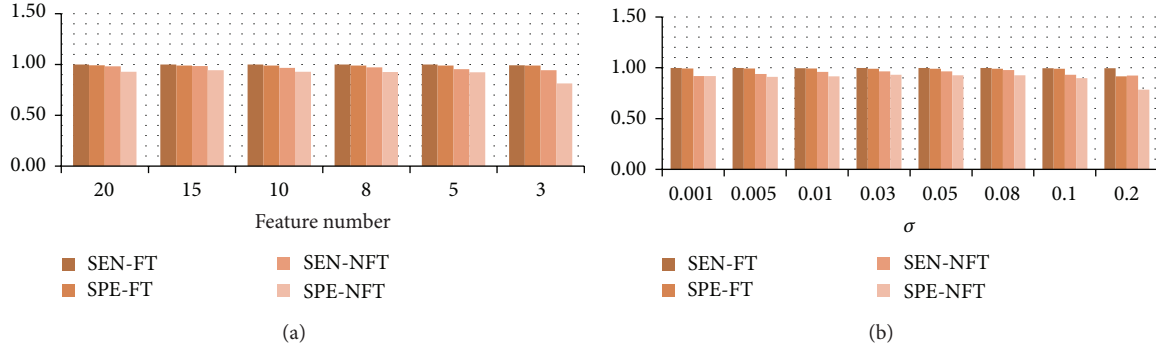


FIGURE 6: Model analysis of two important parameters of R-SAE. (a) Seizure detection performance under different feature numbers; (b) seizure detection performance with different selections of σ . In this figure, SEN-FT and SPE-FT are sensitivity and specificity after fine-tuning and SEN-NFT and SPE-NFT are those before fine-tuning.

TABLE 3: Comparison of seizure detection performance before and after fine-tuning (FT).

Feature	Sensitivity	Specificity
Before FT	$0.90 \pm 1.0 \times 10^{-1}$	$0.84 \pm 1.4 \times 10^{-1}$
After FT	$0.98 \pm 3.1 \times 10^{-2}$	$0.99 \pm 4.7 \times 10^{-3}$

tool for correlation matrix analysis. Studies have shown that the seizure EEG signals commonly lead to a lower-complexity state which could be well reflected by the eigenvalues from SVD of the correlation matrix [10, 22].

To provide a benchmark for the comparison, we also test the seizure detection performance with the original cross-power matrix without further feature extraction. The methods included in the comparison are configured as follows.

- (i) *SVM*: in SVM, the cross-power matrices of time windows are reshaped to vectors and fed into an SVM classifier with RBF kernel. The parameters of the SVM model are selected using 3-fold cross-validation.
- (ii) *SVD(p) + SVM*: for each time window, the cross-power matrix is decomposed by SVD, and the first p eigenvalues are adopted as the features. The feature vectors are then classified by an SVM classifier with RBF kernel. The parameters of the SVM model are selected using 3-fold cross-validation.
- (iii) *R-SAE(q)*: the R-SAE model is configured with 784 input units, 50 hidden units, and q output units. The parameters are set as $\lambda = 0.003$, $\beta = 3$, $\rho = 0.1$, and $\sigma = 0.05$. For this method, all results are averaged over 10 trials.

The seizure detection results of the three methods are given in Table 4. For both SVD + SVM and R-SAE, we test the seizure detection performance under two different choices of parameters of p and q , respectively. Results show that, with the original cross-power matrix classified by SVM, high sensitivities of above 0.99 are achieved for all six patients and the average specificity is 0.91. By the SVD + SVM method with $p = 3$, uneven performance is shown in different patients. For pt03, high sensitivity of 0.96 is reached with

0.99 of specificity. However, low sensitivities are obtained for pt01, pt05, and pt06. For SVD + SVM method with $p = 10$ where more features are preserved, better sensitivities and specificities are achieved. However, the uneven performance over patients still exists, and the average sensitivity is only 0.83. Since the feature extraction process of the SVD-based method loses much useful information, lower performance is obtained compared with SVM benchmark. Besides, the seizure detection performance sees a decrease when fewer eigenvalues are used. By contrast, the proposed R-SAE method achieves better performance than the benchmark SVM method. In R-SAE with $q = 10$, high sensitivities of 1.00 and specificities of 0.99 are achieved for all patients. Equally high performance is obtained with $p = 3$. The R-SAE model keeps robust seizure detection ability even with such small dimension of features.

3.4. Model Analysis. In this experiment, we test the influence of the two important parameters on the seizure detection performance. The first parameter is the output feature number, that is, the number of units of the output layer of the R-SAE model, and the second parameter is the kernel size σ in MCC. The experiment is carried out using the first four patients.

3.4.1. Analysis of Feature Number. The feature number is tuned by the parameter q in Section 3.3. In order to test the influence of q on seizure detection, all the other parameters are fixed as in Section 3.3 and we gradually tune q from 20 to 3. Figure 6(a) illustrates the seizure detection results averaged over four patients under different choices of q . The result shows that the seizure detection performance of R-SAE before fine-tuning sees a slight decrease with the decrease of feature number. However, after the fine-tuning, the seizure detection performance is greatly enhanced that high sensitivities and specificities up to 99% are achieved even with small feature numbers.

3.4.2. Analysis of σ . In the MCC, the kernel size σ serves as an important parameter that an appropriate choice of σ can effectively suppress the outliers and noises. The kernel size or bandwidth is a free parameter that its selection is still an

TABLE 4: Comparison with other methods.

Method	Pt01		Pt02		Pt03		Pt04		Pt05		Pt06		Avg	
	SEN*	SPE*	SEN	SPE	SEN	SPE								
SVM	1.00	0.96	1.00	0.89	1.00	0.93	0.99	0.95	1.00	0.96	1.00	0.78	1.00	0.91
SVD(3) + SVM [10]	0.45	1.00	0.72	0.99	0.96	0.99	0.84	0.95	0.46	0.98	0.64	0.97	0.68	0.98
SVD(10) + SVM [10]	0.61	1.00	0.76	0.99	0.99	1.00	0.80	0.95	0.84	0.93	0.95	0.96	0.83	0.97
R-SAE(3)	1.00	0.99	0.99	0.99	0.98	0.99	1.00	0.99	1.00	0.99	0.92	0.98	0.98	0.99
R-SAE(10) (ours)	1.00	0.99	1.00	0.99	1.00	0.99	1.00	0.99	1.00	0.99	0.99	0.97	1.00	0.99

* SEN indicates sensitivity and SPE is specificity.

open issue in ITL [26, 29, 34]. In practice, the parameter σ can be selected with Silverman's rule [35]. In the experiments of Sections 3.1–3.3, we simply set $\sigma = 0.05$.

Here, we test the influence of parameter σ on overall seizure detection performance. Also, all the other parameters are fixed as in Section 3.3. Figure 6(b) illustrates the seizure detection results under different selections of σ averaged over four patients. Results show that high seizure detection performance could be achieved under a wide choice of σ . Better results are obtained with small σ , and when σ increases from 0.1 to 0.2, the seizure detection performance becomes worse. In practice, the choice of σ should be small to keep good local property of the MCC.

4. Conclusions

In this paper, we have presented a novel deep model which is capable of extracting robust features under large amounts of outliers. Experimental results show that the proposed R-SAE model could learn effective features in EEG signals for high performance seizure detection, and it is promising for clinical applications.

Conflict of Interests

The authors declare that there is no conflict of interests regarding the publication of this paper.

Acknowledgments

This research was supported by Grants from the National Natural Science Foundation of China (no. 61031002), National 973 Program (no. 2013CB329500), National High Technology Research and Development Program of China (no. 2012AA020408), National Natural Science Foundation of China (no. 61103107), and Zhejiang Provincial Science and Technology Project (no. 2013C03045-3).

References

- [1] *Epilepsy*, Factsheet no. 999, World Health Organization, Geneva, Switzerland, 2012.
- [2] R. S. Fisher, W. Van Emde Boas, W. Blume et al., "Epileptic seizures and epilepsy: definitions proposed by the International League Against Epilepsy (ILAE) and the International Bureau for Epilepsy (IBE)," *Epilepsia*, vol. 46, no. 4, pp. 470–472, 2005.
- [3] F. Mormann, R. G. Andrzejak, C. E. Elger, and K. Lehnertz, "Seizure prediction: the long and winding road," *Brain*, vol. 130, no. 2, pp. 314–333, 2007.
- [4] M. E. Saab and J. Gotman, "A system to detect the onset of epileptic seizures in scalp EEG," *Clinical Neurophysiology*, vol. 116, no. 2, pp. 427–442, 2005.
- [5] K. Majumdar and P. Vardhan, "Automatic seizure detection in ECoG by differential operator and windowed variance," *IEEE Transactions on Neural Systems and Rehabilitation Engineering*, vol. 19, no. 4, pp. 356–365, 2011.
- [6] R. Yadav, A. K. Shah, J. A. Loeb, M. N. S. Swamy, and R. Agarwal, "Morphology-based automatic seizure detector for intracerebral EEG recordings," *IEEE Transactions on Biomedical Engineering*, vol. 59, no. 7, pp. 1871–1881, 2012.
- [7] S. Ghosh-Dastidar, H. Adeli, and N. Dadmehr, "Principal component analysis-enhanced cosine radial basis function neural network for robust epilepsy and seizure detection," *IEEE Transactions on Biomedical Engineering*, vol. 55, no. 2, pp. 512–518, 2008.
- [8] A. S. Zandi, M. Javidan, G. A. Dumont, and R. Tafreshi, "Automated real-time epileptic seizure detection in scalp EEG recordings using an algorithm based on wavelet packet transform," *IEEE Transactions on Biomedical Engineering*, vol. 57, no. 7, pp. 1639–1651, 2010.
- [9] C. C. Jouny and G. K. Bergey, "Characterization of early partial seizure onset: Frequency, complexity and entropy," *Clinical Neurophysiology*, vol. 123, no. 4, pp. 658–669, 2012.
- [10] S. Santaniello, S. P. Burns, A. J. Golby, J. M. Singer, W. S. Anderson, and S. V. Sarma, "Quickest detection of drug-resistant seizures: an optimal control approach," *Epilepsy and Behavior*, vol. 22, supplement 1, pp. S49–S60, 2011.
- [11] D. Liu and Z. Pang, "Epileptic seizures predicted by modified particle filters," in *Proceedings of the IEEE International Conference on Networking, Sensing and Control (ICNSC08)*, pp. 351–356, IEEE, Sanya, China, April 2008.
- [12] D. Liu, Z. Pang, and Z. Wang, "Epileptic seizure prediction by a system of particle filter associated with a neural network," *EURASIP Journal on Advances in Signal Processing*, vol. 2009, Article ID 638534, 2009.
- [13] P. Vincent, H. Larochelle, Y. Bengio, and P. Manzagol, "Extracting and composing robust features with denoising autoencoders," in *Proceedings of the 25th International Conference on Machine Learning*, pp. 1096–1103, ACM, July 2008.
- [14] G. E. Hinton, S. Osindero, and Y. Teh, "A fast learning algorithm for deep belief nets," *Neural Computation*, vol. 18, no. 7, pp. 1527–1554, 2006.

- [15] G. E. Hinton and R. R. Salakhutdinov, "Reducing the dimensionality of data with neural networks," *The American Association for the Advancement of Science. Science*, vol. 313, no. 5786, pp. 504–507, 2006.
- [16] Y. Boureau and Y. Cun, "Sparse feature learning for deep belief networks," in *Proceedings of the Advances in Neural Information Processing Systems*, pp. 1185–1192, 2007.
- [17] Y. Bengio, "Learning deep architectures for AI," *Foundations and Trends in Machine Learning*, vol. 2, no. 1, pp. 1–27, 2009.
- [18] R. Salakhutdinov, J. B. Tenenbaum, and A. Torralba, "Learning with hierarchical-deep models," *IEEE Transactions on Pattern Analysis and Machine Intelligence*, vol. 35, no. 8, pp. 1958–1971, 2013.
- [19] H. Lee, R. Grosse, R. Ranganath, and A. Y. Ng, "Convolutional deep belief networks for scalable unsupervised learning of hierarchical representations," in *Proceedings of the 26th International Conference on Machine Learning (ICML '09)*, pp. 609–616, Montreal, Canada, June 2009.
- [20] G. Hinton, L. Deng, D. Yu et al., "Deep neural networks for acoustic modeling in speech recognition: the shared views of four research groups," *IEEE Signal Processing Magazine*, vol. 29, no. 6, pp. 82–97, 2012.
- [21] H. Lee, L. Yan, P. Pham, and A. Y. Ng, "Unsupervised feature learning for audio classification using convolutional deep belief networks," in *Proceedings of the 23rd Annual Conference on Neural Information Processing Systems (NIPS '09)*, vol. 9, pp. 1096–1104, December 2009.
- [22] K. Schindler, H. Leung, C. E. Elger, and K. Lehnertz, "Assessing seizure dynamics by analysing the correlation structure of multichannel intracranial EEG," *Brain*, vol. 130, no. 1, pp. 65–77, 2007.
- [23] K. A. Schindler, S. Bialonski, M. Horstmann, C. E. Elger, and K. Lehnertz, "Evolving functional network properties and synchronizability during human epileptic seizures," *Chaos*, vol. 18, no. 3, Article ID 033119, 2008.
- [24] C. Rummel, M. Müller, G. Baier, F. Amor, and K. Schindler, "Analyzing spatio-temporal patterns of genuine cross-correlations," *Journal of Neuroscience Methods*, vol. 191, no. 1, pp. 94–100, 2010.
- [25] B. Scholkopf and K. Mullert, "Fisher discriminant analysis with kernels," 1999.
- [26] L. Weifeng, P. P. Pokharel, and J. C. Principe, "Correntropy: a localized similarity measure," in *Proceedings of the International Joint Conference on Neural Networks (IJCNN '06)*, pp. 4919–4924, July 2006.
- [27] K. Jeong, W. Liu, S. Han, E. Hasanbelliu, and J. C. Principe, "The correntropy MACE filter," *Pattern Recognition*, vol. 42, no. 5, pp. 871–885, 2009.
- [28] R. He, B. Hu, W. Zheng, and X. Kong, "Robust principal component analysis based on maximum correntropy criterion," *IEEE Transactions on Image Processing*, vol. 20, no. 6, pp. 1485–1494, 2011.
- [29] W. Liu, P. P. Pokharel, and J. C. Principe, "Correntropy: properties and applications in non-Gaussian signal processing," *IEEE Transactions on Signal Processing*, vol. 55, no. 11, pp. 5286–5298, 2007.
- [30] B. A. Olshausen and D. J. Field, "Emergence of simple-cell receptive field properties by learning a sparse code for natural images," *Nature*, vol. 381, no. 6583, pp. 607–609, 1996.
- [31] H. Lee, A. Battle, R. Raina, and A. Ng, "Efficient sparse coding algorithms," *Advances in Neural Information Processing Systems*, vol. 19, pp. 801–808, 2007.
- [32] J. Xie, L. Xu, and E. Chen, "Image denoising and inpainting with deep neural networks," in *Proceedings of the 26th Annual Conference on Neural Information Processing Systems (NIPS '12)*, vol. 25, pp. 350–358, December 2012.
- [33] P. Vincent, H. Larochelle, I. Lajoie, and P. Manzagol, "Stacked denoising autoencoders: learning useful representations in a deep network with a local denoising criterion," *Journal of Machine Learning Research*, vol. 11, pp. 3371–3408, 2010.
- [34] R. He, W. Zheng, B. Hu, and X. Kong, "A regularized correntropy framework for robust pattern recognition," *Neural Computation*, vol. 23, no. 8, pp. 2074–2100, 2011.
- [35] B. Silverman, *Density Estimation for Statistics and Data analysis*, vol. 26, CRC Press, 1986.

Research Article

A Study on Decoding Models for the Reconstruction of Hand Trajectories from the Human Magnetoencephalography

Hong Gi Yeom,^{1,2} Wonjun Hong,³ Da-Yoon Kang,⁴ Chun Kee Chung,^{1,2,5,6} June Sic Kim,^{1,2,5,7} and Sung-Phil Kim⁴

¹ MEG Center, Department of Neurosurgery, Seoul National University Hospital, Seoul 110-744, Republic of Korea

² Interdisciplinary Program in Neuroscience, Seoul National University College of Natural Sciences, Seoul 151-742, Republic of Korea

³ The Planet SK Co., Ltd., Seongnam 463-400, Republic of Korea

⁴ School of Design and Human Engineering, Ulsan National Institute of Science and Technology, Ulsan 689-798, Republic of Korea

⁵ Department of Neurosurgery, Seoul National University College of Medicine, Seoul 110-744, Republic of Korea

⁶ Department of Brain & Cognitive Sciences, Seoul National University College of Natural Sciences, Seoul 151-742, Republic of Korea

⁷ Sensory Organ Research Institute, Seoul National University, Seoul 151-742, Republic of Korea

Correspondence should be addressed to June Sic Kim; jskim@meg.re.kr and Sung-Phil Kim; spkim@unist.ac.kr

Received 28 March 2014; Accepted 21 May 2014; Published 22 June 2014

Academic Editor: Yiwen Wang

Copyright © 2014 Hong Gi Yeom et al. This is an open access article distributed under the Creative Commons Attribution License, which permits unrestricted use, distribution, and reproduction in any medium, provided the original work is properly cited.

Decoding neural signals into control outputs has been a key to the development of brain-computer interfaces (BCIs). While many studies have identified neural correlates of kinematics or applied advanced machine learning algorithms to improve decoding performance, relatively less attention has been paid to optimal design of decoding models. For generating continuous movements from neural activity, design of decoding models should address how to incorporate movement dynamics into models and how to select a model given specific BCI objectives. Considering nonlinear and independent speed characteristics, we propose a hybrid Kalman filter to decode the hand direction and speed independently. We also investigate changes in performance of different decoding models (the linear and Kalman filters) when they predict reaching movements only or predict both reach and rest. Our offline study on human magnetoencephalography (MEG) during point-to-point arm movements shows that the performance of the linear filter or the Kalman filter is affected by including resting states for training and predicting movements. However, the hybrid Kalman filter consistently outperforms others regardless of movement states. The results demonstrate that better design of decoding models is achieved by incorporating movement dynamics into modeling or selecting a model according to decoding objectives.

1. Introduction

Brain-computer interfaces (BCIs) aim to establish an artificial interface between the brain and external systems through which a person can control effectors without physical movements [1–4]. BCIs have been applied to rehabilitation of motor functions lost due to neurological disorders. For instance, a number of studies have demonstrated that patients with tetraplegia could control assistive systems directly using BCIs [5–10]. Also, in conjunction with robotic devices, BCIs have been used to detect motor intentions of stroke patients to develop a self-regulating rehabilitation system [11–14].

Restoration of motor functions particularly in people with paralysis has been mostly investigated using invasive BCIs that harness an ensemble of single-unit spiking activity [5–8]. These BCIs have been designed to generate continuous kinematic parameters such as position, velocity, acceleration, force, and joint angles of limb movements [15–20]. Recently, noninvasive BCIs based on electroencephalography (EEG) or magnetoencephalography (MEG) have also been proposed to predict continuous kinematic parameters of arm movements in humans [21–27].

Inference of continuous kinematic parameters from neural signals requires accurate and reliable neural decoding

models [28–33]. Decoding models aim to find a functional mapping between neural representations and one or more kinematic parameters. A number of mathematical models have been employed as decoding models for invasive and noninvasive BCIs, including the linear filter, Kalman filter, point process models, neural networks, and support vector machine, to name a few [34–40]. Many BCI studies on the construction of decoding models have been focused on proposing a state-of-the-art machine learning technique as a new decoding model or simply comparing different decoding models in terms of decoding performance to choose the best one for their applications [40]. In particular, the design of noninvasive BCIs has been generally rather concentrated on finding optimal neural features than optimizing decoding models. This is partly because the noninvasive BCI output space is more likely limited and usually discrete so that the characteristics of the output space seem less important to designing decoding models. However, when a noninvasive BCI is used to produce continuous kinematic states, which create a much sophisticated and dynamic output state space, one may need to be concerned with how to incorporate the characteristics of kinematic parameters into decoding models. In addition, departing from a simple comparison among candidate models followed by the selection of the best, it would be beneficial if we understand more about how individual decoding models work in different circumstances. It can then provide a useful guideline for BCI researchers to choose a decoding model appropriate for their own applications.

In the present study, we investigate whether consideration of hand movement dynamics in the design of decoding models can enhance decoding performance. The investigation is conducted on the human MEG data collected from a noninvasive BCI experiment in which the human subjects performed point-to-point arm reaching movements. We focus especially on the nonlinear characteristics of the hand speed profile and its independence of movement directions. While many BCI studies have typically decoded the hand velocity from neural signals, the hand speed alone could also be decoded from neural signals during point-to-point reaching movements [19, 41, 42]. Hence, we propose to decompose the hand velocity into its speed and direction parameters and decode each parameter independently. While we use the standard Kalman filter for hand direction estimation, due to the nonlinear characteristics of hand speed profiles, we simply augment the Kalman filter by adding a nonlinear filter for hand speed estimation. Then, we investigate whether such hybrid decoding of speed and direction can improve hand trajectory reconstruction from the human MEG signals.

Also, we investigate how decoding models are affected by varying model design factors. Here we examine the effect of choosing movement states on different decoding models. Specifically, we study the effect of two distinct arm movement states: the rest and reach states [43]. Performance of individual decoding models is evaluated for two cases when each model estimates the reach state only or both states together. As for decoding models, we examine the two most widely used filters for kinematic estimation in BCIs—the

Kalman filter and linear filter—as well as the hybrid filter newly proposed above.

To assess the performance of decoding continuous hand trajectories, we adopt the evaluation measures used for pointing devices [44]. These measures have also been leveraged to assess neural cursor control performance in the previous BCI studies [7, 8, 45] and may well serve to evaluate reconstructed trajectories of pointing movements. Various performance measures used in this study are expected to collectively provide a richer assessment tool for decoding performance.

2. Materials and Methods

2.1. Experimental Procedure. Nine subjects (19–37 years; five males) participated in the study. All the participants were right-handed (>80 on the Edinburgh Handedness Inventory score) and not color-blind. The institutional review board (IRB) of the Seoul National University Hospital approved this study and all the participants provided written informed consent after the study procedure had been explained to them. During the experiment, the participants were instructed to move their right arm in a specified three-dimensional space while their other body parts were fixed (Figure 1(a)). A cushion was placed under the participants' elbow to minimize the potential artifacts from the arm movement. Participants' head movements were restricted by placing their head in a fixed MEG helmet. In addition, the tSSS filtering was applied to the MEG signals, as described in Section 2.3, to reduce artifacts from external sources. Stereographic images were shown on the screen using the STIM2 system (Neuroscan, El Paso, TX, USA) in order to give instructions of the three-dimensional movements.

In the beginning of the experiment, the participants were shown a sphere in the middle of the screen for four seconds. In this period, the participants were instructed to locate their index finger on the sphere. After this initial period, a target sphere appeared for one second in one of the four corners along with a line that connected the target with the center sphere. During this period, the participants were instructed to move their index finger from the center to the target sphere following the line (a center-out task) and to move back to the center sphere as fast as they could. Average movement time was 930.1 ± 330.5 ms (mean \pm SD). A trial ended after this period and continued onto the next initial period of the consecutive trial. No time limit was imposed on a trial because the time interval between trials was large enough (4 s) to allow participants to complete the movement task and rest until the onset of the subsequent movement. The location of target sphere was randomly determined in each of the four corners: upper-left, upper-right, bottom-left, and bottom-right corners. A single session consisted of one hundred twenty trials, including thirty trials per target. Each participant completed two sessions (Figure 1(c)).

2.2. Virtual Stimuli. An anaglyph approach was employed to produce three-dimensional images that were used as stimuli in our experiment. An image generated by the anaglyph approach is invisible when a person sees it with the same

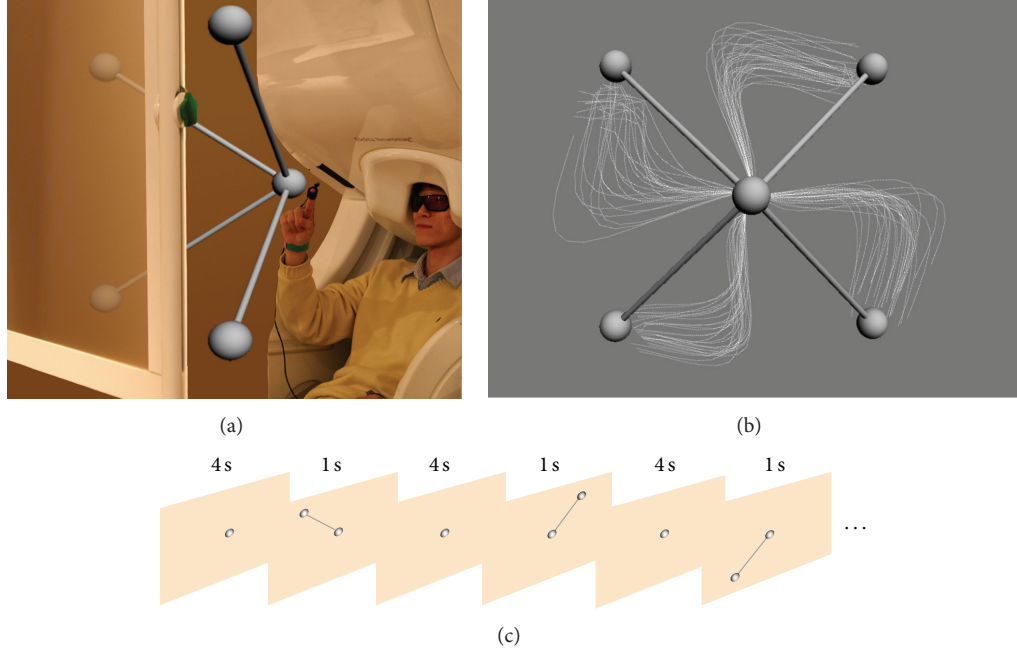


FIGURE 1: Experiment paradigm. (a) A photograph showing the visual stimuli. Whole-head MEG signals were acquired during point-to-point reaching movements (center-out paradigm). (b) Movement speed profiles for different target directions. Each gray line illustrates a speed profile for each reaching movement towards one of four targets (radial) from the center target (middle). (c) Drawings show the sequence of the visual stimuli. At the beginning of the experiment, a sphere was presented on the center of the screen. After 4 s, a target sphere with a stick connected to the center sphere appeared on one corner for 1 s. The subject was instructed to move his/her right index finger from the center to the target and trace back to the center within this 1 s period. The target appeared in a pseudorandom order.

color of glasses as the image color. The participants wore the colored glasses with a red glass on one eye and a blue glass on the other. Then, if a single object was shown as two different images each being colored in red or blue, each eye would only sense the image with opposite color and the object would stand at the intersection of two visual fields, to create a 3D virtual object [27]. We thus generated two images of the same object with different viewpoints (i.e., different angles) using the Autodesk 3ds MAX 2011 program (Autodesk, San Rafael, CA, USA). Those two images were then converted into an anaglyph image using the Anaglyph Maker software (ver. 1.08; <http://www.stereoeye.jp/>).

2.3. MEG Data Acquisition and Processing. A 306-channel whole-head MEG system (VectorView, Elekta Neuromag Oy, Helsinki, Finland) was used to record human MEG signals during the experiment in the magnetic shielded room. The system consisted of 306 sensors in triplets of two planar gradiometers and one magnetometer distributed at the 102 locations over the whole brain. In this study, only gradiometers were used due to their better signal-noise ratio (SNR) than magnetometers [46]. The MEG signal was digitized at a sample frequency of 600.615 Hz and band-pass filtered at 0.1–200 Hz. A three-axis accelerometer (KXN52, Kionix, NY, USA) was attached on the index finger of the participants to record three-dimensional acceleration signals with the same sample rate as the MEG signals.

We further applied the spatiotemporal signal space separation (tSSS) method to the MEG signals to alleviate external interference noise [47]. The MEG signals were then divided into a series of epochs each from −1 to 2 seconds after target onset. The accelerometer signal was band-pass filtered at 0.2–5 Hz so as to remove linear trends. The index finger velocity was obtained by integrating the accelerometer signal.

We selected sixty-eight gradiometer channels at thirty-four locations over bilateral sensorimotor areas for our study (see [27] for the exact location information). The MEG signal from each of these channels was band-pass filtered at 0.5–8 Hz. The filtered signals were downsampled to 50 Hz. The estimated velocity signals at the x -, y -, and z -coordinates were also downsampled to 50 Hz. In this study, we only used the x and y velocity signals to simplify decoding analyses because the most variance of the hand trajectories was present in the x - and y -axis.

2.4. Decoding Models

2.4.1. Linear Filter. The x - and y -coordinates of the hand velocity at time t were estimated by a linear filter (LF) that linearly combined the short history of the MEG signals at each of sixty-eight channels to predict the velocity [25, 27]. The size of the history window applied to each channel was 200 ms, corresponding to 11 sample points (a current time point plus 10 preceding time points with a 50 Hz

sampling rate). The window size was empirically determined with which the optimal decoding performance was achieved [27]. The prediction by LF was executed for each velocity coordinate as follows:

$$\begin{aligned} v_x(t) &= \sum_{i=1}^n \sum_{j=0}^m \alpha_{ij}^x z_i(t-j) + \alpha_0^x, \\ v_y(t) &= \sum_{i=1}^n \sum_{j=0}^m \alpha_{ij}^y z_i(t-j) + \alpha_0^y, \end{aligned} \quad (1)$$

where $v_x(t)$ and $v_y(t)$ are the estimated x - and y -coordinates of velocity at time t , respectively. $z_i(t-j)$ is a MEG signal sample at channel i and time $t-j$, and α_{ij}^x and α_{ij}^y are weights of LF. α_0 is a bias term for each velocity coordinate, n is the number of channels ($n = 68$), and m is the size of the history window ($m = 10$). The weights, α_{ij} and α_0 , were estimated using the multiple linear regression method.

2.4.2. Kalman Filter. The Kalman filter (KF) has been successfully used as a decoding algorithm of kinematic variables such as position, velocity, and acceleration in a number of BCI studies [5, 7, 8, 34]. Construction of KF is based on linear Gaussian system and observation models as follows:

$$\mathbf{z}(t) = H(t) \mathbf{d}(t) + \boldsymbol{\varepsilon}(t), \quad (2)$$

$$\mathbf{x}(t) = A(t) \mathbf{x}(t-1) + \boldsymbol{\nu}(t). \quad (3)$$

The observation model describes how neural observations are generated from movement states (2). $H(t)$ is the matrix of mapping movement states $\mathbf{x}(t)$ to each neural signal and estimated from the training data by the least-squares method. The observation error vector, $\boldsymbol{\varepsilon}(t)$, is assumed to be a multivariate Gaussian random vector with zero mean and a covariance matrix, $Q(t)$. Here we assume that H and Q are time invariant. The system model describes the evolution of movements in time (3). It is assumed to follow a Markov process. The system matrix $A(t)$ is also estimated by the least-squares method. The system error vector $\boldsymbol{\nu}(t)$ is assumed to follow a multivariate Gaussian random vector with zero mean and a covariance matrix of $W(t)$. Again, we assume that A and W are time invariant.

Once the model parameters are estimated from the training data, the hand velocity signals (a 2D velocity state in the case of KF) can be decoded by KF following the two steps. In the first step, the system model predicts the velocity state at time t from the state at $t-1$. In the second step, the observation model estimates a neural vector using the predicted velocity state and updates the predicted velocity state based on a difference between those observed and the predicted neural data. These steps are recursively applied to every neural observation.

2.4.3. A Hybrid Kalman Filter. With an aim to incorporate the arm movement dynamics into a modeling scheme, we exploited two particular aspects of the hand speed characteristics, including nonlinearity and independence. That is, the hand speed exhibits a typical bell-shaped nonlinear

profile during a point-to-point movement and its profile is independent of movement direction (see Figure 1(b)). To this end, we first added new state variables to the velocity state variables to represent the speed state. In particular, we created three speed state variables including $r(t)$, $r(t-1)$, and $r(t-2)$ to represent the states of current speed, the absolute acceleration, and the absolute jerk, respectively. Selection of three speed state variables was based on an observation that the bell-shaped speed profile might be described by at least three temporal terms. Then, the state vector of the new Kalman filter at time t was given by

$$\mathbf{x}(t) = [r(t) \ r(t-1) \ r(t-2) \ d_x(t) \ d_y(t)]^T, \quad (4)$$

where $d_x(t)$ and $d_y(t)$ denote x - and y -direction, respectively.

Next, we augmented the Kalman filter by adding a nonlinear filter. This nonlinear filter predicted the current hand speed from the three speed state variables. We realized the nonlinear filter using a multilayer perceptron (MLP), composed of eighteen hidden units with the hypertangent activation functions and one output unit with the logistic sigmoid activation function. Note that MLP only receives the speed state without direction input to be consistent with our assumption of independence of speed from direction. MLP is trained using the scaled conjugate gradient algorithm.

The hand direction is directly estimated from a subset of the state vector of the Kalman filter, $\mathbf{x}_v(t) = [d_x(t) \ d_y(t)]^T$. At every estimation iteration, the direction vector at time t is normalized by $\mathbf{x}_v(t)/\|\mathbf{x}_v(t)\|$ to have a unit length. The direction vector is multiplied by the estimated speed value from MLP to finally produce a velocity estimate at time t .

2.5. Performance Evaluation. In order to evaluate decoding performance, we first used a conventional measure using root-mean-squared-error (RMSE) to assess gross accuracy. RMSE measures the grand average of the root of squared errors between the true and decoded hand trajectories. In addition, to assess finer characteristics of continuous hand trajectories decoded by BCIs, we evaluated decoded trajectories using pointing device assessment metrics [44]. A decoded hand trajectory was evaluated with respect to the task axis in terms of four metrics: orthogonal direction change (ODC), movement direction change (MDC), movement error (ME), and movement variability (MV). The task axis was defined as an optimal straight path between the starting point and the center of the targets. ODC measures directional changes orthogonal to the task axis. ODC represents the consistency of a decoded trajectory toward the target. MDC measures directional changes in parallel with the task axis. MDC depicts the smoothness of the decoded trajectory. ME measures a mean distance of the decoded trajectory from the task axis. ME exhibits how much a decoded trajectory is different from the optimal path. MV measures the standard deviation between a decoded trajectory and the task axis. MV depicts the straightness of a decoded trajectory. For more details of these four metrics, the reader can be referred to MacKenzie et al. [44].

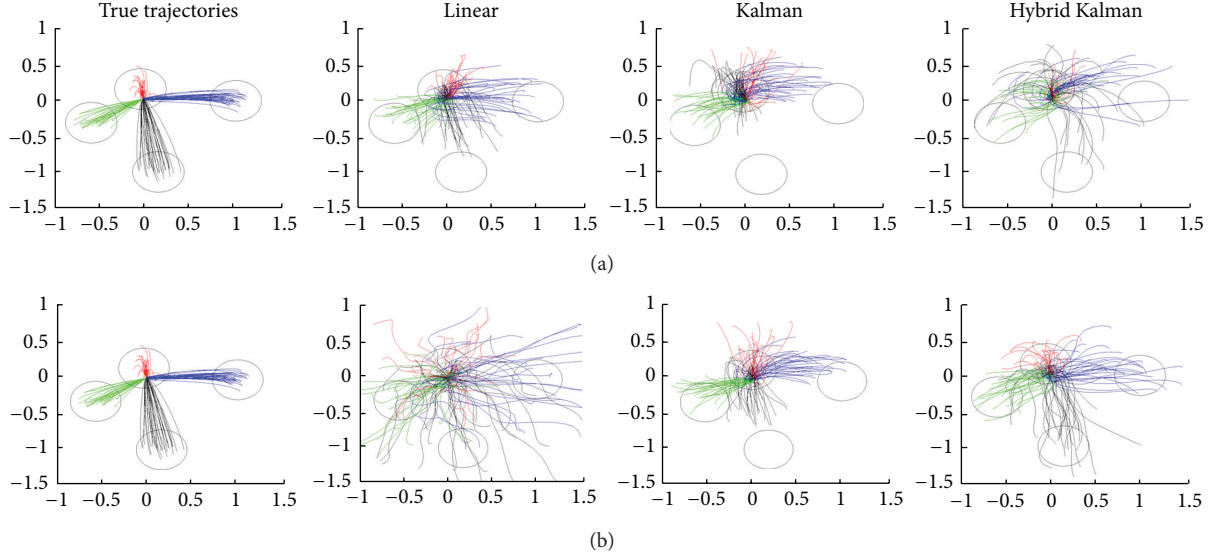


FIGURE 2: Reconstructed 2D hand trajectories by three different algorithms (LF, Kalman, and hybrid Kalman). Each line shows a single trial movement. Different colors indicate reaching movements towards different targets. Circles illustrate a target area. (a) Reconstruction results for both reach and rest. (b) Reconstruction results for reach only.

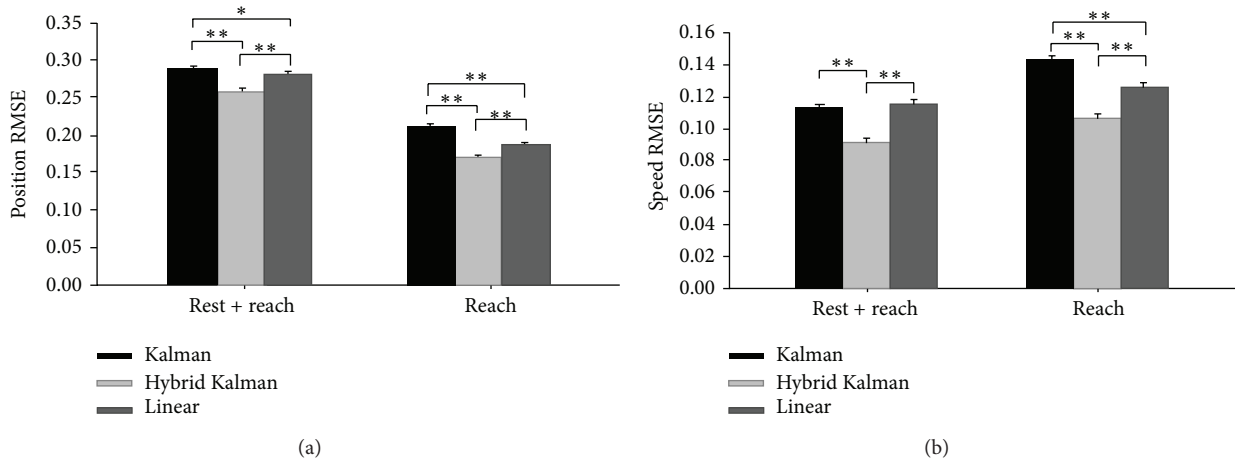


FIGURE 3: The average RMSE between the true and reconstructed hand trajectories decoded by different algorithms (linear, Kalman, and hybrid Kalman filters). (a) The average RMSE of the hand position. Error bars indicate the standard errors of the means. * $P < 0.05$; ** $P < 0.01$. (b) The average RMSE of speed.

3. Results

Using either the reaching only movement data or the reaching and resting movement data, along with the corresponding multichannel MEG data, we trained three different decoding models and reconstructed the hand trajectories. Figure 2 illustrates a sample of the true and reconstructed hand trajectories by each decoding model in the 2D space in one of the participants. Specifically, Figure 2(a) shows the reconstruction of reaching movements after training and estimating both reaching and resting movements, whereas Figure 2(b) shows reaching movements after training and estimating reaching movement only. The reconstructed hand

trajectories followed similar paths to the true trajectories in most trials.

We first evaluated the gross performance using RMSE. We evaluated RMSE of the hand speed as well as the hand position, because we aimed at the improvement of speed decoding. The RMSE measurement revealed that the proposed hybrid Kalman filter produced significantly lower errors than the standard Kalman filter or the linear filter (paired t -test, $P < 0.01$) for both position and speed (Figure 3). Such lower errors were achieved regardless of movement states: reach and rest or reach only. The linear filter exhibited lower position and speed prediction errors than the Kalman filter when the data of reaching movement were only

TABLE 1: Movement prediction performance by different algorithms.

Algorithm	Movements	ODC	MDC	ME	MV
Kalman	Reach + rest	19.728 ± 0.227	23.262 ± 0.242	0.148 ± 0.003	0.190 ± 0.003
Hybrid	Reach + rest	8.015 ± 0.175	9.321 ± 0.180	0.191 ± 0.004	0.251 ± 0.005
Linear	Reach + rest	20.010 ± 0.277	21.585 ± 0.333	0.215 ± 0.004	0.300 ± 0.006
Kalman	Reach	12.995 ± 0.167	16.992 ± 0.181	0.125 ± 0.001	0.169 ± 0.002
Hybrid	Reach	7.956 ± 0.113	9.841 ± 0.153	0.188 ± 0.002	0.258 ± 0.002
Linear	Reach	15.410 ± 0.193	17.441 ± 0.244	0.159 ± 0.002	0.222 ± 0.003

All values are the mean \pm standard error of the mean. ODC: orthogonal direction changes; MDC: movement direction changes; ME: movement error; MV: movement variability.

used ($P < 0.01$). However, the performance of two filters was on par with each other when the data of both reaching and resting movements were used. Notice that overall RMSE of the position decreased when the reaching movement data were only used (Figure 3(a)), whereas overall RMSE of the speed increased for the same case (Figure 3(b)).

Next, we evaluated fine measures including ODC, MDC, ME, and MV for individual trajectories (see Methods for details of each measure). The evaluation results are summarized in Table 1. The hybrid Kalman filter produced the fewest ODC and MDC for both cases of reach and rest or reach only. The linear filter and the Kalman filter, on the other hand, produced more ODC and MDC, showing that the trajectories by these filters were relatively less consistent and smooth. The hybrid Kalman filter reduced ODC and MDS compared to the linear filter by approximately 55% and 51%, respectively. On the contrary, the standard Kalman filter produced the lowest ME and MV compared to the hybrid Kalman filter and the linear filter. The hybrid Kalman filter produced lower ME and MV than the linear filter when the data of both reach and rest were used but higher than the linear filter when the data of reach only were used. The Kalman filter reduced ME and MV compared to the linear filter by approximately 27% and 31%, respectively. Note that the four measures of the linear and Kalman filters were reduced when the reaching movement data was used only (all measures; $P < 0.01$), while those of the hybrid Kalman filter remained relatively steady (ODC; $P = 0.828$, MDC; $P = 0.022$, ME; $P = 0.204$, MV; $P = 0.065$).

4. Conclusions and Discussion

The present study addressed how we could improve the design of a decoding model in an MEG-based noninvasive BCI by incorporating the properties of continuous arm movements. Based on the fact that the hand speed shows nonlinear profiles and is generally independent of movement direction, we designed a model that separately decoded speed and direction to reconstruct hand trajectories from the human MEG. The model was built by adding a nonlinear filter for speed decoding to the Kalman filter while the direction information was directly inferred by the Kalman filter. We demonstrated that this hybrid Kalman filter generated lower prediction errors to reconstruct the hand trajectory and also to estimate the hand speed than the standard Kalman filter and the linear filter. We also investigated how the selection of

movement states affected decoding performance. We found that the linear filter performed better than the Kalman filter when the data of reaching movement was only used. On the other hand, the performance of the two filters was similar when the data of both reaching and resting movements was used. This result demonstrates that the choice of a decoding model may be dependent on the type of continuous movements a BCI is designed to estimate.

We note that speed RMSE increased but position RMSE decreased when we used the data of reaching movements only. It may imply that speed decoding could be improved by training more diverse movements including reach and rest. However, position RMSE could be improved by training more specific movements including reach only and allowing decoding models to focus on movement prediction. We also note that the linear filter outperformed the Kalman filter when the data of reaching movements was only considered. This may imply that, for stereotyped movements, the simple direct decoding approach such as the linear filter could perform reasonably well and the generative decoding approach such as the Kalman filter might provide little advantage. However, when we modified the Kalman filter to fit to the characteristics of BCI output (here, continuous arm movements), we could significantly improve decoding accuracy.

We used a variety of assessment tools to evaluate BCI performance. The fine measures adopted in this study, including ODC, MDC, ME, and MV, allowed us to look into more details of how accurately and reliably the hand trajectories were reconstructed [7, 8, 45]. In fact, four different measures revealed certain advantages and disadvantages of using the new hybrid Kalman filter, demonstrating that a new decoding model should be evaluated in multiple angles. This would not be possible if we only used a gross measure of RMSE. The worse outcomes in terms of ME and MV with the hybrid Kalman filter might be due to its wide range of variability in the reconstructed trajectories. It shows the current limitations of the proposed model and also gives us a direction of how to improve this model to improve the straightness of the trajectory in the following study.

Finally, we would like to underline that the present study demonstrates an approach of improving neural decoding models, not by adopting a cutting-edge machine learning algorithm but by taking the properties of a BCI output into account. Demonstration of decoding improvement by redesigning a current Kalman decoding model based on hand

movement characteristics may indicate the importance of design factors in decoding models and thus in BCIs. We also examined a possibility of estimating the hand speed directly from the KF state variable without adding a nonlinear filter to the state variables. It resulted in a decoding performance significantly worse than the performance of using an MLP ($P < 0.01$). Hence, we verified that adding a nonlinear filter improved performance further. Yet, we also fully recognize that a complete evaluation of a decoding model should be done in a closed-loop BCI system, and therefore we will pursue online BCI studies using our new approach in the future.

Conflict of Interests

The authors declare that there is no conflict of interests regarding the publication of this paper.

Acknowledgments

This research was supported by both the Mid-Career Researcher Program (NRF-2012R1A2A2A04047239) through the National Research Foundation of Korea funded by the Ministry of Science, ICT and Future Planning and the Components and Materials Technology Development Program (10043826) funded by the Ministry of Trade, Industry and Energy.

References

- [1] J. R. Wolpaw, N. Birbaumer, D. J. McFarland, G. Pfurtscheller, and T. M. Vaughan, "Brain-computer interfaces for communication and control," *Clinical Neurophysiology*, vol. 113, no. 6, pp. 767–791, 2002.
- [2] J. P. Donoghue, "Connecting cortex to machines: recent advances in brain interfaces," *Nature Neuroscience*, vol. 5, pp. 1085–1088, 2002.
- [3] A. B. Schwartz, "Cortical neural prosthetics," *Annual Review of Neuroscience*, vol. 27, pp. 487–507, 2004.
- [4] M. A. Lebedev and M. A. L. Nicolelis, "Brain-machine interfaces: past, present and future," *Trends in Neurosciences*, vol. 29, no. 9, pp. 536–546, 2006.
- [5] L. R. Hochberg, D. Bacher, B. Jarosiewicz et al., "Reach and grasp by people with tetraplegia using a neurally controlled robotic arm," *Nature*, vol. 485, no. 7398, pp. 372–375, 2012.
- [6] J. L. Collinger, B. Wodlinger, J. E. Downey et al., "High-performance neuroprosthetic control by an individual with tetraplegia," *The Lancet*, vol. 381, no. 9866, pp. 557–564, 2013.
- [7] J. D. Simeral, S.-P. Kim, M. J. Black, J. P. Donoghue, and L. R. Hochberg, "Neural control of cursor trajectory and click by a human with tetraplegia 1000 days after implant of an intracortical microelectrode array," *Journal of Neural Engineering*, vol. 8, no. 2, Article ID 025027, 2011.
- [8] S.-P. Kim, J. D. Simeral, L. R. Hochberg, J. P. Donoghue, G. M. Fries, and M. J. Black, "Point-and-click cursor control with an intracortical neural interface system by humans with tetraplegia," *IEEE Transactions on Neural Systems and Rehabilitation Engineering*, vol. 19, no. 2, pp. 193–203, 2011.
- [9] T. Yanagisawa, M. Hirata, Y. Saitoh et al., "Electrocorticographic control of a prosthetic arm in paralyzed patients," *Annals of Neurology*, vol. 71, no. 3, pp. 353–361, 2012.
- [10] W. Wang, J. L. Collinger, A. D. Degenhart et al., "An electrocorticographic brain interface in an individual with tetraplegia," *PLoS ONE*, vol. 8, no. 2, Article ID e55344, 2013.
- [11] T. Sakurada, T. Kawase, K. Takano, T. Komatsu, and K. Kansaku, "A BMI-based occupational therapy assist suit: asynchronous control by SSVEP," *Frontiers in Neuroscience*, vol. 7, p. 172, 2013.
- [12] E. Buch, C. Weber, L. G. Cohen et al., "Think to move: a neuromagnetic brain-computer interface (BCI) system for chronic stroke," *Stroke*, vol. 39, no. 3, pp. 910–917, 2008.
- [13] K. K. Ang and C. Guan, "Brain-computer interface in stroke rehabilitation," *Journal of Computing Science and Engineering*, vol. 7, no. 2, pp. 139–146, 2013.
- [14] M. Gomez-Rodriguez, J. Peters, J. Hill, B. Schölkopf, A. Gharabaghi, and M. Grosse-Wentrup, "Closing the sensorimotor loop: haptic feedback facilitates decoding of motor imagery," *Journal of Neural Engineering*, vol. 8, no. 3, Article ID 036005, 2011.
- [15] L. Paninski, M. R. Fellows, N. G. Hatsopoulos, and J. P. Donoghue, "Spatiotemporal tuning of motor cortical neurons for hand position and velocity," *Journal of Neurophysiology*, vol. 91, no. 1, pp. 515–532, 2004.
- [16] W. Wang, S. S. Chan, D. A. Heldman, and D. W. Moran, "Motor cortical representation of position and velocity during reaching," *Journal of Neurophysiology*, vol. 97, no. 6, pp. 4258–4270, 2007.
- [17] E. Stark, R. Drori, I. Asher, Y. Ben-Shaul, and M. Abeles, "Distinct movement parameters are represented by different neurons in the motor cortex," *European Journal of Neuroscience*, vol. 26, no. 4, pp. 1055–1066, 2007.
- [18] M. Saleh, K. Takahashi, and N. G. Hatsopoulos, "Encoding of coordinated reach and grasp trajectories in primary motor cortex," *Journal of Neuroscience*, vol. 32, no. 4, pp. 1220–1232, 2012.
- [19] A. Tankus, Y. Yeshurun, T. Flash, and I. Fried, "Encoding of speed and direction of movement in the human supplementary motor area," *Journal of Neurosurgery*, vol. 110, no. 6, pp. 1304–1316, 2009.
- [20] C. E. Vargas-Irwin, G. Shakhnarovich, P. Yadollahpour, J. M. K. Mislow, M. J. Black, and J. P. Donoghue, "Decoding complete reach and grasp actions from local primary motor cortex populations," *Journal of Neuroscience*, vol. 30, no. 29, pp. 9659–9669, 2010.
- [21] T. J. Bradberry, R. J. Gentili, and J. L. Contreras-Vidal, "Reconstructing three-dimensional hand movements from noninvasive electroencephalographic signals," *Journal of Neuroscience*, vol. 30, no. 9, pp. 3432–3437, 2010.
- [22] A. Presacco, R. Goodman, L. Forrester, and J. L. Contreras-Vidal, "Neural decoding of treadmill walking from noninvasive electroencephalographic signals," *Journal of Neurophysiology*, vol. 106, no. 4, pp. 1875–1887, 2011.
- [23] J. M. Antelis, L. Montesano, A. Ramos-Murguialday, N. Birbaumer, and J. Minguez, "On the usage of linear regression models to reconstruct limb kinematics from low frequency EEG signals," *PLoS ONE*, vol. 8, no. 4, Article ID e61976, 2013.
- [24] A. Toda, H. Imamizu, M. Kawato, and M.-A. Sato, "Reconstruction of two-dimensional movement trajectories from selected magnetoencephalography cortical currents by combined sparse Bayesian methods," *NeuroImage*, vol. 54, no. 2, pp. 892–905, 2011.

- [25] S. Waldert, H. Preissl, E. Demandt et al., "Hand movement direction decoded from MEG and EEG," *Journal of Neuroscience*, vol. 28, no. 4, pp. 1000–1008, 2008.
- [26] S. Waldert, L. Tüshaus, C. P. Kaller, A. Aertsen, and C. Mehring, "fNIRS exhibits weak tuning to hand movement direction," *PLoS ONE*, vol. 7, no. 11, Article ID e49266, 2012.
- [27] H. G. Yeom, J. S. Kim, and C. K. Chung, "Estimation of the velocity and trajectory of three-dimensional reaching movements from non-invasive magnetoencephalography signals," *Journal of Neural Engineering*, vol. 10, no. 2, Article ID 026006, 2013.
- [28] S. Koyama, S. M. Chase, A. S. Whitford, M. Velliste, A. B. Schwartz, and R. E. Kass, "Comparison of brain-computer interface decoding algorithms in open-loop and closed-loop control," *Journal of Computational Neuroscience*, vol. 29, no. 1-2, pp. 73–87, 2010.
- [29] M. Serruya, N. Hatsopoulos, M. Fellows, L. Paninski, and J. Donoghue, "Robustness of neuroprosthetic decoding algorithms," *Biological Cybernetics*, vol. 88, no. 3, pp. 219–228, 2003.
- [30] N. G. Hatsopoulos and J. P. Donoghue, "The science of neural interface systems," *Annual Review of Neuroscience*, vol. 32, pp. 249–266, 2009.
- [31] M. L. Homer, A. V. Nurmikko, J. P. Donoghue, and L. R. Hochberg, "Sensors and decoding for intracortical brain computer interfaces," *Annual Review of Biomedical Engineering*, vol. 15, pp. 383–405, 2013.
- [32] R. Quiroga and S. Panzeri, "Extracting information from neuronal populations: information theory and decoding approaches," *Nature Reviews Neuroscience*, vol. 10, no. 3, pp. 173–185, 2009.
- [33] M. M. Churchland, B. M. Yu, M. Sahani, and K. V. Shenoy, "Techniques for extracting single-trial activity patterns from large-scale neural recordings," *Current Opinion in Neurobiology*, vol. 17, no. 5, pp. 609–618, 2007.
- [34] W. Wu, Y. Gao, E. Bienenstock, J. P. Donoghue, and M. J. Black, "Bayesian population decoding of motor cortical activity using a Kalman filter," *Neural Computation*, vol. 18, no. 1, pp. 80–118, 2006.
- [35] U. T. Eden, L. M. Frank, R. Barbieri, V. Solo, and E. N. Brown, "Dynamic analysis of neural encoding by point process adaptive filtering," *Neural Computation*, vol. 16, no. 5, pp. 971–998, 2004.
- [36] B. M. Yu, C. Kemere, G. Santhanam et al., "Mixture of trajectory models for neural decoding of goal-directed movements," *Journal of Neurophysiology*, vol. 97, no. 5, pp. 3763–3780, 2007.
- [37] C. Kemere, K. V. Shenoy, and T. H. Meng, "Model-based neural decoding of reaching movements: a maximum likelihood approach," *IEEE Transactions on Biomedical Engineering*, vol. 51, no. 6, pp. 925–932, 2004.
- [38] Y. Wang, A. R. C. Paiva, J. C. Príncipe, and J. C. Sanchez, "Sequential Monte Carlo point-process estimation of kinematics from neural spiking activity for brain-machine interfaces," *Neural Computation*, vol. 21, no. 10, pp. 2894–2930, 2009.
- [39] L. Shpigelman, Y. Singer, R. Paz, and E. Vaadia, "Spikernels: predicting arm movements by embedding population spike rate patterns in inner-product spaces," *Neural Computation*, vol. 17, no. 3, pp. 671–690, 2005.
- [40] S. G. Mason, A. Bashashati, M. Fatourechi, K. F. Navarro, and G. E. Birch, "A comprehensive survey of brain interface technology designs," *Annals of Biomedical Engineering*, vol. 35, no. 2, pp. 137–169, 2007.
- [41] J. Ashe and A. P. Georgopoulos, "Movement parameters and neural activity in motor cortex and area 5," *Cerebral Cortex*, vol. 4, no. 6, pp. 590–600, 1994.
- [42] K. Jerbi, J.-P. Lachaux, K. N'Diaye et al., "Coherent neural representation of hand speed in humans revealed by MEG imaging," *Proceedings of the National Academy of Sciences of the United States of America*, vol. 104, no. 18, pp. 7676–7681, 2007.
- [43] S. Darmanjian, S. P. Kim, M. C. Nechyba et al., "Bimodal brain-machine interface for motor control of robotic prosthetic," in *Proceedings of the IEEE/RSJ International Conference on Intelligent Robots and Systems*, pp. 3612–3617, Las Vegas, Nev, USA, October 2003.
- [44] I. S. MacKenzie, T. Kauppinen, and M. Silfverberg, "Accuracy measures for evaluating computer pointing devices," in *Proceedings of the SIGCHI Conference on Human Factors in Computing Systems*, pp. 9–16, Seattle, Wash, USA, March-April 2001.
- [45] E. A. Felton, R. G. Radwin, J. A. Wilson, and J. C. Williams, "Evaluation of a modified Fitts law brain-computer interface target acquisition task in able and motor disabled individuals," *Journal of Neural Engineering*, vol. 6, no. 5, Article ID 056002, 2009.
- [46] M. Hämäläinen, R. Hari, R. J. Ilmoniemi, J. Knuutila, and O. V. Lounasmaa, "Magnetoencephalography—theory, instrumentation, and applications to noninvasive studies of the working human brain," *Reviews of Modern Physics*, vol. 65, no. 2, pp. 413–497, 1993.
- [47] S. Taulu and J. Simola, "Spatiotemporal signal space separation method for rejecting nearby interference in MEG measurements," *Physics in Medicine and Biology*, vol. 51, no. 7, pp. 1759–1768, 2006.

Research Article

Gradually Increased Training Intensity Benefits Rehabilitation Outcome after Stroke by BDNF Upregulation and Stress Suppression

Jing Sun,¹ Zheng Ke,¹ Shea Ping Yip,² Xiao-ling Hu,¹ Xiao-xiang Zheng,³ and Kai-yu Tong¹

¹ Interdisciplinary Division of Biomedical Engineering, The Hong Kong Polytechnic University, Hong Kong

² Department of Health Technology and Informatics, The Hong Kong Polytechnic University, Hong Kong

³ College of Biomedical Engineering and Instrument Science, Zhejiang University, Hangzhou 310027, China

Correspondence should be addressed to Kai-yu Tong; k.y.tong@polyu.edu.hk

Received 28 February 2014; Revised 14 May 2014; Accepted 21 May 2014; Published 19 June 2014

Academic Editor: Yiwen Wang

Copyright © 2014 Jing Sun et al. This is an open access article distributed under the Creative Commons Attribution License, which permits unrestricted use, distribution, and reproduction in any medium, provided the original work is properly cited.

Physical training is necessary for effective rehabilitation in the early poststroke period. Animal studies commonly use fixed training intensity throughout rehabilitation and without adapting it to the animals' recovered motor ability. This study investigated the correlation between training intensity and rehabilitation efficacy by using a focal ischemic stroke rat model. Eighty male Sprague-Dawley rats were induced with middle cerebral artery occlusion/reperfusion surgery. Sixty rats with successful stroke were then randomly assigned into four groups: control (CG, $n = 15$), low intensity (LG, $n = 15$), gradually increased intensity (GIG, $n = 15$), and high intensity (HG, $n = 15$). Behavioral tests were conducted daily to evaluate motor function recovery. Stress level and neural recovery were evaluated via plasma corticosterone and brain-derived neurotrophic factor (BDNF) concentration, respectively. GIG rats significantly ($P < 0.05$) recovered motor function and produced higher hippocampal BDNF (112.87 ± 25.18 ng/g). GIG and LG rats exhibited similar stress levels (540.63 ± 117.40 nM/L and 508.07 ± 161.30 nM/L, resp.), which were significantly lower ($P < 0.05$) than that (716.90 ± 156.48 nM/L) of HG rats. Training with gradually increased intensity achieved better recovery with lower stress. Our observations indicate that a training protocol that includes gradually increasing training intensity should be considered in both animal and clinical studies for better stroke recovery.

1. Introduction

Stroke is the third cause of death after cancer and cardiac diseases [1] and is the leading cause of adult disability in many countries [2]. Ischemic stroke accounts for more than 80% of episodes among patients [1]. Hemiparesis is an inconvenient symptom common in stroke survivors. According to the Hong Kong Authority Statistical Report 2009–2010, the number of annual stroke admissions to public hospitals increased from 24,743 cases in 2005 to 25,614 cases in 2009 [3]. A growing elderly population vulnerable to stroke [2, 4] substantially increases medical care burden in Hong Kong and the developed countries. Thus, effective rehabilitation is essential to help stroke survivors regain impaired motor function for improved quality of life.

Poststroke functional motor training, with repetitive attempts to move paretic limbs, assists the stroke-damaged efferent pathways more effectively in the subacute stroke period when the brain network is sensitive to therapeutic interventions [5]. Studies on efficacy, mechanism, and comparisons of training methods have been performed for many years [6–8]. Training after stroke benefits motor function recovery and promotes neurorehabilitation [8, 9]. Treadmill training, a conventional and easy method, has been employed in both human trials and animal models [10, 11]. Poststroke treadmill training is continually used in rehabilitation due to its effectiveness in both functional mobility and cardiovascular fitness in patients with chronic stroke [11]. Early treadmill training could also reduce brain infarct volume and improve neurologic function compared to spontaneous recovery in

stroke rat models [12, 13]. Moderate treadmill training could upregulate brain-derived neurotrophic factor (BDNF) [14].

BDNF is a protein discovered in the early 1980s which is encoded by BDNF gene and expressed broadly in the central and the peripheral nervous systems [15]. BDNF is one member of the “neurotrophin” family of growth factors that is believed to support the neuron survival and encourages growth and differentiation of new neurons and synapses [16]. BDNF is active in the hippocampus, a region vital to learning, memory, and higher thinking [17]. BDNF is related to neuroplasticity contributing to motor learning, recovery, and neural rehabilitation after stroke [5]. Stroke induces the loss of motor function, and rehabilitation is the process of relearning; thus, higher BDNF concentration in the brain implies learning and neural rehabilitation [18].

Treadmill training can cause stress, leading to a series of physical changes that inhibit neural recovery during rehabilitation [19, 20]. Animals suffer from stress and actually develop similar pathology to humans [21]. Plasma corticosterone (CORT) concentration is widely used as a biomarker of stress in animal models [7, 22, 23]. CORT could downregulate BDNF level in hippocampus [24]. Due to the controversial function of treadmill training after stroke, it is important to evaluate its effect on early stroke physical rehabilitation and the relationship between training loads, motor recovery, and stress levels. We, therefore, designed this study to investigate these relationships via an ischemic stroke rat model.

Intensity is thought to be a key factor in treadmill training and is associated with stress. High-speed treadmill training induces high CORT levels in a stroke rat model [18]. Stress endurance is also enhanced by exercise [25]. Thus, stress level may not only depend on training intensity but also be influenced by subjects’ conditions. Moreover, adjusted training intensity may be directly correlated to rehabilitation outcomes.

Effectiveness of treadmill training intensity in motor function recovery and neurorehabilitation has not yet been completely elucidated. Both clinical and animal studies have focused on fixed training intensity [26, 27]. It remains unclear whether varied training intensity is more effective. In this study, we employed a focal ischemic stroke rat model to evaluate the effect of differing treadmill training intensities on motor function recovery and neurorehabilitation. We also analyzed CORT and BDNF levels in early stroke phase. A gradually increased training intensity was designed to investigate the relationship between intensity, motor recovery, and stress level. This study extends our understanding of treadmill training intensity and influences rehabilitation program design.

2. Methodology

Eighty male Sprague-Dawley (SD) rats (between 2 and 3 months) weighing 280–360 g were used in this study. Rats had free access to food and drink throughout the experimental period. All procedures were approved by the “Animals Subject Ethics Sub-Committee” of the Hong Kong Polytechnic

University and conformed to the guidelines on the care and ethical use of experimental animals [28].

Rats were trained for three days (Figure 1; accommodation protocol in Figure 2(a)) to become accustomed to treadmill exercises. Rats unable to run on the treadmill were removed from the experiment. After three days, rats underwent middle cerebral artery occlusion/reperfusion surgery (MCAo/r) to induce ischemic stroke. After 24 hours, successfully induced stroke rats ($n = 60$) with motor impairment using Longa’s test [29] and behavioral core between 1 and 3 were randomly assigned into 4 groups: control (CG, $n = 15$), low training intensity (LG, $n = 15$), gradually increasing training intensity (GIG, $n = 15$), and high training intensity (HG, $n = 15$). Rats in CG were fed in standard cages for one week, while the rest underwent daily treadmill training with different training intensities. LG rats were allowed to run on the treadmill for 30 minutes with a 10-minute rest between 10 minutes of running section at a velocity of 5 m/min. HG rats ran at 26 m/min with the same training and rest regimens. Rats in GIG ran from 5 m/min on the 1st day (D1) up to 26 m/min on the last day (D7). Daily behavioral scores were recorded via a skilled researcher blind to group assignment. On the last intervention day, rats were anesthetized and sacrificed via decapitation within two hours after the last training. Trunk blood and brain tissues from the hippocampus, striatum, and sensorimotor cortex were collected. Trunk blood samples were immediately centrifuged to acquire plasma. Brain tissue samples were processed according to a standard BDNF sample preparation protocol (Promega, USA). Plasma and brain tissue samples were used for CORT and BDNF detection, respectively.

2.1. Middle Cerebral Artery Occlusion/Reperfusion (MCAo/r) Surgery. The MCAo/r surgery induced focal ischemic stroke rat model by Koizumi [30] in 1986 was employed in this study. Surgery mimicked practices by Ke et al. [7]. Briefly, rats in all groups were anesthetized with 10% chloral hydrate (0.4 mg/kg for induction and 0.02 mg subsequently). Incisions were made at the neck midline to expose the common carotid artery (CCA), and then the external carotid artery was ligated. Subsequently, a commercial filament with a tip diameter of 0.39 ± 0.02 mm (Beijing Sunbio Biotech, China) was inserted into the CCA and advanced along the internal carotid artery until the tip of the filament reached the middle cerebral artery. Occlusion lasted for 60 minutes after which the filament was then withdrawn to allow reperfusion. Six hours after MCAo/r surgery, rats were examined for neurological deficit level using Longa’s test. For Longa’s test, a score of 0 indicates no stroke and 4 represents severe stroke [29]. Rats with a score between 1 and 3 were enrolled in the experiment and kept in individual cages.

2.2. Treadmill Training Intervention. Treadmill training intensity was suggested to affect memory function recovery which is related to neural activity in the hippocampus [31]. Different training intensities bring different stress levels to rats [7]. Velocity is a determining factor in intensity and workload. Different velocities generated different training

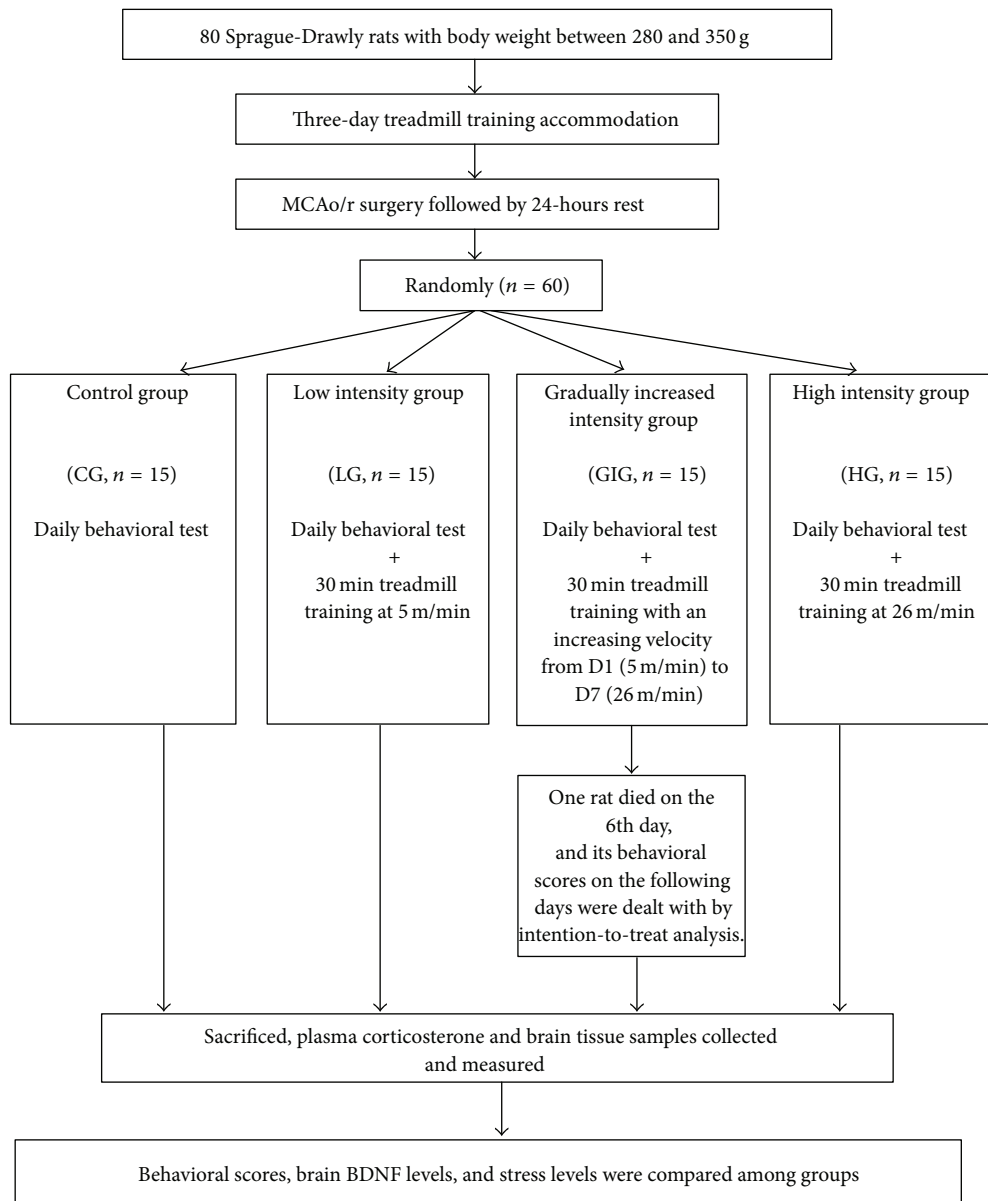


FIGURE 1: Flowchart of the experimental design.

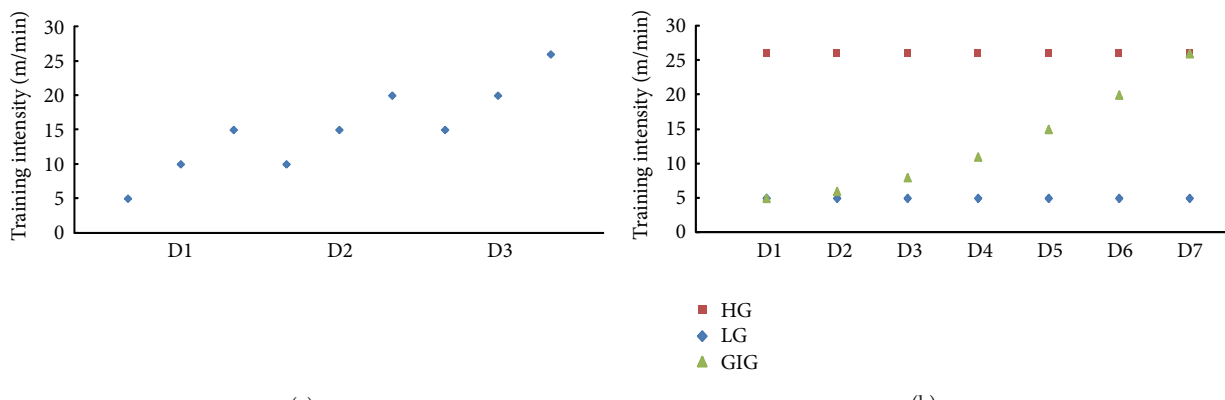


FIGURE 2: Training intensity setup for (a) the 3-day accommodation and (b) poststroke training.

intensities. In previous studies, training intensities mainly were set from 2 m/min to 30 m/min and the daily training time length was mainly set to 30 minutes [6, 8, 31]. In this study, total training time was fixed at 30 minutes, and 5 m/min and 26 m/min were chosen as low and high treadmill training velocities, respectively. In LG and HG, rats ran at a constant velocity through 7 days of training at 5 m/min and 26 m/min, respectively. Rats are generally weak the first several days after stroke but can spontaneously recover [7], gaining better motor function with time. Therefore, the study designated a rat group to gradually increasing intensity from low speed (5 m/min) on the first day to high speed (26 m/min) on the seventh day. Velocity increased slowly in GIG the first four days, and for the following three days, it increased relatively faster. The training setup for all groups is shown in Figure 2(b).

2.3. Motor Function Test. Motor function improvement was evaluated by the De Ryck behavioral test [32] on daily basis throughout the 7-day intervention. Six out of eight tasks evaluate functions including postural reflex, visual placing in the forward and sideways directions, tactile placing of the dorsal and lateral paw surfaces, and proprioceptive placing; the other two tasks examine hindlimb's tactile placing of lateral paw surfaces and proprioceptive placing. The score for each subtask ranges from 0 to 2 with the higher score indicating better motor function. Compared to normal rats, stroke rats cannot place injured limbs normally. Thus, placement function of injured forelimbs and hindlimbs was assessed through the tasks by a skilled researcher blind to group assignments.

2.4. Brain BDNF and Plasma Corticosterone Detection. Brain BDNF and plasma CORT were evaluated using an enzyme-linked immunosorbent assay (ELISA) [6, 7, 33, 34]. All rats were anesthetized within two hours after the last intervention and sacrificed via decapitation. Trunk blood was collected and centrifuged to obtain plasma. The brain was carefully extracted from the skull, and brain tissues including hippocampus, striatum, and affected sensorimotor cortex were then obtained. BDNF Emax ImmunoAssay System (Promega, USA) was used to measure BDNF concentrations. Plasma CORT concentrations were quantified via Cayman's CORT EIA Kit (Cayman, USA).

2.5. Statistical Analysis. All results were expressed as means \pm standard deviations. SPSS (IBM, version 20) was used for data analysis and the level of statistical significance was set at $P = 0.05$. Intention-to-treat analysis was used for any rat that died during the intervention period. The Shapiro-Wilk test was used to examine the normality of all results. Two-way repeated measures analysis of variance (ANOVA) with baseline as covariate and the Bonferroni post hoc test were used to compare motor function scores. One-way ANOVA test was used to compare CORT and BDNF concentrations.

3. Results

Sixty rats underwent successful MCAo/r surgery that induced motor impairment within 24 hours. Stroke rats were randomly assigned into 4 groups (CG, LG, HG, and GIG) with 15 rats in each group. Throughout the experiment, only one rat in the GIG group died on the 6th day. Its behavioral scores on the last two days were the same as that on the 5th day based on the intention-to-treat principle. Results of behavioral scores, CORT concentrations, and BDNF concentrations are shown in Table 1. Through the Shapiro-Wilk test, all results including behavioral scores, CORT concentrations, and BDNF concentrations showed normal distributions ($P > 0.05$). All results were then used for further analysis.

3.1. Motor Function Recovery. Behavioral scores indicating motor function recovery over the experimental period are presented in Figure 3. Significant differences existed among the four groups. GIG rats showed significantly higher behavioral scores from the 3rd to the last day compared to those in the other groups. Rats in LG and HG also exhibited significantly better motor function recovery from the 6th day than the control.

3.2. Brain BDNF and Plasma Corticosterone Concentrations. Hippocampal BDNF concentrations were significantly higher than in both the striatum and cortex for all groups. GIG rats showed the highest BDNF levels in the hippocampus and striatum in Figure 4. Significantly different cortical BDNF levels were observed between GIG and CG rats. BDNF levels in LG and HG rats were not apparently different but were significantly higher in the hippocampus and striatum than CG rats (Figure 4). Figure 5 shows plasma CORT concentrations. Rats in the 3 training groups exhibited significantly higher CORT levels over control. CORT levels in GIG rats were significantly lower than HG but similar to LG.

4. Discussion

We show that treadmill training intensities for ischemic stroke rats affect motor function recovery, BDNF concentration, and stress level over the 7-day intervention. We set up three training intensity levels including low, high, and gradually increased intensity from low to high. Gradually increased training intensity (GIG) induced significantly better motor function recovery. Rats in this group showed similar stress levels in comparison to LG, but BDNF concentrations in brain tissues (hippocampus and striatum) were significantly higher than LG. Rats in HG were stressed more than LG; however, functional recovery rates were similar to LG and significantly lower than GIG. Results indicated that rats with treadmill gradually increased intensities better regain motor function recovery.

Consistent with other studies, BDNF levels were lower in striatum and cortex than in the hippocampus [7, 35]. The hippocampus plays an important role in learning and memory, and rehabilitation is a process of relearning, making hippocampal neurons active [17]. BDNF level is highly related

TABLE 1: An Overview of Rehabilitation Outcomes of Motor Function, BDNF Levels in Hippocampus, Striatum and Cortex, and Plasma Corticosterone (CORT).

Items	Group	Pre-training	Post-training	Post hoc (<i>P</i>)
Motor Function				CG vs LG (0.018*)
	CG	5.36 ± 1.41	8.23 ± 1.69	CG vs GIG (<0.001*)
	LG	4.89 ± 0.78	10.01 ± 0.73	CG vs HG (0.041*)
	GIG	5.37 ± 1.64	12.00 ± 1.00	LG vs GIG (0.009*)
	HG	5.50 ± 0.81	9.64 ± 0.90	LG vs HG (1.00)
				GIG vs HG (<0.001*)
BDNF level in hippocampus				CG vs LG (0.044*)
	CG	—	47.68 ± 13.25	CG vs GIG (<0.001*)
	LG	—	74.46 ± 25.57	CG vs HG (0.032*)
	GIG	—	112.87 ± 25.18	LG vs GIG (<0.001*)
	HG	—	76.41 ± 34.68	LG vs HG (0.523)
				GIG vs HG (0.001*)
BDNF level in striatum				CG vs LG (1.00)
	CG	—	14.16 ± 13.25	CG vs GIG (0.004*)
	LG	—	18.04 ± 11.61	CG vs HG (1.00)
	GIG	—	27.77 ± 15.57	LG vs GIG (0.044*)
	HG	—	17.94 ± 10.26	LG vs HG (1.00)
				GIG vs HG (0.030*)
BDNF level in cortex				CG vs LG (0.980)
	CG	—	11.73 ± 7.18	CG vs GIG (0.001*)
	LG	—	14.69 ± 3.60	CG vs HG (1.00)
	GIG	—	19.24 ± 4.94	LG vs GIG (0.203)
	HG	—	14.64 ± 6.50	LG vs HG (1.00)
				GIG vs HG (0.194)
Plasma CORT Level				CG vs LG (0.044*)
	CG	—	347.03 ± 181.02	CG vs GIG (0.009*)
	LG	—	508.07 ± 161.30	CG vs HG (<0.001*)
	GIG	—	540.63 ± 117.40	LG vs GIG (1.000)
	HG	—	716.90 ± 156.48	LG vs HG (0.003*)
				GIG vs HG (0.017*)

Values: means ± standard deviations; *P* value: significance level of 2-way Repeated Measures ANOVA multiple comparisons with covariate for behavioral scores; significance level of one-way ANOVA for BDNF levels and plasma CORT concentrations.

*Significant differences observed; post hoc test was conducted to specify the differences between groups.

to neural survival, growth, and differentiation [16], probably producing a high hippocampal BDNF level. GIG rats showed the highest BDNF concentrations in the hippocampus and striatum and had the best motor function recovery. Importantly, we found a significantly positive relationship (correlation coefficient: 0.537; *P* < 0.01) between motor function recovery rate and hippocampal BDNF concentrations (Figure 6). BDNF has been used to treat photothrombotic stroke rats and it improved motor function recovery when compared to spontaneous recovery [36]. Other studies also show that higher BDNF level in the brain indicates better motor function recovery after stroke [7, 37]. Our results remain consistent with those of previous studies. Significant

higher BDNF levels were found in GIG rats, leading to significantly better motor function recovery. Similar BDNF levels were observed in LG and HG rats that showed similar motor function recovery.

Ploughman considered exercise brain food that ultimately enhances brain functions like memory and learning [38]. Additionally, Ploughman et al. [39] suggest that moderate exercise has positive effects on physically disabled young people aided by their high brain plasticity. Both prolonged and short-term moderate exercises increase hippocampal BDNF levels and brain mitochondrial biogenesis in rats [14, 40, 41]. Physical training for stroke rat models was reported to facilitate motor function recovery and upregulate

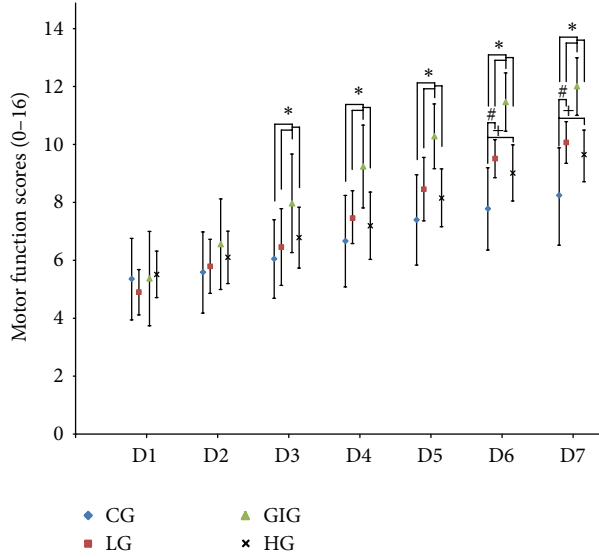


FIGURE 3: Behavioral scores over the seven-day intervention. A higher behavioral score indicates better motor function. *: significant difference observed via 2-way repeated measures ANOVA with the score on D1 as covariate when comparing GIG to the other three groups. #,: significant difference observed via 2-way repeated measures ANOVA with the score on D1 as covariate when comparing LG and HG to CG, respectively. From D3 to D7, rats in GIG scored significantly higher for behavioral score compared to LG, HG, and CG, while rats in LG and HG showed better motor function on D6 and D7 compared to CG. Results suggested that gradually increased training intensity can facilitate motor function recovery during the subacute stroke period.

BDNF levels [42]. Four-week consecutive low-speed treadmill training started on the 4th day after stroke was found to improve hippocampal function in a MCAo induced stroke rat model [31]. Thus, exercise seems to upregulate brain BDNF concentrations, a result supported by this study. Moreover, GIG training improves BDNF production in brain tissues after stroke, indicating better brain function recovery.

Early physical training facilitates rehabilitation after stroke, but it is also a source of stress that mediates BDNF regulation. CORT is a steroid hormone produced by the hypothalamic-pituitary-adrenal axis and is released into the blood. Adrenalectomized Wistar rats were used to investigate the time course and dose-dependency of CORT's effect on BDNF mRNA and protein, with results showing short-term corticosterone concentration changes having transient and dose-dependent downregulation effects for both hippocampal BDNF mRNA and protein [24]. Forced treadmill training induces stress and has been suggested to lower physical rehabilitation and BDNF levels in the hippocampus compared to voluntary wheel running; yet it still stimulates functional recovery [7]. Treadmill training intensity could affect memory function recovery, while the hippocampus determines memory function [31]. Training intensity, thus, may affect hippocampal activity. Stress level is highly related to training intensity. High training intensity causes significantly high stress level, as a result of our study.

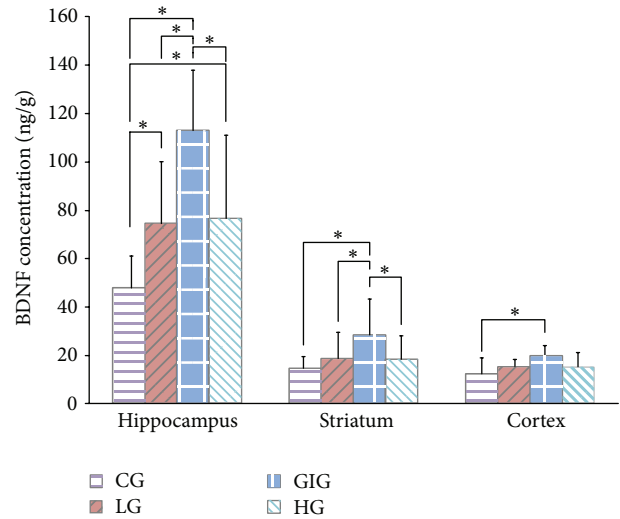


FIGURE 4: BDNF concentration in the hippocampus, striatum, and cortex. *: significant differences between groups acquired via one-way ANOVA with post hoc test. The hippocampus showed significantly higher BDNF level than striatum and cortex in all groups. GIG rats exhibited significantly higher BDNF levels in the hippocampus and striatum than the other groups. Significantly different cortical BDNF levels were only observed between the GIG and the CG. BDNF levels in LG and HG rats were not apparently different in all of the brain tissues; both were significantly higher than CG in the hippocampus and striatum.

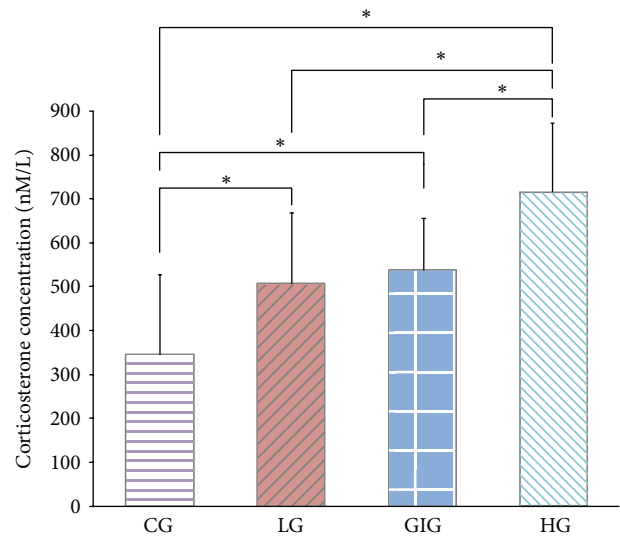


FIGURE 5: Plasma corticosterone concentrations on the last day. Higher values represent higher stress. *: significant differences between groups acquired via one-way ANOVA with post hoc test. HG rats were stressed the most, and LG and GIG rats showed similar stress levels which were significantly higher than CG. Although GIG rats ran at the same velocity as HG, their average stress level was significantly lower.

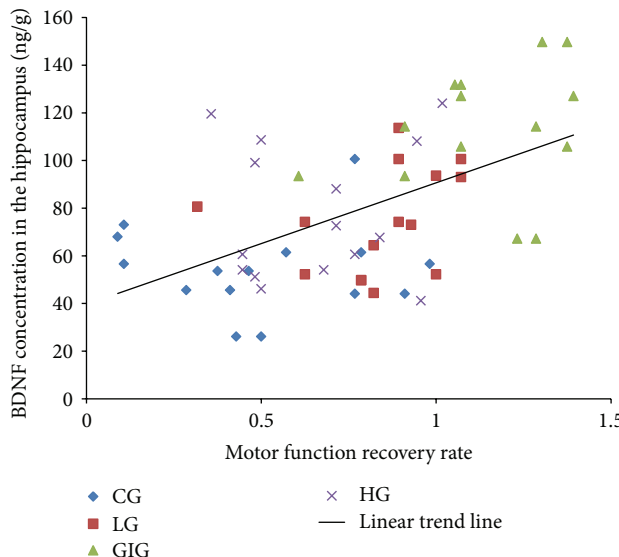


FIGURE 6: Correlation between hippocampal BDNF concentration and motor function recovery rate. BDNF levels in the hippocampus correlated with motor function recovery rate, meaning that BDNF levels could indicate motor function recovery rate.

Hippocampal BDNF level could represent neural activity in the hippocampus. Higher BDNF levels in the hippocampus indicate better neural activity. Thus, stress level may correlate with hippocampal BDNF level. On one hand, in this study, consistent low and high training intensity induced low and high stress levels associated with similar hippocampal BDNF level; however, gradually increased intensity induced stress levels between low and high intensities and close to low intensity: stress may inhibit brain BDNF production. On the other hand, rats with low training intensity were stressed significantly more than those without training but still exhibited significantly better motor function recovery, suggesting that stress was not the only factor mediating BDNF production during rehabilitation. Exercise should be another important factor determining rehabilitation outcomes. It could increase muscle and brain mitochondrial biogenesis, strengthening fatigue resistance and endurance performance [25]. In this study, GIG training may better improve stress endurance and it obtained better recovery. Training intensity, thus, should be appropriately chosen for better recovery after stroke.

Repeated training is an important tool applied widely in clinics and laboratories to improve recovery after stroke. Intensity in forced training is a critical stress-inducing factor. We thus designed a gradually increasing treadmill training intensity regimen for stroke rats. We found that the training intensity should be designed to match recovery rate and minimize stress. Training with gradually increased intensity can produce significantly better motor function rehabilitation compared to stably low and high training intensity. We extended the understanding of the importance of training intensity in rehabilitation after stroke. A training protocol that includes gradually increasing training intensity should be considered in both animal and clinical human studies.

Conflict of Interests

The authors declare that there is no conflict of interests regarding the publication of this paper.

Acknowledgments

This study was supported by Research Grants Council of the Hong Kong Special Administrative Region (Grant no. PolyU 527511). The funders did not participate in study design, data collection and analysis, decision to publish, or preparation of the paper. The authors also thank the Centralized Animal Facilities of the Hong Kong Polytechnic University for the animal husbandry support.

References

- [1] B. M. Kelly, P. H. Pangilinan Jr., and G. M. Rodriguez, "The stroke rehabilitation paradigm," *Physical Medicine and Rehabilitation Clinics of North America*, vol. 18, no. 4, pp. 631–650, 2007.
- [2] M. M. Pinter and M. Brainin, "Rehabilitation after stroke in older people," *Maturitas*, vol. 71, no. 2, pp. 104–108, 2012.
- [3] Hospital Authority, "Hospital authority statistical report (2009–2010)," 2011, http://www.ha.org.hk/upload/publication_15/321.pdf.
- [4] G. A. Donnan, M. Fisher, M. Macleod, and S. M. Davis, "Stroke," *The Lancet*, vol. 371, no. 9624, pp. 1612–1623, 2008.
- [5] J. A. Hosp and A. R. Luft, "Cortical plasticity during motor learning and recovery after ischemic stroke," *Neural Plasticity*, vol. 2011, Article ID 871296, 9 pages, 2011.
- [6] K. Hayes, S. Sprague, M. Guo et al., "Forced, not voluntary, exercise effectively induces neuroprotection in stroke," *Acta Neuropathologica*, vol. 115, no. 3, pp. 289–296, 2008.
- [7] Z. Ke, S. P. Yip, L. Li, X.-X. Zheng, and K.-Y. Tong, "The effects of voluntary, involuntary, and forced exercises on brain-derived neurotrophic factor and motor function recovery: a rat brain ischemia model," *PLoS ONE*, vol. 6, no. 2, Article ID e16643, 2011.
- [8] R.-Y. Wang, Y.-R. Yang, and S.-M. Yu, "Protective effects of treadmill training on infarction in rats," *Brain Research*, vol. 922, no. 1, pp. 140–143, 2001.
- [9] M. A. Alomari, O. F. Khabour, K. H. Alzoubi, and M. A. Alzoubi, "Forced and voluntary exercises equally improve spatial learning and memory and hippocampal BDNF levels," *Behavioural Brain Research*, vol. 247, pp. 34–39, 2013.
- [10] A. M. Moseley, A. Stark, I. D. Cameron, and A. Pollock, "Treadmill training and body weight support for walking after stroke," *Stroke*, vol. 34, no. 12, article 3006, 2003.
- [11] R. F. Macko, F. M. Ivey, L. W. Forrester et al., "Treadmill exercise rehabilitation improves ambulatory function and cardiovascular fitness in patients with chronic stroke: a randomized, controlled trial," *Stroke*, vol. 36, no. 10, pp. 2206–2211, 2005.
- [12] Y.-R. Yang, R.-Y. Wang, and P. S.-G. Wang, "Early and late treadmill training after focal brain ischemia in rats," *Neuroscience Letters*, vol. 339, no. 2, pp. 91–94, 2003.
- [13] Y.-R. Yang, R.-Y. Wang, P. S.-G. Wang, and S.-M. Yu, "Treadmill training effects on neurological outcome after middle cerebral artery occlusion in rats," *Canadian Journal of Neurological Sciences*, vol. 30, no. 3, pp. 252–258, 2003.
- [14] A. F. B. Ferreira, C. C. Real, A. C. Rodrigues, A. S. Alves, and L. R. G. Britto, "Short-term, moderate exercise is capable of

- inducing structural, bdnf-independent hippocampal plasticity,” *Brain Research*, vol. 1425, pp. 111–122, 2011.
- [15] Y. A. Barde, D. Edgar, and H. Thoenen, “Purification of a new neurotrophic factor from mammalian brain,” *EMBO Journal*, vol. 1, no. 5, pp. 549–553, 1982.
- [16] N. Weishaupt, A. Blesch, and K. Fouad, “BDNF: the career of a multifaceted neurotrophin in spinal cord injury,” *Experimental Neurology*, vol. 238, no. 2, pp. 254–264, 2012.
- [17] W. J. Tyler, M. Alonso, C. R. Bramham, and L. D. Pozzo-Miller, “From acquisition to consolidation: on the role of brain-derived neurotrophic factor signaling in hippocampal-dependent learning,” *Learning and Memory*, vol. 9, no. 5, pp. 224–237, 2002.
- [18] H. Soya, T. Nakamura, C. C. Deocaris et al., “BDNF induction with mild exercise in the rat hippocampus,” *Biochemical and Biophysical Research Communications*, vol. 358, no. 4, pp. 961–967, 2007.
- [19] B. Leuner and E. Gould, “Structural plasticity and hippocampal function,” *Annual Review of Psychology*, vol. 61, pp. 111–140, 2010.
- [20] B. S. McEwen, “Stress and hippocampal plasticity,” *Annual Review of Neuroscience*, vol. 22, pp. 105–122, 1999.
- [21] G. P. Moberg and J. A. Mench, *The Biology of Animal Stress Basic Principles and Implications for Animal Welfare*, CAB International Press, Wallingford, UK, 2000.
- [22] R. V. L. Contarteze, F. D. B. Manchado, C. A. Gobatto, and M. A. R. de Mello, “Stress biomarkers in rats submitted to swimming and treadmill running exercises,” *Comparative Biochemistry and Physiology*, vol. 151, no. 3, pp. 415–422, 2008.
- [23] R. Contarteze, F. Manchado-Gobatto, C. Gobatto, and M. A. R. Mello, “Different stress biomarkers sensitivity during acute treadmill running exercise in rats,” *Journal of Exercise Physiology Online*, vol. 11, no. 1, pp. 18–27, 2008.
- [24] M. J. M. Schaaf, J. de Jong, E. R. de Kloet, and E. Vreugdenhil, “Downregulation of BDNF mRNA and protein in the rat hippocampus by corticosterone,” *Brain Research*, vol. 813, no. 1, pp. 112–120, 1998.
- [25] J. L. Steiner, E. A. Murphy, J. L. McClellan, M. D. Carmichael, and J. M. Davis, “Exercise training increases mitochondrial biogenesis in the brain,” *Journal of Applied Physiology*, vol. 111, no. 4, pp. 1066–1071, 2011.
- [26] M. MacKay-Lyons, A. McDonald, J. Matheson, G. Eskes, and M.-A. Klus, “Dual effects of body-weight supported treadmill training on cardiovascular fitness and walking ability early after stroke: a randomized controlled trial,” *Neurorehabilitation and Neural Repair*, vol. 27, no. 7, pp. 644–653, 2013.
- [27] S. Tian, Y. Zhang, S. Tian et al., “Early exercise training improves ischemic outcome in rats by cerebral hemodynamics,” *Brain Research*, vol. 1533, pp. 114–121, 2013.
- [28] E. D. Olfert, B. M. Cross, and A. A. McWilliam, *Guide to the Care and Use of Experimental Animals*, vol. 1, Canadian Council on Animal Care, Canada, 2nd edition, 1993.
- [29] E. Z. Longa, P. R. Weinstein, S. Carlson, and R. Cummins, “Reversible middle cerebral artery occlusion without craniectomy in rats,” *Stroke*, vol. 20, no. 1, pp. 84–91, 1989.
- [30] K.-A. Hossmann, “Experimental models for the investigation of brain ischemia,” *Cardiovascular Research*, vol. 39, no. 1, pp. 106–120, 1998.
- [31] H. Shimada, M. Hamakawa, A. Ishida, K. Tamakoshi, H. Nakashima, and K. Ishida, “Low-speed treadmill running exercise improves memory function after transient middle cerebral artery occlusion in rats,” *Behavioural Brain Research*, vol. 243, no. 1, pp. 21–27, 2013.
- [32] M. de Ryck, J. van Reempts, M. Borgers, A. Wauquier, and P. A. J. Janssen, “Photochemical stroke model: flunarizine prevents sensorimotor deficits after neocortical infarcts in rats,” *Stroke*, vol. 20, no. 10, pp. 1383–1390, 1989.
- [33] A. Quiríe, M. Hervieu, P. Garnier et al., “Comparative effect of treadmill exercise on mature BDNF production in control versus stroke rats,” *PLoS ONE*, vol. 7, no. 9, Article ID e44218, 2012.
- [34] D. F. Hawley, K. Morsch, B. R. Christie, and J. L. Leisure, “Differential response of hippocampal subregions to stress and learning,” *PLoS ONE*, vol. 7, no. 12, Article ID e53126, 2012.
- [35] H. Nawa, J. Carnahan, and C. Call, “BDNF protein measured by a novel enzyme immunoassay in normal brain and after seizure: partial disagreement with mRNA levels,” *European Journal of Neuroscience*, vol. 7, no. 7, pp. 1527–1535, 1995.
- [36] W.-R. Schäbitz, C. Berger, R. Kollmar et al., “Effect of brain-derived neurotrophic factor treatment and forced arm use on functional motor recovery after small cortical ischemia,” *Stroke*, vol. 35, no. 4, pp. 992–997, 2004.
- [37] Y. Zhang and W. M. Pardridge, “Blood-brain barrier targeting of BDNF improves motor function in rats with middle cerebral artery occlusion,” *Brain Research*, vol. 1111, no. 1, pp. 227–229, 2006.
- [38] M. Ploughman, “Exercise is brain food: the effects of physical activity on cognitive function,” *Developmental Neurorehabilitation*, vol. 11, no. 3, pp. 236–240, 2008.
- [39] M. Ploughman, S. Granter-Button, G. Chernenko et al., “Exercise intensity influences the temporal profile of growth factors involved in neuronal plasticity following focal ischemia,” *Brain Research*, vol. 1150, no. 1, pp. 207–216, 2007.
- [40] M. Ploughman, S. Granter-Button, G. Chernenko, B. A. Tucker, K. M. Mearow, and D. Corbett, “Endurance exercise regimens induce differential effects on brain-derived neurotrophic factor, synapsin-I and insulin-like growth factor I after focal ischemia,” *Neuroscience*, vol. 136, no. 4, pp. 991–1001, 2005.
- [41] H. Ogonovszky, I. Berkes, S. Kumagai et al., “The effects of moderate-, strenuous- and over-training on oxidative stress markers, DNA repair, and memory, in rat brain,” *Neurochemistry International*, vol. 46, no. 8, pp. 635–640, 2005.
- [42] P. Zhang, Y. Zhang, J. Zhang et al., “Early exercise protects against cerebral ischemic injury through inhibiting neuron apoptosis in cortex in rats,” *International Journal of Molecular Sciences*, vol. 14, no. 3, pp. 6074–6089, 2013.

Research Article

Muscle-Based Pharmacokinetic Modeling of Marrow Perfusion for Osteoporotic Bone in Females

Heather Ting Ma,¹ James F. Griffith,² and Ping-Chung Leung³

¹ Department of Electronic and Information Engineering, Harbin Institute of Technology Shenzhen Graduate School, Room 205C, C Building, HIT Campus, Shenzhen University Town, Xili, Nanshan District, Shenzhen 518055, China

² Department of Imaging and Interventional Radiology, Prince of Wales Hospital, The Chinese University of Hong Kong, Shatin, Hong Kong

³ Jockey Club Centre for Osteoporosis Care and Control, Public Health School, Prince of Wales Hospital, The Chinese University of Hong Kong, Shatin, Hong Kong

Correspondence should be addressed to Heather Ting Ma; heather.tma@gmail.com

Received 27 February 2014; Revised 29 April 2014; Accepted 5 May 2014; Published 9 June 2014

Academic Editor: Xiaoling Hu

Copyright © 2014 Heather Ting Ma et al. This is an open access article distributed under the Creative Commons Attribution License, which permits unrestricted use, distribution, and reproduction in any medium, provided the original work is properly cited.

The pharmacokinetic model has been widely used in tissue perfusion analysis, such as bone marrow perfusion. In the modeling process, the arterial input function is important to guarantee the reliability of the fitting result. However, the arterial input function is variable and hard to control, which makes it difficult to compare results across different studies. The purpose of this study was to establish a muscle-based pharmacokinetic model for bone marrow perfusion without using arterial input function. Erector spinae muscle around the vertebral body was selected as the reference region. The study was carried out in elderly females with different bone mineral densities (normal, osteopenia, and osteoporosis). Quantitative parameters were extracted from the pharmacokinetic model. Parameter $K^{trans,BM}$ (contrast agent extravasation rate constants for blood perfusion of the bone marrow) showed a significant reduction in subjects with lower bone mineral density, which is consistent with previous studies. However, muscle perfusion parameters remained unchanged among different groups. The results indicated that the muscle-based model was stable for bone marrow perfusion modeling. Additionally, nonsignificant change in muscle parameters indicated that the diminished perfusion is only a local rather than a systematic change in the bone marrow for osteoporosis.

1. Introduction

Osteoporosis is a common metabolic bone disorder in elderly and its consequence has become one of the most increasing health concerns [1, 2]. When bone mineral content loss and structural deterioration proceed until bone strength becomes sufficiently poor, the cancellous bone increases susceptibility to fracture. As a result, the osteoporotic state has been reached. Studies in recent decades showed a link between peripheral vascular disease and osteoporosis in terms of clinics, epidemiology, and histology [3–5]. Such association indicated a varied blood supply mechanism in the osteoporotic bone. Technically, the microcirculation can

be reflected by the dynamic contrast enhanced (DCE) MRI, which provides a direct measurement of tissue perfusion in a living system [6, 7]. Bone marrow perfusion is a physiological process, which can be affected by multiple factors, such as tissue blood flow, capillary capacitance and permeability, interstitial diffusion, interstitial space volume, and venous return [8, 9].

Bone perfusion by DCE-MRI can be assessed by semi-quantitative method [10–14] and pharmacokinetic model [15–18]. The former method provides a direct measure of the bone perfusion with semiquantitative parameters derived from the perfusion curves. In comparison, the latter approach has a more complex process, including modeling and curve fitting,

but the derived model parameters directly related to inherent physiology. Most pharmacokinetic models include the arterial input function (AIF) [19], such as Tofts model [9]. They adopt the AIF as the input of the tissue perfusion so that the variation in the AIF will change the pharmacokinetics in the tissue. Therefore, the results from such studies depend much on the accuracy of the AIF modeling and the experiment protocol. Brix model [16] is a pharmacokinetic model without using AIF and has been introduced in the bone perfusion study [20]. However, it assumes that the AIF has a fixed pattern, which may not reflect the true physiological process. As a consequence, it is difficult to compare the perfusion function across different studies.

In order to have a more robust analysis, we introduced a new pharmacokinetic model for analyzing bone marrow perfusion, which employed a well-characterized reference region instead of AIF. The erector spinae muscle around the vertebral body was selected as the reference region because its big muscle bulk is easy to be recognized in the images and would be able to derive the DCE-MRI signal with a good signal-to-noise ratio (SNR). The perfusion function of the muscle was quantified by a proposed model to obtain analytic results. The purpose of this study is to characterize bone marrow perfusion properties in subjects with different bone mineral density (BMD) by a muscle-based pharmacokinetic model.

2. Methods

2.1. Subjects. In order to avoid gender influence, only female subjects were included in current study. The investigation involved a reassessment of DCE-MRI raw data obtained in one previous study [11]. Subjects were excluded if they had (a) clinical or imaging evidence of renal osteodystrophy or other metabolic bone diseases other than osteoporosis or a known malignancy, (b) a history of lumbar spinal surgery or irradiation, or (c) MR imaging evidence of large intravertebral disk herniation, hemangioma, or moderate-to-severe vertebral fracture of L3. Finally, 76 subjects (age 72.5 ± 3.4 years) in total were involved in this retrospective study. The study was approved by the Ethics Committee, Chinese University of Hong Kong, with all participating subjects providing written consent.

2.2. Data Acquisition. Area bone mineral density (BMD) of L3 level was measured by the dual-energy X-ray absorptiometry (DXA). MR imaging was performed at a 1.5 T whole body imaging system (Intera NT; Philips Medical Systems, Best, The Netherlands) with a maximum gradient strength of 30 mT/m. Axial T1-weighted (TR/TE, 450/11 ms; 4 mm thick) MR image of the mid-L3 vertebrae was obtained (shown in Figure 1). Dynamic contrast enhancement MRI (DCE-MRI) data were acquired through the mid-L3 vertebral body region. Dynamic MR imaging was performed using a short T1-weighted gradient-echo sequence (TR/TE, 2.7/0.95 ms; prepulse inversion time, 400 ms; flip angle, 15°; section thickness, 10 mm; number of slice, one; field of view, 250 mm; acquisition matrix, 256 × 256; number of signals acquired,

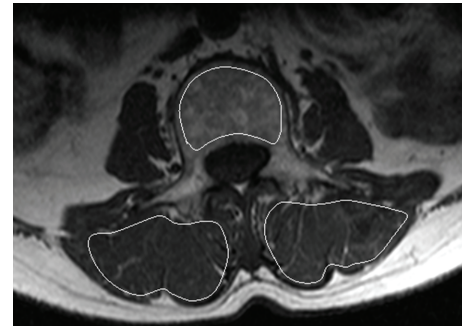


FIGURE 1: T1-weighted MR image in axial plane (from a subject with normal BMD). The image shows manually drawn ROI positioned within cortical margins of L3 vertebral body and erector spinae muscle for time-signal intensity data points measured from dynamic contrast enhanced images.

one). A bolus of gadoteric acid (Dotarem, Guerbet, Aulnay, France) at a concentration of 0.15 mmol per kilogram body weight was injected via a power injector (Spectris; Medrad, Indianola, PA, USA) at a rate of 2.5 mL/s through a 20-gauge antecubital vein intravenous catheter (Angiocath; Infusion Therapy Systems, Sandy, UT, USA). Injection was followed by a 20 mL saline flush. Dynamic MR imaging started at the same time the contrast medium injection started. A total of 160 dynamic images were obtained with a temporal resolution of 543 ms, resulting in a total scanning time of 87 seconds.

2.3. Data Processing and Modeling of DCE Data. In order to extract the signal intensity curves pixel by pixel, region of interest (ROI) was drawn manually for muscle bulk area of erector spinae and bone marrow area on axial image. The ROIs were drawn following the contour of the erector spinae muscle on both sides and encompassing trabecular bone of vertebral body (as shown in Figure 1). The time-signal intensity curve was generated by averaging signal intensity within each ROI.

A muscle-based pharmacokinetic model was established, which was modified from a reference region (RR) model [21, 22], to analyze the DCE-MRI data of bone marrow. The model contains three compartments, plasma, muscle, and bone marrow, as shown in Figure 2. When contrast agent is injected into the vessel system, it will go throughout the body with the fluid dynamics, where C_p is the concentration in the supplying artery of the local area for lumbar. By perfusion process, the contrast agent will reach bone marrow and surrounding muscles simultaneously with concentration of C_{BM} and C_m , respectively. Contrast agent perfusion is modeled by extravasation rate constants, $K^{trans.BM}$ and $K^{trans.m}$, as in bone marrow and muscle, respectively. The perfusion space is modeled as extravascular-extracellular volume fraction, which is $\nu_{e.BM}$ and $\nu_{e.m}$ for bone marrow and muscle, respectively. The model describes association of the contrast agent concentration among three compartments, that is, plasma, bone marrow, and muscle.

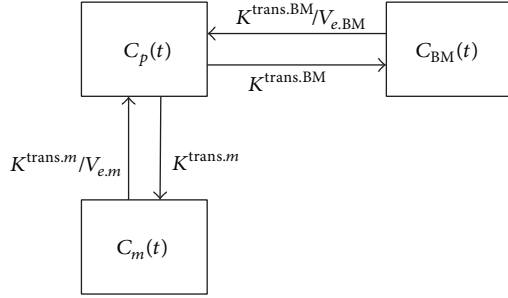


FIGURE 2: Muscle-based pharmacokinetic modeling scheme. C_p , C_{BM} , and C_m are contrast agent concentrations in the artery, bone marrow, and erector spinae muscle, respectively.

Based on the modeling structure shown in Figure 2, the contrast agent concentration in bone marrow and muscle can be formulated as the following differential equations:

$$\frac{dC_m(t)}{dt} = K^{\text{trans}.m} \cdot C_p(t) - \left(\frac{K^{\text{trans}.m}}{v_{e,m}} \right) \cdot C_m(t) \quad (1)$$

$$\frac{dC_{BM}(t)}{dt} = K^{\text{trans}.BM} \cdot C_p(t) - \left(\frac{K^{\text{trans}.BM}}{v_{e,BM}} \right) \cdot C_{BM}(t). \quad (2)$$

It is obvious that both $C_m(t)$ and $C_{BM}(t)$ are dependent on $C_p(t)$, which represents AIF. Merging the two equations will balance out $C_p(t)$ so that we can formulate the relationship between $C_{BM}(t)$ and $C_m(t)$ as

$$\begin{aligned} C_{BM}(t) &= \frac{K^{\text{trans}.BM}}{K^{\text{trans}.m}} C_m(t) \\ &+ \left(\frac{K^{\text{trans}.m}}{v_{e,m}} - \frac{K^{\text{trans}.BM}}{v_{e,BM}} \right) \cdot C_m(t) \\ &\otimes \exp \left(\frac{-K^{\text{trans}.BM}}{v_{e,BM}} \right), \end{aligned} \quad (3)$$

which can be simplified as

$$\begin{aligned} C_{BM}(t) &= R \cdot C_m(t) + R \cdot \left[\left(\frac{K^{\text{trans}.m}}{v_{e,m}} \right) - \left(\frac{K^{\text{trans}.BM}}{v_{e,BM}} \right) \right] \\ &\cdot \int_0^t C_m(\tau) \cdot \left(\frac{\exp(-K^{\text{trans}.BM})}{v_{e,BM}} \right) (t - \tau) d\tau, \end{aligned} \quad (4)$$

where $R \equiv K^{\text{trans}.BM}/K^{\text{trans}.m}$.

The blood supplying arteries for lumbar vertebra, normally called segmental arteries, are originated from the abdominal aorta. They surround the vertebral body in axial plane and transport the blood to the vertebral marrow and spinal cord by some branches, where some other branches supply the blood to the paravertebral muscles, such as the erector spinae. Because the vertebrae and its surrounding muscles are supplied by the same segmental artery, C_p would influence C_{BM} and C_m simultaneously. Based on such

association, relationship between the pharmacokinetics of bone marrow and surrounding muscle can be formulated by balancing out the AIF. In other words, it is possible to derive the physiological parameters in bone marrow by taking the muscle as the reference. Therefore, the established muscle-based model (4) can derive the contrast concentration in bone marrow based on that in muscle, which also reflects the contrast dynamics in the artery.

Because DCE-MRI employs fast imaging sequence, the image quality is poor. For extracting characteristic curve, normally people would draw ROI to average the signal intensity of all the included pixels. For AIF acquisition, the area of the artery is too small to get a quality DCE signal. On the other hand, AIF is sensitive to the contrast injection procedure, which also makes the AIF variable. In contrast, the area of muscle bulk is larger to derive a quality DCE signal, which will be easier for analysis. In addition, the pharmacokinetics in muscle is the result after the interaction between the muscle and the artery so that it is not that sensitive to the contrast injection procedure. Therefore, the DCE-MRI signal in muscle is much more stable than in the artery. As a result, the muscle-based modeling would provide a more robust analysis for bone marrow perfusion.

In order to get an analytical solution of (4), an exponential model is employed to formulate the contrast concentration in erector spinae muscle $C_m(t)$, as shown in the following:

$$\begin{aligned} C_m(t) &= A \cdot t \cdot \exp(-t \cdot B) + C [1 - \exp(-t \cdot D)] \cdot \exp(-t \cdot E), \end{aligned} \quad (5)$$

where A, B, C, D , and E are density and time constants, respectively. By substituting (5) into (4), the contrast concentration in the bone marrow can be finally formulated as

$$\begin{aligned} C_{BM}(t) &= R \cdot C_m(t) + R \cdot \left[\left(\frac{K^{\text{trans}.m}}{v_{e,m}} \right) - \left(\frac{K^{\text{trans}.BM}}{v_{e,BM}} \right) \right] \cdot f(t), \end{aligned} \quad (6)$$

where the $f(t)$ is formulated as

$$\begin{aligned} f(t) &= \frac{[A \cdot B^2 \cdot t^2 - 2A \cdot \exp(B \cdot t) - 2A \cdot B \cdot t + 2A]}{[B^3 \cdot v_{e,BM} \cdot \exp(K^{\text{trans}.BM} + B \cdot t)]} \\ &+ \frac{[C \cdot E \cdot t - C \cdot \exp(E \cdot t) + C]}{[E^2 \cdot v_{e,BM} \cdot \exp(K^{\text{trans}.BM} + E \cdot t)]} \\ &+ \frac{[C \cdot D \cdot t - C \cdot \exp(t \cdot D + t \cdot E) + C \cdot E \cdot t + C]}{[v_{e,BM} \cdot \exp(K^{\text{trans}.BM} + D \cdot t + E \cdot t) (D + E)^2]} \\ &+ \frac{[C \cdot t / \exp(E \cdot t) - C \cdot t]}{[E \cdot v_{e,BM} \cdot \exp(K^{\text{trans}.BM})]} \end{aligned}$$

$$\begin{aligned}
 & + \frac{[C \cdot t / \exp(t \cdot D + t \cdot E) - C \cdot t]}{[\nu_{e,BM} \cdot \exp(K^{trans,BM}) (D + E)]} \\
 & - \frac{[A \cdot B \cdot t^2 - A \cdot t \cdot \exp(B \cdot t) + A \cdot t]}{[B^2 \cdot \nu_{e,BM} \cdot \exp(K^{trans,BM} + B \cdot t)]}.
 \end{aligned} \tag{7}$$

For each data set, the coefficients in the muscle model (5) were first derived by fitting the DCE-MRI signal from muscle ROI with (5). Then, the fixed coefficients were substituted into (6) to derive the pharmacokinetic parameters, $K^{trans,BM}$, $K^{trans,m}$, $\nu_{e,BM}$, and $\nu_{e,m}$, by fitting the DCE-MRI signal of bone marrow. The curve fitting was performed on the DCE-MRI signal with the time course from the starting point to the end of the signal. Figure 3 shows examples of the curve fitting for the DCE-MRI signals from muscle and bone marrow, respectively. The curve fitting was conducted by using the least square method. In total, 304 parameters of 76 subjects were analyzed. The subjects were classified into three groups according to the T-score derived from the BMD and World Health Organization criteria.

2.4. Statistical Analysis. The investigated subjects were classified into three groups (normal, osteopenia, and osteoporosis) according to their BMD. The statistical descriptions of the model parameters were derived by curve fitting for each subject. Then, the data were compared across the three BMD groups. Analysis of variance method (ANOVA) was employed to evaluate differences in parameters among groups. Statistical analysis was performed using statistical software (SPSS 13.0). A P value of less than 0.05 was considered statistically significant.

3. Results

Based on the pharmacokinetic model, the perfusion process can be quantitatively analyzed. Table 1 shows the comparison results by ANOVA analysis. From Table 1, it can be observed that $K^{trans,BM}$ reduces gradually and significantly ($P = 0.009$) in osteopenia and osteoporosis groups compared to the group with normal BMD. For $\nu_{e,BM}$, the gradual reduction with the decreasing BMD can be observed but the change does not reach the significant level ($P = 0.637$). However, for the muscle pharmacokinetic parameters, $K^{trans,m}$ and $\nu_{e,m}$ have no significant difference among three groups and no changing trend among the groups.

It indicates that the extravasation rate is significantly reduced during the bone loss process. In other words, the lower the BMD is, the slower the exchange rate in the fluid perfusion from the capillary to the bone marrow is. Although the extravascular-extracellular volume fraction of bone marrow is also decreased in the subjects with lower BMD, it is statistically nonsignificant. While it is interesting

to find out that neither extravasation rate nor extravascular-extracellular volume fraction has significant change in erector spinae muscle among the groups with different BMD, further, there is no changing trend of the muscle pharmacokinetic parameters with the reduction of the BMD. It may imply that, with the bone loss process, the surrounding muscle still keeps a normal perfusion function.

4. Discussions

With the development of medical imaging, perfusion in tissue can be assessed by DCE-MRI, which, in recent years, has been used to study bone perfusion in a variety of physiological and disease conditions [13, 17, 23–26]. Further, pharmacokinetic models have been employed to analyze bone perfusion function in patients with multiple myeloma, bone edema, and Paget's disease of bone [17, 18, 23]. Bone is composed of trabecular and cortical bone. All of the trabecular bone and the inner two-thirds of the cortical bone receive their blood supply from the marrow cavity [27]. Taking advantage of DCE-MRI, some studies have shown how perfusion parameters are reduced in osteoporotic bone [10–12]. After a bolus injection, tissue concentration of gadolinium is determined by local blood flow, capillary capacitance, vessel permeability, interstitial space, and interstitial diffusion [8]. This is the first study to investigate bone perfusion of osteoporosis by a pharmacokinetic model without directly using AIF.

Most previous work employed Tofts model to assess the bone perfusion [14, 17, 18], of which the analysis of the bone perfusion was much dependent on AIF. It is good to involve the contrast dynamics in the artery when analyzing the perfusion in the tissue. However, because of the small area of vessel in the image and the pulsation of the blood, AIF is quite variable even under the same experiment protocol [21]. Some work used Brix model to assess the bone perfusion [19, 20], where AIF was not included. Such model assumes the MR signal intensity is linearly proportional to the concentration of contrast agent. This assumption may not hold true for different experiment conditions. Therefore, establishing a pharmacokinetic modeling scheme, which is reliable and stable enough but still reflects the contrast dynamics in the vessel, will provide a more precise assessment of perfusion function. The proposed muscle-based model achieved such purpose for investigating bone perfusion.

Firstly, the parameter $\nu_{e,BM}$ was observed to be reduced with a decreased BMD, which indicated a reduced capacity for blood perfusion in osteoporotic bone. Increased marrow fat in osteoporotic bone may be one reason for the decreased extravascular-extracellular volume fraction in bone marrow. A previous work reported an increased marrow fat content in the osteoporosis patients by using MR spectroscopy [28]. Our previous studies for osteoporosis also supported this finding [10, 20]. In osteoporotic bone, the increased marrow fat would reduce interstitial space for perfusion, which could result in a diminished extravascular-extracellular volume fraction [10–12, 28, 29]. However, the change in $\nu_{e,BM}$ among the three groups was nonsignificant, indicating that the marrow fat

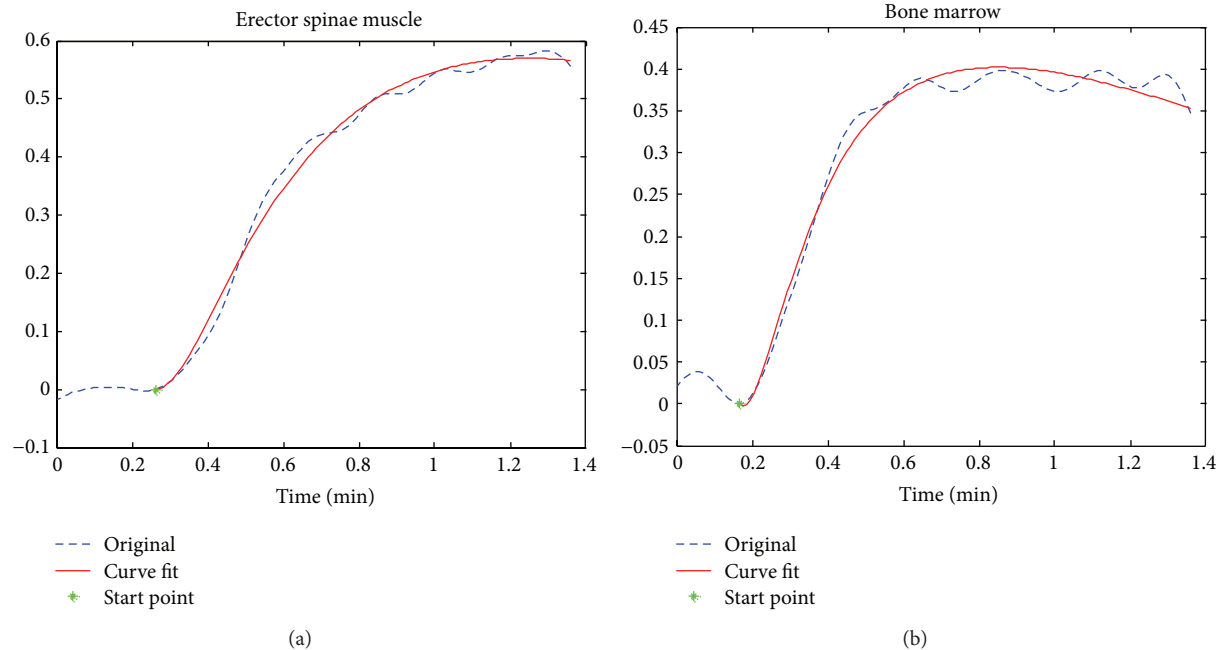


FIGURE 3: Data processing on DCE data from a subject with normal BMD. (a) Erector spinae muscle curve fitting by muscle-based model to derive characteristic parameters; (b) bone marrow curve fitting by (1).

TABLE 1: Comparison among groups.

Parameter	Group (<i>N</i>)	Mean	SD	<i>P</i> value
$K^{\text{trans},\text{BM}} (\text{min}^{-1})$	Normal (<i>n</i> = 11)	0.369	0.129	0.009
	Osteopenia (<i>n</i> = 26)	0.334	0.110	
	Osteoporosis (<i>n</i> = 39)	0.255	0.135	
$K^{\text{trans},m} (\text{min}^{-1})$	Normal (<i>n</i> = 11)	0.303	0.101	0.623
	Osteopenia (<i>n</i> = 26)	0.310	0.116	
	Osteoporosis (<i>n</i> = 39)	0.280	0.136	
$v_{e,\text{BM}}$	Normal (<i>n</i> = 11)	0.191	0.245	0.637
	Osteopenia (<i>n</i> = 26)	0.146	0.214	
	Osteoporosis (<i>n</i> = 39)	0.125	0.184	
$v_{e,m}$	Normal (<i>n</i> = 11)	0.186	0.286	0.662
	Osteopenia (<i>n</i> = 26)	0.114	0.177	
	Osteoporosis (<i>n</i> = 39)	0.159	0.276	

content change may not be the main contribution to the perfusion function degeneration in osteoporosis.

Secondly, $K^{\text{trans},\text{BM}}$ was also found decreased in subjects with lower BMD, implying a degenerated blood supply function. Such degeneration could also diminish the nutrition exchange between the bone tissue and the artery. It appears that the exchange rate across the vessel wall is reduced as BMD decreases. Multiple factors can affect this exchange rate, such as capillary endothelial permeability and interstitial or intraosseous pressure. For the latter factor, higher interstitial pressures will limit diffusion of molecules between the capillary bed and the interstitial space. It has been revealed by a previous study [30] that increased marrow fat increases intraosseous pressure. The increased marrow fat content would limit exchange between the intravascular

and interstitial spaces resulting in a weakened perfusion rate. Reduction of arterial capillary density could be another reason for the decreased $K^{\text{trans},\text{BM}}$ in the bone with lower BMD. Patients with proximal femoral osteoporosis have been reported with reduced density of arterial capillaries and more frequent arteriosclerotic vascular lesions [31]. Another study on multiple myeloma infiltration of vertebral bodies found that the reduction of the blood volume during the perfusion mirrored bone marrow vessel density assessed histologically [23].

Thirdly, it is interesting that muscle perfusion indices did not change with BMD ($P > 0.6$). With respect to vascular inflow, previous studies have shown that the perfusion anomalies occurring in osteoporosis most likely originate within bone but not within adjacent muscle [11, 12]. In other

words, decreased perfusion function in osteoporosis is a local degeneration of bone rather than a systematic circulatory disturbance.

This retrospective study had one main limitation. The data acquisition duration was relatively short at 87 seconds, which may limit the assessment of the full wash-out phase and thus the influence the parameter derivation. The derived parameters may be deviated from the true value. However, the trend for the parameter change among different groups still reflects the real situation and is supported by other studies.

In conclusion, a muscle-based pharmacokinetic model was proposed for bone marrow perfusion without using AIF. Such model avoided the direct association with the variable contrast agent dynamics in the artery and could provide a more reliable analysis. The perfusion indices, $v_{e,BM}$ and $K^{trans,BM}$, were both decreased in osteoporotic bone. Decreased interstitial space and reduced capillary density are possible reasons for the degenerated perfusion function. Further, these factors should be considered in the mechanism investigation of osteoporosis.

Conflict of Interests

The authors declare that there is no conflict of interests regarding the publication of this paper.

Acknowledgments

This study is supported by the Research Grants Council of the Hong Kong Special Administrative Region, China (Project no. 465111), the National Natural Science Foundation of China (81000647), the Basic Research Foundation (Outstanding Young Investigator Track) of Shenzhen (JC201005260124A), and the High-End Talent Oversea Returnees Foundation of Shenzhen (KQC201109020052A).

References

- [1] Y. Z. Bagger, L. B. Tankó, P. Alexandersen, H. B. Hansen, G. Qin, and C. Christiansen, "The long-term predictive value of bone mineral density measurements for fracture risk is independent of the site of measurement and the age at diagnosis: results from the Prospective Epidemiological Risk Factors study," *Osteoporosis International*, vol. 17, no. 3, pp. 471–477, 2006.
- [2] E. Dennison, M. A. Mohamed, and C. Cooper, "Epidemiology of osteoporosis," *Rheumatic Disease Clinics of North America*, vol. 32, no. 4, pp. 617–629, 2006.
- [3] S. Y. S. Wong, T. Kwok, J. Woo et al., "Bone mineral density and the risk of peripheral arterial disease in men and women: results from Mr. and Ms Os, Hong Kong," *Osteoporosis International*, vol. 16, no. 12, pp. 1933–1938, 2005.
- [4] P. Pennisi, S. S. Signorelli, S. Riccobene et al., "Low bone density and abnormal bone turnover in patients with atherosclerosis of peripheral vessels," *Osteoporosis International*, vol. 15, no. 5, pp. 389–395, 2004.
- [5] M. T. Vogt, J. A. Cauley, L. H. Kuller, and M. C. Nevitt, "Bone mineral density and blood flow to the lower extremities: the study of osteoporotic fractures," *Journal of Bone and Mineral Research*, vol. 12, no. 2, pp. 283–289, 1997.
- [6] I. C. Benjaminsen, B. A. Graff, K. G. Brurberg, and E. K. Rofstad, "Assessment of tumor blood perfusion by high-resolution dynamic contrast-enhance MRI: a preclinical study of human melanoma xenografts," *Magnetic Resonance in Medicine*, vol. 52, no. 2, pp. 269–276, 2004.
- [7] J. P. B. O'Connor, A. Jackson, G. J. M. Parker, and G. C. Jayson, "DCE-MRI biomarkers in the clinical evaluation of antiangiogenic and vascular disrupting agents," *British Journal of Cancer*, vol. 96, no. 2, pp. 189–195, 2007.
- [8] R. Luyopaert, S. Boujraf, S. Sourbron, and M. Osteaux, "Diffusion and perfusion MRI: basic physics," *European Journal of Radiology*, vol. 38, no. 1, pp. 19–27, 2001.
- [9] P. S. Tofts, "Modeling tracer kinetics in dynamic Gd-DTPA MR imaging," *Journal of Magnetic Resonance Imaging*, vol. 7, no. 1, pp. 91–101, 1997.
- [10] J. F. Griffith, D. K. W. Yeung, G. E. Antonio et al., "Vertebral bone mineral density, marrow perfusion, and fat content in healthy men and men with osteoporosis: dynamic contrast-enhanced MR imaging and MR spectroscopy," *Radiology*, vol. 236, no. 3, pp. 945–951, 2005.
- [11] J. F. Griffith, D. K. W. Yeung, G. E. Antonio et al., "Vertebral marrow fat content and diffusion and perfusion indexes in women with varying bone density: MR evaluation," *Radiology*, vol. 241, no. 3, pp. 831–838, 2006.
- [12] J. F. Griffith, D. K. W. Yeung, P. H. Tsang et al., "Compromised bone marrow perfusion in osteoporosis," *Journal of Bone and Mineral Research*, vol. 23, no. 7, pp. 1068–1075, 2008.
- [13] N. M. Menezes, E. A. Olear, X. Li et al., "Gadolinium-enhanced MR images of the growing piglet skeleton: ionic versus nonionic contrast agent," *Radiology*, vol. 239, no. 2, pp. 406–414, 2006.
- [14] V. Savvopoulou, T. G. Maris, L. Vlahos, and L. A. Moulopoulos, "Differences in perfusion parameters between upper and lower lumbar vertebral segments with dynamic contrast-enhanced MRI (DCE MRI)," *European Radiology*, vol. 18, no. 9, pp. 1876–1883, 2008.
- [15] G. Brix, W. Semmler, R. Port, L. R. Schad, G. Layer, and W. J. Lorenz, "Pharmacokinetic parameters in CNS Gd-DTPA enhanced MR imaging," *Journal of Computer Assisted Tomography*, vol. 15, no. 4, pp. 621–628, 1991.
- [16] U. Hoffmann, G. Brix, M. V. Knopp, T. Hess, and W. J. Lorenz, "Pharmacokinetic mapping of the breast: a new method for dynamic MR mammography," *Magnetic Resonance in Medicine*, vol. 33, no. 4, pp. 506–514, 1995.
- [17] J. H. Lee, J. P. Dyke, D. Ballon, D. M. Ciombor, G. Tung, and R. K. Aaron, "Assessment of bone perfusion with contrast-enhanced magnetic resonance imaging," *Orthopedic Clinics of North America*, vol. 40, no. 2, pp. 249–257, 2009.
- [18] M. Libicher, C. Kasperk, M. Daniels, W. Hosch, H.-U. Kauczor, and S. Delorme, "Dynamic contrast-enhanced MRI in Paget's disease of bone-correlation of regional microcirculation and bone turnover," *European Radiology*, vol. 18, no. 5, pp. 1005–1011, 2008.
- [19] H. T. Ma, J. F. Griffith, X. Zhao, H. Lv, D. K. Yeung, and P. C. Leung, "Relationship between marrow perfusion and bone mineral density: a pharmacokinetic study of DCE-MRI," in *Proceedings of the Annual International Conference of the IEEE Engineering in Medicine and Biology Society (EMBC '12)*, pp. 377–379, IEEE, 2012.
- [20] H. T. Ma, J. F. Griffith, D. K. Yeung, and P. C. Leung, "Modified brix model analysis of bone perfusion in subjects of varying bone mineral density," *Journal of Magnetic Resonance Imaging*, vol. 31, no. 5, pp. 1169–1175, 2010.

- [21] T. E. Yankeelov, J. J. Luci, M. Lepage et al., "Quantitative pharmacokinetic analysis of DCE-MRI data without an arterial input function: a reference region model," *Magnetic Resonance Imaging*, vol. 23, no. 4, pp. 519–529, 2005.
- [22] T. E. Yankeelov, G. O. Cron, C. L. Addison et al., "Comparison of a reference region model with direct measurement of an AIF in the analysis of DCE-MRI data," *Magnetic Resonance in Medicine*, vol. 57, no. 2, pp. 353–361, 2007.
- [23] S. Nosàs-Garcia, T. Moehler, K. Wasser et al., "Dynamic contrast-enhanced MRI for assessing the disease activity of multiple myeloma: a comparative study with histology and clinical markers," *Journal of Magnetic Resonance Imaging*, vol. 22, no. 1, pp. 154–162, 2005.
- [24] T. T.-F. Shih, C.-J. Chang, C.-Y. Hsu, S.-Y. Wei, K.-C. Su, and H.-W. Chung, "Correlation of bone marrow lipid water content with bone mineral density on the lumbar spine," *Spine*, vol. 29, no. 24, pp. 2844–2850, 2004.
- [25] T. T.-F. Shih, H.-A. Hou, C.-Y. Liu et al., "Bone marrow angiogenesis magnetic resonance imaging in patients with acute myeloid leukemia: peak enhancement ratio is an independent predictor for overall survival," *Blood*, vol. 113, no. 14, pp. 3161–3167, 2009.
- [26] H. Sheng, G. Zhang, Y.-X. Wang et al., "Functional perfusion MRI predicts later occurrence of steroid-associated osteonecrosis: an experimental study in rabbits," *Journal of Orthopaedic Research*, vol. 27, no. 6, pp. 742–747, 2009.
- [27] M. L. Knothe Tate, P. Niederer, and U. Knothe, "In vivo tracer transport through the lacunocanalicular system of rat bone in an environment devoid of mechanical loading," *Bone*, vol. 22, no. 2, pp. 107–117, 1998.
- [28] D. K. W. Yeung, J. F. Griffith, G. E. Antonio, F. K. H. Lee, J. Woo, and P. C. Leung, "Osteoporosis is associated with increased marrow fat content and decreased marrow fat unsaturation: a proton MR spectroscopy study," *Journal of Magnetic Resonance Imaging*, vol. 22, no. 2, pp. 279–285, 2005.
- [29] T. T.-F. Shih, H.-C. Liu, C.-J. Chang, S.-Y. Wei, L.-C. Shen, and P.-C. Yang, "Correlation of MR lumbar spine bone marrow perfusion with bone mineral density in female subjects," *Radiology*, vol. 233, no. 1, pp. 121–128, 2004.
- [30] K. Miyanishi, T. Yamamoto, T. Irisa et al., "Bone marrow fat cell enlargement and a rise in intraosseous pressure in steroid-treated rabbits with osteonecrosis," *Bone*, vol. 30, no. 1, pp. 185–190, 2002.
- [31] M. Laroche, I. Ludot, M. Thiechart et al., "Study of the intraosseous vessels of the femoral head in patients with fractures of the femoral neck or osteoarthritis of the hip," *Osteoporosis International*, vol. 5, no. 4, pp. 213–217, 1995.

Research Article

Neural Decoding Using a Parallel Sequential Monte Carlo Method on Point Processes with Ensemble Effect

Kai Xu,^{1,2} Yiwen Wang,^{1,3} Fang Wang,^{1,2} Yuxi Liao,^{1,2} Qiaosheng Zhang,^{1,2}
Hongbao Li,^{1,2} and Xiaoxiang Zheng^{1,2,3}

¹ *Qiushi Academy for Advanced Studies, Zhejiang University, Hangzhou 310027, China*

² *Department of Biomedical Engineering, Zhejiang University, Hangzhou 310027, China*

³ *Key Laboratory of Biomedical Engineering of Ministry of Education, Zhejiang University, Hangzhou 310027, China*

Correspondence should be addressed to Yiwen Wang; eewangyw@zju.edu.cn

Received 28 February 2014; Accepted 17 April 2014; Published 18 May 2014

Academic Editor: Ting Zhao

Copyright © 2014 Kai Xu et al. This is an open access article distributed under the Creative Commons Attribution License, which permits unrestricted use, distribution, and reproduction in any medium, provided the original work is properly cited.

Sequential Monte Carlo estimation on point processes has been successfully applied to predict the movement from neural activity. However, there exist some issues along with this method such as the simplified tuning model and the high computational complexity, which may degenerate the decoding performance of motor brain machine interfaces. In this paper, we adopt a general tuning model which takes recent ensemble activity into account. The goodness-of-fit analysis demonstrates that the proposed model can predict the neuronal response more accurately than the one only depending on kinematics. A new sequential Monte Carlo algorithm based on the proposed model is constructed. The algorithm can significantly reduce the root mean square error of decoding results, which decreases 23.6% in position estimation. In addition, we accelerate the decoding speed by implementing the proposed algorithm in a massive parallel manner on GPU. The results demonstrate that the spike trains can be decoded as point process in real time even with 8000 particles or 300 neurons, which is over 10 times faster than the serial implementation. The main contribution of our work is to enable the sequential Monte Carlo algorithm with point process observation to output the movement estimation much faster and more accurately.

1. Introduction

Brain machine interfaces (BMIs) attempt to build direct links between brains and artificial devices, such as computer cursors and robotic arms [1–5]. They are considered as potential solutions to help paralyzed patients restore motor control, especially for those suffering from stroke, spinal cord injury, or amyotrophic lateral sclerosis [6–8]. In the past decade, the research on BMIs has made a great progress due to the rapid growth and development in neuroscience, computer science, and engineering. Many experimental demonstrations have shown the ability to estimate continuous movement of the limbs by exploiting the spatial and temporal structure of the motor cortical activity [9–11].

To make the direct control of the prosthetic devices practical for those patients, the estimation of the movement should be highly accurate and fast enough for real-time

implementation. Several signal processing approaches have been applied to extract the functional relationship between the neural activity and the corresponding movement [12–18]. Recently, sequential Monte Carlo estimation with point process observation (SMCPP) is proposed to decode the spike trains, in which the spike trains are regarded as point processes and the spiking timing information is exploited by estimating the instantaneous firing rate in a much shorter interval (~10 msec) [19–21], while this information is discarded by many previous decoding algorithms which directly predict the movement from binned spike trains [12, 13, 18]. In addition, compared with many state-space model based algorithms, such as Kalman filter and point process adaptive filter [15, 16, 22, 23], there is no restriction on the posterior distribution of the state, which makes the SMCPP more flexible and suitable for the highly nonlinear systems such as BMIs. The experiment has demonstrated that the removal

of the Gaussian assumption on state distribution and the utilization of the neural tuning model to estimate firing rate could increase the decoding accuracy [20].

Although the SMCPP performs well in previous studies, several issues can be further improved. The first one is the tuning model, which reflects the physiological knowledge of neurons responding to stimuli. Properly building the tuning model helps the SMCPP estimation since the posterior state density is updated based on the discrepancy between the actual neural firings and the instantaneous firing rates estimated from the model. In previous studies, the tuning models in SMCPP are usually either a parametric or nonparametric function that assume firing rates of neurons are only dependent on the kinematics. However, recent studies have demonstrated that they also depend on extrinsic covariates, as well as many other factors. Truccolo et al. find that the spiking of a single neuron could be better predicted by the spiking history of ensemble [24, 25]. Pillow et al. analyze the correlated firing in a population of macaque parasol retinal ganglion cells and find that the spike times can be more accurately predicted when the spiking of other neurons is taken into account. Furthermore, the optimal, model-based decoding can extract 20% more information when the ensemble activity is included in the tuning function [26]. However, in the above study, the stimulus is binary sequence and the spikes are recorded from retinal cells. Another way to build a better tuning model is to explain the unknown factors using multidimensional hidden states [27, 28]. Although the results demonstrated that this approach can achieve a better decoding accuracy, a potential problem is that the hidden state needs to be estimated by an Expectation Maximization algorithm at every iteration, which may result into instability and extra computational complexity. Another issue of the SMCPP is the high computational complexity because of the posterior density estimation by large number of particles, which brings the challenge to the real-time BMI systems. To increase the decoding speed, the main method before is to increase the processor clock speed, while it becomes plateaued in recent years. An alternative way is to add multiple cores into CPU. However, the number of cores in most commercially available CPUs is 2 or 4 and some may be up to 8. Another solution is to implement the decoding algorithm on dedicated hardware architectures such as FPGA [29–31]. But the hardware-based solution is often difficult to develop and maintain and lacks flexibility.

In this paper, we attempt to address the issues of the SMCPP mentioned above, making the decoding algorithm more efficient and applicable for the high-performance BMI systems. Firstly, we propose to extend the state-space model [20] by incorporating the recent ensemble activity into the tuning functions of neurons and the state transition model. The predicting power of tuning models with and without ensemble activity is evaluated and compared. The continuous kinematics of a monkey performing a target-pursuit task are decoding from the neural recordings in the primary motor cortex using the SMCPP based on such new models. The statistical performances are evaluated on multiple days. We do the experiment to see whether the decoding accuracy of the SMCPP can be improved when the ensemble effect

is taken into account. Another contribution of our work is the speedup of the decoding algorithm for the demands of real-time implementation. We implement the SMCPP in a fully parallel way based on CUDA, which is a technology that can increase the computing performance dramatically by utilizing the hundreds of cores in graphics processing unit (GPU). Significant improvement has been obtained by using the graphics processing unit to perform the feature extraction in real-time brain computer interface [32]. In our implementation, the particles are propagated and updated in parallel. We use the parallel prefix scan algorithm to perform the weight summation which is often done serially before. The decoding speed of the proposed algorithm is observed to examine whether it satisfies the requirement of real-time BMI systems especially when the number of particles is large. Due to the great development of the neural recording technology in the last decade, hundreds of neurons can be simultaneously recorded to build a high-dimensional data space [33]. We apply our proposed algorithm on such a scenario to validate its real advantages.

This paper is organized as follows. Section 2 introduces data recording and the BMI task. The details of SMCPP algorithm, the corresponding neural tuning model, the state transition model, and the parallel implementation are described in Section 3. In Section 4, we evaluate the predicting power of different tuning models and compare the decoding accuracy using sequential Monte Carlo algorithm with and without including the recent ensemble activity. In addition, we observe the decoding speed of our proposed algorithm to see whether it fulfills the requirement of real-time BMI systems. We discuss the results and conclude in Section 5.

2. Experiment Setup and Data Recording

The paradigm of the motor brain machine interface was designed and implemented in the Qiushi Academy for Advanced Studies at Zhejiang University. An adult male monkey was trained to perform a two-dimensional target-reaching task. After a target circle was presented on a computer screen, the monkey moved the cursor towards the target by controlling a handheld joystick. When the target was intersected with the cursor for a certain time, it would disappear and another target would show in a new position nearby the current one. The monkey was rewarded when the task was performed successfully for a while. The corresponding position of the joystick was recorded continuously with a sampling rate of 20 Hz, the velocity was estimated as the difference between current and previous positions, and the acceleration was estimated as the first-order difference from the velocity.

A Utah array (1.0 mm electrode length, 96 channels with ICS-96 connector, Blackrock Microsystems) was chronically implanted in the arm area of primary motor cortex (M1) contralateral to the hand performing the task. Details about the surgical procedure could be found in [34, 35]. After the surgical procedure, a 128 Cerebus Data Acquisition system (Blackrock Microsystems, USA) was used to record

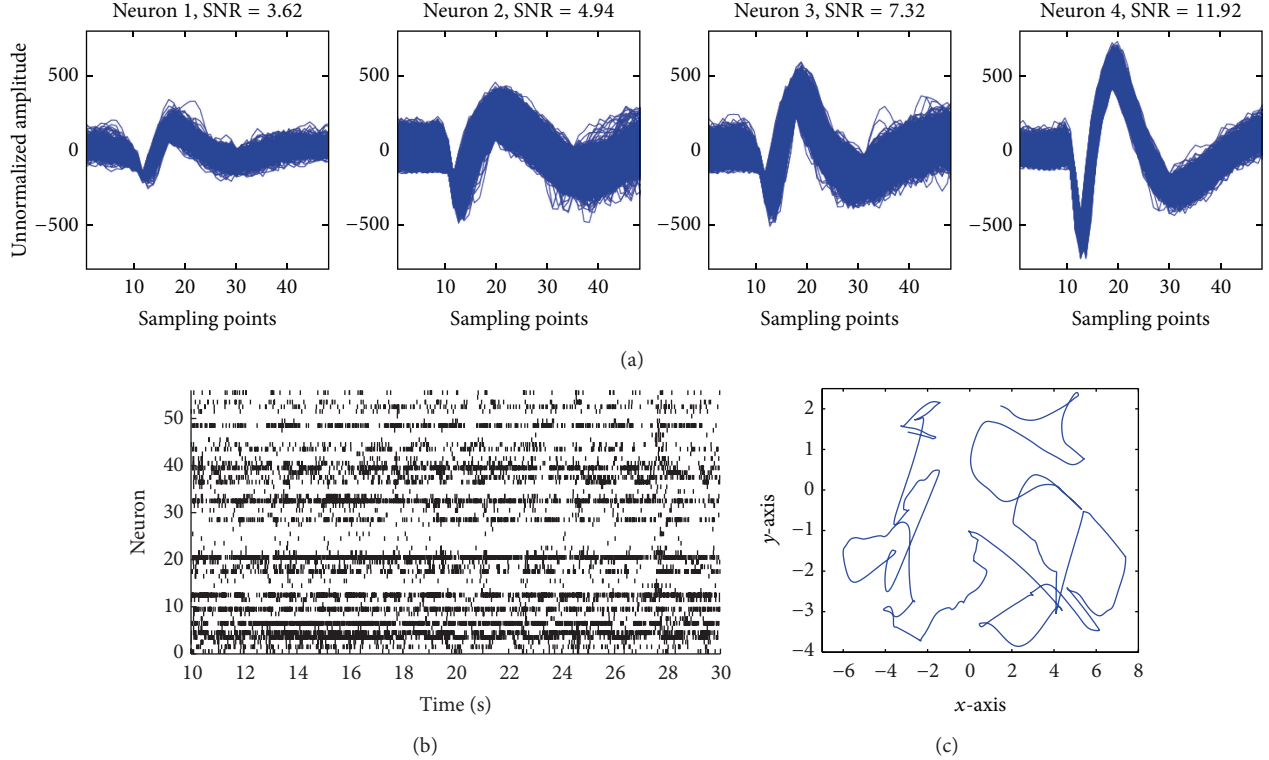


FIGURE 1: (a) The spike waveforms from 4 neurons with different SNRs. (b) The raster graph of the population activities during the task. (c) The arm trajectory in the 2D plane corresponding to the ensemble activity in (b).

the neuronal action potentials during the experiment. The sampling rate was 30 kHz and the action potentials were detected by a thresholding method. The waveforms of the spikes were amplified and band-pass filtered from 250 Hz to 7.5 kHz. Only the neurons whose firing rates were larger than 1 Hz and SNR that were larger than 2 were isolated to avoid the nonrobustness during the computation. Figure 1(a) depicts the spikes recorded from 4 neurons with different SNRs.

The time of each spike was recorded and the firing rate was computed as the number of spikes within 10 ms time windows. We found that over 99% of these counts were either 0 or 1, which made the ensemble activity as multichannel point process observation. Meanwhile, all the kinematics recorded were interpolated and synchronized with the spike trains. Figure 1(b) shows a raster graph of the ensemble activity during a time interval, and Figure 1(c) plots the corresponding trajectory of the position in 2D plane.

3. Methods

3.1. Tuning Function with Ensemble Correlation. Given a time interval $(0, T]$, a spike train consists of J spikes of a neuron observed at time $0 < u_1 < u_2 < \dots < u_J < T$. Therefore, it can be regarded as a point process which is composed of a set of binary events that occur in continuous time, which can be fully characterized by its conditional intensity function:

$$\lambda(t) = \lim_{\Delta \rightarrow 0} \frac{P(N(t + \Delta) - N(t) = 1)}{\Delta}, \quad (1)$$

where $N(t)$ is the number of spikes fired in the time interval $(0, t]$. Based on the theory of point process, if Δ is small enough, the probability of observing a spike in the interval between t and $t + \Delta$ can be well approximated by the following equation:

$$P(dN(t)) = \exp(dN(t) \log(\lambda(t)\Delta) - \lambda(t)\Delta), \quad (2)$$

where $dN(t)$ is the activity of the neuron at time t . If there is a spike at time t , then $dN(t)$ equals 1, otherwise 0.

The conditional intensity functions of spike trains can be defined as the neuronal tuning functions which reflect the tuning property of neurons and characterize the relationship between the covariates and the neuronal response. The function should be designed properly because in decoding stage the posterior state distribution is updated based on the discrepancy between the firing of neurons and the instantaneous firing rate $\lambda(t)$ estimated from it. In previous decoding algorithms, the tuning function was usually assumed to be only dependent on the current kinematics $x(t)$. However, the studies in neuroscience demonstrate that the spiking activity of a single neuron is dependent not only on external covariates, but also on the spiking history of the neuron itself and spiking activities of other neurons due to the coupling between them. We propose to apply a more general tuning function which extends the traditional ones and estimate the instantaneous firing rate based on both the kinematics and recent ensemble activity. Let x_t and H_t represent the kinematics and the recent ensemble activity at

time t , respectively. More specifically, H_t^i is defined as the number of spikes fired during the time interval $[t-l \rightarrow t]$ for the neuron i , where l is the time length which will be determined in the following analysis. Then our tuning function can be formulated as

$$\lambda(t) = \lambda(x_t, H_t) = \exp\left(\alpha_0 + \sum_{i=1}^D \alpha_i x_t^i + \sum_{j=1}^C \beta_j H_t^j\right), \quad (3)$$

where D is the dimension of the kinematic vector, $\exp(\alpha_0)$ is the background firing rate, α_i is the modulation in firing rate of the i th component of kinematic vector, C is the number of neurons in the ensemble, and β_j represents the influence of the j th neuron on the target neuron. The above equation takes the movement, the spiking history of the target neuron, and the contributions of other neurons into account and is referred to as full tuning model in the following. By contrast, the tuning equation which only depends on the movement is referred to as mov tuning model. It is similar to (3) but without the third term in the exponential function.

In the full tuning model, the time length l of the recent ensemble activity is a parameter that needs to be determined. If the value of l is too small, then information contained in the rest of ensemble activity will be wasted. While if the value is too large, which means too much ensemble activity is included, it is likely to incorporate irrelevant information which could bias the estimation of the firing rate. Therefore, it is necessary to assess the performance of the tuning model with different length of recent ensemble activity. In addition, we also need to compare its performance with mov tuning model to demonstrate the superiority. Due to the point process property of a spike train, traditional distance measures like mean square error could not be applied directly. In this paper, we adopt the receiver operating characteristic (ROC) analysis and Kolmogorov-Smirnov (KS) plot to evaluate the performance of tuning models.

Receiver Operating Characteristic Analysis. Suppose the parameters of the tuning function have been estimated from the training data; then, for any neuron, we can compute the instantaneous firing rate $\lambda(t)$. To get the ROC curve, we make a threshold and compute the spike prediction $\hat{r}_c(t)$ as follows:

$$\begin{aligned} \hat{r}_c(t) &= 1 && \text{if } \lambda(t) \geq c \\ \hat{r}_c(t) &= 0 && \text{if } \lambda(t) < c. \end{aligned} \quad (4)$$

For each threshold c , the ratio of the true positive rate (TPR) to the false positive rate (FPR) given the recorded spikes data could be computed, resulting in the ROC curve. The area under the curve (AUC) corresponds to the probability that the proposed model will assign a higher probability to the sample from the spike population compared to the sample from the no-spike population. Therefore it provides an assessment of the goodness of fit of the model.

Kolmogorov-Smirnov Plot. Based on the time-rescaling theorem, we can transform a point process into a Poisson process with unit rate which is appropriate for goodness of fit assessment [36]. Firstly, the tuning function is fitted to

the spike train data based on the proposed model. Then the rescaled times z_j could be computed as follows:

$$z_j = 1 - \exp\left\{\int_{u_j}^{u_{j+1}} \lambda(t) dt\right\}, \quad (5)$$

where $j = 1, \dots, J-1$. If the proposed model is correct, z_j will be random variables sampled uniformly from the interval $[0, 1]$. The z_j values are ordered from smallest to largest, generating a new sequence z_k . And a uniform density is defined as $b_k = (k-1/2)/n$ for $k = 1, \dots, n$ against z_k . Finally, the cumulative distribution function of the uniform density could be plotted, which is named KS plot. If the model is correct, points in the KS plot will be on a 45-degree line. More details can be found in [36].

3.2. Sequential Monte Carlo Estimation and Parallel Implementation. The state-space model based algorithms are widely used in brain machine interfaces to infer the latent state like the kinematics from neural activity. In this work, (3) and (2) constitute the observation model. In previous studies, the movement was often assumed to be a random-walk model, where the current state only depended on the previous state plus some noise. In this paper, we also incorporate the ensemble activity into the state vector, resulting in an augmented state vector $s_k = [x_k \ H_k]$, and then the new state equation is defined as

$$x_k = As_{k-1} + w, \quad (6)$$

where A is the system evolution matrix and w is a zero-mean Gaussian noise with covariance matrix Q . As a result, the current state depends not only on the previous state, but also on the recent ensemble activity. We term the state-space model that includes the recent ensemble activity as the full model and whose state and observation models only depend on movements as mov model.

Once the transition and the observation functions have been defined as above, the state can be formulated as the posterior distribution given the observations, which can be estimated recursively as follows:

$$p(x_k | N_{1:k}) = \frac{p(x_k | N_{1:k-1}) p(dN_k | x_k, H_k)}{p(dN_k | N_{1:k-1})}, \quad (7)$$

$$\begin{aligned} p(x_k | N_{1:k-1}) \\ = \int p(x_k | x_{k-1}, H_k) p(x_{k-1} | N_{1:k-1}) dx_{k-1}, \end{aligned} \quad (8)$$

where $N_{1:k} = [dN_1, dN_2, \dots, dN_k]$ is the population activity up to time k , $p(x_k | N_{1:k-1})$ is the one-step prediction which could be calculated according to (8), and the value of $p(dN_k | x_k, H_k)$ can be computed based on the observation model.

An issue with the above recursive estimation is that (8) is difficult to compute because of the integration operation, and the posterior density is usually multimodal or highly skewed. Sequential Monte Carlo estimation provides a good solution to this problem [37]. The basic idea is to represent the posterior density as a set of weighted particles without restricting

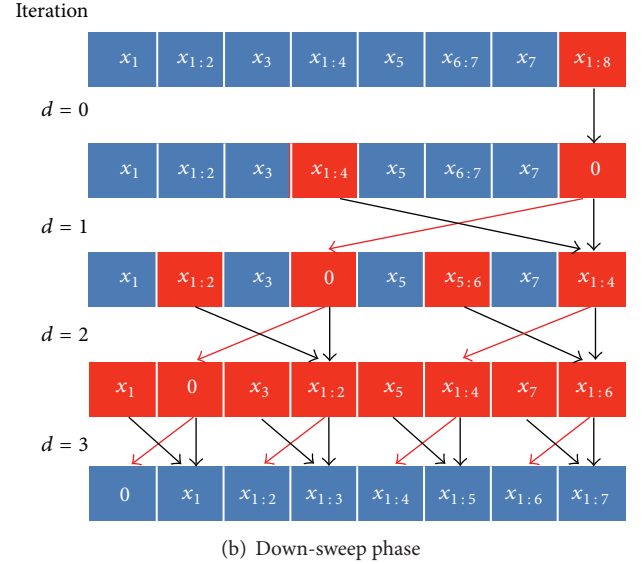
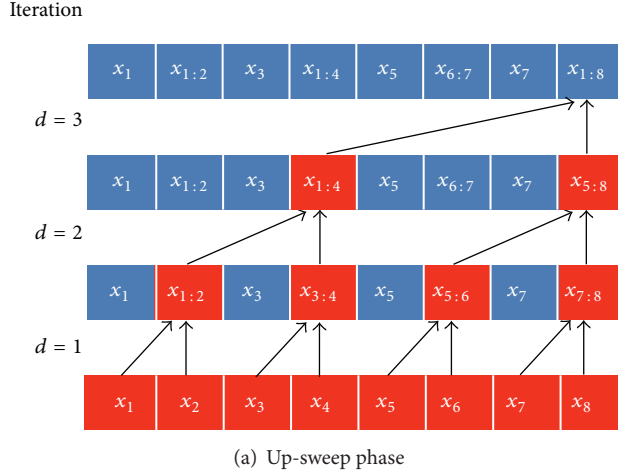


FIGURE 2: An illustration of the parallel prefix scan algorithm. (a) The up-sweep phase. (b) The down-sweep phase.

it to be any particular distribution. Initially, the weighted particles $\{x_{1:k}^i, w_k^i\}_{i=1}^{Ns}$ are generated from a prior density, and all the weights are set to $1/Ns$. Then the algorithm runs in an iterative way. For each iteration, particles x_k^i are generated from $p(x_k | x_{k-1}, H_k)$; then the importance weights are updated according to the equation $w_k^i = w_{k-1}^i p(dN_k | x_k^i, H_k)$. After the importance weights are all updated and normalized, the posterior density of state at time k can be approximated as

$$p(x_k | N_{1:k}) = \sum_{i=1}^{Ns} w_k^i k(x_k - x_k^i, \delta), \quad (9)$$

where $k(x_k - x_k^i, \delta)$ is a Gaussian kernel whose mean is x_k^i and covariance is δ . One principal purpose of BMI systems is to control the external device. A common way for the BMI decoder to output a control command is to average the posterior density. A phenomenon named degeneracy will appear after the algorithm runs over a few iterations, leading to a large amount of computational effort being wasted on the samples with small importance weights [38]. To overcome this problem, a resampling stage is introduced at the end of each iteration. In this paper, we adopt systematic resampling method and the details can be found in [39].

We adopt the root mean square error (RMSE) between the actual and the reconstructed trajectories as an assessment of the decoding algorithm and compare the decoding accuracy of the SMCPP based on the full model and mov model.

Parallel Implementation. To accelerate the computational speed, we implement the SMCPP in a massively parallel manner based on the compute unified device architecture (CUDA). It is computationally feasible for particles generation and weights calculation to concurrently execute, since the operation on each particle is independent of others. Then the resampling stage becomes a bottleneck because

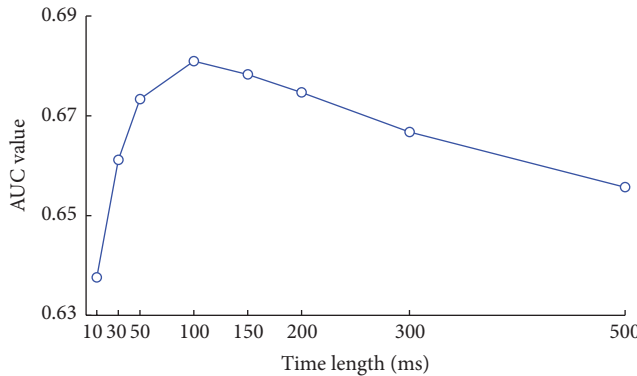
of its sequential in essence. In systematic resampling, the cumulation of the weights runs serially since the operation on current step is dependent on the result computed on last step. It takes N steps to get the result. We adopt parallel prefix sum algorithm which could dramatically reduce the computational complexity of calculating the cumulative sum [40]. The basic idea is to build a balanced binary tree based on the input data; then the prefix sum can be computed by sweeping the tree to and from its root. The algorithm is demonstrated in Figure 2, where the red blocks represent the active nodes and $x_{i:j} = \sum_{k=i}^j x_k$. The algorithm consists of two phases: the up-sweep phase which is depicted in Figure 2(a) and the down-sweep phase presented in Figure 2(b). During the up-sweep phase, at each iteration, half of the threads active at last iteration are still active and compute the partial sum of internal nodes with a distance of 2^d . The down-sweep phase followed by the up-sweep phase is like the reverse of the previous phase. In each iteration, in addition to the computation of partial sum, each active node passes its values to its left child. The computational complexity of the parallel prefix sum algorithm is $O(\log_2 N)$, which is much more efficient than the serial version above whose computational complexity is $O(N)$. More details of the algorithm can be found in [40].

4. Results and Analysis

A total number of 8 datasets recorded on different days are used in the following analysis. The summary of these datasets is listed in Table I. Firstly, we determine the optimal length of the recent ensemble activity which enables the best performance of full tuning model. Then the performances of the mov tuning model and the full tuning model are compared. Since the importance weights are updated by the discrepancy between the neural firings and the tuning model, a well-defined tuning model is necessary to an

TABLE 1: The summary of the 8 datasets used in the analysis.

Datasets	1	2	3	4	5	6	7	8
Number of neurons	40	38	39	58	40	36	27	31
Signal-to-noise ratio	4.34	4.33	4.17	3.52	3.58	3.89	4.06	4.01
Firing rate (Hz)	8.15	10.50	9.90	6.66	9.83	6.72	5.81	4.31
Length (sec)	400	400	400	400	400	400	400	300

FIGURE 3: The AUC values of the full tuning model evaluated on all the neurons recorded. The x -axis represents the time length of recent ensemble activity included in the full tuning model.

accurate estimation of posterior density. We demonstrate the superiority of the tuning model considering the ensemble effect based on the receiver operating characteristic (ROC) analysis and Kolmogorov-Smirnov (KS) plot. For a high-performance real-time brain machine interface system, an accurate and fast prediction of the state is required. So we evaluate the decoding accuracy of the sequential Monte Carlo methods based on the mov model and the full model. Then, the decoding speed of the algorithm is compared between the parallel implementation running on GPU and the traditional one running on CPU.

4.1. Tuning Model Analysis. We adopt the AUC values to assess the predictive performance of full tuning models with different length of recent ensemble activity. The AUC value, which is the area under the ROC curve, is dependent on all possible thresholds of the firing rate and computed by the true and false positive rates. If the model is perfect, the AUC value will be 1. Figure 3 shows the relation between the time length of the ensemble activity and the AUC values which are averaged among all neurons recorded. We can observe that the AUC value increases rapidly as the more recent ensemble activity is included before 100 ms. However, when the time length exceeds 100 ms, the value decreases. It means that most information about the current firing probability is contained in the kinematics and the latest 100 ms ensemble activity. And incorporating the latest 100 ms ensemble activity with the kinematics could make the observation model gain the best performance.

We also make a comparison of the predicting powers between mov tuning model and the full tuning model. Figure 4 shows that histograms of AUC values evaluated on

all the neurons in the total 8 datasets. The x -axis is the possible AUC values and y -axis represents the number of neurons with the corresponding value. The average AUC value for each model is shown in red color. Compared with the model only considering kinematics, the one including ensemble effect has a significantly better predictive performance. Figure 5 shows the KS plots of 10 typical neurons. The x -axis represents the quantiles and the y -axis represents the cumulative distribution function with respect to the uniform distribution when the conditional intensity function equals the true one. It is easy to see that the mov tuning model tends to underestimate the conditional intensity especially at middle quantiles, while incorporation of the ensemble effect into the tuning model can greatly improve the explanation of the spike activity. The black thin lines in the figure represent the 95% confidence interval. We can observe that, for most neurons, the KS plots based on our proposed model fall within the 95% confidence limits. This improvement of the fitness demonstrates that, in addition to the kinematics, the recent ensemble activity affects the spiking of the current neuron.

4.2. Decoding Accuracy. Based on the models with and without the ensemble effect, we decode the neural activity recorded during the subject performing the movement task using sequential Monte Carlo estimation. Figure 6 shows a segment of the reconstructed kinematics. The upper and down panels, respectively, show the predicted kinematics for normalized position values on x -axis and y -axis. In each subplot, the red solid line indicates the true signal, the dash black line indicates the estimation by mov model, and the solid blue line is the estimation by the full model. It is obvious that the full model provides the more consistent reconstruction compared to the previous one.

We apply the two kinds of models on all of the 8 datasets to decode the kinematics. The first 200s of each dataset is used as training data, and the rest is for testing. Figure 7 shows the statistical performance evaluated on the 8 datasets. The red and blue bars depict the decoding accuracy evaluated by the models with and without incorporating ensemble effect, respectively. It is clear that the decoding error is greatly reduced if the ensemble activity is combined with the kinematics in the model. Furthermore, among the kinematics the position gains the highest improvement (about 23.6%), and the improvement of the acceleration is not so much obvious (about 5.02%). Here we perform the left-tail paired Student t -test against the alternative that the decoding error of our proposed method is smaller. All the tests are performed on the null hypothesis at $\alpha = 0.05$ significance level. The P values are shown in Table 2. Not surprisingly, the SMCPP method based on the full model provides smaller decoding error than the one based on mov model statistically ($P < 0.05$, left tail, paired Student's t -test). In most brain machine interface applications, we usually use the position values to control an external device. Therefore, the incorporation of ensemble effect in the decoding algorithm is helpful to high-performance BMI systems.

We vary the time length of the recent ensemble activity included in the full model and evaluate the corresponding

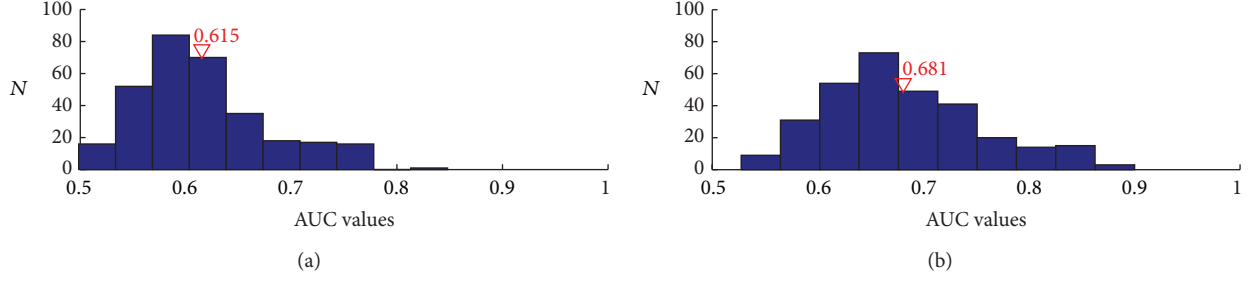


FIGURE 4: The histograms of AUC values of the tuning models evaluated on all the neurons recorded. The x -axis is the possible AUC values and y -axis is the number of neurons with the corresponding value. The numbers in red color are the averaged AUC values. (a) Mov tuning model. (b) Full tuning model with the recent 100 ms ensemble activity.

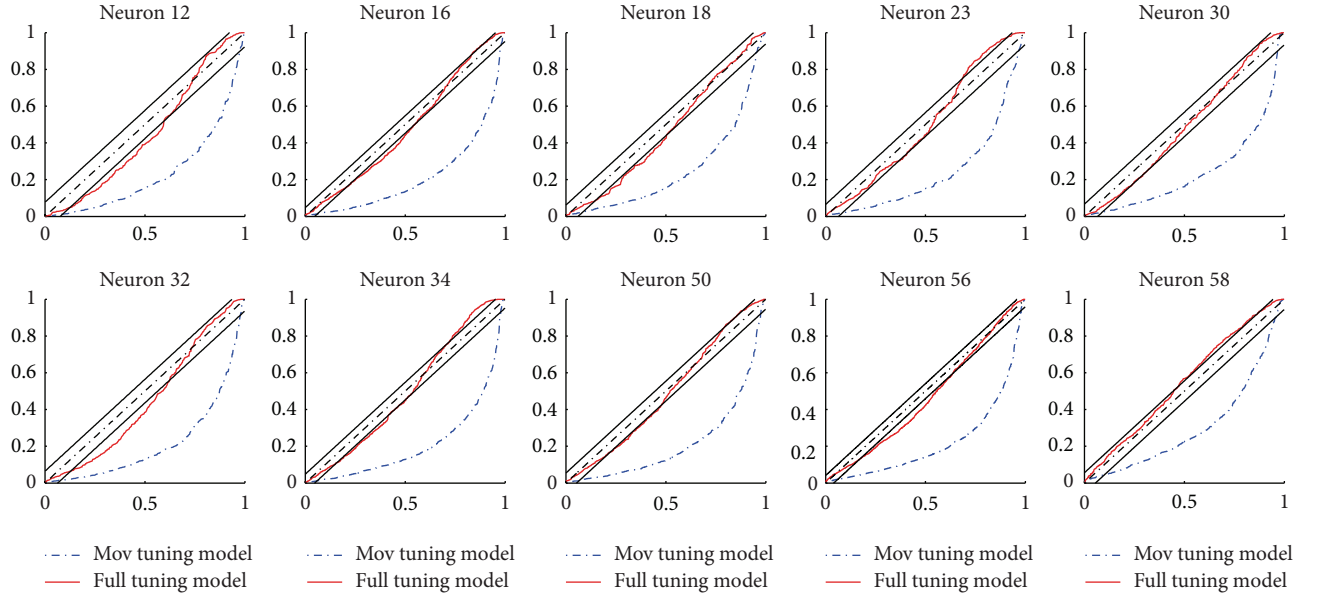


FIGURE 5: KS plots of 10 neurons for the mov tuning model and the full tuning model. The x -axis represents the quantiles and the y -axis represents the cumulative distribution function. The black thin lines in the figure represent the 95% confidence interval. Compared with mov tuning model, the improvement by full tuning model is considerable.

decoding accuracy. The results are displayed in Figure 8. The y -axis of two subplots represents the root mean square errors evaluated on the position and velocity, respectively. The left subplot demonstrates that incorporating the latest 100 ms ensemble activity could achieve the best decoding result on position. It is consistent with the result obtained from Figure 3 that 100 ms is the best time length for the ensemble activity included in the tuning model. The right plot demonstrates that if we want the velocity to be accurately reconstructed, then the latest 50 ms ensemble activity is a better choice. However, regardless of the position or velocity, the corresponding decoding accuracy always improves at the beginning as more ensemble activity included and then drops when the time length continues to increase.

4.3. Decoding Speed. A high-performance real-time brain machine interface system requires not only the decoding result to be accurate but also the decoding speed to be fast enough. A challenge to the application of sequential

Monte Carlo estimation in such kind of system is the high computational complexity. To accelerate the decoding speed, we implement the algorithm in fully parallel based on CUDA and compare the performance with the one that runs serially. The serial version of the algorithm runs on the i7 CPU with a clock rate of 2.4 GHz, and the RAM of the computer is 4 GB. The GPU used by our parallel algorithm is NVIDIA GT730M, in which the clock rate is 758 MHz, the number of CUDA cores is 384, and the global memory is 1 GB. The clock rate of CPU is much faster than the one of GPU.

The experimental results are plotted in Figure 9. Figure 9(a) shows the relationship between the number of particles and the decoding speed of corresponding algorithms. The blue dash line represents the serial implementation running on CPU, and the red solid line is our proposed one running in parallel on GPU. As the number of particles increases, the computational time needed for each bin becomes much longer. For our parallel implementation, the computational time for each bin is less than 8 ms and

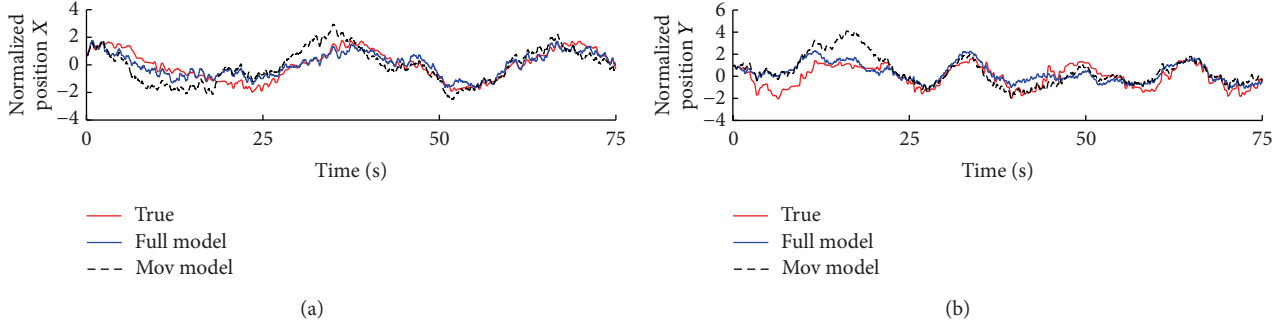


FIGURE 6: Reconstructed positions for a target-reaching task estimated by sequential Monte Carlo method. The red lines are actual movement, the blue lines represent the estimation based on full model, and the black dash lines are predicted based on the mov model.

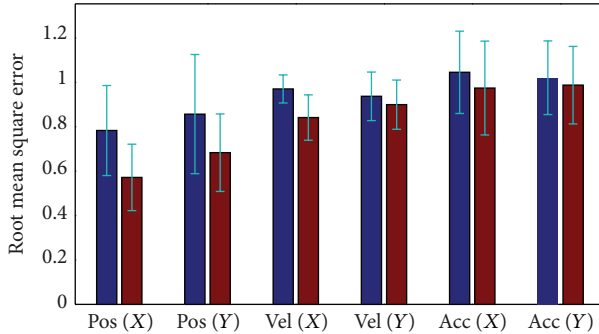


FIGURE 7: The statistical performance provided by the sequential Monte Carlo estimation with different models. Blue bars and red bars represent the mov model and full model, respectively. It is obvious that the full model can dramatically reduce the error during the estimation of movement trajectory.

TABLE 2: P values (left-tail, paired Student's t -test, $\alpha = 0.05$).

	Pos(X)	Pos(Y)	Vel(X)	Vel(Y)	Acc(X)	Acc(Y)
Full model versus mov model	$2.58e - 5$	0.0412	0.0053	0.0049	$9.30e - 4$	0.0372

even the number of particles is as large as 8000, while one for the serial version is as high as 80 ms. In neural decoding with point process observation, a common choice for the temporal resolution of spike trains is 10 ms, which means that our algorithm can work well in real-time brain machine interface applications even with a large number of particles. In addition, we evaluate the decoding time with different number of neurons. Since the number of neurons recorded is limited, we duplicate the neurons many times to get a large ensemble size. The results are plotted in Figure 9(b). It shows that when the number of neurons exceeds 100, for the serial version of the algorithm, the computational time of each bin is larger than 10 ms and increases rapidly as more neurons are used. While our proposed method can decode the neural activity in 10 ms even the number of neurons is as much as 300, which is feasible nowadays due to the development of single-unit recording technology.

5. Conclusion and Discussion

In this work, we attempt to improve the decoding performance of the SMCPP algorithm by addressing two issues in previous studies. One is the simplified tuning considering no neural ensemble effect, which may degenerate the decoding performance. The other is the high computational complexity, which brings the challenge for real-time implementation. We propose to include neural ensemble effect into the tuning function and find that 100 ms is the optimal time length of the ensemble activity which enables the model to perform the best, while previous SMCPP methods usually assume the instantaneous firings only depend on the movement. The goodness of fit analysis demonstrates that the tuning model which takes the ensemble effect into account can greatly increase the predicting power on the neuronal response. It is more consistent with the neurophysiologic knowledge since cortical neurons are interconnected in a large network by a huge number of synaptic inputs which can induce some kind of coupling [25].

Given the tuning function, the sequential Monte Carlo estimation can be applied directly on the spike trains to predict the movement. The posterior density of movement is represented by a set of weighted samples, and the importance weights are updated based on current neural firings and the instantaneous firing rate estimated from the tuning model. Therefore, the tuning model which is well consistent with the true one is necessary for a good estimation of states. In addition, we also incorporate the ensemble activity into the state transition equation. Based on the state and tuning models we propose, a SMCPP algorithm is built and applied to predict the movement from the neural activity recorded in primary motor cortex. We evaluate the statistical decoding accuracy on multiple datasets. The results demonstrate that our proposed model which takes the recent ensemble activity into account can improve the decoding accuracy, especially on position, compared to the model which only depends on the movement. Furthermore, we find that the best accuracy on position is achieved by including the latest 100 ms ensemble activity.

Though the SMCPP can predict the movement more accurately by taking the recent ensemble activity into account, the high computational complexity is still an issue

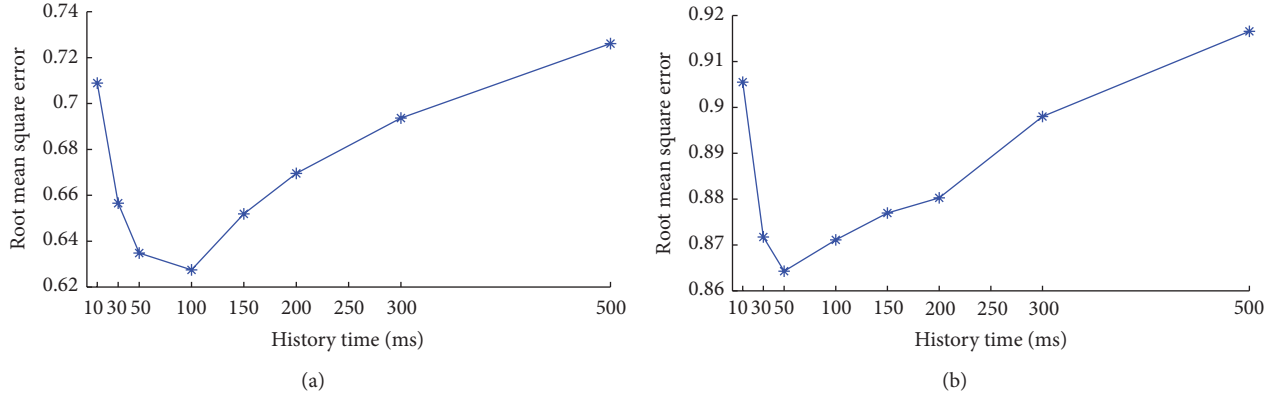


FIGURE 8: The decoding accuracy evaluated based on the tuning model with different time length of recent ensemble activity. (a) Average root mean square error of position. (b) Average root mean square error of velocity.

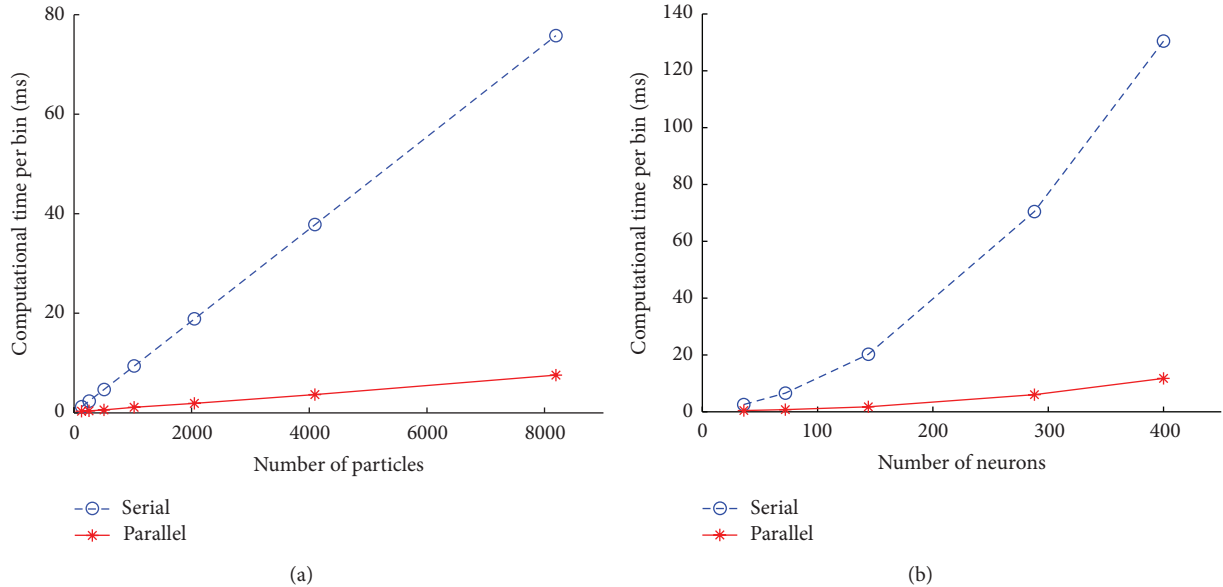


FIGURE 9: (a) The computational time of a single bin with different number of particles. (b) The computational time of a single bin with different number of neurons.

which prevents it from being used in real-time brain machine interfaces. To accelerate the decoding speed, we implement the algorithm in fully parallel based on CUDA. The weighted particles are propagated, updated, and resampled simultaneously on hundreds of cores in GPU. The result shows, for our method, the computational time for each 10 ms data input is only about 8 ms and even the number of particles is larger than 8000. We also find that our algorithm can also fulfill the time resolution of real-time BMI systems and even over 3 hundred neurons are recorded. Compared with the serial implementation running on GPU, our parallel method runs over 10 times fast. Another advantage of our proposed algorithm is that the GPU is relatively cheap and simple to be upgraded compared with the CPU.

Our work enables the sequential Monte Carlo algorithm with point process observation to output the movement estimation much faster and more accurate, which is helpful

to the high-performance BMI systems. Decoding accuracy can be improved by taking the recent ensemble activity into account. Meanwhile the decoding speed is much faster compared to the traditional ones running on CPU. Although the results are interesting, the signal processing approaches for spike trains can be further developed. A feasible way is to improve the encoding model by considering the sparseness of the neural connections. The more accurate model can reduce the bias during the update of the importance weights and is potential to increase the decoding accuracy.

Conflict of Interests

The authors declare that there is no conflict of interests regarding the publication of this paper.

Acknowledgments

This research was supported by Grants from the National High Technology Research and Development Program of China (no. 2012AA011602), the National Basic Research Program of China (no. 2013CB329506), the National Natural Science Foundation of China (nos. 61305146, 61031002, and 31371001), Zhejiang Provincial Key Science and Technology Program for International Cooperation (no. 2012C24025), and Zhejiang Provincial Natural Science Foundation of China (no. LY14F030015). The corresponding author Yiwen Wang thanks Kainuan Yang and Shenglong Xiong for their assistance with animal care and training.

References

- [1] J. K. Chapin, K. A. Moxon, R. S. Markowitz, and M. A. L. Nicolelis, "Real-time control of a robot arm using simultaneously recorded neurons in the motor cortex," *Nature Neuroscience*, vol. 2, no. 7, pp. 664–670, 1999.
- [2] P. R. Kennedy, R. A. E. Bakay, M. M. Moore, K. Adams, and J. Goldwaith, "Direct control of a computer from the human central nervous system," *IEEE Transactions on Rehabilitation Engineering*, vol. 8, no. 2, pp. 198–202, 2000.
- [3] M. D. Serruya, N. G. Hatsopoulos, L. Paninski, M. R. Fellows, and J. P. Donoghue, "Instant neural control of a movement signal," *Nature*, vol. 416, no. 6877, pp. 141–142, 2002.
- [4] D. M. Taylor, S. I. H. Tillery, and A. B. Schwartz, "Direct cortical control of 3D neuroprosthetic devices," *Science*, vol. 296, no. 5574, pp. 1829–1832, 2002.
- [5] L. R. Hochberg, D. Bacher, B. Jarosiewicz et al., "Reach and grasp by people with tetraplegia using a neurally controlled robotic arm," *Nature*, vol. 485, no. 7398, pp. 372–375, 2012.
- [6] R. B. Stein, P. H. Peckham, and D. B. Popović, Eds., *Neural Prostheses: Replacing MotOr Function After Disease Or Disability*, Oxford University Press, 1992.
- [7] M. A. Lebedev and M. A. L. Nicolelis, "Brain-machine interfaces: past, present and future," *Trends in Neurosciences*, vol. 29, no. 9, pp. 536–546, 2006.
- [8] J. P. Donoghue, "Bridging the brain to the world: a perspective on neural interface systems," *Neuron*, vol. 60, no. 3, pp. 511–521, 2008.
- [9] J. Wessberg, C. R. Stambaugh, J. D. Kalil et al., "Real-time prediction of hand trajectory by ensembles of cortical neurons in primates," *Nature*, vol. 408, no. 6810, pp. 361–365, 2000.
- [10] J. M. Carmena, M. A. Lebedev, R. E. Crist et al., "Learning to control a brain-machine interface for reaching and grasping by primates," *PLoS Biology*, vol. 1, no. 2, 2003.
- [11] M. Velliste, S. Perel, M. C. Spalding, A. S. Whitford, and A. B. Schwartz, "Cortical control of a prosthetic arm for self-feeding," *Nature*, vol. 453, no. 7198, pp. 1098–1101, 2008.
- [12] J. C. Sanchez, S. P. Kim, D. Erdogmus et al., "Input-output mapping performance of linear and nonlinear models for estimating hand trajectories from cortical neuronal firing patterns," in *Proceedings of the 12th IEEE Workshop on Neural Networks for Signal Processing*, vol. 2002, pp. 139–148.
- [13] S.-P. Kim, J. C. Sanchez, D. Erdogmus et al., "Divide-and-conquer approach for brain machine interfaces: nonlinear mixture of competitive linear models," *Neural Networks*, vol. 16, no. 5–6, pp. 865–871, 2003.
- [14] A. E. Brockwell, A. L. Rojas, and R. E. Kass, "Recursive bayesian decoding of motor cortical signals by particle filtering," *Journal of Neurophysiology*, vol. 91, no. 4, pp. 1899–1907, 2004.
- [15] W. Wu, M. J. Black, D. Mumford, Y. Gao, E. Bienenstock, and J. P. Donoghue, "Modeling and decoding motor cortical activity using a switching Kalman filter," *IEEE Transactions on Biomedical Engineering*, vol. 51, no. 6, pp. 933–942, 2004.
- [16] W. Wu, Y. Gao, E. Bienenstock, J. P. Donoghue, and M. J. Black, "Bayesian population decoding of motor cortical activity using a Kalman filter," *Neural Computation*, vol. 18, no. 1, pp. 80–118, 2006.
- [17] L. Srinivasan, U. T. Eden, S. K. Mitter, and E. N. Brown, "General-purpose filter design for neural prosthetic devices," *Journal of Neurophysiology*, vol. 98, no. 4, pp. 2456–2475, 2007.
- [18] K. Xu, Y. Wang, S. Zhang et al., "Comparisons between linear and nonlinear methods for decoding motor cortical activities of monkey," in *Proceedings of the 33rd Annual International Conference of the IEEE Engineering in Medicine and Biology Society (EMBS '11)*, pp. 4207–4210, September 2011.
- [19] A. Ergun, R. Barbieri, U. T. Eden et al., "Construction of point process adaptive filter algorithms for neural systems using sequential Monte Carlo methods," *IEEE Transactions on Biomedical Engineering*, vol. 54, no. 3, pp. 419–428, 2007.
- [20] Y. Wang, A. R. C. Paiva, J. C. Príncipe, and J. C. Sanchez, "Sequential Monte Carlo point-process estimation of kinematics from neural spiking activity for brain-machine interfaces," *Neural computation*, vol. 21, no. 10, pp. 2894–2930, 2009.
- [21] Y. Wang and J. C. Príncipe, "Point process modeling on decoding and encoding for brain machine interfaces," in *Proceedings of the 7th Asian Control Conference (ASCC '09)*, pp. 1000–1005, August 2009.
- [22] A. C. Smith and E. N. Brown, "Estimating a state-space model from point process observations," *Neural Computation*, vol. 15, no. 5, pp. 965–991, 2003.
- [23] U. T. Eden, L. M. Frank, R. Barbieri, V. Solo, and E. N. Brown, "Dynamic analysis of neural encoding by point process adaptive filtering," *Neural Computation*, vol. 16, no. 5, pp. 971–998, 2004.
- [24] W. Truccolo, U. T. Eden, M. R. Fellows, J. P. Donoghue, and E. N. Brown, "A point process framework for relating neural spiking activity to spiking history, neural ensemble, and extrinsic covariate effects," *Journal of Neurophysiology*, vol. 93, no. 2, pp. 1074–1089, 2005.
- [25] W. Truccolo, L. R. Hochberg, and J. P. Donoghue, "Collective dynamics in human and monkey sensorimotor cortex: predicting single neuron spikes," *Nature Neuroscience*, vol. 13, no. 1, pp. 105–111, 2010.
- [26] J. W. Pillow, J. Shlens, L. Paninski et al., "Spatio-temporal correlations and visual signalling in a complete neuronal population," *Nature*, vol. 454, no. 7207, pp. 995–999, 2008.
- [27] W. Wu, J. E. Kulkarni, N. G. Hatsopoulos, and L. Paninski, "Neural decoding of hand motion using a linear state-space model with hidden states," *IEEE Transactions on Neural Systems and Rehabilitation Engineering*, vol. 17, no. 4, pp. 370–378, 2009.
- [28] V. Lawhern, W. Wu, N. Hatsopoulos, and L. Paninski, "Population decoding of motor cortical activity using a generalized linear model with hidden states," *Journal of Neuroscience Methods*, vol. 189, no. 2, pp. 267–280, 2010.
- [29] F. Zhou, J. Liu, Y. Yu et al., "Field-programmable gate array implementation of a probabilistic neural network for motor cortical decoding in rats," *Journal of Neuroscience Methods*, vol. 185, no. 2, pp. 299–306, 2010.

- [30] X. Zhu, R. Jiang, Y. Chen, S. Hu, and D. Wang, "FPGA implementation of Kalman filter for neural ensemble decoding of rat's motor cortex," *Neurocomputing*, vol. 74, no. 17, pp. 2906–2913, 2011.
- [31] D. Wang, Y. Hao, X. Zhu et al., "FPGA implementation of hardware processing modules as coprocessors in brain-machine interfaces," in *Proceedings of the 33rd Annual International Conference of the IEEE Engineering in Medicine and Biology Society (EMBS '11)*, pp. 4613–4616, September 2011.
- [32] J. A. Wilson and J. C. Williams, "Massively parallel signal processing using the graphics processing unit for real-time brain-computer interface feature extraction," *Frontiers in Neuroengineering*, vol. 2, no. 11, 2009.
- [33] M. A. L. Nicolelis, D. Dimitrov, J. M. Carmena et al., "Chronic, multisite, multielectrode recordings in macaque monkeys," *Proceedings of the National Academy of Sciences of the United States of America*, vol. 100, no. 19, pp. 11041–11046, 2003.
- [34] Q. S. Zhang, S. M. Zhang, Y. Y. Hao et al., "Development of an invasive brain-machine interface with a monkey model," *Chinese Science Bulletin*, vol. 57, no. 16, pp. 2036–2045, 2012.
- [35] K. Xu, Y. Wang, Y. Wang et al., "Local-learning-based neuron selection for grasping gesture prediction in motor brain machine interfaces," *Journal of Neural Engineering*, vol. 10, no. 2, Article ID 026008, 2013.
- [36] E. N. Brown, R. Barbieri, V. Ventura, R. E. Kass, and L. M. Frank, "The time-rescaling theorem and its application to neural spike train data analysis," *Neural Computation*, vol. 14, no. 2, pp. 325–346, 2002.
- [37] A. Doucet, *Sequential Monte Carlo Methods*, John Wiley & Sons, 2001.
- [38] A. Doucet, S. Godsill, and C. Andrieu, "On sequential monte carlo sampling methods for Bayesian filtering," *Statistics and Computing*, vol. 10, no. 3, pp. 197–208, 2000.
- [39] R. Douc, O. Cappé, and E. Moulines, "Comparison of resampling schemes for particle filtering," in *Proceedings of the 4th International Symposium on Image and Signal Processing and Analysis (ISPA '05)*, pp. 64–69, September 2005.
- [40] M. Harris, S. Sengupta, and J. D. Owens, "Parallel prefix sum (scan) with CUDA," *GPU Gems*, vol. 3, no. 39, pp. 851–876, 2007.

Research Article

Nonlinear EEG Decoding Based on a Particle Filter Model

Jinhua Zhang, Jiongjian Wei, Baozeng Wang, Jun Hong, and Jing Wang

Xi'an Jiaotong University, Qujiang Campus, West Building No. 5, No. 99 YanXiang Road, YanTa District, Xi'an, Shaanxi 710045, China

Correspondence should be addressed to Jun Hong; jhong@mail.xjtu.edu.cn

Received 28 February 2014; Revised 16 April 2014; Accepted 18 April 2014; Published 15 May 2014

Academic Editor: Ting Zhao

Copyright © 2014 Jinhua Zhang et al. This is an open access article distributed under the Creative Commons Attribution License, which permits unrestricted use, distribution, and reproduction in any medium, provided the original work is properly cited.

While the world is stepping into the aging society, rehabilitation robots play a more and more important role in terms of both rehabilitation treatment and nursing of the patients with neurological diseases. Benefiting from the abundant contents of movement information, electroencephalography (EEG) has become a promising information source for rehabilitation robots control. Although the multiple linear regression model was used as the decoding model of EEG signals in some researches, it has been considered that it cannot reflect the nonlinear components of EEG signals. In order to overcome this shortcoming, we propose a nonlinear decoding model, the particle filter model. Two- and three-dimensional decoding experiments were performed to test the validity of this model. In decoding accuracy, the results are comparable to those of the multiple linear regression model and previous EEG studies. In addition, the particle filter model uses less training data and more frequency information than the multiple linear regression model, which shows the potential of nonlinear decoding models. Overall, the findings hold promise for the furtherance of EEG-based rehabilitation robots.

1. Introduction

With the growth of the aging population, treatment needs for nervous system diseases (e.g., spinal cord injury or stroke) have become bigger and bigger. As an advanced form of medical technology, rehabilitation robots have great potential in terms of both rehabilitation treatment and nursing. In recent years, the rehabilitation robot has become a research hotspot in the fields of brain science, biomedical and rehabilitation engineering, intelligent information processing, bionics, and so on. The control strategies of rehabilitation robots include force control, force field control, and bioelectrical signal (EMG, EEG, etc.) control. Brain signals are recorded by electrodes, reflecting the summation of the synchronous and rhythmic activity of neurons. Compared with EMG, brain signals contain more motion patterns and are available for more people; they are thus more suitable as an information source for rehabilitation robots. Brain signals can be obtained by invasive or noninvasive methods, though signals acquired by invasive methods have high signal-to-noise ratio and spatial resolution, and invasive method-based rehabilitation robot research has made great strides in animal experiments [1–4].

Due to the inherent risks of surgery and the gradual degradation of signal integrity, the invasive method is difficult to promote in clinical application. Although neuronal data acquired noninvasively from the scalp via electroencephalography (EEG) has comparatively low signal-to-noise ratio and spatial resolution, it is more suitable to be used in rehabilitation robots and in clinical applications because of its directness, its security, the simplicity of its acquisition equipment, its easy operation, its lower cost, and its fewer environmental restrictions.

In recent years, researchers have tried to read human mind from the EEG to determine the movement intent of people to achieve a noninvasive intelligent prosthetic control using, for example, the motor imagery-based rehabilitation system [5], the MindWalker of the Twente University [6], and the lower exoskeleton control system studied by the University of Houston [7]. Researchers, who study the EEG signals, concentrated more on pattern classification and feature extraction based on event-related potentials [8], visual evoked potential [9], and mental tasks [10].

In order to better control prostheses using EEG, researchers have been trying to get more movement information from the EEG signal besides pattern recognition

or time-frequency analysis to identify the intent to achieve movement. For instance, Zhao et al. used the duration of a specific image to define the intensity of the task control commands, thus providing continuous control of an additional parameter [11]. Logar controlled the clamping force according to the phase demodulation method based on EEG [12]. The literature [13] analyzed the relationship between the actual movement velocity and the image. But, this movement information for intelligent prosthesis control is also far less.

Researchers have conducted studies on motion information extraction from EEG based on research on motion information extraction methods from an invasive signal (mainly decoding method includes linear filtering [14–16], Kalman filtering [17, 18], linear equation of state [19], and support vector machines [20]). In 2009, Bradberry et al. proposed a method to continuously decode hand position, velocity, and acceleration from 55-channel EEG signals and established a mapping model between EEG and motion information [14]. On this basis, in 2010, Bradberry continuously decoded 2D center-out movements, unconstrained 3D center-out movements, and 3D finger gestures, showing that EEG signals also contain rich motion information in the macroscale movement [15]. Lv et al. used a Kalman filter to predict the hand velocity in a “self-routed” movement based on features such as amplitude and power spectrum [21]. Antelis et al. established a mapping model between EEG and motion information by training the recorded trajectory from the initial point to the fixed point or any target point and the features of EEG in the spatial and time-frequency domain through the support vector machine (SVM) [22]. However, the researches above are limited to the decoding of specific limb trajectory. In 2011, Presacco et al. proposed a method that decoded unconstrained treadmill walking from EEG [16] and successfully obtained the linear and angular kinematics of the ankle, knee, and hip joints during walking.

During research on motion information extraction from EEG, most researchers have used a multiple linear regression decoding model based on a neural decoding method from invasive signals. Antelis et al. pointed out that the use of a linear regression model implies that the relevant EEG component has to be in the same frequency range as the signal to be decoded and suggested that a nonlinear model should be used to relate the limb kinematics to EEG temporal sequences [23]. Because EEG is a recording of electrical activity along the scalp, which comes from the neurons via the skull, the conductivity of the skull is nonlinear. The multiple linear regression model cannot reflect the nonlinear component of EEG.

Some nonlinear invasive neural decoding methods such as neural networks, support vector machines, and particle filter [24] for the movement decoding from EEG provide a reference. Particle filter is a technique for implementing a recursive Bayesian filter by Monte Carlo simulations. The key idea is to represent the required density function by set of random samples (particles) with associated weights. Particle filtering algorithm has been successfully applied in invasive neural decoding. For example, Wood et al. used particle filtering to recursively infer hand kinematics and attentional

state conditioned on neural firing rates with a monkey [25]. Kelly and Lee decoded the V1 neuronal activity using particle filtering with Volterra kernels [26]. Gao et al. described the Bayesian decoding of hand motion from firing activity using a particle filter [27].

This paper proposes a nonlinear decoding model based on a particle filter. The multiple linear regression model and particle filter model are evaluated and compared using two- and three-dimensional hand motion decoding experiments.

2. Decoding Methods

2.1. Decoding Model by Multiple Linear Regression. The multiple linear regression model assumes that the kinematics of the hand are related to the EEG signals at present and the EEG signals at the previous moment and assumes that the relationship between the EEG signals of each channel is linear. The corresponding weight of each EEG channel can be obtained through multiple linear regression, and the decoding model is given by

$$\begin{aligned} x(t) &= a_x + \sum_{n=1}^N \sum_{k=0}^L b_{nkx} S_n(t-k), \\ y(t) &= a_y + \sum_{n=1}^N \sum_{k=0}^L b_{nky} S_n(t-k), \\ z(t) &= a_z + \sum_{n=1}^N \sum_{k=0}^L b_{nkz} S_n(t-k), \end{aligned} \quad (1)$$

where $x(t)$, $y(t)$, and $z(t)$ are, respectively, the horizontal, vertical, and depth position of the hand at time sample t , N is the number of EEG channels, L is the number of time lags, $S_n(t-k)$ is the voltage measured at EEG channel n at time lag k , and the a and b variables are weights obtained through multiple linear regression.

2.2. Decoding Model by Particle Filter. We have implemented a particle filtering method for reconstructing hand movement information from EEG signals. And, in particle filter decoding (or Bayesian decoding), the object is to find, for each time t , the distribution of the unobserved signal C_t (where $C_t = [x(t), y(t), z(t)]$ has been used to represent the position of hand at time step t , with two- or three-dimensional vector) that is the key position information, given observations $S_{1:t}$, while the observation S_t represented the vector of EEG. Hence, we view the decoding problem as a statistical inference problem in which we could get a Bayesian estimate of the posterior $p(C_t | S_{1:t})$ at every time step. Making certain independence and first-order Markov assumptions leads to a recursive estimate of the posterior:

$$\begin{aligned} p(C_t | S_{1:t}) &= \frac{1}{\lambda} p(S_t | C_t) \\ &\times \int p(C_t | C_{t-1}) p(C_{t-1} | S_{1:t-1}) dC_{t-1}, \end{aligned} \quad (2)$$

where $1/\lambda$ is a normalizing constant.

Particle filter decoding consists of two statistical models: (1) a state motion model (or temporal prior), $p(C_t | C_{t-1})$, for a process C_t describing the evolution of the state we are trying to predict (here, position of hand) and (2) a measurement model (or an observation model, or likelihood), $p(S_t | C_t)$, specifying the probability distribution of the data S_t given the underlying state C_t .

2.2.1. The State Motion Model. The state motion model describes the distribution of the unobserved signal one step in the future, C_{t+1} , given the current value of the signal C_t . Here, we use a second-order model, and the state motion model is as follows:

$$C_{t+1} = AC_t + W, \quad (3)$$

where $C_t = [x(t), y(t), z(t)]$ is the key position information, A is the transfer matrix, and W is the Gaussian noise.

2.2.2. The Measurement Model. The measurement model specifies the relationship between the unobserved signal C_t and the observation S_t . We assume the conditional independence of the EEG channels where the likelihood for the EEG signals is taken to be a Gaussian distribution. So, with some other usual assumption [23], the measurement model can be expressed as

$$\begin{aligned} p(S_t | C_t) &\approx (2\pi)^{-m/2} |\Sigma|^{-1/2} \\ &\times \exp \left(-\frac{1}{2} (S_t - \mu)^T \Sigma^{-1} (S_t - \mu) \right), \end{aligned} \quad (4)$$

where the m -dimensional vector μ is the mean and the covariance is the positive definite matrix Σ . The main steps of the particle filter decoding model are as follows.

- (1) Initialization. Produce the particle swarm $\{c_0^i\}_{i=1}^{N_s}$ by the prior probability, and the weight of each particle is $1/N_s$.
- (2) Update. Update the particle weights at time k :

$$w_k^i = w_{k-1}^i p(s_k | c_k^i), \quad i = 1, 2, \dots, N_s. \quad (5)$$

Then, normalize

$$w_k^i = \frac{w_k^i}{\sum_{i=1}^{N_s} w_k^i}. \quad (6)$$

The least mean-square estimate of the unknown parameter x at time k can be obtained from

$$\hat{x}_k \approx \sum_{i=1}^{N_s} w_k^i c_k^i. \quad (7)$$

- (3) Resampling. Get a new particle collection $\{c_{0:k}^{i*}, i = 0, 1, 2, \dots, N_s\}$.
- (4) Prediction. Use the state equation to predict the unknown parameter c_{k+1}^i .
- (5) At time $k = k + 1$, return to step (2).

We use one set of experimental data to train the particle filter model and another experimental data set to verify the model. The Pearson correlation coefficient (r) between the measured and reconstructed hand positions was computed.

3. Experimental Design

After giving informed consent, six healthy, right-handed subjects, aged 20–25 (4 men and 2 women) and with no history of neurological disease, participated in the experiments. The experiments included two- and three-dimensional hand motions. To verify the applicability of the two decoding methods, we first tested their validity in two-dimensional hand motion, and then we further tested their validity in three-dimensional hand motion.

3.1. Two-Dimensional Hand Motion Experiment. As shown in Figure 1, participants sat upright in a chair in front of the computer screen; the chair could be adjusted to obtain an appropriate height. During the experiment, participants were instructed to move their right arm/finger to track a computer-controlled cursor that moved along a spiral line in two dimensions on the computer screen. Meanwhile, EEG of participants was acquired. Participants were asked to keep other parts of their body except the right arm still and not to blink to reduce EMG and ocular artifacts. The most frontal electrodes (Fp1, Fp2) were removed offline from participants, as they are usually contaminated by eye blinks.

3.2. Three-Dimensional Hand Motion Experiment. As Figure 2 shows, while wearing an EEG cap, participants held a target object whose three-dimensional motion was tracked by the optical tracking system. Participants swung their hands within a certain range in space slowly and freely. The body of participants remained still except for hand motions to minimize interference from EMG during the experiment, avoiding blinks to reduce ocular artifacts. The EEG signals from the Fp1 and Fp2 channels were also removed in the three-dimensional motion decoding. The optical tracking system was a PST IRIS motion capture device (PS-tech, Amsterdam, The Netherlands) with acquisition frequency of 120 Hz.

A Neuroscan NuAmps Express system (Compumedics Ltd., VIC, Australia) was used to acquire EEG signals with the reference on the right mastoid process behind the right ear. The number of EEG channels, collection frequency, notch frequency, and low-pass cut-off frequency were 30, 500 Hz, 50 Hz, and 100 Hz, respectively. The location of 30 electrodes according to the extended international 10–20 system is shown in Figure 3.

In the two experiments, the hand movement and EEG signals were both acquired with timestamps. And they can be synchronized according to the timestamps.

3.3. Preprocessing. Vertical electroocular signals (VEOG) were measured with two electrodes attached superior and inferior to the orbital fossa of the left eye. And horizontal

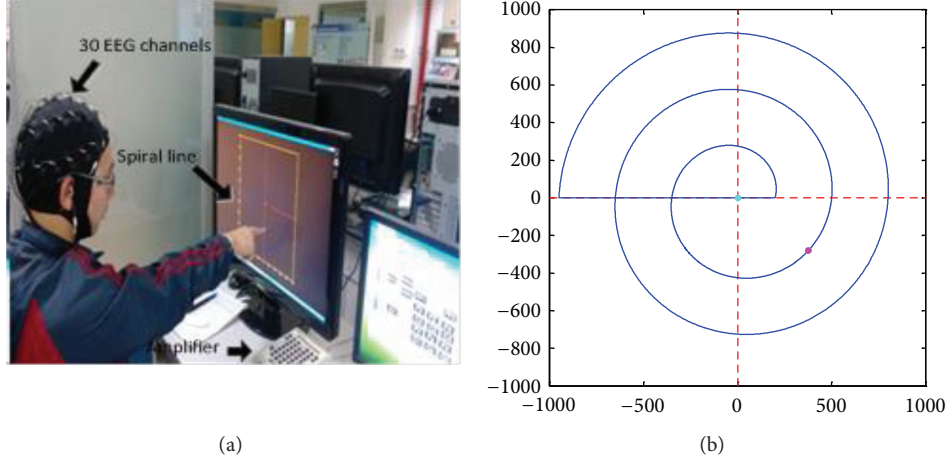


FIGURE 1: In the two-dimensional experiment, the participant moved his finger to track a computer-controlled cursor along the spiral line.

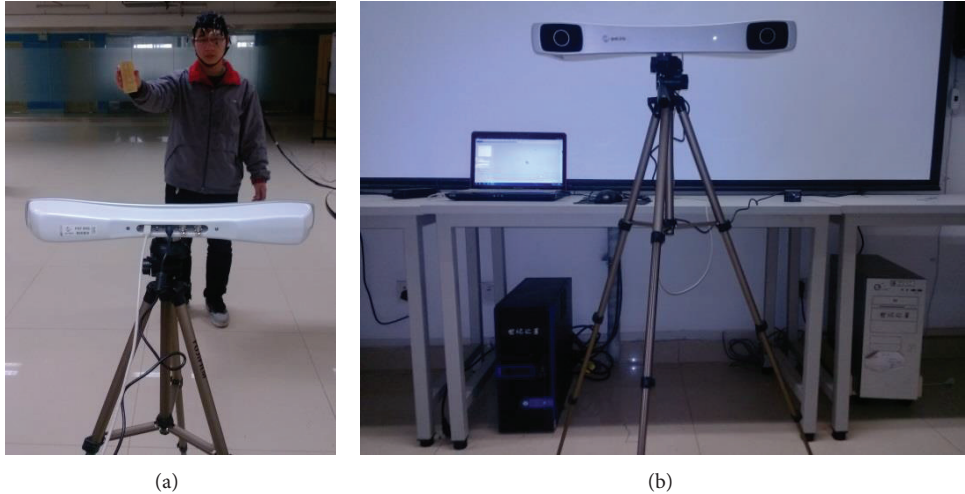


FIGURE 2: In the three-dimensional experiment, the participant swung his hand in space and his hand movement was tracked by the PST IRIS optical tracking system.

electroocular signals (HEOG) were measured with two electrodes attached to external canthi. In EEG signals recorded by a DC amplifier, baseline drift can occur artificially and simultaneously. First, the effects of baseline drift were removed. And the eye movements were removed from the EEG using a regression analysis. Then, the EEG signals were filtered with a 5th-order, low-pass Butterworth filter with a cut-off frequency of 2 Hz. The movement time of the small ball along the spiral line was 48 s in the two-dimensional experiment, and the number of coordinate positions of the small ball was 3079, so the ball movement sampling frequency (i.e., the sampling frequency of the hand motion) was about 64 Hz. Subsequently, the signals from each EEG channel were resampled from 500 Hz to 64 Hz, to ensure the same sampling frequency as that of the hand motion. The sampling frequency of the hand motion was 120 Hz in the three-dimensional experiment, so the EEG signals needed to be

resampled from 500 Hz to 120 Hz. Then, the signals from each EEG channel were standardized according to the following:

$$\text{normalize}(\text{EEG}) = \frac{(\text{EEG} - \text{mean}(\text{EEG}))}{\text{std}(\text{EEG})}, \quad (8)$$

where $\text{normalize}(\text{EEG})$ is the normalized EEG signals, $\text{mean}(\text{EEG})$ is the mean of EEG signals, and $\text{std}(\text{EEG})$ is the standard deviation of EEG signals.

The X, Y, and Z coordinates of the hand position during the hand movement were also standardized using the same equation. Finally, the hand position was decoded from EEG signals using the multiple linear regression and particle filter models. The entire process is shown in Figure 4.

4. Results

4.1. Multiple Linear Regression Model. For each subject, data of 10 trials was collected under each experimental condition

TABLE 1: The Pearson correlation coefficient (r) using the multiple linear regression model for Subject 1.

Two-dimensional	Test Data 1	Test Data 2	Test Data 3	Test Data 4	Test Data 5	Test Data 6
R_X	0.6736	0.7875	0.8733	0.8586	0.6895	0.7408
R_Y	0.8824	0.6723	0.7870	0.5195	0.8544	0.9019
Three-dimensional	Test Data 1	Test Data 2	Test Data 3	Test Data 4	Test Data 5	Test Data 6
R_X	0.4214	0.4354	0.5385	0.6813	0.5339	0.4097
R_Y	0.4558	0.3772	0.5237	0.6784	0.4995	0.3745
R_Z	0.4656	0.3708	0.5028	0.6674	0.4918	0.3672

TABLE 2: The Pearson correlation coefficient (r) using the particle filter model for Subject 1.

Two-dimensional	Test Data 2	Test Data 3	Test Data 4	Test Data 5	Test Data 6
R_X	0.6416	0.9248	0.7025	0.8658	0.8071
R_Y	0.6884	0.8561	0.6761	0.7820	0.7532
Three-dimensional	Test Data 1	Test Data 2	Test Data 3		
R_X	0.4512	0.5073	0.1390		
R_Y	0.4635	0.5941	0.1569		
R_Z	0.4687	0.3452	0.2849		

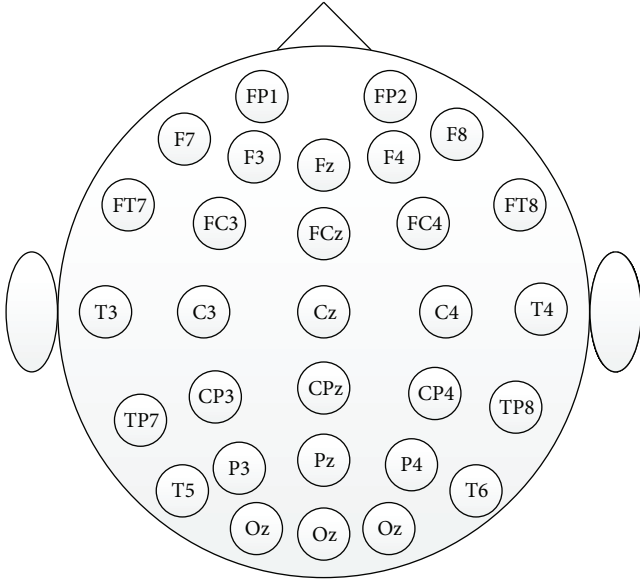


FIGURE 3: The location of 30 electrodes is an extended international 10-20 system.

(2D, 3D (data length: 8 s, 15 s, and 30 s)). And 6 trials were selected from all the 10 trials according to the state of the subjects (concentration, movement of the body, etc.) during the trial. A 6×6 -fold cross-validation procedure was employed to assess the reconstruction accuracy of the hand position from the EEG signals. In this procedure, the data of 5 trials was used for training; the remaining 1 trial data was used for testing. Figures 5(a) and 5(b) show, respectively, examples of the measured (red) and reconstructed (blue) hand positions in two and three dimensions in terms of decoding accuracy. The lengths of the data in the three-dimensional experiment include 8 s, 15 s, and 30 s. The 6×6 -fold cross-validation procedure was used for every data

length. In Figure 5(b), Test Data 1 and Test Data 4 are the results for data lengths of 8 s, Test Data 2 and Test Data 5 are the results for data lengths of 15 s, and Test Data 3 and Test Data 6 are the results for data length of 30 s. Table 1 reports the Pearson correlation coefficients (r) in the two- and three-dimensional experiments for Subject 1.

4.2. Particle Filter Model. As a nonlinear decoding model, the particle filter model can reflect the nonlinear components of EEG signals and only needs one set of experimental data to train the model. For the two-dimensional experiment, we used Test Data 1 to train the particle filter model and the other five sets of experimental data to verify the model. The measured (red) and reconstructed (blue) hand positions in two dimensions are shown in Figure 6(a). For the three-dimensional experiment, we used the particle filter model for data of lengths 8 s, 15 s, and 30 s; the measured (red) and reconstructed (blue) hand positions in three dimensions are shown in Figure 6(b). The Pearson correlation coefficients (r) of Subject 1 in the two-dimensional and three-dimensional experiments are reported in Table 2.

The measured positions and decoded positions of hand movement in 2- and 3-dimensional spaces are shown in Figure 7. In order to avoid mess, we only selected a part of the hand trajectory in 3-dimensional space. As can be seen from Figure 7, the reconstructed position curve fits the measured position curve well.

With the multiple linear regression model, the mean and SD of the correlation coefficients across cross-validation procedure for all subjects are reported in Table 3, while the results of the particle filter model are shown in Table 4.

In the two-dimensional experiment, multiple linear regression model and particle filter model have similar decoding accuracy (Figure 8). However, the three-dimensional decoding results of the multiple linear regression model are a little bit better than those of the particle filter model. The standard deviation of r from particle filter model

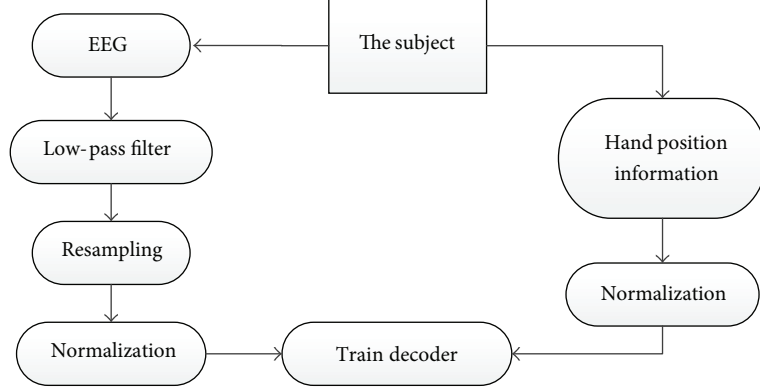


FIGURE 4: Experimental procedure. EEG and hand position information were recorded when subjects were conducting the experiment. After preprocessing, they were used to train and test the decoder.

TABLE 3: Decoding accuracy using multiple linear regression model for all six subjects.

	Subject 1	Subject 2	Subject 3	Subject 4	Subject 5	Subject 6
Two-dimensional						
R_X	0.77 ± 0.08	0.43 ± 0.13	0.67 ± 0.12	0.56 ± 0.09	0.61 ± 0.06	0.49 ± 0.07
R_Y	0.77 ± 0.15	0.48 ± 0.09	0.71 ± 0.09	0.63 ± 0.12	0.58 ± 0.15	0.41 ± 0.11
Three-dimensional						
R_X	0.5 ± 0.1	0.36 ± 0.07	0.42 ± 0.09	0.41 ± 0.1	0.37 ± 0.11	0.35 ± 0.08
R_Y	0.48 ± 0.11	0.39 ± 0.05	0.44 ± 0.11	0.42 ± 0.08	0.35 ± 0.09	0.33 ± 0.02
R_Z	0.48 ± 0.11	0.38 ± 0.05	0.45 ± 0.08	0.40 ± 0.13	0.34 ± 0.1	0.33 ± 0.05

TABLE 4: Decoding accuracy using particle filter model for all six subjects.

	Subject 1	Subject 2	Subject 3	Subject 4	Subject 5	Subject 6
Two-dimensional						
R_X	0.79 ± 0.12	0.46 ± 0.07	0.65 ± 0.07	0.59 ± 0.05	0.6 ± 0.04	0.52 ± 0.05
R_Y	0.75 ± 0.07	0.48 ± 0.1	0.63 ± 0.1	0.64 ± 0.03	0.57 ± 0.1	0.46 ± 0.08
Three-dimensional						
R_X	0.37 ± 0.13	0.33 ± 0.03	0.36 ± 0.03	0.35 ± 0.02	0.39 ± 0.07	0.33 ± 0.03
R_Y	0.39 ± 0.08	0.31 ± 0.07	0.37 ± 0.04	0.32 ± 0.05	0.34 ± 0.06	0.29 ± 0.06
R_Z	0.47 ± 0.09	0.4 ± 0.08	0.40 ± 0.07	0.33 ± 0.08	0.37 ± 0.08	0.35 ± 0.04

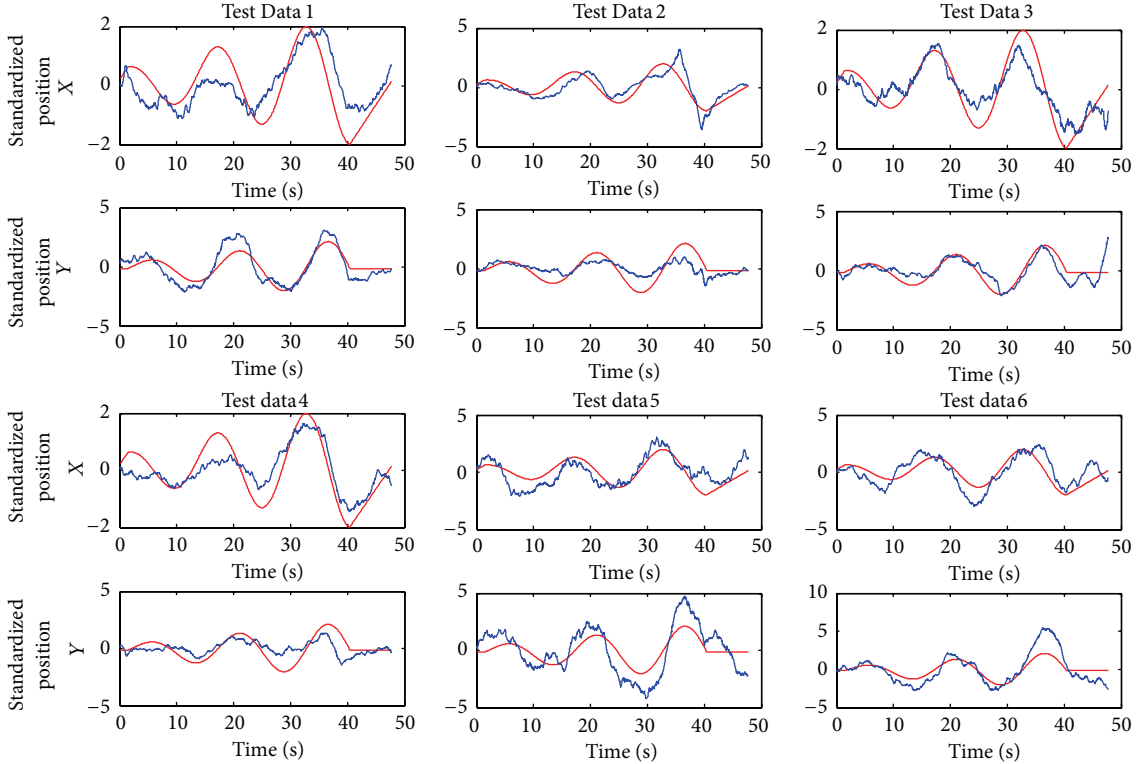
is smaller, which means that it is more stable. It is evident that the decoding accuracy among subjects is variable. The results of Subject 1 are the best because he has conducted the experiments many times and became more adaptive.

The topographies of the contribution of each electrode in the multiple linear regression model (at the best lag) and in the particle filter model were plotted in Figure 9. For the particle filter model, we used EEG signals of only one electrode to decode hand movement each time. And the correlation coefficient got from one electrode decoding was used to represent the contribution of this electrode. After the one electrode decoding procedure was used in all 30 electrodes, we can get the contribution of each electrode in the particle filter model. The topography of multiple linear regression model shows contributions from primary motor sensory area and occipital region. For the particle filter model, electrode locations at F4, Fc4, P3, P6, and TP8 are relevant for decoding right hand movement. It can be inferred that neural

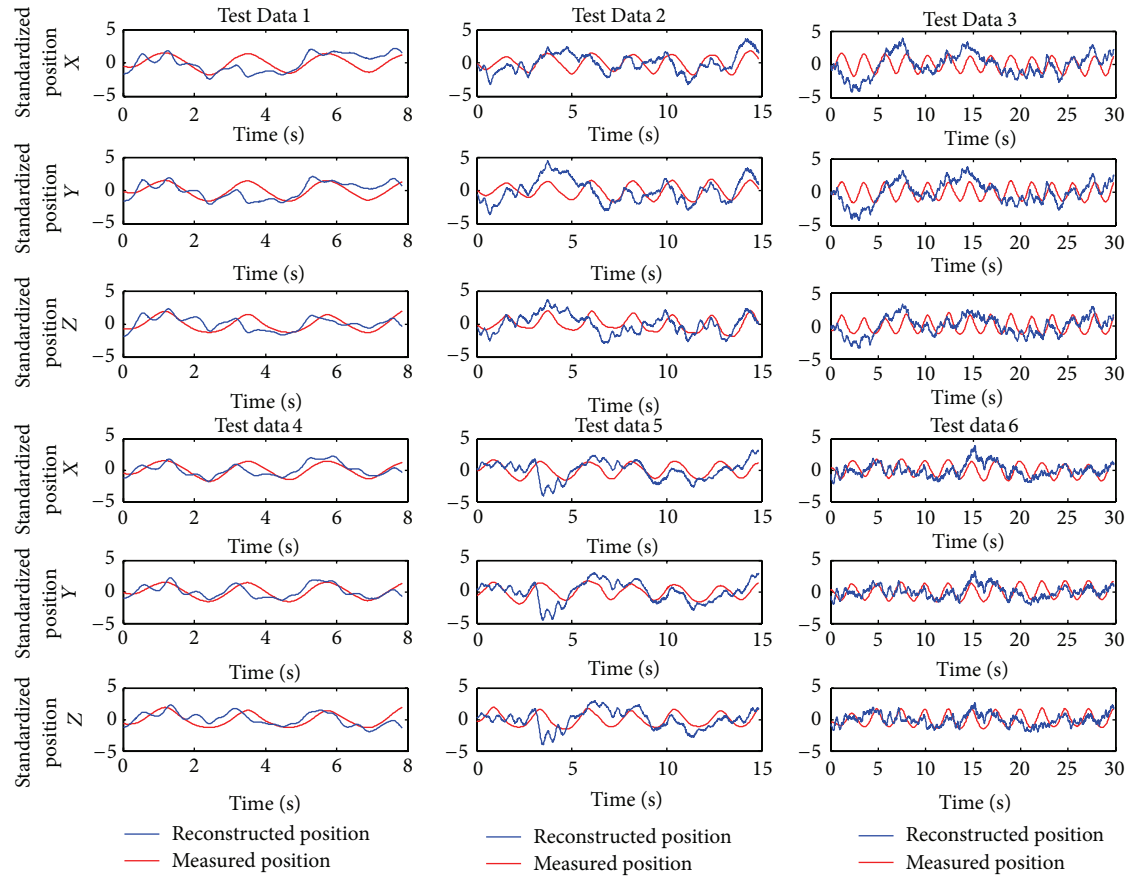
information about right hand movement is distributed across both hemispheres and the areas contributing to decoding are different in two decoding models.

5. Discussion

As can be seen from Figure 5, the reconstructed curves in the X and Y directions in the two-dimensional experiment and the reconstructed curves in the X, Y, and Z directions in the three-dimensional experiment fit the measured curves well, showing the validity of the multiple linear regression model in the extraction of motion information from the EEG. However, there are high-frequency fluctuations in the reconstructed curves. One reason may be that the cut-off frequency of the low-pass filter during preprocessing is too high. As can be seen from Figure 10, the reconstructed curve with the cut-off frequency of 4 Hz has more frequent fluctuations than the one with the cut-off frequency of 2 Hz.



(a) The results of the two-dimensional experiment



(b) The results of the three-dimensional experiment

FIGURE 5: The measured and reconstructed hand position using the multiple linear regression model for Subject 1.

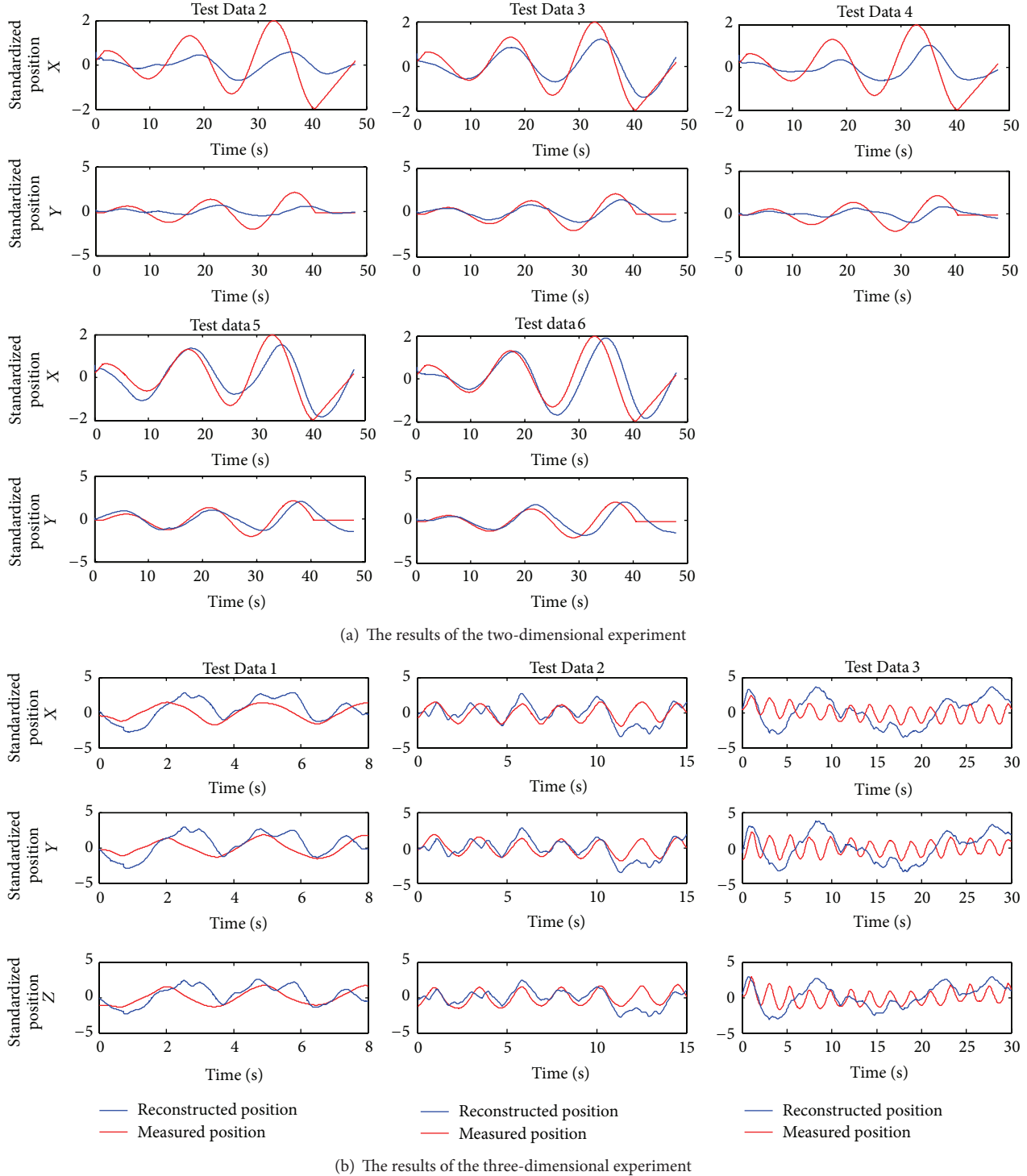


FIGURE 6: The measured and reconstructed hand positions using the particle filter model for Subject 1.

It indicates that the cut-off frequency has an impact on the reconstructed curve. Reducing the cut-off frequency of the low-pass filter during preprocessing, or smoothing the reconstructed curve with a low-pass Butterworth filter, can effectively reduce these high-frequency fluctuations. Compared with the results in the two-dimensional experiment, the decoding accuracy in the three-dimensional experiment

is low. The increased movement complexity may increase the difficulty of decoding.

In Figure 6(a), the reconstructed curves from the five sets of test data using the particle filter model fit the measured curves well in the trend. However, the decoding accuracies for Test Data 2 and Test Data 4 were relatively low, and the corresponding Pearson correlation coefficients are small.

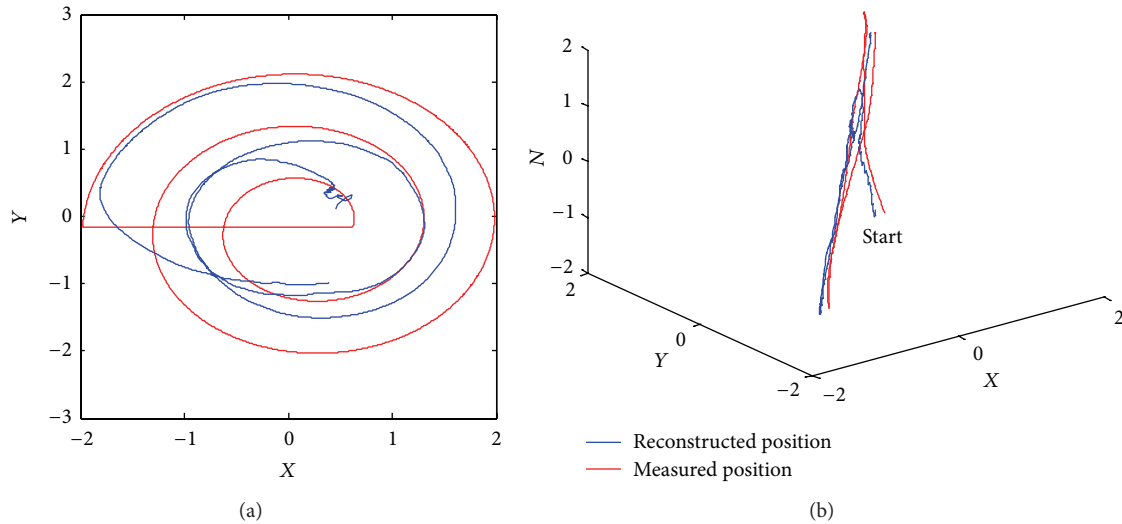


FIGURE 7: An example of hand movement trajectory of the subjects in 2- and 3-dimensional spaces. The word “start” in 3-dimensional space means the starting point.

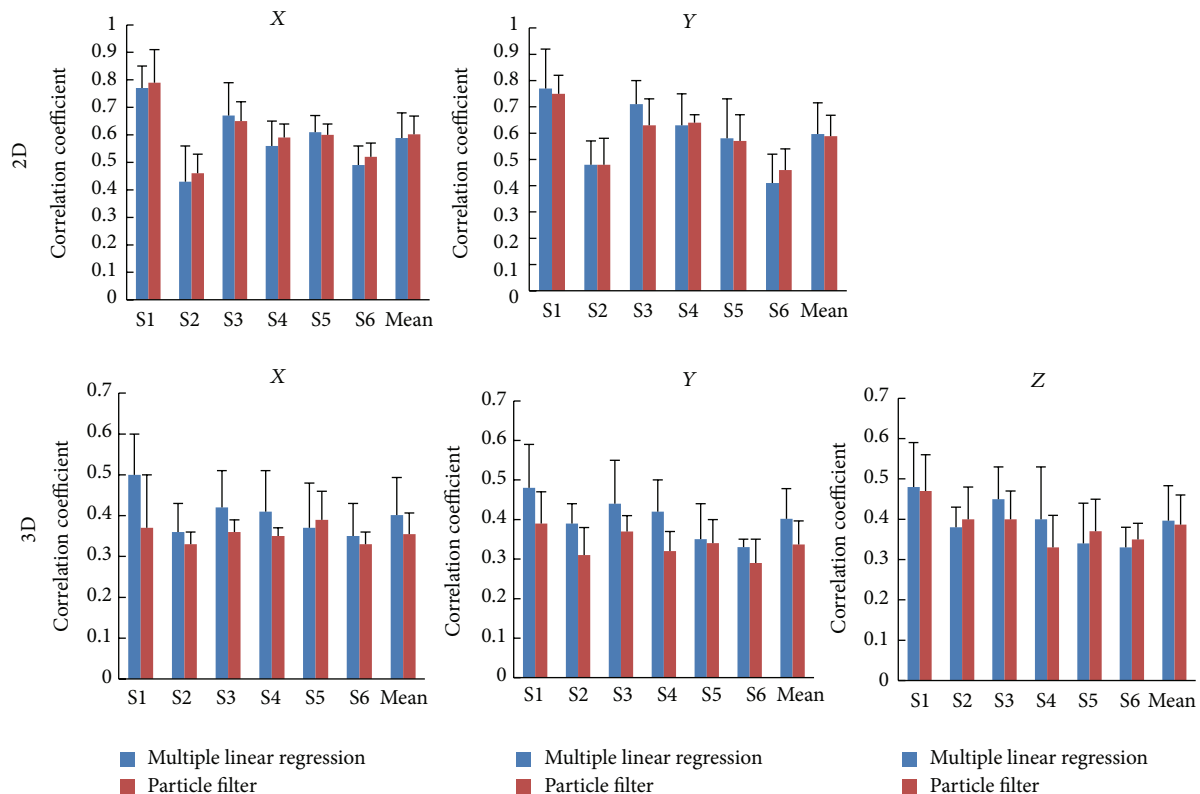


FIGURE 8: The mean value ($n = 6$) and standard deviation of correlation coefficients between measured and reconstructed hand positions for the six subjects (S1 through S6) using multiple linear regression model (blue) and particle filter model (red). The first row is for the two-dimensional experiment. The second row is for the three-dimensional experiment. The left column is for X direction, the middle column is for Y direction, and the right column is for Z direction.

This may have been caused by inattention, eye blinks, or the movements of other parts of the body that introduced noise in the EEG data acquisition process for Test Data 2 and Test Data 4. The decoding accuracy for the three-dimensional experiment is smaller than that of the two-dimensional

experiment, and Table 2 shows that the Pearson correlation coefficients for the data of lengths 8 s and 30 s in the three-dimensional experiment are smaller than that of the 15 s data. The same phenomenon exists when we analyze a large amount of data offline. Thus, the particle filter model may

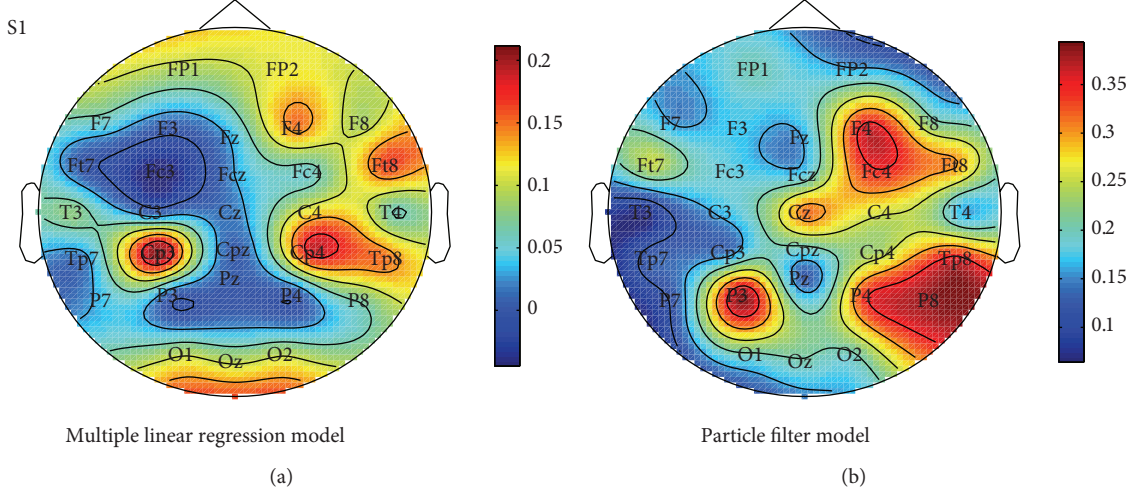


FIGURE 9: Spatial distribution of the contribution of each electrode for Subject 1 in multiple linear regression model (left) and particle filter model (right).

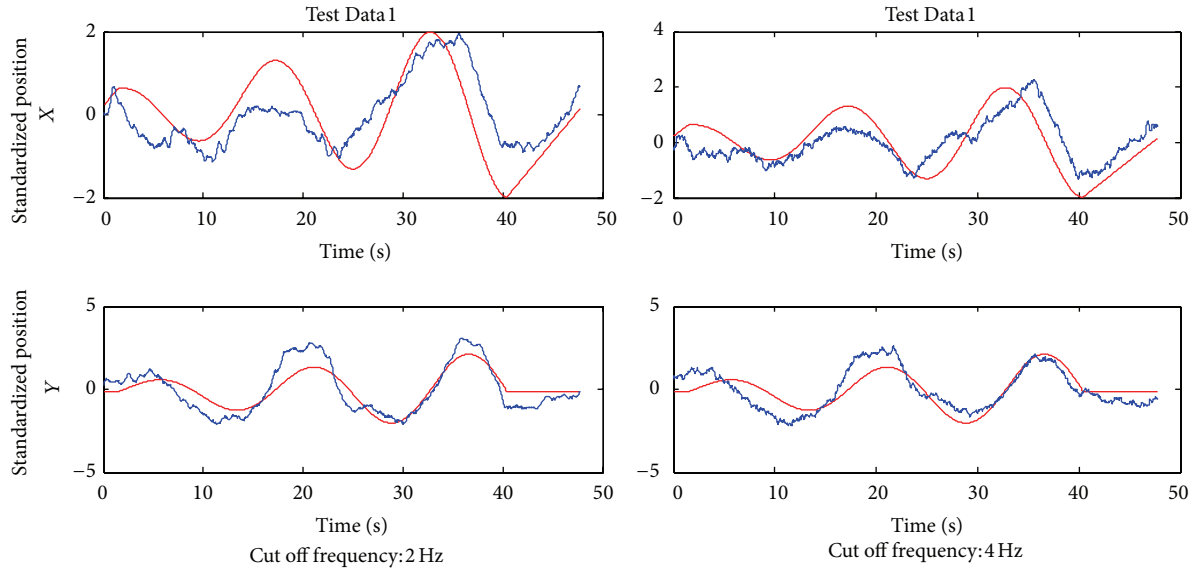


FIGURE 10: The decoding results using the multiple linear decoding model at different cut-off frequency of the low-pass filter.

have an optimal data length. When the data length is shorter than the optimal data length, the number of iterations is small and leads to a low decoding accuracy. However, when the data length is longer than the optimal data length, the difference between the training data and test data becomes bigger, which also leads to a low decoding accuracy. Compared with the multiple linear regression model, the reconstructed curves from the particle filter model are smoother and have no high-frequency fluctuations. The Pearson correlation coefficients of the results—except Test Data 2 and Test Data 4 in the two-dimensional experiment—are above 0.7, showing a strong positive correlation. The reconstructed curves in the three-dimensional experiments, except Test Data 3, fit the measured curves well in the trend, showing the validity of the particle filter model.

Compared with the multiple linear regression model, the particle filter model uses less training data. Figure 11 shows the decoding results using the multiple linear regression model when the number of the training data sets increases from 1 to 5. Table 5 reports the corresponding Pearson correlation coefficients. Figure 12 shows how the Pearson correlation coefficient changes with the number of training data sets in the X and Y directions, respectively.

As can be seen from Figure 12, the decoding accuracy of the multiple linear regression model in the X and Y directions increases as the number of training data sets increases. When the number of training data sets is small, the decoding accuracy increases rapidly with the increase in training data sets, and when the number of training data sets is large, the decoding accuracy increases slowly with

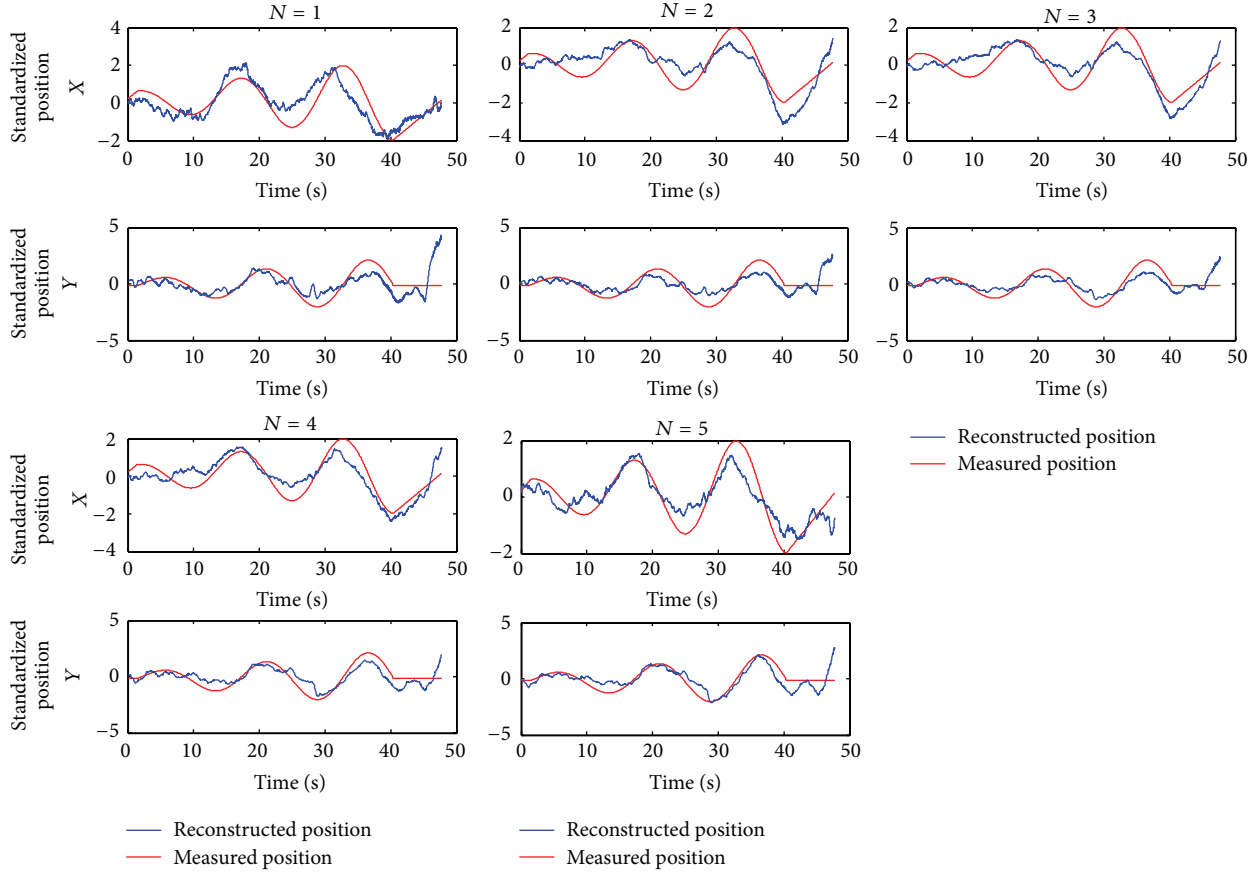
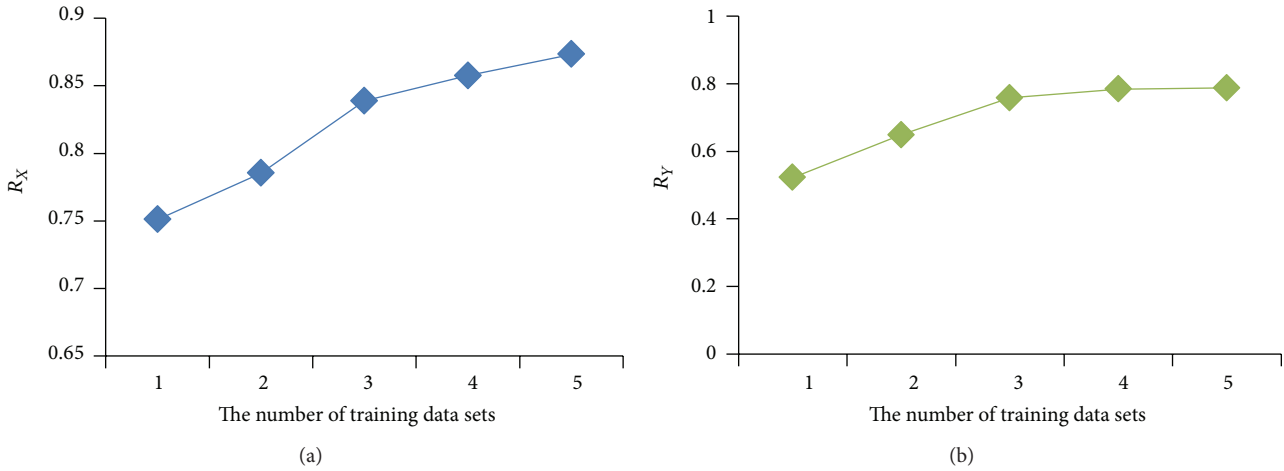


FIGURE 11: The influence of the number of training data sets on the multiple linear regression model.

FIGURE 12: The changes in the Pearson correlation coefficient in the X direction (a) and the Y direction (b) with the number of training data sets.TABLE 5: The Pearson correlation coefficients in the X and Y directions at different number of training data sets.

The number of data sets	$N = 1$	$N = 2$	$N = 3$	$N = 4$	$N = 5$
R_X	0.751	0.7853	0.8389	0.8576	0.8733
R_Y	0.5225	0.6488	0.7577	0.7838	0.787

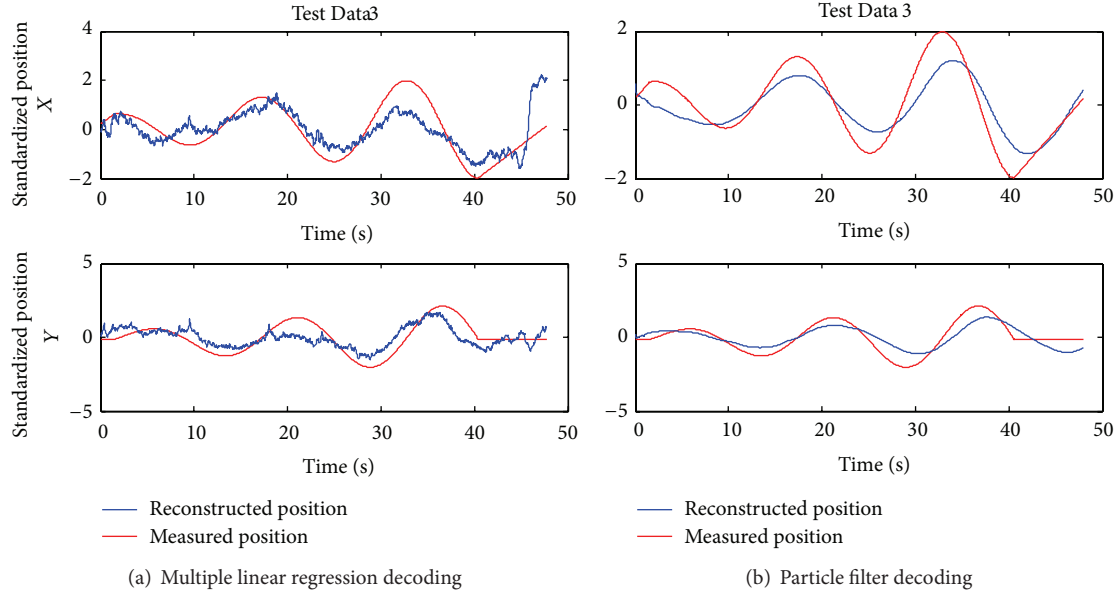


FIGURE 13: The two methods' processing capacities for high-frequency components of the EEG. The reconstructed positions from multiple linear regression model have fluctuations while the reconstructed positions from particle filter model are much smoother.

the increase in training data sets. This is because when the number of training data sets is small, the influence of random interference factors, such as noise, in the training data is big. The influence of the random interference factors decreases with the increase of training data sets, as they can cancel each other out. As a result, a large training data set leads to a high decoding accuracy. When training data sets increase to a certain number, the impact of increasing the training data sets on the improvement of decoding accuracy becomes weaker. Thus, the decoding accuracy tends to stabilize. The decoding results in two dimensions in Table 2 show that the particle filter model can achieve high decoding accuracy using only one training data set. So when the number of experimental data is small, it is easier for the particle filter model to achieve high decoding accuracy.

The high-frequency EEG components will cause high-frequency fluctuations in the reconstructed curves in the multiple linear regression model and lower its decoding accuracy. However, the particle filter model can process the high-frequency components of the EEG directly and use the information in a wide range of frequencies. Both the training data and test data are not low-pass filtered and are then used to decode the EEG using the multiple linear regression model and particle filter model. The decoding results are shown in Figure 13.

Figure 13 shows the two different methods' processing capacities for high-frequency components with the same EEG signal as an input. In Figure 13(a), for multiple linear regression, the Pearson correlation coefficients for the X and Y directions are 0.7228 and 0.6927, respectively, lower than the decoding accuracy of the results after low-pass filtering in Table 1, and have a bad denoising ability. Only when the EEG signal frequency is consistent with the hand-moving frequency can a high decoding accuracy be achieved.

In experiments, the hand-moving frequency is below 2 Hz; hence, the EEG signals need to be processed by a low-pass filter with a cut-off frequency of 2 Hz. In Figure 13(b), for the particle filter decoding results, the Pearson correlation coefficients for the X and Y directions are 0.9044 and 0.8421, respectively, little different from the results after low-pass filtering in Table 2. Furthermore, it has a good effect on the processing of the high-frequency components. This is because the particle filter can process the high-frequency components of EEG in its algorithm, so the low-pass filter is not necessary. Moreover, the high-frequency components of the EEG may contain motion information; hence, the particle filter model can make use of more extensive frequency information, which may improve the decoding accuracy.

6. Conclusion

This paper used the multiple linear regression model and the particle filter model to decode the hand motion information in two and three dimensions from EEG signals and analyzed the decoding results and the factors that influenced it to compare the decoding features of the two methods and their usability. The experimental results showed that the multiple linear regression model needed multiple sets of training data to train and only worked well for low-frequency decoding. Conversely, for the particle filter model, only one set of training data was necessary, and the model could process EEGs containing high-frequency components, which means a more extensive utilization of frequency information. Nevertheless, the length of the EEG data affected the decoding accuracy. With this in mind, the decoding model should be carefully chosen in accordance with the model features and its application scenario.

Our future work is to research the influence of other factors on the decoding, optimize the particle filter method to improve its decoding accuracy, and try to perform online decoding and manipulator control.

Conflict of Interests

The authors declare that there is no conflict of interests regarding the publication of this paper.

Acknowledgments

The authors thank the anonymous referees for their helpful comments. The support of the Overseas Returnees Foundation of the Ministry of Education of China and the Special Program of the Postdoctoral Science Foundation of China (Approval no. XJ2013045) is gratefully acknowledged.

References

- [1] J. E. O'Doherty, M. A. Lebedev, P. J. Ifft et al., "Active tactile exploration using a brain-machine-brain interface," *Nature*, vol. 479, no. 7372, pp. 228–231, 2011.
- [2] S. T. Clanton, *Brain-computer interface control of an anthropomorphic robotic arm [Ph.D. thesis]*, Massachusetts Institute of Technology, Cambridge, Mass, USA, 2011.
- [3] M. Velliste, S. Perel, M. C. Spalding, A. S. Whitford, and A. B. Schwartz, "Cortical control of a prosthetic arm for self-feeding," *Nature*, vol. 453, no. 7198, pp. 1098–1101, 2008.
- [4] J. M. Carmena, M. A. Lebedev, R. E. Crist et al., "Learning to control a brain-machine interface for reaching and grasping by primates," *PLoS Biology*, vol. 1, no. 2, article e42, 2003.
- [5] A. H. Do, P. T. Wang, C. E. King, S. N. Chun, and Z. Nenadic, "Brain-computer interface controlled robotic gait orthosis: a case report," *Journal of NeuroEngineering and Rehabilitation*, vol. 10, article 111, 2013.
- [6] <https://mindwalker-project.eu>.
- [7] <http://www.egr.uh.edu/news/201204/brain-controlled-exo-skeleton-one-step-closer-reality>.
- [8] T. W. Picton, S. Bentin, P. Berg et al., "Guidelines for using human event-related potentials to study cognition: recording standards and publication criteria," *Psychophysiology*, vol. 37, no. 2, pp. 127–152, 2000.
- [9] Y. J. Kim, M. Graboweczyk, K. A. Paller, K. Muthu, and S. Suzuki, "Attention induces synchronization-based response gain in steady-state visual evoked potentials," *Nature Neuroscience*, vol. 10, no. 1, pp. 117–125, 2007.
- [10] N.-Y. Liang, P. Saratchandran, G.-B. Huang, and N. Sundararajan, "Classification of mental tasks from EEG signals using extreme learning machine," *International Journal of Neural Systems*, vol. 16, no. 1, pp. 29–38, 2006.
- [11] Q. B. Zhao, Q. L. Zhang, and C. Andrzej, "EEG based on asynchronous BCI car navigation system in 3D virtual reality environment," *Chinese Science Bulletin*, vol. 53, no. 23, pp. 2888–2895, 2008.
- [12] V. Logar, I. Škrnjanc, A. Belič et al., "Gripping-force identification using EEG and phase-demodulation approach," *Neuroscience Research*, vol. 60, no. 4, pp. 389–396, 2008.
- [13] H. Yuan, C. Perdoni, and B. He, "Relationship between speed and EEG activity during imagined and executed hand movements," *Journal of Neural Engineering*, vol. 7, no. 2, Article ID 026001, 2010.
- [14] T. J. Bradberry, R. J. Gentili, and J. L. Contreras-Vidal, "Decoding three-dimensional hand kinematics from electroencephalographic signals," in *Proceedings of the IEEE Annual International Conference of Engineering in Medicine and Biology Society*, pp. 5010–5013, Minneapolis, Minn, USA, 2009.
- [15] T. J. Bradberry, R. J. Gentili, and J. L. Contreras-Vidal, "Reconstructing three-dimensional hand movements from noninvasive electroencephalographic signals," *Journal of Neuroscience*, vol. 30, no. 9, pp. 3432–3437, 2010.
- [16] A. Presacco, R. Goodman, L. Forrester, and J. L. Contreras-Vidal, "Neural decoding of treadmill walking from noninvasive electroencephalographic signals," *Journal of Neurophysiology*, vol. 106, no. 4, pp. 1875–1887, 2011.
- [17] W. Wu, A. Shaikhouni, J. P. Donoghue, and M. J. Black, "Closed-loop neural control of cursor motion using a kalman filter," in *Proceedings of the 26th Annual International Conference of the IEEE Engineering in Medicine and Biology Society*, pp. 4126–4129, San Francisco, Calif, USA, September 2004.
- [18] W. Wu, M. J. Black, D. Mumford, Y. Gao, E. Bienenstock, and J. P. Donoghue, "Modeling and decoding motor cortical activity using a switching Kalman filter," *IEEE Transactions on Biomedical Engineering*, vol. 51, no. 6, pp. 933–942, 2004.
- [19] W. Wu, J. E. Kulkarni, N. G. Hatsopoulos, and L. Paninski, "Neural decoding of hand motion using a linear state-space model with hidden states," *IEEE Transactions on Neural Systems and Rehabilitation Engineering*, vol. 17, no. 4, pp. 370–378, 2009.
- [20] L. Shpigelman, Y. Singer, R. Paz, and E. Vaadia, "Spikernels: predicting arm movements by embedding population spike rate patterns in inner-product spaces," *Neural Computation*, vol. 17, no. 3, pp. 671–690, 2005.
- [21] J. Lv, Y. Li, and Z. Gu, "Decoding hand movement velocity from electroencephalogram signals during a drawing task," *BioMedical Engineering Online*, vol. 9, article 64, 2010.
- [22] J. M. Antelis, L. Montesano, and J. Minguez, "Towards decoding 3D finger trajectories from EEG," *International Journal of Bioelectromagnetism*, vol. 13, no. 3, pp. 112–114, 2011.
- [23] J. M. Antelis, L. Montesano, A. Ramos-Murguiaday, N. Birbaumer, and J. Minguez, "On the usage of linear regression models to reconstruct limb kinematics from low frequency EEG signals," *PLoS ONE*, vol. 8, no. 4, Article ID e61976, 2013.
- [24] A. E. Brockwell, A. L. Rojas, and R. E. Kass, "Recursive Bayesian decoding of motor cortical signals by particle filtering," *Journal of Neurophysiology*, vol. 91, no. 4, pp. 1899–1907, 2004.
- [25] F. Wood, P. Prabhat, J. P. Donoghue, and M. J. Black, "Inferring attentional state and kinematics from motor cortical firing rates," in *Proceedings of the 27th Annual International Conference of the Engineering in Medicine and Biology Society (IEEE-EMBS '05)*, pp. 149–152, Shanghai, China, September 2005.
- [26] R. C. Kelly and T. S. Lee, "Decoding V1 neuronal activity using particle filtering with volterra kernels," in *Proceeding of Advances in Neural Information Processing Systems*, vol. 16, Vancouver, Canada, 2003.
- [27] Y. Gao, M. J. Black, E. Bienenstock, S. Shoham, and J. P. Donoghue, "Probabilistic inference of hand motion from neural activity in motor cortex," *Advances in Neural Information Processing Systems*, vol. 14, pp. 221–228, 2002.

Research Article

Change of Muscle Architecture following Body Weight Support Treadmill Training for Persons after Subacute Stroke: Evidence from Ultrasonography

Peng Liu, Yanjun Wang, Huijing Hu, Yurong Mao, Dongfeng Huang, and Le Li

Department of Rehabilitation Medicine, The First Affiliated Hospital of Sun Yat-sen University, Guangzhou 510080, China

Correspondence should be addressed to Le Li; lile5@mail.sysu.edu.cn

Received 3 December 2013; Revised 30 January 2014; Accepted 14 February 2014; Published 24 March 2014

Academic Editor: Xiaoling Hu

Copyright © 2014 Peng Liu et al. This is an open access article distributed under the Creative Commons Attribution License, which permits unrestricted use, distribution, and reproduction in any medium, provided the original work is properly cited.

Although the body weight support treadmill training (BWSTT) in rehabilitation therapy has been appreciated for a long time, the biomechanical effects of this training on muscular system remain unclear. Ultrasonography has been suggested to be a feasible method to measure muscle morphological changes after neurological diseases such as stroke, which may help to enhance the understanding of the mechanism underlying the impaired motor function. This study investigated the muscle architectural changes of tibialis anterior and medial gastrocnemius in patients after subacute stroke by ultrasound. As expected, we found the effect of BWSTT on the muscular system. Specifically, the results showed larger pennation angle and muscle thickness of tibialis anterior and longer fascicle length of medial gastrocnemius after the training. The findings of this study suggest that the early rehabilitation training of BWSTT in subacute stage of stroke provides positive changes of the muscle architecture, leading to the potential improvement of the force generation of the muscle. This may not only help us understand changes of subacute stroke in muscular system but also have clinical implications in the evaluation of rehabilitation training after neurological insults.

1. Introduction

Stroke survivors often develop spasticity, contractures, muscle weakness, and decreased range of motion, which severely affect their activities of daily living [1, 2]. Three months after the onset of stroke, approximately 25% of the surviving patients are still using wheelchair, and, in 50% of the survivors, the gait velocity and endurance are considerably reduced [3]. Therefore, restoration and improvement of gait after stroke are major aspects of neurorehabilitation.

Body weight supported treadmill training (BWSTT) is a type of step training with task-specific nature and partial body weight of the subjects is held [4]. This interactive locomotor training first came from animal experiment which demonstrated recovery of locomotion and the spinalized cats could regain normal gait pattern after 1 to 3 months partial weight supported walking on treadmill [5]. Clinically, BWSTT is proved to be a promising technique for the restoration of gait in stroke and paralytic subjects [6–8]. It enables the harness-secured patients to practice numerous

steps assisted by therapists at an early stage after neurological insult [6]. Previous studies have showed that BWSTT is more effective for the restoration of gait and improving walking capacity by establishing symmetric and efficient gait as compared to regular physiotherapy in people after stroke [7, 8]. However, others reported conflicted findings that BWSTT is not superior to the conventional gait training [9]. This discrepancy might relate to the limitation of evaluation methods and the limited understanding of the recovery mechanism of treadmill training.

To evaluate the effects of BWSTT, clinical tests and scales are often used [10]. Clinical scales are relatively subjective in the evaluation of the efficiency of different stroke rehabilitation programs. In addition, these evaluations do not reveal the underlying mechanisms of those interventions to the neuromuscular system. The motor recovery of limb function is related to spinal locomotor pools, which include a central pattern generator for activity of automatic, alternating flexor, and extensor lower limb muscles. Spinal locomotor pools are highly responsive to phasic segmental sensory

inputs and show evidence of learning during step training [11]. Previous results showed that BWSTT could reduce the level of loading on the lower limbs and enable the human lumbosacral spinal cord to modulate efferent output in a manner that may facilitate the generation of stepping [12]. However, to our knowledge, there is still a lack of study or evidence to investigate the biomechanical mechanism of motor function improvement after BWSTT in the peripheral neuromuscular system, especially from the muscle fascicle level.

Muscle architecture, defined here as a geometrical arrangement of fascicle, affects the muscle function [13]. In a pinnate muscle, fascicles (bundles of fibres) are arranged parallel and obliquely with respect to the tendon; then the forces exerted by muscle fibers are in turn modified by this pennation angle when they are transmitted to tendon [14]. Muscle architecture therefore characterizes and specifies the force-generating capability of a muscle. Although MRI has been widely accepted as a gold standard in measuring the muscle parameters, especially cross-section area [15], it is costly and limited in cooperation with other instruments and in different testing conditions with muscle contraction [16]. As a noninvasive medical imaging technology, ultrasonography has been applied to measure human skeletal muscle architecture *in vivo* [17]. It is a feasible method to measure pennation angle, muscle fascicle length, and muscle thickness. Based on the normal subjects and highly-trained bodybuilders, Kawakami et al. found a significant correlation between muscle thickness and pennation angles at triceps brachii [18]. Recently, ultrasonic studies have been conducted to examine hypertonic muscles in patients with neurologic disorders [19, 20]. Our previous study showed that persons after chronic stroke had shorter muscle fascicle length at brachialis compared to unaffected side [19], and Gao and his colleagues also found smaller pennation angle and shorter muscle fibre length in gastrocnemius of chronic stroke survivors compared to age-matched healthy control [20]. However, how the muscle morphology change on persons in subacute stroke remains unclear, and how the early stage of exercise training improves muscle function needs investigation.

The purpose of this study was, therefore, to measure the muscle architectural parameters of tibialis anterior and medial gastrocnemius in patients after subacute stroke by ultrasound and to investigate their changes after BWSTT together with other clinical scores, muscle strength, and walking speed to assess the effectiveness of the intervention, which would help us understand the biomechanical mechanism of the training. We hypothesize that ultrasound could differentiate the changes after stroke and that the training effects on motor recovery after BWST might be related to the changes of muscle architecture.

2. Methods

2.1. Participants. Fifteen adults with subacute stroke (9 men, 6 women; mean, 60.5 y; age range, 51–73 y) and eight age-matched healthy subjects (5 men, 3 women; mean, 57.0 y; age range 41–75 y) were recruited in this study. The inclusion

criteria for the hemiparetic subjects included (1) having hemiparesis for no more than 3 months resulting from first stroke insult; (2) presence of clinically detectable spasticity in the ankle dorsiflexor, with a Modified Ashworth Score (MAS) larger than 1 (maximal value, 4); (3) a passive range of motion in the ankle joint on the paretic side from -15° (dorsiflexed direction) to 45° (plantarflexed direction), here, 0° was defined as ankle in neutral position (the sole of the foot perpendicular to the tibia); (4) adequate mental capacity to attempt the tasks as instructed; and (5) an absence of other significant medical complications. Table 1 shows the baseline demographic and clinical characteristics for the people after subacute stroke. This study was approved by the Human Subjects Ethics Committee of The First Affiliated Hospital of Sun Yat-sen University. All the participants gave informed consent following the ethical procedures.

2.2. Ultrasound Measures of Muscle Parameters. The stroke survivors were randomly assigned to conventional rehabilitative treatment plus BWSTT (BWSTT group, $n = 8$) and conventional treatment plus over-ground gait training only (CGT group, $n = 7$). A B-mode ultrasonography scanner (DP6600, Mindray Inc, China) with a 7.5 MHz, 38 mm probe (imaging resolution, 0.3 mm; frame rate, 25/s), and a hand-held dynamometer (MicroFET3, Hoggan Inc, UT, USA; with the precision of 0.4 N and range from 13 N~1330 N) were used in the present study.

During the experiment, the subjects were laid supine on a checking bed and were supported with a towel roll under ankle while hip and knee joints were in full extension [18]. During the testing for tibialis anterior (TA), the ultrasound probe was put perpendicularly to the dermal surface of central region of TA muscle, which is half-distance between the malleoli and the proximal end of the tibia, over the mid-sagittal plane [21]. For median gastrocnemius (MG) muscle, the probe was placed on a site on the muscle 30% proximal between the medial malleolus of the fibula and the medial condyle of the tibia [22]. The size of the probe is 38 mm and the probe was put on the muscle belly. The position of muscle belly was confirmed based on the contraction of the muscle as well as the experience of the experienced physical therapist. A marker pen was used to set the position on the skin to localize the probe position. Coupling gel was applied to enhance ultrasound conduction between the ultrasound probe and skin surface. Accuracy of the ultrasound method in measuring muscle architectural features has been previously demonstrated to show good agreement with direct anatomical measurement on cadaver [23]. The experiment consisted of two different conditions: muscle at rest and at maximum voluntary contraction (MVC). For each condition, ankle joint was measured ranging from dorsiflexion 15° to plantar flexion 45° with increments of 15° using the hand-held dynamometer and, for each position, three trials of muscle contractions were tested. We followed the similar procedure of our previous study using ultrasound measurement on muscle architecture at rest and MVC [19]. The hand-held dynamometer was held by an experienced physical therapist and the testing position is referenced with text book [24]. In the rest condition, subjects were required to relax during the measurement. In

TABLE 1: Baseline demographic and clinical characteristics of the patients.

Characteristics	BWSTT (<i>n</i> = 8)	Control (<i>n</i> = 7)	<i>P</i> value*
Age (years)	61.63 (8.43)	59.29 (9.11)	0.821
Female	3 (37.5%)	3 (42.86%)	1.00
Height (cm)	165.88 (6.81)	165.71 (7.54)	0.612
Bodyweight (Kg)	60.75 (4.43)	61.14 (5.46)	0.472
Ischemic stroke	2 (25.0%)	2 (28.57)	1.00
Affected side at left	4 (50.0%)	5 (71.43%)	0.608
Days after stroke	45.25 (17.60)	58.71 (19.52)	0.644
FMA-LE	23.13 (4.29)	22.0 (4.51)	0.375
MAS	1.69 (0.26)	1.64 (0.24)	0.738

Data are presented as mean (SD) or *n* (%); BWSTT: body weight support treadmill training; FMA-LE: Fugl-Meyer assessment of lower limb; MAS: Modified Ashworth Scale.

* Based on the independent *t*-test or Fisher's exact test.

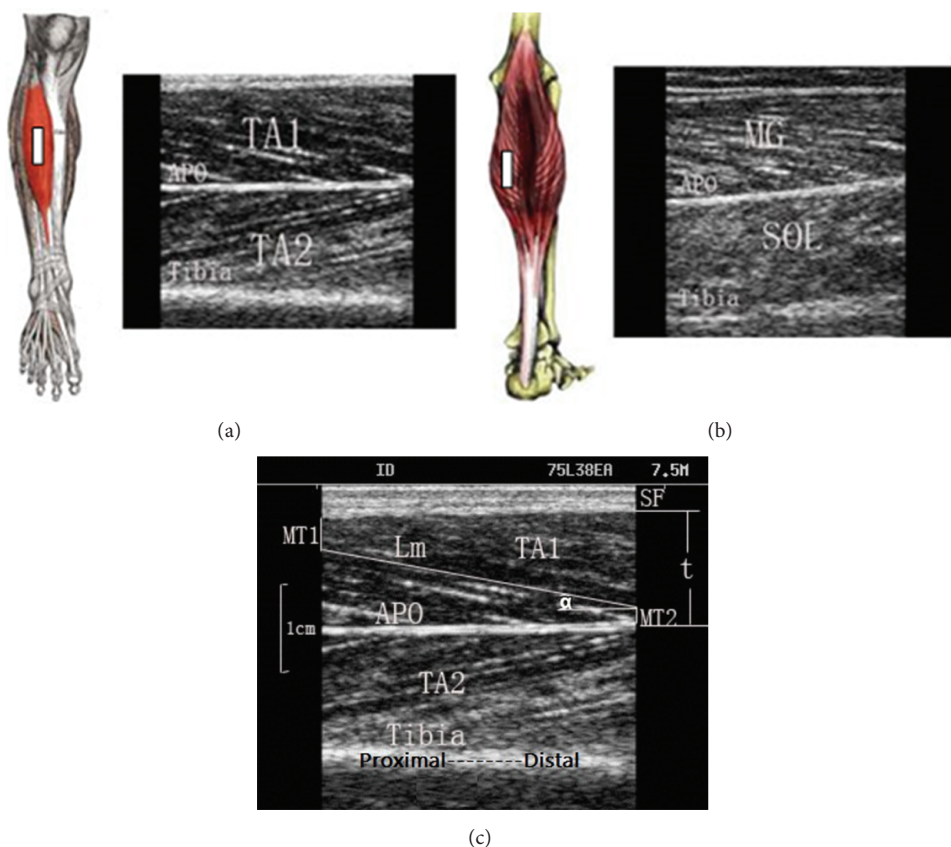


FIGURE 1: Probe positions on the measured muscles and typical ultrasound images for measurement on (a) TA and (b) MG. (c) Demonstration of the labels for muscle parameters. The bright fringe in the lower region of the image shows the muscle-tibia boundary. Aponeurosis (APO) is the boundary between the superficial and deep layer of TA. SF is subcutaneous fat. L_m is the visualized part of the entire muscle fascicle length and can be measured directly; MT_1 and MT_2 are the distance of the fiber proximal end point to the superficial aponeurosis and the distance of the fiber distal end to the bone, respectively; α is the pennation angle; TA1 is the superficial layer of the TA; and TA2 is the deep layer of TA.

the MVC condition, subjects were instructed to take 1 or 2 s to come to maximal effort and hold for 3–5 s then the muscle strength was measured by the tester using the hand-held dynamometer. Ultrasound images were collected simultaneously. All subjects were instructed to avoid eversion-inversion and adduction-abduction of the foot during MVC. The test

was performed three times with a 30 s interval to avoid muscle fatigue. Ultrasound measurements were conducted at the first of enrollment and last day after the 3-week training.

Probe position and typical ultrasound images of TA and MG are shown in Figure 1. The white fringe of the tibia bone and the dark muscle fascicle are displayed in the ultrasound

image. Pennation angle (α) was directly measured from the image, and the entire muscle fascicle length (L_f) was estimated using a trigonometry method by assuming a linear continuation of the muscle fascicle [19]. Consider

$$L_f = L_m + \frac{MT_1}{\sin \alpha} + \frac{MT_2}{\sin \alpha}, \quad (1)$$

where L_f is the entire estimated muscle fascicle length, L_m is the visible part of the muscle fiber, and α is the pennation angle. MT_1 and MT_2 denote the distance of the fiber distal end point to the superficial aponeurosis and the distance of the fiber proximal end to the bone, which is also used to calculate muscle thickness.

2.3. Training Protocol. All the stroke survivors were treated in 60-minute walking training sessions every weekday for 3 weeks with a total of 15 sessions. For BWSTT, the initial BWS (body weight support) amount was set at 30%~40%, and the speed of the treadmill was set at 0.5 mph (miles per hour). We followed the training schedule both with the recommendation from literature on BWSTT [4] as well as our patients' conditions and response being evaluated by experienced physical therapist and physicians. In Hesse's study [4], he recommended that the initial body weight support should be no more than 30% BW and, during therapy, treadmill speed should be increased and body weight support reduced as soon as possible. The training intensity at the first week was around 20 mins and increased to 40 mins in the third week, while the treadmill speed increased to around 2.0 mph. For the control group, they received over-ground walking training of 60 mins daily.

For all the recruited subjects, another two-hour therapy program of nongait activity such as bed mobility, transfers, strengthening, and balance training was also scheduled as normal training at in-patient section of hospital. All physical therapists involved in the study were trained according to the protocol and documented participants' daily compliance with the protocol. In addition, the entire rehabilitation team was educated concerning the experimental study protocol to ensure compliance when participants were not working with therapy staff.

3. Other Outcome Measures

Besides the ultrasound measurements, other outcome measures were the muscle strength, 10 meters walking speeds, Modified Ashworth Scale (MAS), and the lower limb subscale of Fugl-Meyer assessment (FMA-LE). Assessments were made at baseline and after the treatment by an examiner who was blinded to the group information of the subjects.

3.1. Statistical Analysis. In this study, values for muscle architectural parameters and muscle strength were presented as mean \pm SD. SPSS (version 15.0, SPSS Inc, Chicago, IL, USA) was used to compare the difference of outcome measurements. Analysis of variance (ANOVA) with Bonferroni post hoc test was used to evaluate the changes of the parameters across conditions. Independent *t* test was used to compare the

data of rest and MVC condition at each specific joint angle. A paired *t* test was used to compare muscle architectural parameters, muscle strength, FMA-LE scores, and walking speed before and after the training. Rank-sum test was used to compare MAS scores before and after the training. Pearson correlation analysis was conducted between muscle architecture parameters and muscle strength. The significant level was set as 0.05 for all statistical tests.

4. Results

The baseline measures of common demographic variables, the lower limb subscale of Fugl-Meyer assessment, and the Modified Ashworth Score did not significantly differ between the BWST group and control group (Table 1). Subject disposition is detailed in the flow chart (Figure 2).

For TA muscle, it was found that the measured muscle pennation angle and fascicle length were joint-angle-dependent in all three groups at the rest and MVC condition (Figures 3(a)–3(d)). Further comparisons between groups found that the pennation angles and muscle thickness of the affected side were significantly smaller ($P < 0.05$) than the unaffected side and those of healthy group at both two conditions, whereas there was no significant difference of muscle fascicle length among the groups in rest condition. There were no significant difference of muscle thickness ($P > 0.05$) between rest and MVC (Table 2). Compared to the baseline value, pennation angle ($6.15 \pm 1.28^\circ$) and muscle thickness (1.02 ± 0.09 cm) at the affected side of BWSTT group at rest condition significantly increased to $7.26 \pm 1.62^\circ$ ($P < 0.05$) and 1.09 ± 1.12 cm ($P < 0.05$) after the training, while there were no significant differences in CGT group (Table 2). A similar trend was also shown in MVC condition. Muscle strength of dorsiflexion at affected side in BWSTT group significantly increased from 49.04 ± 28.12 N to 83.75 ± 42.72 N after the training, while there were no significant changes in the unaffected side and both two sides in CGT group (Table 3).

For the MG muscle, pennation angle and fascicle length were joint-angle-dependent in all three groups at the rest and MVC condition (Figures 3(e)–3(h)). Comparison between groups showed that the affected fascicle lengths were significantly shorter ($P < 0.05$) than the unaffected side and the healthy group. There were no significant difference of muscle thickness ($P > 0.05$) between rest and MVC (Table 2). After the training, the fascicle length of affected side (5.23 ± 1.07 cm) was significantly longer than that of baseline value (4.66 ± 1.06 cm, $P < 0.05$) (Table 2). In addition, the plantarflexors strength of affected side significantly increased from 93.67 ± 40.94 N to 115.39 ± 65.37 N after the training. However, this trend of muscle fascicle and strength was not found in unaffected side and CGT group ($P > 0.05$).

The clinical scores of affected side showed the improvement after the training. FMA-LE was significantly increased ($P < 0.05$) and MAS was significantly decreased ($P < 0.05$), while there was no significant difference in the CGT group (Table 4). 10-meter walking test of self-selected speed showed that the BWST has a significant increase ($P < 0.05$), while there were no such changes in CGT group (Table 4).

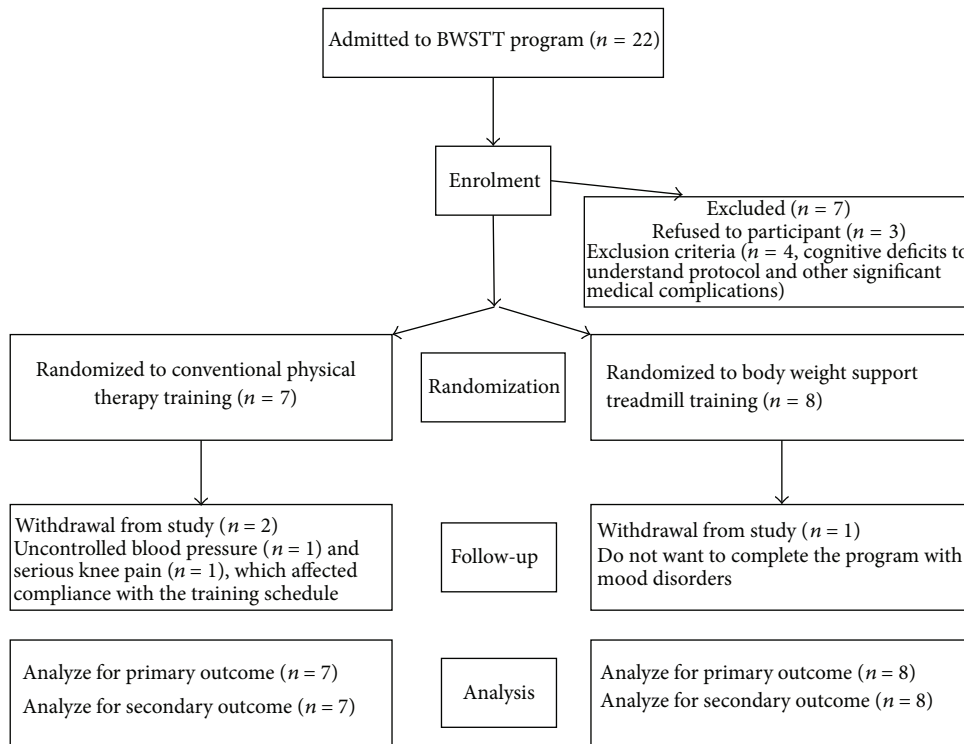


FIGURE 2: The study flow chart.

5. Discussion

In this study, ultrasound measurements were conducted on the TA and MG of subacute stroke survivors together with muscle strength and clinical scores before and after 3 weeks BWSTT. The results demonstrated the muscular morphological changes in larger pennation angle and muscle thickness of tibialis anterior and longer fascicle length of medial gastrocnemius after the training, as well as muscle strength. This suggests that the early rehabilitation training of BWSTT is helpful to the changes of the muscle architecture which contributes to the potential of the force generation of the muscle [25].

Our findings showed that the muscular architectural parameters in the affected side and in the unaffected side were different and were joint-angle-dependent at the rest condition. Previous study found significant decrease in pennation angle and fiber length of gastrocnemius medialis muscle at the affected side of chronic stroke survivors [20]. The immobilization of the flexor in a shortened position and increased muscle stiffness might cause these muscle architectural changes. The reason of the shorted muscle fascicle length may be due to reduction in the number of sarcomeres in the spastic muscle fiber [26] and decrease of the pennation angle related to muscle disuse [27]. During muscle maximum voluntary contraction, force generated by muscle elongates the tendon and aponeurosis, changing the architecture of muscle; that is, pennation angle increased and fascicle length shortened. This phenomenon is widely known from previous studies [15, 16, 18]. The findings in our study

share agreement of the phenomenon, while fascicle length of both TA and MG has shortened and pennation angle of them has increased at MVC condition. Compared to unaffected side, smaller pennation angle and fascicle length changes were found in the affected side during isometric contraction, and these smaller changes might be due to weakness in the muscle after the onset of stroke. We found that there are no significant differences of muscle thickness between rest and MVC which supports the simple planar muscle model [28] and previous results from Manal et al. [29]. In this planar muscle model, it is assumed that muscle thickness is constant in contraction condition. Therefore, our results demonstrate that ultrasound imaging technique is feasible to evaluate the muscle architectural changes after subacute stroke, which could facilitate the understanding of muscle functional recovery after intervention.

There are many studies that had demonstrated the muscle morphology changes after training both in athletes and subjects with neurological insults, which are similar to the findings of this current study. Blazevich et al. found the muscle thickness of rectus femoris enlarged from 2.08–2.4 cm to 2.5–2.58 cm and fascicle length increased from 10.6–16 cm to 14.7–21.6 cm in athletes after 5 weeks resistance training [30]. Brorsson and coworkers found the cross-section area of extensor digitorum communis increased after a six-week hand exercise programme in patients with rheumatoid arthritis [31]. In line with these studies, increased muscle thickness in TA and longer fascicle length in MG were also found in subacute stroke after 3-week treadmill training, which may demonstrate that the training could counteract the muscle

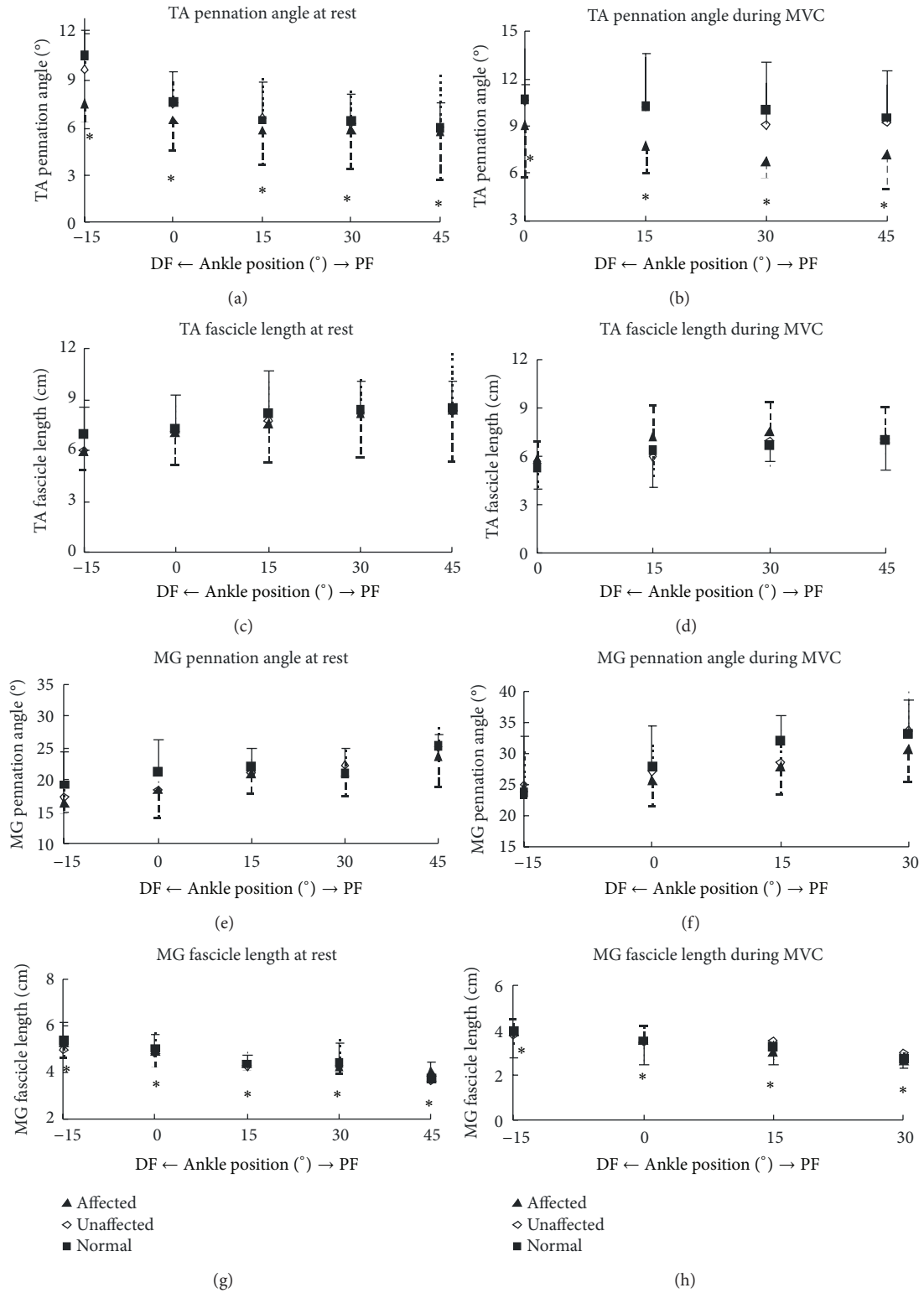


FIGURE 3: Pennation angle and fascicle length of TA ((a)–(d)) and MG ((e)–(h)) in the affected side, the unaffected side of the subjects after stroke, and the right side of healthy subjects as a function of ankle joint angle at the rest condition and MVC. The error bar represents 1 standard deviation (SD). *Any significant difference between the affected group and the unaffected group (t test, $P < 0.05$).

TABLE 2: Changes of muscle architectural parameters of TA and MG after 3-week BWSTT.

TA mean (SD)		BWSTT group		CGT group	
		Affected	Unaffected	Affected	Unaffected
Pennation angle (°)	Rest	Before	6.15 (1.28)	7.60 (2.58)	6.47 (1.26)
		After	7.26 (1.62)*	7.81 (2.07)	6.05 (0.86)
	MVC	Before	7.65 (2.20)	9.78 (2.82)	8.16 (1.49)
		After	9.11 (1.95)*	10.29 (2.46)	7.94 (1.18)
Muscle thickness (cm)	Rest	Before	1.02 (0.09)	1.14 (0.16)	0.90 (0.16)
		After	1.09 (1.12)*	1.09 (0.12)	0.86 (0.11)
	MVC	Before	1.16 (0.07)	1.26 (0.17)	1.02 (0.11)
		After	1.21 (0.11)*	1.22 (0.14)	1.01 (0.10)
Fascicle length (cm)	Rest	Before	7.52 (1.90)	7.45 (2.28)	6.48 (0.87)
		After	7.43 (1.88)	7.28 (1.79)	6.38 (1.01)
	MVC	Before	7.45 (1.80)	7.18 (2.27)	6.12 (1.25)
		After	7.13 (2.32)	6.79 (2.04)	6.03 (1.17)

MG mean (SD)		BWSTT group		CGT group	
		Affected	Unaffected	Affected	Unaffected
Pennation angle (°)	Rest	Before	18.73 (3.44)	19.74 (5.66)	20.82 (6.44)
		After	19.32 (3.86)	21.35 (4.50)	19.05 (6.70)
	MVC	Before	26.75 (4.17)	26.12 (5.65)	27.48 (5.29)
		After	25.57 (4.26)	30.45 (6.89)	28.69 (7.31)
Muscle thickness (cm)	Rest	Before	1.50 (0.21)	1.60 (0.32)	1.53 (0.31)
		After	1.61 (0.26)	1.64 (0.32)	1.58 (0.36)
	MVC	Before	1.59 (0.27)	1.67 (0.27)	1.66 (0.17)
		After	1.63 (0.27)	1.66 (0.23)	1.65 (0.24)
Fascicle length (cm)	Rest	Before	4.66 (1.06)	5.13 (1.17)	4.65 (0.66)
		After	5.23 (1.07)*	5.15 (1.06)	4.84 (0.93)
	MVC	Before	3.76 (1.08)	3.74 (1.18)	3.74 (0.57)
		After	4.02 (4.14)*	3.41 (1.04)	3.54 (0.90)

SD: standard deviation.

TABLE 3: Muscle strength comparison of dorsiflexion and plantarflexion before and after training.

(a)				
Dorsiflexion (N) Mean (SD)	Before	After	t	P
BWSTT affected	49.04 (28.12)	83.75 (42.72)	-4.780	0.000*
BWSTT unaffected	142.85 (32.57)	134.57 (41.70)	0.985	0.333
CGT affected	47.08 (25.01)	55.71 (25.50)	-1.928	0.069
CGT unaffected	129.45 (33.15)	122.78 (40.85)	0.687	0.503

(b)				
Plantarflexion (N) Mean (SD)	Before	After	t	P
BWSTT affected	93.67 (40.94)	115.39 (65.37)	-2.144	0.041*
BWSTT unaffected	188.95 (56.07)	179.78 (75.38)	0.470	0.643
CGT affected	85.48 (43.83)	96.25 (43.83)	-1.348	0.193
CGT unaffected	175.20 (37.87)	173.11 (56.16)	0.202	0.842

*P < 0.05.

SD: standard deviation.

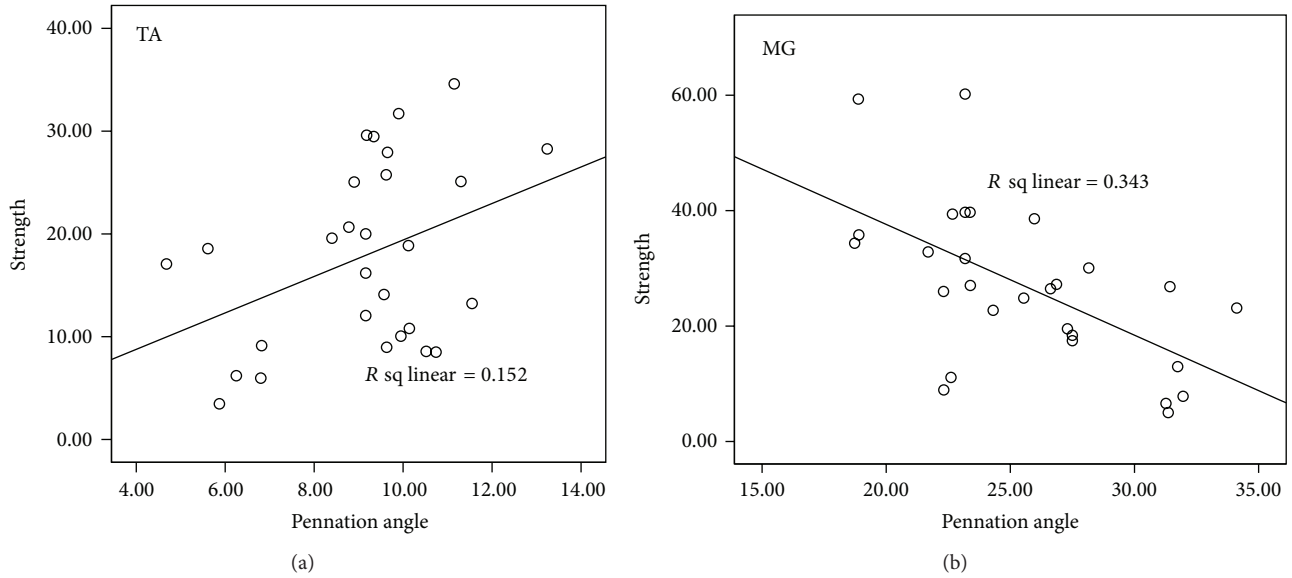


FIGURE 4: Correlation coefficient results of pennation angle and muscle strength on TA (a) and MG (b) of the affected side of BWSTT group after training.

TABLE 4: Comparison of FMA and MAS scores and 10-metre walking speeds before and after training.

		Before	After	P
FMA	BWSTT	23.14 (4.63)	25.57 (4.69)	0.002*
Mean (SD)	CGT	21.8 (4.49)	24.2 (2.95)	0.051
MAS	BWSTT	1.64 (0.24)	1.48 (0.59)	0.038*
Mean (SD)	CGT	1.21 (0.24)	1.14 (0.59)	0.095
10-metre walking speeds (m/s)	BWSTT	0.36 (0.15)	0.55 (0.20)	0.004*
	CGT	0.46 (0.21)	0.47 (0.23)	0.854

* $P < 0.05$.

SD: standard deviation.

atrophy and enlarge the muscle volume. In the current study, the muscle strength of dorsiflexion at the affected side at BWSTT group was significantly increased after the training and showed better performance in walking ability (Table 4). Furthermore, the strength of ankle dorsiflexors and ankle plantarflexors obtained in our study (Table 3) is close to Dorsch et al.'s results of stroke survivors (ankle dorsiflexors: 66 ± 37 ; ankle plantarflexors: 93 ± 53) [32]. This may suggest that with the proper setup, hand-held dynamometry could be applied to measure the muscle strength in patients with neurological diseases, such as stroke. Meanwhile, our results showed that the plantarflexors strength significantly increased in the BWSTT group. This is in line with the study of Brincks and Nielsen who found that instantaneous plantarflexion power and enough work done in the push-off phase ensure the generation of walking speed [33]. In addition, Pradon and coworkers also demonstrated that the muscle strength had significant positive association with walking distance in persons after stroke [34]. These results may indicate that it is clinically meaningful to measure muscle architectural parameters after stroke after exercise

training, which help to evaluate the muscle performance and motor function recovery.

In order to investigate the relationship between muscle architectural parameters with muscle strength, correlation analysis was performed (Figure 4). The results showed that after the training, there is significant positive correlation between TA pennation angle and muscle strength, and negative correlation between MG pennation angle and muscle strength in the affected side of BWSTT group (Table 5). The relationship between the increased pennation angle and muscle force changes needs further discussion. It is believed that muscle pennation angle has advantageous effects (more muscle fibre and contractile material attached to tendon) [35] and disadvantageous (less efficient force transmission from muscle fibers to tendon) [23] on force generation. Therefore, according to our results, BWSTT facilitates more muscle fibre packed in the same cross-section area which may have larger effects than the force transfer effects to the tendon. That is the reason why the correlation showed a positive relationship in TA. Similarly, Kawakami and coworkers found that load training of upper limb could increase both the pennation

TABLE 5: Correlation of muscle strength with muscle pennation angles of TA and MG before and after training.

		Correlation coefficient (r)		P value
TA	BWSTT	Before	-0.148	0.316
		After	0.390	0.04*
	CGT	Before	-0.291	0.213
		After	0.646	0.002*
MG	BWSTT	Before	-0.259	0.075
		After	-0.586	0.001*
	CGT	Before	-0.141	0.552
		After	-0.312	0.180

* $P < 0.05$.

angle of triceps brachii and the performance of the subjects [36]. The relation between pennation angle and force might depend on the pennation value itself. If the pennation angle is larger than 20° , it has great significance on the transferred force [21]. This could explain the negative relationship between pennation angle of MG and its muscle strength. Further investigations with other lower limb muscles, that is, hamstring and rectus femoris, are warranted to see the effects of pinnate muscle architecture on the muscle force generation ability after stroke.

There are still discussions about training intensities and time window of applying body weight support training to optimize the effects on the outcomes to the stroke survivors. In this study, we applied BWSTT in a group of subacute stroke survivors with average suffering days of 37.5, which is in line with the concept that rehabilitation should be as early as possible to be involved in [37]. Our results demonstrated that after 3 weeks of BWSTT, the patients improved in FMA-LE, MAS, and walking speed (Table 4). Our training effects on walking speed are similar with literature [9]. For example, Franceschini used treadmill training with body weight support on early stage of stroke, and, after 10 sessions of training, their data of 10-meter walking speed is 0.4 m/s (with range of 0.3~0.6 m/s). There is study showing that if too much body weight is supported, the affected side could not get enough stimulus from exercise training and will not benefit the motor recovery of the lower limb function [4]. In the current study, the subject would have an initial body weight support less than 40% which could ensure that the two sides of the lower limb touch on the treadmill and the subjects are safe. During the training process, the weight support will be gradually reduced and all our subjects need not the support in the end of the training. Previous study had showed that the optimal speed should be similar to normal walking speed [38]. In our study, the patients at least had a speed of 1.3 mph in the end of the training which is similar to this finding. Although there is no huge change of vital parameters and observation in our study which may prove that the training is safe for subacute stroke survivors, we will suggest measuring blood pressure and heart rate after each training session.

There are still limitations that need to be discussed in this study about using ultrasound to evaluate muscle architecture. In literature, no consensus has been achieved on the body

posture during measurement. We followed muscle testing manual as well as the literature on the body posture and fixation of the hand-held dynamometer on the lower limb. Further study is warranted to evaluate the effects of body posture and limb position on the muscle measurement. Secondly, although the correlation of muscle strength with muscle pennation angles of TA and MG before and after training has significant changes in the results, the correlation coefficient is still relatively small. This might be related to the variation of our patients' improvement on motor recovery after intervention. Further studies with larger sample size or multicenter design are needed to assess the clinical effects of BWST on muscle function in early treatment after stroke. For the future applications of current study, since the individual muscle force could not be measured with a noninvasive way, the relationship between muscle architectural changes as measured in this study and the generated muscle force could not be interpreted directly. Neuromusculoskeletal model has been applied to calculate individual muscle force based on musculotendon parameters and to predict joint movement [39]. Forward dynamic modeling method will be applied to calculate individual muscle force and the results could be used to compare with joint moment measurement for further evaluating the muscle function for persons after stroke.

6. Conclusions

This study showed that ultrasound measurement is a feasibility method to evaluate the muscle architectural changes in subacute stage of stroke and there are considerable changes in tibialis anterior and medial gastrocnemius fascicle architecture, which may contribute directly to the impaired lower limb motor functions. BWSTT can improve muscle strength, walking speed, and motor functions of persons with subacute stroke and the functional changes of lower limb are related to muscle architecture of TA and MG. Our results demonstrate that BWSTT is a feasible and effective gait training method for subacute stroke in an early stage.

Conflict of Interests

No commercial party having a direct financial interest in the results of the research supporting this paper has or will confer

a benefit upon the authors or upon any organization with which the authors are associated.

Acknowledgments

This work was supported by the National Natural Science Foundation of China (no. 31100669), the Fundamental Research Funds for the Central Universities of China (no. IlyRpy22), and Guangdong Provincial Medical Research Fund (B2013331).

References

- [1] N. J. O'Dwyer, L. Ada, and P. D. Neilson, "Spasticity and muscle contracture following stroke," *Brain*, vol. 119, no. 5, pp. 1737–1749, 1996.
- [2] L. Ada, C. G. Canning, and S.-L. Low, "Stroke patients have selective muscle weakness in shortened range," *Brain*, vol. 126, no. 3, pp. 724–731, 2003.
- [3] D. T. Wade, V. A. Wood, A. Heller, J. Maggs, and R. L. Hewer, "Walking after stroke. Measurement and recovery over the first 3 months," *Scandinavian Journal of Rehabilitation Medicine*, vol. 19, no. 1, pp. 25–30, 1987.
- [4] S. Hesse, "Treadmill training with partial body weight support after stroke: a review," *NeuroRehabilitation*, vol. 23, no. 1, pp. 55–65, 2008.
- [5] H. Barbeau and S. Rossignol, "Recovery of locomotion after chronic spinalization in the adult cat," *Brain Research*, vol. 412, no. 1, pp. 84–95, 1987.
- [6] K. J. McCain, F. E. Pollo, B. S. Baum, S. C. Coleman, S. Baker, and P. S. Smith, "Locomotor treadmill training with partial body-weight support before overground gait in adults with acute stroke: a pilot study," *Archives of Physical Medicine and Rehabilitation*, vol. 89, no. 4, pp. 684–691, 2008.
- [7] S. H. Peurala, O. Airaksinen, P. Huuskonen et al., "Effects of intensive therapy using gait trainer or floor walking exercises early after stroke," *Journal of Rehabilitation Medicine*, vol. 41, no. 3, pp. 166–173, 2009.
- [8] S. Hesse, M. Konrad, and D. Uhlenbrock, "Treadmill walking with partial body weight support versus floor walking in hemiparetic subjects," *Archives of Physical Medicine and Rehabilitation*, vol. 80, no. 4, pp. 421–427, 1999.
- [9] M. Franceschini, S. Carda, M. Agosti, R. Antenucci, D. Malgrati, and C. Cisari, "Walking after stroke: what does treadmill training with body weight support add to overground gait training in patients early after stroke? A single-blind, randomized, controlled trial," *Stroke*, vol. 40, no. 9, pp. 3079–3085, 2009.
- [10] I. T. da Cunha Jr., P. A. Lim, H. Qureshy, H. Henson, T. Monga, and E. J. Protas, "Gait outcomes after acute stroke rehabilitation with supported treadmill ambulation training: a randomized controlled pilot study," *Archives of Physical Medicine and Rehabilitation*, vol. 83, no. 9, pp. 1258–1265, 2002.
- [11] P. R. Trueblood, "Partial body weight treadmill training in persons with chronic stroke," *NeuroRehabilitation*, vol. 16, no. 3, pp. 141–153, 2001.
- [12] S. J. Harkema, S. L. Hurley, U. K. Patel, P. S. Requejo, B. H. Dobkin, and V. R. Edgerton, "Human lumbosacral spinal cord interprets loading during stepping," *Journal of Neurophysiology*, vol. 77, no. 2, pp. 797–811, 1997.
- [13] T. Fukunaga, Y. Kawakami, S. Kuno, K. Funato, and S. Fukashiro, "Muscle architecture and function in humans," *Journal of Biomechanics*, vol. 30, no. 5, pp. 457–463, 1997.
- [14] P. W. Hodges, L. H. M. Pengel, R. D. Herbert, and S. C. Gandevia, "Measurement of muscle contraction with ultrasound imaging," *Muscle and Nerve*, vol. 27, no. 6, pp. 682–692, 2003.
- [15] M. D. Mendis, S. J. Wilson, W. Stanton, and J. A. Hides, "Validity of real-time ultrasound imaging to measure anterior hip muscle size: a comparison with magnetic resonance imaging," *Journal of Orthopaedic and Sports Physical Therapy*, vol. 40, no. 9, pp. 577–581, 2010.
- [16] T. Fukunaga, M. Miyatani, M. Tachi, M. Kouzaki, Y. Kawakami, and H. Kanehisa, "Muscle volume is a major determinant of joint torque in humans," *Acta Physiologica Scandinavica*, vol. 172, no. 4, pp. 249–255, 2001.
- [17] C. English, L. Fisher, and K. Thoiris, "Reliability of real-time ultrasound for measuring skeletal muscle size in human limbs in vivo: a systematic review," *Clinical Rehabilitation*, vol. 26, pp. 934–944, 2012.
- [18] Y. Kawakami, Y. Ichinose, K. Kubo, M. Ito, M. Imai, and T. Fukunaga, "Architecture of contracting human muscles and its functional significance," *Journal of Applied Biomechanics*, vol. 16, no. 1, pp. 88–97, 2000.
- [19] L. Li, K. Y. Tong, and X. Hu, "The effect of poststroke impairments on brachialis muscle architecture as measured by ultrasound," *Archives of Physical Medicine and Rehabilitation*, vol. 88, no. 2, pp. 243–250, 2007.
- [20] F. Gao, T. H. Grant, E. J. Roth, and L.-Q. Zhang, "Changes in passive mechanical properties of the gastrocnemius muscle at the muscle fascicle and joint levels in stroke survivors," *Archives of Physical Medicine and Rehabilitation*, vol. 90, no. 5, pp. 819–826, 2009.
- [21] C. N. Maganaris and V. Baltzopoulos, "Predictability of in vivo changes in pennation angle of human tibialis anterior muscle from rest to maximum isometric dorsiflexion," *European Journal of Applied Physiology and Occupational Physiology*, vol. 79, no. 3, pp. 294–297, 1999.
- [22] T. Ikezoe, N. Mori, M. Nakamura, and N. Ichihashi, "Atrophy of the lower limbs in elderly women: is it related to walking ability?" *European Journal of Applied Physiology*, vol. 111, no. 6, pp. 989–995, 2011.
- [23] M. V. Narici, T. Binzoni, E. Hiltbrand, J. Fasel, F. Terrier, and P. Cerretelli, "In vivo human gastrocnemius architecture with changing joint angle at rest and during graded isometric contraction," *Journal of Physiology*, vol. 496, no. 1, pp. 287–297, 1996.
- [24] H. J. Hislop, *Daniels and Worthingham's Muscle Testing: Techniques of Manual Examination*, Elsevier Science Health Science Division, 8th edition, 2007.
- [25] J. M. Thom, C. I. Morse, K. M. Birch, and M. V. Narici, "Influence of muscle architecture on the torque and power-velocity characteristics of young and elderly men," *European Journal of Applied Physiology*, vol. 100, no. 5, pp. 613–619, 2007.
- [26] J. Harlaar, J. G. Becher, C. J. Snijders, and G. J. Lankhorst, "Passive stiffness characteristics of ankle plantar flexors in hemiplegia," *Clinical Biomechanics*, vol. 15, no. 4, pp. 261–270, 2000.
- [27] E. M. Halar, W. C. Stolov, and B. Venkatesh, "Gastrocnemius muscle belly and tendon length in stroke patients and able-bodied persons," *Archives of Physical Medicine and Rehabilitation*, vol. 59, no. 10, pp. 476–484, 1978.

- [28] E. Otten, "Concepts and models of functional architecture in skeletal muscle," *Exercise and Sport Sciences Reviews*, vol. 16, pp. 89–137, 1988.
- [29] K. Manal, D. P. Roberts, and T. S. Buchanan, "Optimal pennation angle of the primary ankle plantar and dorsiflexors: variations with sex, contraction intensity, and limb," *Journal of Applied Biomechanics*, vol. 22, no. 4, pp. 255–263, 2006.
- [30] A. J. Blazevich, N. D. Gill, R. Bronks, and R. U. Newton, "Training-specific muscle architecture adaptation after 5-wk training in athletes," *Medicine and Science in Sports and Exercise*, vol. 35, no. 12, pp. 2013–2022, 2003.
- [31] S. Brorsson, M. Hilliges, C. Sollerman, and A. Nilsson, "A six-week hand exercise programme improves strength and hand function in patients with rheumatoid arthritis," *Journal of Rehabilitation Medicine*, vol. 41, no. 5, pp. 338–342, 2009.
- [32] S. Dorsch, L. Ada, C. G. Canning, M. Al-Zharani, and C. Dean, "The strength of the ankle dorsiflexors has a significant contribution to walking speed in people who can walk independently after stroke: an observational study," *Archives of Physical Medicine and Rehabilitation*, vol. 93, no. 6, pp. 1072–1076, 2012.
- [33] J. Brincks and J. F. Nielsen, "Increased power generation in impaired lower extremities correlated with changes in walking speeds in sub-acute stroke patients," *Clinical Biomechanics*, vol. 27, no. 2, pp. 138–144, 2012.
- [34] D. Pradon, N. Roche, L. Enette, and R. Zory, "Relationship between lower limb muscle strength and 6-minute walk test performance in stroke patients," *Journal of Rehabilitation Medicine*, vol. 45, pp. 105–108, 2013.
- [35] D. A. Jones and O. M. Rutherford, "Human muscle strength training: the effects of three different regimes and the nature of the resultant changes," *Journal of Physiology*, vol. 391, pp. 1–11, 1987.
- [36] Y. Kawakami, Y. Ichinose, and T. Fukunaga, "Architectural and functional features of human triceps surae muscles during contraction," *Journal of Applied Physiology*, vol. 85, no. 2, pp. 398–404, 1998.
- [37] S. H. Hayes and S. R. Carroll, "Early intervention care in the acute stroke patient," *Archives of Physical Medicine and Rehabilitation*, vol. 67, no. 5, pp. 319–321, 1986.
- [38] S. Hesse, C. Werner, T. Paul, A. Bardleben, and J. Chaler, "Influence of walking speed on lower limb muscle activity and energy consumption during treadmill walking of hemiparetic patients," *Archives of Physical Medicine and Rehabilitation*, vol. 82, no. 11, pp. 1547–1550, 2001.
- [39] L. Li, K. Y. Tong, X. L. Hu, L. K. Hung, and T. K. K. Koo, "Incorporating ultrasound-measured musculotendon parameters to subject-specific EMG-driven model to simulate voluntary elbow flexion for persons after stroke," *Clinical Biomechanics*, vol. 24, no. 1, pp. 101–109, 2009.

Research Article

Optogenetic Activation of the Excitatory Neurons Expressing CaMKII α in the Ventral Tegmental Area Upregulates the Locomotor Activity of Free Behaving Rats

Songchao Guo,¹ Sicong Chen,² Qiaosheng Zhang,¹ Yueming Wang,¹ Kedi Xu,¹ and Xiaoxiang Zheng^{1,2}

¹ *Qiushi Academy for Advanced Studies, Zhejiang University, Hangzhou 310027, China*

² *Institute of Biomedical Engineering, Zhejiang University, Hangzhou 310027, China*

Correspondence should be addressed to Kedi Xu; xukd@zju.edu.cn

Received 4 December 2013; Accepted 14 January 2014; Published 10 March 2014

Academic Editor: Ting Zhao

Copyright © 2014 Songchao Guo et al. This is an open access article distributed under the Creative Commons Attribution License, which permits unrestricted use, distribution, and reproduction in any medium, provided the original work is properly cited.

The ventral tegmental area (VTA) plays an important role in motivation and motor activity of mammals. Previous studies have reported that electrical stimulations of the VTA's neuronal projections were able to upregulate the locomotor activity of behaving rats. However, which types of neurons in the VTA that take part in the activation remain elusive. In this paper we employed optogenetic technique to selectively activate the excitatory neurons expressing CaMKII α in the VTA region and induced a higher locomotor activity for free behaving rats. Further behavioral studies indicated that reward learning mediated in the enhancement of the rat locomotor activity. Finally the immunohistochemistry studies explored that the excitatory neurons under the optogenetic activation in VTA were partly dopaminergic that may participate as a vital role in the optogenetic activation of the locomotor activity. In total, our study provided an optogenetic approach to selectively upregulate the locomotor activity of free behaving rats, thus facilitating both neuroscience researches and neural engineering such as animal robotics in the future.

1. Introduction

Optogenetics comprises a set of techniques that integrate the opsin genes into specific types of neurons to selectively probe the neural circuits [1, 2] and has currently been introduced into a growing number of neuroscience researches [3–6] and neural engineering systems such as the brain-machine interfaces [7, 8]. The optogenetic technique enables either excitation or inhibition of selected neural populations under the delivery of light at specific wavelengths [9, 10]. Basically the opsin genes are able to express light-sensitive membrane ion channels, produce ion flows, and thus induce or suppress the action potentials in living neural populations [9]. The channelrhodopsin-2 (ChR2), one of the opsin cation channels [10, 11], is typically transduced into excitatory neurons [12, 13] under the guidance of certain promoters such as the calcium-modulin dependent kinase II type- α (CaMKII α) promoters.

The specific neurons with ChR2 and CaMKII α expressions would produce action potentials upon the delivery of blue light at a central wavelength of 473 nm [1, 2].

In animal brains, the vast majority of the excitatory neurons expressing CaMKII α are distributed in cortex areas and hippocampus [1, 14]. For rats, the CaMKII α was also found in deep brain regions, for example, the ventral tegmental area (VTA) within the ventral striatum [15, 16]. The VTA comprises a variety of neurons located on the floor of the midbrain that relate to the mesolimbic dopaminergic system and is widely implicated in the natural reward circuitry of the brain as well as drug addiction and motor activity. Particularly, electrical stimulations of the medial forebrain bundle (MFB), one of the neuronal projections from the VTA region, were able to upregulate the rat locomotor activity as a part of the rat-robot systems [17, 18]. However, the precise mechanisms underlying such rat-robot systems remain unclear, largely due

to the extensive and unselective effect of electrical stimulation on all types of neurons. Actually, besides dopaminergic neurons, the VTA also contains glutamatergic neurons [19] that are regarded as a type of excitatory neurons expressing CaMKII α . Yet few researches have been engaged in how such excitatory neurons take part in the VTA neuronal activities and whether these neurons alone could influence behavioral conditionings such as locomotor activities.

In this paper we selectively activated the excitatory neurons in the VTA region by optogenetic transductions of the CaMKII α -ChR2-mCherry virus into the rat brain. Both histological and electrophysiological methods verified the robustness of the optogenetic manipulations. We found that the optical activations on these VTA neurons were able to induce an enhanced locomotor activity of free roaming rats. Further results revealed that these VTA neurons under optogenetic activation may involve the reward learning mechanisms and were partly dopaminergic, consistent with previous reports on both structural and functional properties of the VTA [20–24]. Taken together, our study based on the optogenetic techniques has provided a novel method to selectively upregulate the locomotor activity of free behaving rats, which could be integrated into the rat-robot systems for precise controls. Also we have further approached the explanation of mechanisms underlying the rat-robot control strategies, thus facilitating future work on both animal robotics and neuroscience researches.

2. Material and Methods

2.1. Animal Subjects. Adult male Sprague-Dawley rats with 180 ± 10 g body weight were chosen from Zhejiang Academy of Medical Sciences (Hangzhou, China). All the rats were housed in a temperature-controlled room ($23 \pm 3^\circ\text{C}$) with access to water and mildly food-deprived to 85% of free-feeding body weight. The rats were kept in individual cages on a 12 h light/dark cycle (lights on at 6 am).

2.2. Surgeries

2.2.1. Optrode Implantation. The optrode array device used in this paper was designed in our previous study [25]. The implantation of the array device was implemented by craniotomy on the rats over four postnatal weeks. In general the rats were anesthetized with 1.0% sodium pentobarbital, sheared over the head, and fixed in a stereotaxic apparatus (Stoelting Co., Ltd., USA). For each subject, the craniotomy was centered on the brain region dorsal to the left VTA region: -4.8 mm posterior to the bregma (AP), 1.0 mm lateral to the midline (ML), and -8.0 mm ventral to the cortical surface (DV) according to the atlas of Paxinos and Watson. A series of skull holes were drilled for placement of four skull screws to provide mechanical support as well as common ground references for the implanted array device. In particular, a round craniotomy window with 1.0 mm diameter was drilled for implanting the array device. The dura matter was carefully peeled away using a sterilized needle with operations under microscopy. Then the array device,

yet without the optical fiber, was stereotactically implanted through the craniotomy window into the targeted brain area exactly above the left VTA region. In addition, a ground reference electrode from the array device was bundled firmly on all the skull screws. Finally the craniotomy window was filled with clinical ionized gel for protecting the inner brain and the entire scalp area was covered up using dental acrylic. The rats were allowed to recover for 5–7 days before use in the viral delivery and the optical fiber implantation.

2.2.2. Viral Delivery and Fiber Implantation. The surgeries for viral delivery and optical fiber implantation were implemented via the optrode array device as described above. The rats were anesthetized with 1.0% sodium pentobarbital and again stereotactically fixed. Adenoassociated viral vector serotype 5 (AAV-5) carrying the opsin gene of ChR2 and the gene for red fluorescent protein (mCherry) under CaMKII type- α promoter (Figure 1(a), AAV-CaMKII α -ChR2-mCherry, $\sim 5 \times 10^{12}$ titer, Neuron Biotech, Shanghai, China) was delivered into the rat brain using the microinjector (World Precision Instruments, Co., Ltd.) fixed on the stereotaxic apparatus. For each rat, 1.0 μL of viral vector was injected through the guide cannula of the optrode array device into the left VTA (DV = -8.5 mm). The timing procedure of the viral injection was consistent with [11]. The microinjector and surgical apparatus were thoroughly sterilized after viral injection.

Upon finishing the viral delivery, an optical fiber with one-end FC tail was stereotactically implanted through the guide cannula such that the fiber tip reached the dorsal edge of the VTA region (DV = -8.0 mm, 0.5 mm upper than the viral injection site) and the FC tail lay above the optrode cannula. Finally the optical fiber was covered up and mounted firmly on the entire array device using dental acrylic. The rats were kept for recovery and ChR2 expression for four weeks.

2.3. In Vivo Optical Stimulation and Electrophysiology. The optical instruments consisted of a 500 mW laser emitting 473 nm blue light (BL473T5-320FC, Shanghai Laser & Optics Century Inc., China) and a 3-meter optical fiber jumper with 50/125 multimodal glass optical fibers inside. The fiber jumper was connected to the laser and coupled to the optical fiber on the rat head by a plastic, tube-shaped FC-FC interface adapter [25]. The laser was triggered by transistor-transistor logic (TTL) pulses generated from a PG4000A digital stimulator (Cygnus Technology Inc., USA). The light power was measured by an optical power meter (LTE-1A, Chinese Academy of Sciences, Beijing, China). Usually a light power of 1–3 mW at the end of optical fiber jumper was approved for the following *in vivo* studies.

For *in vivo* electrophysiology, the electrical signals were recorded from the free behaving ChR2 rats via the Omnetics connector [25] jointed on the optrode device over the rat head. The signals were processed by a Plexon Multichannel Acquisition Processor (1–40 kHz rate, Plexon Inc., Dallas, TX). Signal preprocessing, including amplifications on programmable gain and filtering (set at 150 Hz–8 kHz band pass) for spikes, was implemented using the OmniPlex Controller

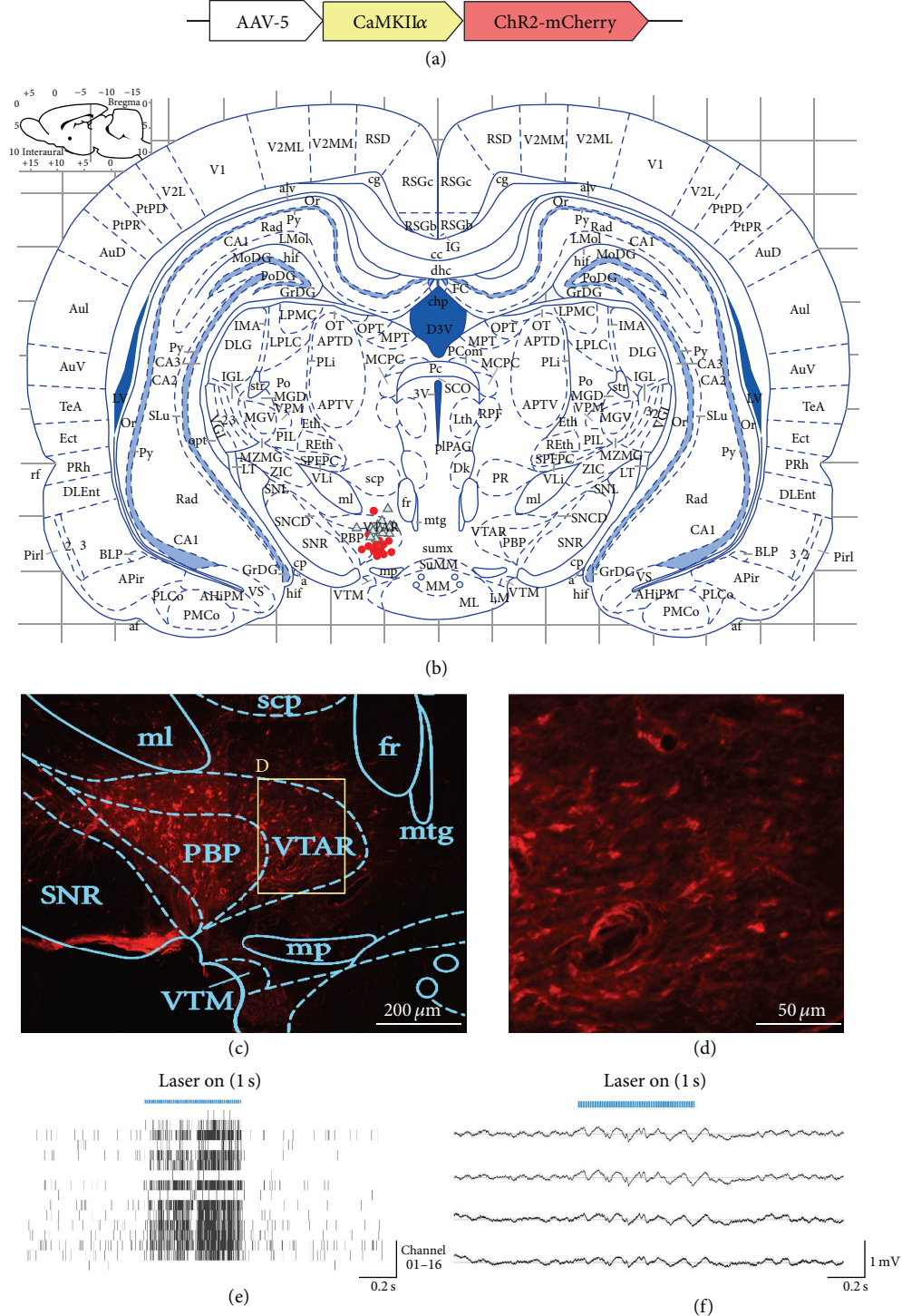


FIGURE 1: Histology and *in vivo* electrophysiology for verification of the optogenetic studies. (a) Sketch of the AAV vector used for the optogenetic transductions in this study. (b) The centers of viral-delivery regions (the red circular dots) and the placements of optical fiber tips (the blue triangular dots) for all the optogenetic rats ($n = 6$ for the free-moving tasks, $n = 6$ for the lever-pressing tasks, and $n = 2$ for erroneous displacements). These two series of dots were measured by individually locating the traces of optrode fiber tips and of the microinjector observed under microscopy. Both series of traces were measured in the targeted brain slices with AP = -4.8 mm from Bregma and overlapped into the atlas of Paxinos and Watson. (c) A typical view of the ChR2-mCherry expressions on the neurons expressing CaMKII α in and around the brain region of VTA that was overlapped with the brain atlas. (d) An inner set of (c) obtained from the region of interest (ROI) from the VTA region (including VTAR and PBP). ((e)-(f)) *In vivo* electrophysiology recorded from the implanted optrode device. The blue bar shown in both figures represents a shot of laser stimulations with 15 ms pulse width, 50 Hz frequency, 1.0 s duration, and a light power around 1 mW. (e) presents spike activities from all the sixteen channels of the optrode device where each short straight bar represents one spike firing, and (f) is the LFP signals recorded from four typical channels of the optrode device.

as a part of the Plexon platform. Local field potentials (LFPs) were also recorded with band pass filtering at 10–170 Hz and digitized at 1 kHz sampling rate.

2.4. Design of Behavioral Experiments

2.4.1. Free-Roaming Tasks with Field Tracking. The optogenetic rats were taken a series of behavioral experiments for free roaming in a circular field with 1.2 meters in diameter and were video-tracked throughout the experiments. The free-roaming tasks were given for 6 consecutive days. During each day, the rats were given three individual sessions, denoted as the *nonstim*, *optic stim*, and *optic blocking* sessions. For each session, the rats were allowed for 15 minutes free behaving to adapt the environment in the field with the optical fiber connected on its head, followed with a 10-minute test session: for the *nonstim* session, no laser stimulus was given; for the *optic stim* session, the rat was given a series of laser stimuli once every 0.6 second during the entire 10 min session with 15 ms pulse width, 50 Hz frequency, 0.2 s duration, and a light power at 1–3 mW; yet for the *optic blocking* session, the same laser stimuli were given, but the laser was blocked on its path at the FC interface over the rat head (using a thin ceramic chip). The rat movements were video-recorded across the whole test session for further analyses.

The video recorded from each session was processed for rat figure recognition using the OpenCV techniques [26] such that the rat locations during the test session were captured as the planar coordinate data (x, y) for the rat's gravity center. The data were then traced and jointed together to form a tracking map for free roaming in the field throughout the session (by MATLAB version 6.5, Mathwork software, USA), and the total intrasession distance of the free roaming rat was then calculated.

2.4.2. Lever-Pressing Tasks. The lever-pressing tasks involved two groups of rats: the optogenetic rats ($n = 6$) with ChR2 expression in the VTA region and the control rats ($n = 6$) with microinjection of saline instead of the viral vector. The lever-pressing tasks were conducted for 6 consecutive days with a 30-minute test session per day for each rat. During the test session, the rat again connected with the optical fiber on its head was gently placed into the chamber for lever pressing with a fixed-ratio 1 (FRI) schedule: upon one lever press, the lever would automatically trigger the PG4000A stimulator and the laser device to generate a 1.0-second laser stimulus with the same pattern as in the free-roaming tasks. A video camera was mounted on the top for video recording. Basically, the rat pressing the lever with its forepaws was judged as a “correct” or an “active” press; the lever pressing or hitting by other parts of the rat body was regarded as an “incorrect” or “passive” press. Both the numbers of correct and incorrect lever presses were individually counted.

2.5. Histological Studies. The rats after the behavioral experiments were anesthetized with a lethal dose (240 mg/kg) of sodium pentobarbital and perfused transcardially with 300 mL saline at room temperature (RT) followed by 300 mL

4% paraformaldehyde (PFA). The head was removed following perfusion and embedded in 4% formaldehyde solution for two days at 4°C fridge. The brains were then transferred into 30% sucrose and embedded for one day before the frozen section. The brains were sectioned into 40 μ m coronal slices. The frozen brain slices were used for verification of the recording and optical stimulating sites by observing the different optrode traces inside the slices under a microscope. Fluorescent images were taken to identify the distribution of ChR2-mCherry expression in and around the left VTA region. Two sets of traces on the brain slices, one was the centers of viral delivery and the other was the tips of optrode fibers, were individually measured with the assistance of the atlas of Paxinos and Watson for neuroanatomical studies.

Immunohistochemistry was conducted with the 40 μ m coronal brain slices prepared in the same manner. The brain sections were rehydrated by free-floating in the phosphate buffer solution (PBS) for 15 minutes. Tissues were next incubated in –20°C pure methanol for 10 minutes. Thereafter the brain slices were incubated with the primary antibody (Rat antityrosine hydroxylase, Ab6211, Abcam, Cambridge, MA, USA) at a concentration of 1:500 diluted with 0.1% Triton X-100 and 4% Bovine serum albumin (BSA) in 4°C fridge over two days. After incubation with the primary antibody, the brain slices were then washed with PBS for 10 min \times 5 times. The secondary antibodies (Alexa Fluor 488, rabbit anti guinea pig, Invitrogen, Carlsbad, CA, USA) at a concentration of 1:1000 in PBS were employed and the tissues were incubated for 2 hours at RT. Then the washing steps for the primary antibodies were repeated. The brain tissues were then carefully mounted on glass slides for later observations with confocal microscopy. For each optogenetic rat, part of the sections containing optrode traces was selected for detail analyses.

2.6. Data Analysis. Data acquired from the free-roaming studies were analyzed with two-way repeated measures ANOVAs, while Student's *t*-test was employed to compare the average distances across 6 sessions under the *nonstim*, the *optic blocking*, and the *optic stim* as well as the trained *optic stim* patterns individually, where $P < 0.05$ indicated statistical differences.

For the lever-pressing tasks, numbers of lever pressing during one 30-minute session for both optogenetic rats and control rats were individually averaged for each day and were mapped to time-course curves. The data of both groups for the six days were individually compared again using *t*-test with $P < 0.05$ indicating statistical differences.

3. Results

3.1. Optogenetic Expression and Optical Activation of Neural Activities in the VTA Region. For optogenetic transductions, the AAV-type-5 viral vectors carrying CaMKII α -ChR2-mCherry (see Figure 1(a)) were injected into the VTA region of the rat brains. Figures 1(c) and 1(d) provided typical views of the histological data, which revealed a high density of ChR2-mCherry expressions in the targeted VTA region

(VTAR and PBP) with normal cell morphologies. The center of the opsin expressions (red dots in Figure 1(b)) and the location of the optical fiber end (blue dots in Figure 1(b)) of each rat were presented on the brain slices as shown in Figure 1(b). The assemblies of trace labels revealed that the ChR2 optogenetic expressions were precisely located in the VTA region with the optrode fiber tip ~ 0.5 mm above for most of the rats, appropriate for light penetrating on the brain regions with opsin expressions.

The neuronal activities of the VTA neurons during optical stimulations were electrically recorded *in vivo* via the implanted optrode array devices. Figures 1(e) and 1(f) showed the spike firing activities and local field potentials recorded from multiple channels in the VTA region, respectively. The laser bars displayed in both Figures 1(e) and 1(f) indicated 473 nm laser delivery with the same stimulating pattern as in the free-roaming tasks (see Section 2.4.1). It was observed that a 1.0-second laser stimulus induced a significant increase in spike firing activities reflected in most channels (13 out of 16) from the array device, and after the end of laser stimulus the spike activity fell to the basic level. Similar results were observed in LFP changes where the field potentials exhibited a higher magnitude during the 1.0 s laser stimulus. Both results indicated that the *in vivo* optical stimulations on the optogenetic neurons enabled an increased neuronal activity in the VTA region.

3.2. The Optogenetic Rats Exhibited an Increased Locomotor Activity upon Light Stimulation during Free-Roaming Tasks. The optogenetic rats were performed with free-roaming behavioral tasks to illustrate the influence of optical stimulation on their locomotor activities. Two typical tracking maps of the rat in-field roaming during a *nonstim* and an *optic stim* session, respectively, were shown in Figures 2(a) and 2(b). Normally in the *nonstim* session the rat would exhibit a short-term roaming for exploration and then stay still against the edge wall for the rest of the session. While, in the *optic stim* session, the rat exhibited a more intense and long-term free roaming that it would travel more laps along the circular field. Also it was observed that during the *optic stim* session the rats took far more approaches into the center region of the field which is considered as an open field where normal rats seldom stay [27]. The time courses of the intrasession distances revealed statistical differences between *optic stim* and *nonstim* sessions for most days of free-roaming tasks (see Figure 2(d)). The bar plot of average intrasession distances across the six task days further indicated that the rats during *optic stim* sessions ran a significantly higher distance over *nonstim* sessions (see Figure 2(e)). The above data suggested that the rats under the optogenetic stimulation in VTA were able to exhibit a higher locomotor activity in the free-roaming tasks.

Although the rats had shown an increased locomotor activity in the above tasks, one might doubt that the “light leakage” during laser stimulations would influence on the behaving rats by light flashings over the rat eyes. An alternative series of free-roaming sessions with the laser blocked at the FC interface over the rat head (denoted

optic blocking) was designed to eliminate the “light leakage” influences. Figure 2(c) displayed the tracking map from a typical *optic blocking* session. Compared with Figure 2(a) from the *nonstim* session, little change was observed either on traveling laps or on approaches into the center field. The time courses of *optic blocking* sessions versus *nonstim* sessions revealed no statistical differences for the task days (see Figure 2(d)), and nor did the average bar plot show differences (see Figure 2(e)). Interestingly, it was observed from the plots that the *optic blocking* sessions held a slightly higher locomotion than the *nonstim* ones, yet with no statistical changes. This phenomenon was probably related to certain baseline properties of the rats’ behavioral conditions, such as the curiosity to or being frightened with the frequent light flashings that we usually observed at the beginning of the free-roaming tasks. In general the data above suggested that simple light flashing over the rat eyes had no significant influences on the locomotor activity of the free behaving optogenetic rats. Totally, the behavioral data of free-roaming studies shown in Figure 2 supported our hypothesis that optogenetic activation of the excitatory neurons expressing CaMKII α in the VTA has positive reinforcement properties on the locomotor activity of free behaving rats.

3.3. Optogenetic Rats Achieved Better Performances in Lever-Pressing Tasks That Involves Reward Learning. The underlying mechanisms of the optogenetic activation in the free-roaming tasks were probably depending on the reinforcing properties of VTA in the process of reward learning. Thereby we hypothesized that the optogenetic excitation of the VTA neurons expressing CaMKII α played a role of “virtual reward” that could induce reward seeking behaviors. For further investigation we conducted a set of lever-pressing tasks with optical self-stimulation in the VTA region for both optogenetic rats and controls as mentioned in Section 2.4.1. The data plotted in Figures 3(a) and 3(b) showed that the total intrasession lever presses of optogenetic rats were significantly higher than those of controls in most sessions. Also we note that the time course of optogenetic rats revealed an ascending tendency over the sessions. Besides, the plots of “correct rate” indicating the percentage of active lever presses during each session (see Figures 3(c) and 3(d)) showed that the optogenetic rats held a significantly higher correct rate than the controls for most sessions. Likewise, the time course of optogenetic rats in Figure 3(c) revealed an ascending tendency, whereas the course of controls appeared random with no tendency at all. In total, the data of lever-pressing tasks indicated that the optogenetic rats tend to make far more lever presses than the controls for obtaining the optical stimulation. Since the lever-pressing study is considered as a typical test for validation of reward learning, the results from the above data provided evidence to our hypothesis that the optogenetic activation of the excitatory neurons expressing CaMKII α in VTA played a role of virtual reward that led to a positive effect on the reward learning processes.

Besides the learning of lever pressing, the learning of free roaming for obtaining the optical “reward” was also behaviorally conditioned on the optogenetic rats in this study.

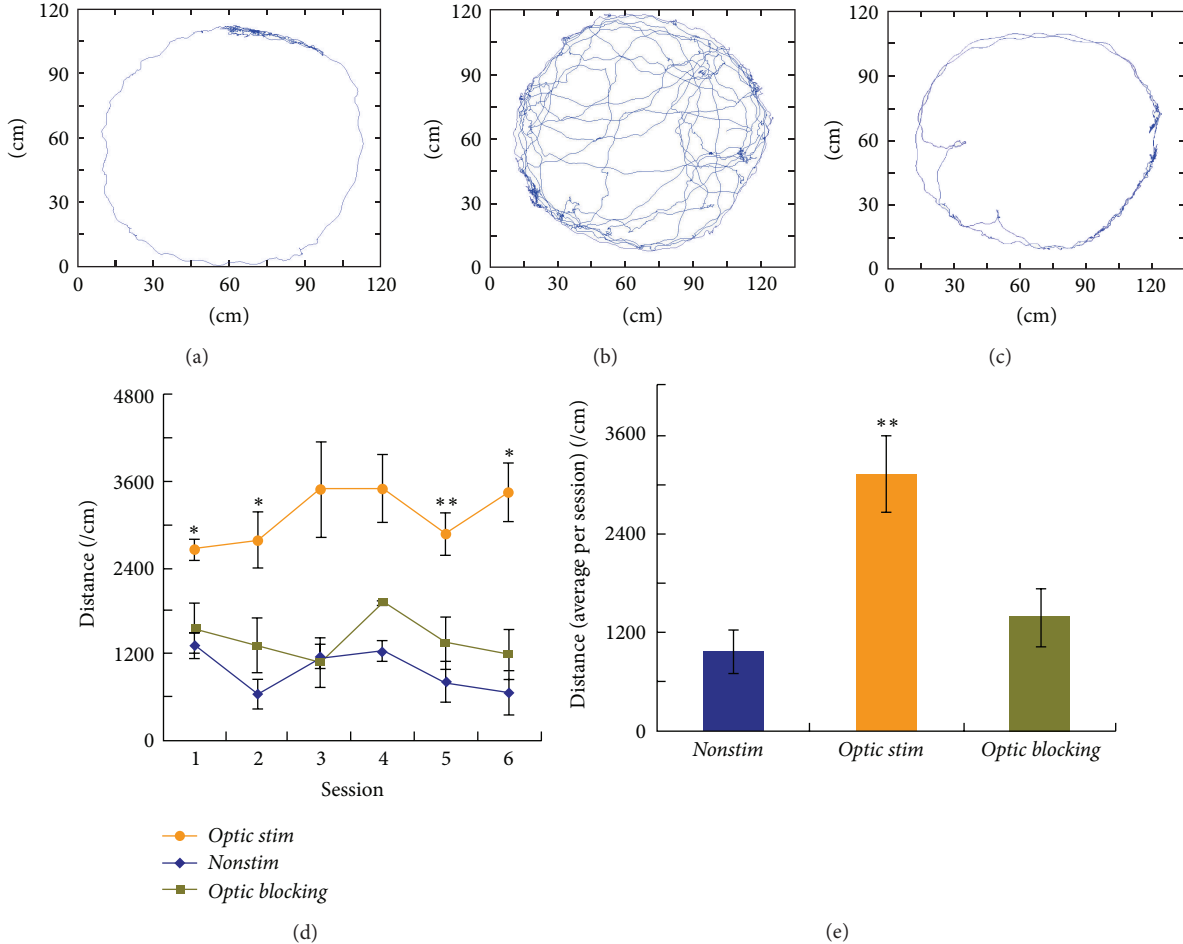


FIGURE 2: Data of the free-roaming tasks between the *nonstim*, *optic stim*, and *optic blocking* sessions. ((a)–(c)) Field tracking maps typically for the *nonstim*, the *optic stim*, and the *optic blocking* session, respectively. (d) Time courses of the intrasession distances for the above three sessions (see the figure legends). The error bar in each session dot represents the standard deviation of all the rats for the session ($n = 6$ for each session dot). Single asterisks represent statistical differences between the session dots of *optic stim* and *nonstim*, whereas double asterisks represent significant differences between them. (e) The results from the time course (d) were averaged and then bar-plotted over the three sessions. Double asterisks represent a significant difference compared to the results of *nonstim* sessions.

The procedures of training were basically the same with previous free-roaming tasks except that the laser stimulations were given manually once the rat started roaming. After six days of training, we repeated the free-roaming tasks on these trained rats over both *optic stim* (or the *trained stim*) and *nonstim* sessions. From the tracking maps (Figures 4(a) and 4(b)) a far more intense roaming in the *trained stim* session than the *nonstim* one appeared. Moreover, the time course of the *trained stim* sessions displayed a significant higher level over the *nonstim* one (see Figure 4(c)). Besides, a clear view of ascending tendency was observed from the *trained stim* course, which probably indicated the enhancement of reward learning processes of the rats. Both bar plots (Figures 4(d) and 4(e)) revealed that the average intrasession locomotion in the *trained stim* sessions was significantly higher than the *nonstim* ones and appeared the greatest among all the four types of sessions (*nonstim*, *optic blocking*, *optic stim*, and *trained stim*). Remarkably, the results of the *trained stim* sessions were statistically higher than those of the *optic stim* sessions before

training, consistent with the properties of reward learning behaviors. Taken together, the above results suggested that reward learning took part in the mechanism underlying the optogenetic activation of the neurons expressing CaMKII α in the VTA of behaving rats and that by the reinforcement of reward learning, better performances on the rat locomotor activity were likely to be achieved.

3.4. The VTA Neurons under the Optogenetic Activation Were Partly Dopaminergic. In the above experiments we employed optogenetic manipulations on the excitatory neurons in the rat VTA region and conditioned a higher locomotor activity of free behaving rats based on the mechanism of reward learning. It is usually considered that dopaminergic (DA) neurons in the ventral striatum mediate in the reward learning mechanisms. Thus we investigated whether the DA neurons in VTA were selectively activated by the optogenetic manipulations in our study. The immunohistochemistry studies were employed to assess the locations of both the cell

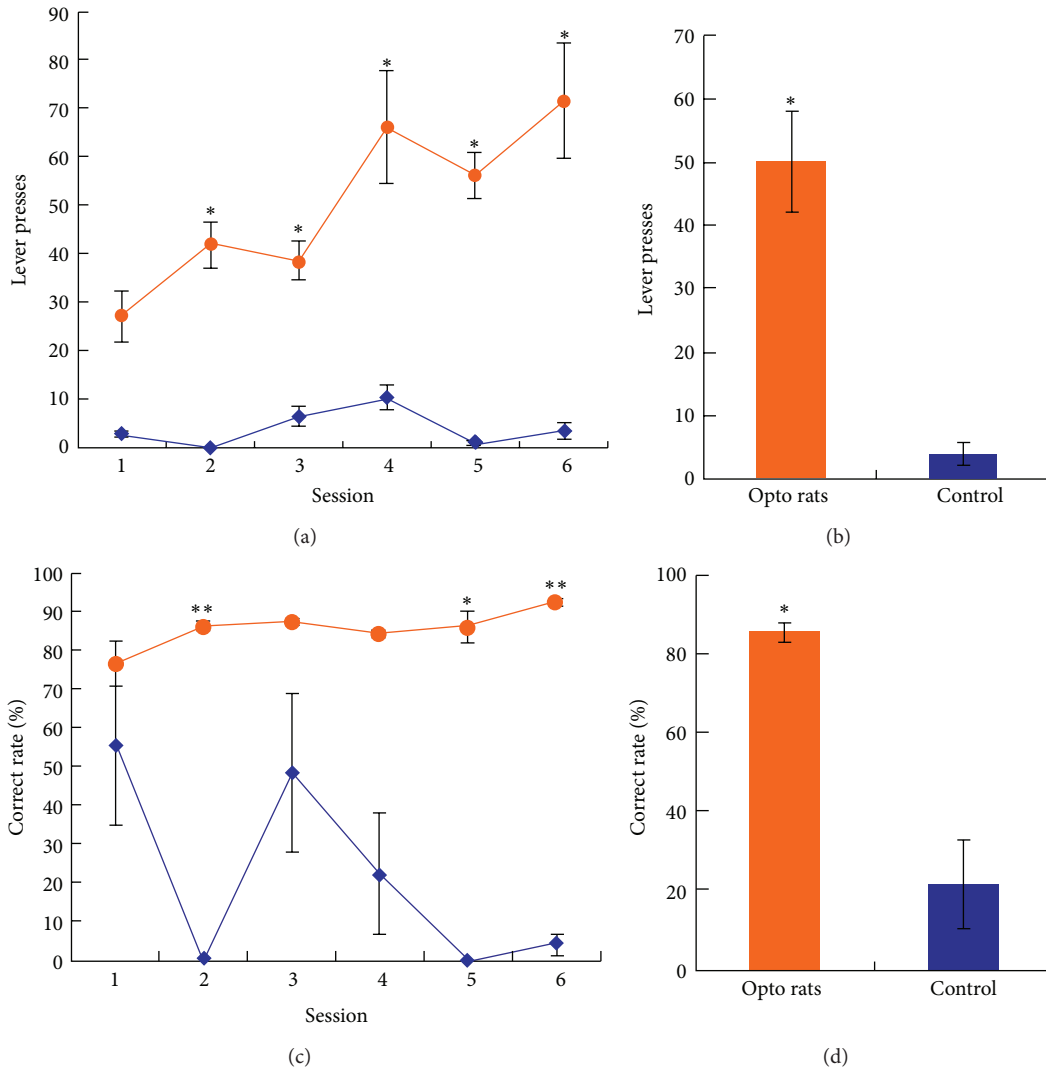


FIGURE 3: Data of the lever-pressing tasks for both optogenetic rats (denoted “opto rats”) and control rats. (a) Time courses of the total lever presses intrasession for opto rats and control rats individually (see the figure legends). (b) The total lever presses from (a) were averaged across all the six sessions and bar-plotted. (c) The correct rates, indicating the percentages of active lever presses within single sessions, were plotted as time courses for opto rats and control rats (see the figure legends). (d) Bar plot of the correct rates calculated from a total collection of lever-pressing data. For all the subfigures, the error bars in session dots or in bars represent the standard deviation of all the rats undertaking the session ($n = 6$ for each session dot or bar). Single asterisks represent statistical differences between the opto rats and controls, whereas double asterisks represent significant differences between them.

bodies labeling tyrosine hydroxylase- (TH-) GFP, a marker for DA neurons, and the cell bodies expressing CaMKII α -mCherry by optogenetic transduction in the VTA region. Figure 5 displayed a typical set of the results. Figures 5(a)–5(c) revealed that both the expressions of CaMKII α -mCherry and TH-GFP were distributed in relative narrow area that contains the VTA. It was observed that the TH positive neurons appeared a higher density than the neurons expressing CaMKII α , consistent with previous reports that DA neurons held a predominant percentage in VTA [22]. Both the expressions of CaMKII α -mCherry and TH-GFP were ranged over the VTA region. Figures 5(d)–5(f) revealed that most TH positive neurons and CaMKII α positive neurons differed in cell morphologies. However, despite the fact that most

TH positive neurons do not express CaMKII α , and many CaMKII α positive ones do not contain TH [19], there existed a substantial number of neurons expressing both CaMKII and TH (see Figure 5(f) and white arrows in Figure 5(i)). The immunohistochemistry data above indicated that part of the VTA neurons expressing CaMKII α corelease TH, thus exhibiting a dopaminergic property. These “dopaminergic” neurons appeared to take only a small percentage of the vast DA neurons within the VTA region.

4. Discussion

In this study we employed *in vivo* optogenetic transduction on the excitatory neurons in the brain region of VTA for

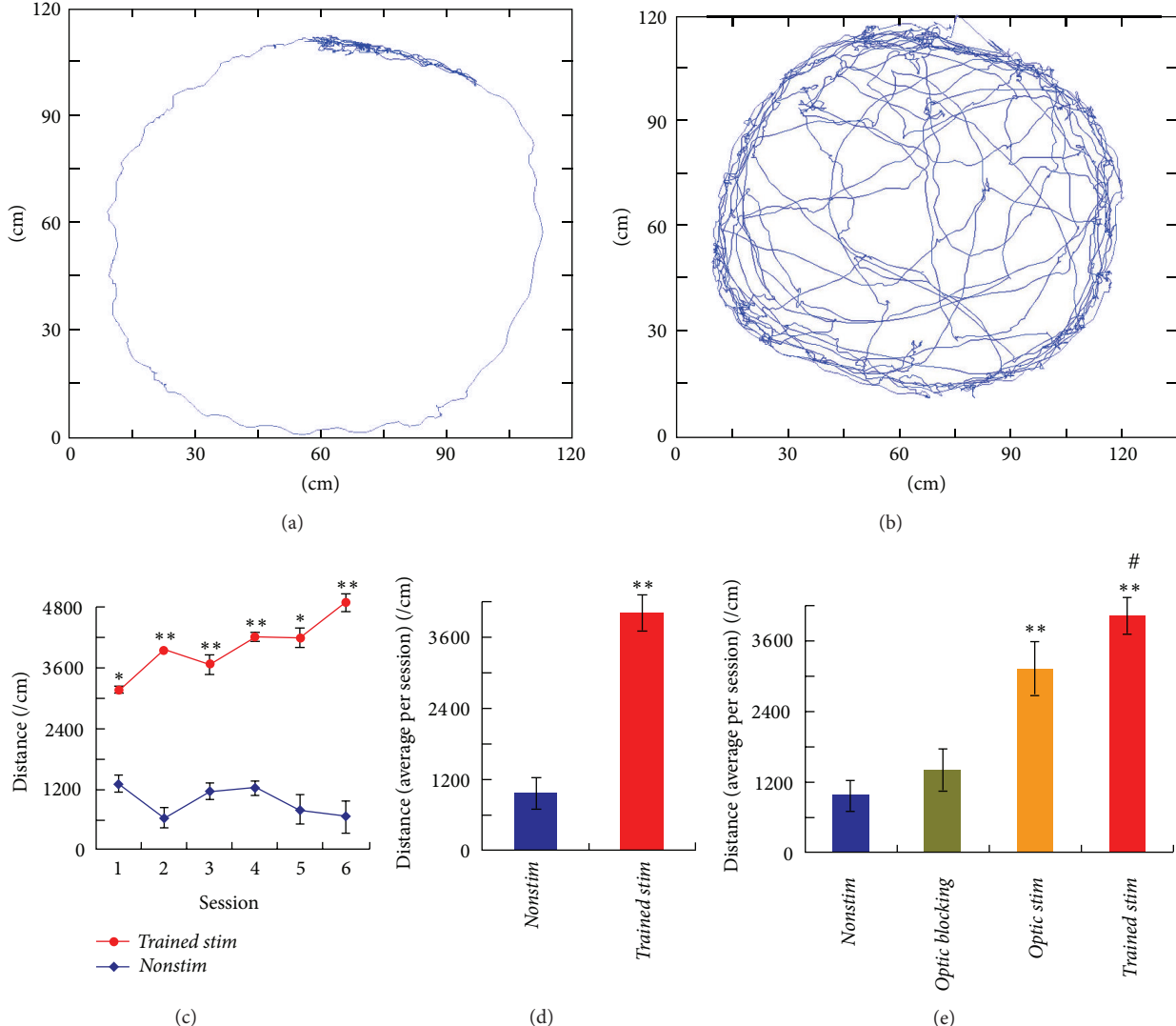


FIGURE 4: Data of free-roaming tasks combined with the *trained stim* sessions. (a and b) Field tracking maps of the *nonstim* and the *trained stim* session, respectively. Data and figures were acquired in the same manner as in Figure 2. (c) Time courses of the intrasession distances for both the *trained stim* and the *nonstim* sessions (see the figure legends). The error bar in each session dot represents the standard deviation of all the rats for the session ($n = 6$ for each session dot). Double asterisks represent significant differences between the session dots of *trained stim* and *nonstim*. (d) The intrasession distances were averaged from (c) and were bar-plotted over the *trained stim* and the *no-stim* sessions, where double asterisks represent a significant difference between them. (e) The bar plot of the average intrasession distances for all the four types of free-roaming sessions, the *nonstim*, the *optic blocking*, the *optic stim*, and the *trained stim*. Double asterisks represent significant differences compared to the *nonstim* data, while the sharp represents a statistical difference between the *optic stim* and the *trained stim* sessions.

adult rats by viral delivery of the AAV vector carrying ChR2 opsin genes. Our findings on the free-roaming tasks demonstrated that the optogenetic rats with ChR2 expression in the excitatory neurons expressing CaMKII α in VTA behaved at an increased locomotor activity upon 473 nm light activation while freely roaming in the circular field. This phenomenon was not likely owing to simple “light leak” effects with the blue light emitting over the rat eyes.

Further results on the lever-pressing tasks revealed that reward learning was mediating in the mechanisms underlying the CaMKII optogenetic activation in VTA in the above studies. These findings were consistent with previous

reports that the activation of VTA neurons was able to induce reward learning behaviors for receiving the intracranial self-stimulations (ICSSs) [28]. Remarkably, in previous studies the highly frequent lever-pressing behaviors were typically induced by electrical stimulations, during which all the neural populations within the VTA were activated compulsively, making it unclear whether any type of subpopulations was involved in the reward learning behaviors. In this paper, however, we specifically activated the excitatory neurons expressing CaMKII α in the VTA by optogenetic manipulations and induced similar lever-pressing behaviors of the rats. These results indicated that these excitatory neurons

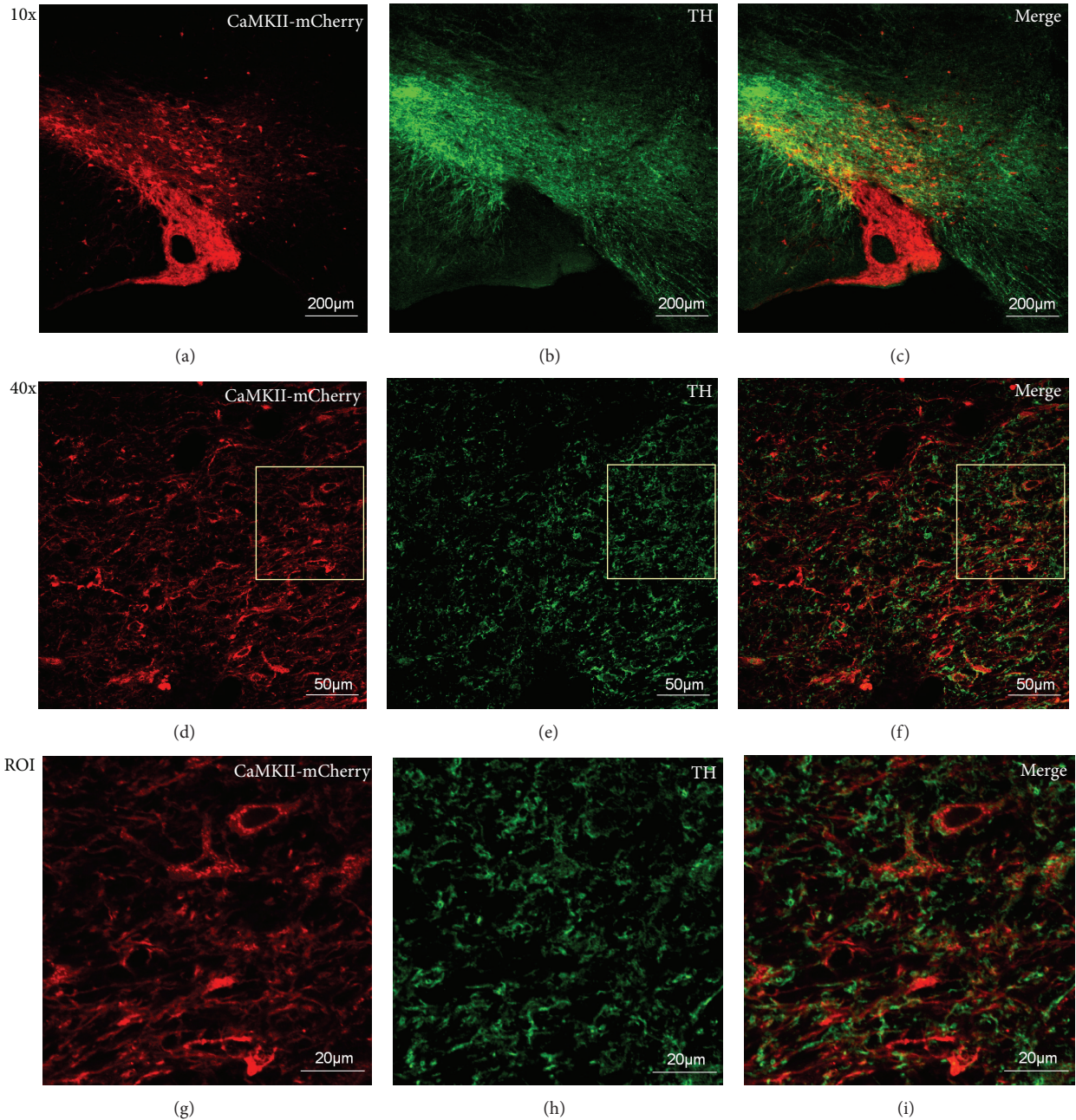


FIGURE 5: Immunochemistry results from the VTA region of brain slices from the optogenetic rats. All the subfigures were photographed under confocal microscopy and processed using the FV1000 software (Olympus Inc., Japan). The red channels represent CaMKII α -mCherry expressions and the green channels represent TH expressions, whereas the right column (Figures 5(c), 5(f), and 5(i)) indicates the merged two channels. ((a)-(c)) A typical view of the CaMKII α -mCherry and TH-GFP expressions under 10x microscopy. ((d)-(f)) A selected VTA region observed under 40x microscopy where the CaMKII α and TH expressions overlapped. ((g)-(i)) A region of interest (ROI) from the rectangular window shown in ((d)-(f)). The white arrows in (i) point out the several neuronal cell bodies merged with red and green channels, indicating that these neurons coexpress CaMKII α and TH.

expressing CaMKII α were probably a key population in the VTA that played a vital role in the conditioning of reward learning as in the lever-pressing tasks. Moreover, we repeated the free-roaming tasks on the optogenetic rats after a short-term training where light stimuli were given, while the rat was roaming forward, and observed that the rats performed a higher locomotor activity than before. These results further

indicated that the reinforcement of reward learning placed a positive effect on the results of free-roaming tasks.

The immunohistochemistry further explored the nature of the excitatory neurons expressing CaMKII α in VTA under the optogenetic manipulation. The results revealed that those neurons expressing CaMKII α were partly collocated with dopaminergic neurons at the VTA region. The “collocated”

neurons” took only a small percentage of the VTA DA neurons, but they were observed in an appropriate area where light stimulations were reachable, which suggested that these neurons coexpressing CaMKII α and DA were activated upon light stimulations and probably took an active part in the behavioral conditionings in this study. Since the expressions of CaMKII α were widely implicated in glutamatergic neurons [1], those “collocated neurons” were likely to be neurons that corelease DA and glutamine in nature, consistent with previous reports that there exist a substantial area of excitatory neurons in the VTA region that corelease dopamine and glutamine and contribute to the functioning of reward learning and related behavioral conditionings [29, 30].

However, it was suggested from the immunohistochemistry results that there existed an alternative type of neurons that expresses CaMKII α but does not express TH. These neurons differed in cell morphology from the dopaminergic neurons and exhibited an expression of CaMKII α -mCherry. Based on the results above, it is inferred that those nondopaminergic neurons were probably simple glutamatergic neurons, consistent with previous reports that glutamatergic neurons were present in the VTA [19, 31]. According to previous reports, the exists a type of glutamatergic neurons in the VTA region that release VGlutT2 but do not release dopamine, and they exhibit different electrophysiological properties and neuronal projections apart from the VTA neurons coexpressing glutamine and dopamine [32]. Moreover, these nondopaminergic neurons expressing CaMKII α were also located in VTA within the region of light activation, which indicated that these neurons were likely to take part in the optogenetic activations as well. Combined together, the excitatory neurons expressing CaMKII α in the VTA under optogenetic activations were composed of different types of neuronal subpopulation: one is the dopaminergic neurons that may corelease glutamine, and the other neurons were probably purely glutamatergic. Both types of neurons were likely to play vital roles in the behavioral conditionings as we conducted in this paper.

In conclusion, we employed optogenetic manipulations for free behaving animals based on viral transduction of ChR2 in the brain region of VTA and behavioral conditionings on reward learning. The results demonstrated that optogenetic activations of the excitatory neurons expressing CaMKII α in the VTA were able to upregulate the locomotor activity of free behaving rats and that by reinforcement of the reward learning behaviors the rats’ locomotor activities were getting even enhanced. Further immunohistochemistry results revealed the nature of these VTA neurons expressing CaMKII α , which were partly dopaminergic that may play a vital role in the above behavioral conditionings. Future work may include further investigations on the nature of these neurons under the optogenetic activation in this study, such as the relationships between the neurons expressing CaMKII α and glutamatergic neurons in the VTA. Moreover, this study has provided a novel method to upregulate the locomotor activity by inducing the reward seeking behavior and by reward learning the “reward-motion” connectivity had gotten enhanced for the optogenetic rats, thus indicating

further applications in the field of neural engineering such as animal robotics for precise control of animal behaviors.

Conflict of Interests

The authors declare that there is no conflict of interests regarding the publication of this paper.

Acknowledgments

The work of this paper was supported by Grants from the National Basic Research Program of China (2011CB504405), the National High Technology Research and Development Program of China (2012AA011602), the National Natural Science Foundation (NSF) of China (61233015), the National NSF of China (61103107; 61001172, 61003150, 61305145, 61305146, and 31371001), the Specialized Research Fund for the Doctoral Program of Higher Education (20100101120104, 20100101120154, and 20100101120166), the Fundamental Research Funds for the Central Universities, and the Zhejiang provincial international science and technology cooperation program (2012C24025). The authors would thank Chaonan Yu for providing technical support on the fabrication of the optrode array device and on part of the surgery of craniotomy. Also the authors thank Professor Shumin Duan, Dr. Rui Zhou, and Dr. Hongbin Yang for providing tutorials on the immunohistochemistry studies in this paper.

References

- [1] O. Yizhar, L. E. Fenno, T. J. Davidson, M. Mogri, and K. Deisseroth, “Optogenetics in Neural Systems,” *Neuron*, vol. 71, no. 1, pp. 9–34, 2011.
- [2] K. Deisseroth, G. Feng, A. K. Majewska, G. Miesenböck, A. Ting, and M. J. Schnitzer, “Next-generation optical technologies for illuminating genetically targeted brain circuits,” *Journal of Neuroscience*, vol. 26, no. 41, pp. 10380–10386, 2006.
- [3] I. B. Witten, E. E. Steinberg, S. Y. Lee et al., “Recombinase-driver rat lines: tools, techniques, and optogenetic application to dopamine-mediated reinforcement,” *Neuron*, vol. 72, no. 5, pp. 721–733, 2011.
- [4] K. M. Tye and K. Deisseroth, “Optogenetic investigation of neural circuits underlying brain disease in animal models,” *Nature Reviews Neuroscience*, vol. 13, no. 4, pp. 251–266, 2012.
- [5] K. Zalocusky and K. Deisseroth, “Optogenetics in the behaving rat: integration of diverse new technologies in a vital animal model,” *Optogenetics*, vol. 1, pp. 1–17, 2013.
- [6] V. Gradinariu, K. R. Thompson, F. Zhang et al., “Targeting and readout strategies for fast optical neural control in vitro and in vivo,” *Journal of Neuroscience*, vol. 27, no. 52, pp. 14231–14238, 2007.
- [7] A. M. Aravanis, L.-P. Wang, F. Zhang et al., “An optical neural interface: in vivo control of rodent motor cortex with integrated fiberoptic and optogenetic technology,” *Journal of Neural Engineering*, vol. 4, no. 3, pp. S143–S156, 2007.
- [8] T. Tokuda, S. Nakajima, Y. Maezawa et al., “An in vitro demonstration of CMOS-based optoelectronic neural interface device for optogenetics,” in *Proceedings of the 35th Annual*

- International Conference of the IEEE Engineering in Medicine and Biology Society (EMBS '13)*, pp. 799–802, Osaka, Japan, 2013.
- [9] K. Deisseroth, "Optogenetics," *Nature Methods*, vol. 8, no. 1, pp. 26–29, 2011.
 - [10] F. Zhang, L.-P. Wang, E. S. Boyden, and K. Deisseroth, "Channelrhodopsin-2 and optical control of excitable cells," *Nature Methods*, vol. 3, no. 10, pp. 785–792, 2006.
 - [11] J. A. Cardin, M. Carlén, K. Meletis et al., "Targeted optogenetic stimulation and recording of neurons in vivo using cell-type-specific expression of Channelrhodopsin-2," *Nature Protocols*, vol. 5, no. 2, pp. 247–254, 2010.
 - [12] H. Wang, J. Peca, M. Matsuzaki et al., "High-speed mapping of synaptic connectivity using photostimulation in Channelrhodopsin-2 transgenic mice," *Proceedings of the National Academy of Sciences of the United States of America*, vol. 104, no. 19, pp. 8143–8148, 2007.
 - [13] J. T. Ting and G. Feng, "Development of transgenic animals for optogenetic manipulation of mammalian nervous system function: progress and prospects for behavioral neuroscience," *Behavioural Brain Research*, vol. 255, pp. 3–18, 2013.
 - [14] Y.-P. Zhang, N. Holbro, and T. G. Oertner, "Optical induction of plasticity at single synapses reveals input-specific accumulation of α CaMKII," *Proceedings of the National Academy of Sciences of the United States of America*, vol. 105, no. 33, pp. 12039–12044, 2008.
 - [15] M. Papa, L. Diewald, M. P. Carey, F. J. Esposito, U. A. Gironi Carnevale, and A. G. Sadile, "A rostro-caudal dissociation in the dorsal and ventral striatum of the juvenile SHR suggests an anterior hypo- and a posterior hyperfunctioning mesocorticolimbic system," *Behavioural Brain Research*, vol. 130, no. 1-2, pp. 171–179, 2002.
 - [16] B. J. Wiltgen, M. Law, S. Ostlund, M. Mayford, and B. W. Balleine, "The influence of Pavlovian cues on instrumental performance is mediated by CaMKII activity in the striatum," *European Journal of Neuroscience*, vol. 25, no. 8, pp. 2491–2497, 2007.
 - [17] S. K. Talwar, S. Xu, E. S. Hawley, S. A. Weiss, K. A. Moxon, and J. K. Chapin, "Rat navigation guided by remote control," *Nature*, vol. 417, no. 6884, pp. 37–38, 2002.
 - [18] Z.-Y. Feng, W.-D. Chen, X.-S. Ye et al., "A remote control training system for rat navigation in complicated environment," *Journal of Zhejiang University: Science A*, vol. 8, no. 2, pp. 323–330, 2007.
 - [19] T. Yamaguchi, W. Sheen, and M. Morales, "Glutamatergic neurons are present in the rat ventral tegmental area," *European Journal of Neuroscience*, vol. 25, no. 1, pp. 106–118, 2007.
 - [20] L. W. Swanson, "The projections of the ventral tegmental area and adjacent regions: a combined fluorescent retrograde tracer and immunofluorescence study in the rat," *Brain Research Bulletin*, vol. 9, no. 1-6, pp. 321–353, 1982.
 - [21] R. A. Wise, "Brain reward circuitry: insights from unsensed incentives," *Neuron*, vol. 36, no. 2, pp. 229–240, 2002.
 - [22] H. L. Fields, G. O. Hjelmstad, E. B. Margolis, and S. M. Nicola, "Ventral tegmental area neurons in learned appetitive behavior and positive reinforcement," *Annual Review of Neuroscience*, vol. 30, pp. 289–316, 2007.
 - [23] K. Schierberl, J. Hao, T. F. Tropea et al., " $\text{Ca}_v1.2$ l-type Ca^{2+} channels mediate cocaine-induced glial trafficking in the nucleus accumbens, a long-term adaptation dependent on ventral tegmental area $\text{Ca}_v1.3$ channels," *Journal of Neuroscience*, vol. 31, no. 38, pp. 13562–13575, 2011.
 - [24] J. D. Lenz and M. K. Lobo, "Optogenetic insights into striatal function and behavior," *Behavioural Brain Research*, vol. 255, pp. 44–54, 2013.
 - [25] S. Guo, H. Zhou, J. Zhang, K. Xu, and X. Zheng, "A multi-electrode array coupled with fiberoptic for deep-brain optical neuromodulation and electrical recording," in *Proceedings of the 35th Annual International Conference of the IEEE Engineering in Medicine and Biology Society (EMBS '13)*, pp. 2752–2755, Osaka, Japan, 2013.
 - [26] C. Sun et al., "Automatic navigation for rat-robots: ubiquitous computing in animals," *Journal of Bionic Engineering*, vol. 10, no. 1, pp. 46–56, 2013.
 - [27] R. N. Walsh and R. A. Cummins, "The open-field test: a critical review," *Psychological Bulletin*, vol. 83, no. 3, pp. 482–504, 1976.
 - [28] J. F. Cheer, B. J. Aragona, M. L. A. V. Heien, A. T. Seipel, R. M. Carelli, and R. M. Wightman, "Coordinated accumbal dopamine release and neural activity drive goal-directed behavior," *Neuron*, vol. 54, no. 2, pp. 237–244, 2007.
 - [29] N. Chuhma, H. Zhang, J. Masson et al., "Dopamine neurons mediate a fast excitatory signal via their glutamatergic synapses," *Journal of Neuroscience*, vol. 24, no. 4, pp. 972–981, 2004.
 - [30] H.-C. Tsai, F. Zhang, A. Adamantidis et al., "Phasic firing in dopaminergic neurons is sufficient for behavioral conditioning," *Science*, vol. 324, no. 5930, pp. 1080–1084, 2009.
 - [31] A. Dobi, E. B. Margolis, H.-L. Wang, B. K. Harvey, and M. Morales, "Glutamatergic and nonglutamatergic neurons of the ventral tegmental area establish local synaptic contacts with dopaminergic and nondopaminergic neurons," *Journal of Neuroscience*, vol. 30, no. 1, pp. 218–229, 2010.
 - [32] T. S. Hnasko, G. O. Hjelmstad, H. L. Fields, and R. H. Edwards, "Ventral tegmental area glutamate neurons: electrophysiological properties and projections," *The Journal of Neuroscience*, vol. 32, no. 43, pp. 15076–15085, 2012.